Micromachined Electrostatic Force and Vertical Field Mill ac/dc Electric Field Sensors

By

Tao Chen

A thesis submitted to
the Faculty of Graduate Studies
in partial fulfilment of
the requirements for the degree of
Doctor of Philosophy

Department of Electrical and Computer Engineering
Faculty of Engineering
University of Manitoba
Winnipeg, Manitoba

September 2018

Abstract

This thesis explores several types of micromachined electric field sensors to address the main drawbacks of traditional electric field mills, namely high power consumption, big size, and the requirement of frequent maintenance. Micromachined devices possessing significantly smaller size, less power to move mechanical parts, and free of rotating parts, therefore avoid the wear and tear of moving elements.

Two types of sensors were designed. One is based on electrostatic force deflection, and another is based on a vertical movement shutter type field mill. Compared to other micromachined electric field mill (MEFM) sensors, both types of sensors overcome the issue of grounded shutter displacement under a large electric field (> 100kV/m) and provide comparable or even higher performance.

Two force deflection sensor actuators were designed and fabricated – SOI membrane and metal ribbon array. Capacitance measurement was applied to both actuators, and both show the ability to measure fields greater than 50 kV/m. When the laser monitor system was used to test the SOI membrane, similar sensitivity was achieved. In addition, the ac modulated method was applied to improve the sensitivity of the optical measurement. Providing 118.8 V (peak to peak) ac bias signal on the SOI membrane, sensitivity of 20 V/m was achieved with the ac modulated method.

The vertical movement shutter field mill is a novel design. It employs one or two pairs of bimaterial thermal actuators to provide vertical movement for the grounded shutter. It solves the problem of shutter displaced under the large field problem in existing micromachined electric field mills (MEFMs). Three types of bimaterial thermal actuators were modeled: SiO_2-Al, SU-8-Al, and Si-Al. Due to the high stress of SiO_2 thin film, the first attempt was to fabricate a SU-8-Al actuator. However, it was found that SU-8-Al actuator has a permanent deformation issue when heat up to over 100 ºC. Then efforts were focused on the Si-Al actuator, and the device was successfully fabricated. The sensor mechanical performance test shows that the shutter movement agree with the simulation at various temperature between 25 – 100 ºC. When drive the thermal actuator by digital hot plate, the measured induced current generated by an alternative electric filed also agree with the calculation.

Acknowledgements

I would like to take this opportunity to express my sincerest thanks to a number of people. First, I would like to thank my supervisor, Dr. Cyrus Shafai for his patient guidance, encouragement and advice throughout this work. I have been very lucky to have a supervisor who has been so influential in ensuring my academic, professional, financial, and moral well-being, which will be always appreciated.

I would like to express my gratitude to the Natural Sciences and Engineering Research Council (NSERC) of Canada for providing my research funding. Also I would like to thank Dr. David Swatek for his help and suggestions on this research.

I would also like to thank my dear friends in Winnipeg as well as my colleagues in the Nano-Systems Fabrication Laboratory (NSFL) of the University of Manitoba for all the academic discussion, mutual support, encouragement, and happy times working together.

I would like to express my deep love and appreciation to my family members for their unconditional love and support throughout my life. Finally, my special thanks to my wife, my son and my daughter for their love, understand and support during the past seven years.

Dedication

To my wife, my son and my daughter

Table of Contents

Abstract i

Acknowledgements ii

Table of Contents iv

List of Tables ix

List of Figures xi

Chapter 1 - Introduction 1

3.1. Existing electric field sensors 1
3.2. Microfabricated electric field sensors 2
3.3. Electric field sensors developed in this thesis 3
3.4. Thesis outline 4

Chapter 2 - Electric Field Sensors 5

4.1. Induction Probe 5
4.1.1. Traditional induction probe 5
4.1.2. MEMS induction probe 6
4.2. Traditional dc electric field mill 7
4.3. Micromachined field mills 10
4.3.1. Lateral vibration shutter field mills 10
4.3.2. Shutter and sensing electrode in the same plane field mill 12
4.3.3. Vertical vibration shutter field mill 13
4.4. Electrostatic force deflected membrane 13
4.5. Other micromachined electric field sensors 14
4.5.1. Electron deflection sensor 14
4.5.2. Electro-optic E-field sensor 15
4.6. Comparison of different techniques 15

Chapter 3 - Electrostatic Force Deflected SOI Membrane Sensor 16

5.1. Force deflection theory introduction ... 16

5.1.1. Force deflection and ac modulation ... 16

5.2. SOI membrane electric field sensor design ... 19

5.2.1. SOI membrane force deflection simulation ... 21

5.3. SOI membrane fabrication ... 25

5.3.1. SOI membrane fabrication process ... 25

5.3.2. SOI wafer fabrication experiences ... 27

5.3.3. Spring constant measurement ... 34

5.4. Motion measurement techniques ... 34

5.4.1. Grating electric field sensor ... 34

5.4.2. Field Effect transistor ... 35

5.4.3. Sensor motion capacitance measurement ... 37

5.4.4. Capacitive sensor interface electronics ... 40

5.5. SOI membrane capacitance testing ... 47

5.5.1. SOI membrane capacitance test setup ... 47

5.5.2. SOI membrane capacitance test results ... 48

5.6. ac Modulation on Capacitance Measurement ... 50

5.7. Summary ... 54

Chapter 4 - Ribbon Array Capacitance Sensor 55

6.1. Ribbon design ... 56

6.1.1. Ribbon connection simulation ... 56

6.1.2. Effect of width ... 57

6.1.3. Varying Jog Angles ... 59

6.1.4. Effect of gravity ... 62

6.2. Ribbon array fabrication process ... 64

6.3. Ribbon array capacitance test results ... 66

6.4. Capacitance measurement sensor enclosure ... 67

6.5. Summary ... 68

Chapter 5 - SOI Membrane Sensor Optical Measurement 71

7.1. Optical measurement introduction ... 71

7.2. SOI membrane optical interrogation ... 72

7.3. Compact laser position monitoring system ... 75

7.4. SOI membrane ac modulation measurement ... 75

7.4.1. SOI membrane initial testing ... 75

7.4.2. Effect of membrane bias voltage amplitude: ... 78

7.4.3. Sensor response vs. modulation frequency ... 79

7.4.4. Sensor tests at resonance and using high bias voltage: ... 81

7.4.5. Electric field under a power line ... 83

7.4.6. Sensor Testing Under Mock Transmission Line ... 84

7.5. Summary ... 88

Chapter 6 - Vertical Moving Shutter Field Mill 89

8.1. Vertical moving shutter field mill concept ... 89

8.1.1. Double side comb shutter design simulation ... 91

8.1.2. Large scale model study ... 93

8.2. Thermal actuation of the shutter ... 96

8.2.1. Design 1: SiO_2-Al thermal actuator ... 96

8.2.2. Design 2: SU-8 –aluminum thermal actuator ... 100

8.2.3. Design 3: Si-Al thermal actuator ... 103

8.2.4. Si-Al actuator resonant frequency ... 110

8.2.5. Si-Al sensor spring constant ... 111

8.2.6. Si-Al thermal actuator thermal dynamic simulation ... 111

8.3. The fabrication of designs 2 and 3 ... 113

8.3.1. SU-8-Al thermal actuator fabrication ... 113

8.3.1.1. Fabrication process ... 113

8.3.1.2. Fabrication attempt 1 ... 115

8.3.1.3. Fabrication attempt 2 ... 116

8.3.1.4. The relief of the aluminum tensile stress ... 117

8.3.1.5. The wire bonding result for the sensor: ... 118
8.3.2. Si-Al thermal actuator fabrication ... 119
8.3.2.1. Fabrication process ... 119
8.3.2.2. Fabrication attempt 1: ... 120
8.3.2.3. Fabrication attempt 2: ... 121
8.4. The test of Si-Al thermal actuator ... 122
8.4.1. Heating up the sensor in an oven ... 122
8.4.2. Driving shutter with thermal actuator ... 123
8.4.3. Sensor experimental testing ... 124
8.4.3.1. dc electric field measurement: ... 124
8.4.3.2. Shielding effect test: ... 127
8.5. The fix of isolation issue ... 132
8.5.1.1. Aluminum residue on sidewall ... 132
8.5.1.2. Preventing bad quality of the SiO_2 isolation layer ... 134
8.5.1.3. Sensor testing ... 135
8.6. Summary ... 136
8.6.1. Minimize thermal actuator size ... 137
8.6.2. Narrower finger space ... 137

Chapter 7 – Summary, conclusions and future Work 139

9.1. Summary ... 139
9.2. Conclusions and future work ... 139
9.2.1. Electrostatic force deflected SOI membrane sensor ... 140
9.2.2. Ribbon array capacitance sensor ... 140
9.2.3. SOI membrane sensor optical measurement ... 140
9.2.4. Vertical moving shutter field mill ... 141

Appendix A Charge simulation model 143

Appendix B SU-8 –Aluminum Bridge shaped thermal actuator simulation model 145

Appendix C SU-8 –Aluminum fork-shaped thermal actuator simulation model 147

Appendix D Sensor angle in the field 149

References 152

List of Tables

Table 2.1 Comparison of MEMS electric field sensors. 15

Table 3.1 Membrane displacement simulation results. 22

Table 3.2 Photoresist HPR 504 Lithograph process recipe 1. 27

Table 3.3 Si_4N_3 plasma etch recipe 1. 28

Table 3.4 Photoresist HPR 504 Lithograph process recipe 2. 28

Table 3.5 Si_4N_3 plasma etch recipe 2. 28

Table 3.6 HPR504 plasma etch recipe. 29

Table 3.7 Silicon plasma etch recipe. 29

Table 3.8 High stress copper film sputter recipe. 31

Table 3.9 Sputtered aluminum thin film stress measurement. 32

Table 3.10 Sputtered copper thin film stress measurement. 32

Table 3.11 Low stress copper film sputter recipe. 32

Table 3.12 Silicon anisotropic plasma etch experiment results. 33

Table 3.13 Measured membrane displacement vs. electric field. 34

Table 4.1 Ribbon array with connections simulation results. 57

Table 4.2 Ribbon with different width simulation. 59

Table 4.3 Ribbon with different jog angle simulation results. 62

Table 4.4 Gravity effect on ribbons simulation results. 64

Table 4.5 Comparison of SOI membrane and Ribbon array sensor. 69

Table 5.1 Summaries results of Figure 5.8. 79

Table 6.1 Large scale model shutter shielding effect test results. 95

Table 6.2 SiO_2 mechanical properties. 97

Table 6.3 Sensor output current as a function of shutter height and frequency for 1 kV/m dc electric field. 99

Table 6.4 SU-8 mechanical properties. 101

Table 6.5 Silicon mechanical properties. 104

Table 6.6 Si-Al sensor resonant frequency simulation results. 110

Table 6.7 Si-Al sensor spring constant simulation results. 111

Table 6.8 The simulated Sensor output current as a function of shutter height and frequency for 1 kV/m dc electric field. 112

Table 6.9 Fork-shaped thermal actuator test. 124

Table 6.10 Bridge-shaped thermal actuator test. 124

List of Figures

Figure 2.1 Induction probe type electric field sensor. 5

Figure 2.2 Surface dc Voltmeter Model SVM2, Manufactured by AlphaLab, Inc. 6

Figure 2.3 PZT thin film sensor and its measurement system. 7

Figure 2.4 Field mill with its electronic circuit. 8

Figure 2.5 EFM-100 Electric Field Monitor and its installation, manufactured by Boltek. 9

Figure 2.6 CS110 electric field sensor and its installation, manufactured by Campbell Scientific. 9

Figure 2.7 Typical electric field level for power transmission lines. 10

Figure 2.8 Illustration of an electric field chopping by the shutter. 11

Figure 2.9 Thermal actuator lateral movement shutter sensor. 11

Figure 2.10 Electric field sensor with shutter and sensing electrode in the same plane. 12

Figure 2.11 PZT actuated MEMS electric field sensor concept. 13

Figure 2.12 Schematic of electrostatic force deflected sensor. 14

Figure 3.1 Force deflected membrane working principle. 17

Figure 3.2 Electrostatic force vs. the distance to voltage source *d* and the membrane bias voltage V_{ac} under 1 kV dc source voltage. 19

Figure 3.3 Copper spring supported membrane in [19]. 20

Figure 3.4 Structure of the SOI wafer been used in this project. 21

Figure 3.5 Copper coated silicon membrane supported by micro-springs. 21

Figure 3.6 Membrane displacement simulation. 22

Figure 3.7 Sensor output variation with different modulation frequencies. 23

Figure 3.8 Simulation of sensor resonant frequency vs. temperature and external electric field. 24
Figure 3.9 Micro-spring study model, spring width: 20 μm. 24
Figure 3.10 Micro-spring nonlinear response simulation. 25
Figure 3.11 Illustration of main sensor fabrication steps. 26
Figure 3.12 Plasma photoresist clean use high RIE power. 29
Figure 3.13 SOI membrane fabrication attempts. 31
Figure 3.14 Silicon plasma etch undercut. 33
Figure 3.15 Schematic of grating sensors. 35
Figure 3.16 Schematic drawing of a P-channel MOSFET on state. 36
Figure 3.17 Schematic of membrane displacement measurement using MOSFET. 37
Figure 3.18 Schematic of SOI membrane capacitance measurement. 37
Figure 3.19 Sensor response for various initial *d*. Membrane size: 1 mm × 1 mm, spring constant k = 0.1 N/m. 39
Figure 3.20 Sensor response for various spring constants. Membrane size: 1 mm × 1 mm, initial air gap 10 μm. 40
Figure 3.21 Basic Colpitt oscillator circuit. 41
Figure 3.22 Capacitance square wave measurement simulation. 42
Figure 3.23 Capacitance square wave measurement simulation output. 42
Figure 3.24 Phase shift capacitance measurement simulation. 44
Figure 3.25 Phase shift capacitance measurement simulation result when $C_1=5\mu F$. 44
Figure 3.26 Phase shift capacitance measurement simulation result when $C_1=10\mu F$. 45
Figure 3.27 CDC simplified block diagram. 46

Figure 3.28 dc capacitance measurement schematic. 48

Figure 3.29 First version of AD7747 capacitance interagation system. 48

Figure 3.30 SOI membrane sensor dc field test result. 49

Figure 3.31 Membrane curvature and spring deformation observed by a Fogale system. 50

Figure 3.32 Capacitance sensor sensitivity vs. initial distance. 50

Figure 3.33 Lock-in capacitance measurement schematic.. 51

Figure 4.1 Ribbon array capacitance measurement schematic. 55

Figure 4.2 Ribbon array with connections simulation. 57

Figure 4.3 Ribbon array with different ribbon width simulation. 58

Figure 4.4 Jog angle defination. 59

Figure 4.5 Ribbon with different jog angles. 60

Figure 4.6 Ribbon with different jog angles simulation. 61

Figure 4.7 Gravity effect on ribbons. 63

Figure 4.8 fabricated aluminum ribbon array. 64

Figure 4.9 Ribbon dimension. 64

Figure 4.10 Ribbon array fabrication process. 65

Figure 4.11 Ribbon heights (μm, ±2 μm) over electrode 3 mm×3 mm. 66

Figure 4.12 Ribbon array sensor measurement result (±4 fF). 67

Figure 4.13 Sensor package schematic diagram. 68

Figure 4.14 Sensor enclosure assembly. 68

Figure 5.1 Optical sensor working principle. (a) Shows the case when no external electric field is present. (b) Shows the case with an external electric field caused by voltage V_S. 72

Figure 5.2 SOI membrane optical measurement test assembly. 73

Figure 5.3 dc optical measurement. 73

Figure 5.4 dc optical measurement, membrane 2, with 500 ms average. 74

Figure 5.5 Sensor and laser position system integrated in the acrylic frame. 75

Figure 5.6 SOI membrane ac modulation initial sensor testing schematic diagram. 76

Figure 5.7 Sensor response with varied Lock in amplifier integration time for a 100 kV/m electric field, and a membrane bias voltage of $10sin(\omega t)$ V at 500 Hz. 77

Figure 5.8 Sensor test with a 46 kV/m dc field, for various ac bias voltages at 500 Hz. The lock-in amplifier was set to a gain of 5,000x and an integration time of 300 ms. 79

Figure 5.9 Sensor output variation with different modulation frequencies. 80

Figure 5.10 Simulation of sensor resonant frequency vs. temperature and external electric field. 81

Figure 5.11 Sensor tested with a normal dc electric field of 77 V/m, and membrane biased with V_m = 118sin(ωt) V at resonance of 610 Hz. 82

Figure 5.12 Sensor tested with a normal ac electric field of 77 V/m at 610 Hz, and a membrane biased with V_m = 120 V. 83

Figure 5.13 Electric field distribution along a line calculation model. 84

Figure 5.14 Compact laser monitor system, measuring the electric field from a biased copper pipe 0.75 m above the sensor. 85

Figure 5.15 Electric field distribution along a line simulation. 86

Figure 5.16 Sensor measurement of mock dc transmission line, with V_m = 118sin(ωt) V at 610 Hz (resonant sensor operation), using 1s lock-in amplifier integration time. 87

Figure 5.17 Sensor measurement of mock dc transmission line, with V_m = 118$sin(\omega t)$ V at 500 Hz (non-resonant sensor operation), using 1s lock-in amplifier integration time. 87

Figure 6.1 Visualization of comb shaped shutter and sensing electrodes. 90

Figure 6.2 Schematic of a vertically moving shutter resulting in variable electric field shielding on underlying sense electrodes. 90

Figure 6.3 Model built in COMSOL to explore shutter dimensions. 91

Figure 6.4 Percent shielding of underlying electrodes as a function of shutter height. 92

Figure 6.5 Differential charge on sense electrodes as a function of shutter height. 92

Figure 6.6 Shutter, sensing electrodes and amplifier. 93

Figure 6.7 Schematic of the experimental setup and electronics. 94

Figure 6.8 Large scale model shutter shielding effect test setup. 94

Figure 6.9 Normalized measurement response vs. simulation. 95

Figure 6.10 Schematic of the sensor design with thermal actuator. 96

Figure 6.11 Simulation of shutter displacement during actuation. 97

Figure 6.12 SiO_2-Al thermal actuator cooling transient simulation. 98

Figure 6.13 Thermal actuator interference simulation. 100

Figure 6.14 Bridge-shaped thermal actuator simulation. 101

Figure 6.15 Bridge-shaped thermal actuator temperature distribution. 102

Figure 6.16 SU-8-Al fork-shaped thermal actuator displacement simulation. 103

Figure 6.17 SU-8-Al fork-shaped thermal actuator temperature simulation. 103

Figure 6.18 Titanium heater silicon based vertical shutter model. 105

Figure 6.19 Si-Al thermal actuator with titanium heater shutter movement simulation. 105

Figure 6.20 Si-Al thermal actuator with titanium heater temperature distribution. 106

Figure 6.21 Bridge shaped Si-Al thermal actuator without the titanium heater shutter movement simulation. 107

Figure 6.22 Bridge shaped Si-Al thermal actuator temperature simulation. 107

Figure 6.23 Fork shaped Si-Al thermal actuator shutter movement simulation. 108

Figure 6.24 Fork shaped Si-Al thermal actuator temperature simulation. 108

Figure 6.25 Fork shaped Si-Al thermal actuator shutter movement simulation without heater. 109

Figure 6.26 Fork shaped Si-Al thermal actuator temperature simulation without heater. 109

Figure 6.27 Si-Al thermal actuator shutter movement vs. charge variation simulation. 110

Figure 6.28 Si-Al actuator cooling transient simulation. 112

Figure 6.29 SU-8-Al thermal actuator fabrication process. 114

Figure 6.30 SU-8-Al thermal acturators release unsuccessfully. 115

Figure 6.31 SU-8 finger and shutter release. 115

Figure 6.32 Fork thermal actuator fabrication result. 116

Figure 6.33 Before wire bonding bake at 100 ºC. 117

Figure 6.34 SU-8, aluminum, and copper stress study. 118

Figure 6.35 After wire bonding bake at 100 ºC for 1 hour. 119

Figure 6.36 Si-Al thermal actuator fabrication process. 120

Figure 6.37 Si-Al fabricated fork-shaped actuator. 121

Figure 6.38 Si-Al fabricated bridge-shaped actuator. 121

Figure 6.39 Shutter movement simulation for sensor heat up with various silicon thickness at 100 ºC. 123

Figure 6.40 A Shutter with 12.5 µm thick silicon movement at temperature 25 – 100 ºC. 123

Figure 6.41 dc electric field test setup schematic diagram. 125

Figure 6.42 Sensor test pre-amplifier schematic diagram. 125

Figure 6.43 Pre-amplifier frequency response. 126
Figure 6.44 Conductivity between the sensing electrodes, thermal actuators and the ground line. 126
Figure 6.45 Testing for the sensor with sensing electrodes electrically connects to ground. .. 127
Figure 6.46 Shielding effect test schematic diagram. 129
Figure 6.47 Sensor test pre-amplifier schematic diagram. 129
Figure 6.48 Coaxial cable generated electric field simulation model. 130
Figure 6.49 Shielding effect test setup. 130
Figure 6.50 Fork shaped shutter response simulation vs. measurement. 131
Figure 6.51 Bridge shaped shutter response simulation vs. measurement. 131
Figure 6.52 Aluminum damaged after using BOE to etch SiO_2. 134
Figure 6.53 Released sensors based on re-grow SiO_2 isolation layer. 135
Figure 6.54 The burned actuators. 136
Figure 7.1 Narrower finger spacing shielding effect simulation. 138
Figure A.1 The grounded parts in charge simulation model. 143
Figure A.2 The sensing electrodes in charge simulation model 144
Figure A.3 Voltage on the top of the air box. 144
Figure B.1 COMSOL model of the SU-8 –Aluminum bride-shaped actuator. 145
Figure B.2 Titanium heater on the SU-8 –Aluminum bride-shaped actuator. 146
Figure B.3 Aluminum heater on the SU-8 –Aluminum bride-shaped actuator. 146
Figure C.1 COMSOL model of the SU-8 –Aluminum fork-shaped actuator. 147
Figure C.2 Titanium heater on the SU-8 –Aluminum fork-shaped actuator. 148
Figure C.3 Aluminum heater on the SU-8 –Aluminum fork-shaped actuator. 148

Figure D.1 Model for sensor angle in the field. 149

Figure D.2 Model top apply a positive potential. 150

Figure D.3 Model grounded parts. 150

Figure D.4 Simulation results of sensor angle vs. electric field normal to sensor. 151

Chapter 1 - Introduction

Much of the modern electrical distribution grid is based on ac networks; however, recently there is increased interest in dc networks and hybrid ac/dc networks. This is due to several factors. For example, dc networks are of benefit for grid interconnectivity, and HVDC for transmission of power over very long distances, which can be the situation when connecting remote energy sources (hydroelectric, wind, solar) to urban areas [1]. The HVDC technique also benefits undersea transmission due to low capacitance, resulting in lower power deliver cost [2]. Recent driving forces behind hybrid ac/dc networks are the increasing use of dc power sources such as photovoltaic generation and battery storage, and dc loads for which power is lost in converting between ac and dc voltages. Load examples include solid state lighting, modern consumer electronics, and battery storage in electric vehicles.

There is need, therefore, for instrumentation for measuring dc electric fields. Beyond usage in the above examples, measurement of dc electric fields is also of benefit for environmental monitoring near HVDC power lines [3], for development of improved insulators, to measure surface charge on equipment and tools, to ensure safety in live line work, and to measure voltage remotely in HVDC protection and control systems [4]-[6].

3.1. Existing electric field sensors

A variety of dc electric field sensors have been developed in recent decades, and most of them are based on three mechanisms: induction probes, optical sensors, and field mills. The induction probe measures the potential of a conductive plate that has been equilibrated to the local ambient potential with respect to a reference ground plane. Optical sensors employ a third method which is to induce a physical change in an optical fiber thereby changing its optical properties which are then analyzed. However, induction probes fail to provide long term measurement due to zero drift caused by charging [33]. For example, the SVM2 hand held induction probe manufactured by AlphaLab requires manual re-zeroing every 20 minutes [7]. Optical sensors usually suffer from phase bias, temperature stability problems [8] and charging issues.

Field mills consist of a grounded perforated shutter and a set of electrodes underneath. When the shutter periodically covers and exposes the electrodes to the electric field, an induced ac current is generated. The strength of the current is proportional to the intensity of the electric field. Due to its long-term stability, field mills have been widely used in atmospheric science to detect lightning and thunderstorms, and by power utilities. A typical commercial field mill consists of a rotating shutter, which consumes significant power relative to battery capacity. The traditional rotating shutter field mill requires frequent maintenance, and also the operation costs, especially when installed along transmission lines far away from cities or in difficult terrain. Details of the traditional field mill will be introduced in section 4.2.

For the case when there is need to detect surface charge on small sized live line tools, the probe size needs to be smaller than the object size. Currently, in power engineering area, the smallest electric field meter has a probe radius of 1cm, which was built by A. R. Johnston and H. Kirkham in [9], [10]. Therefore, in such applications, there is a need for an electric field sensor possessing characteristics of low power consumption, small size, high reliability, and also providing comparable sensitivity and signal quality with commercialized products.

3.2. Microfabricated electric field sensors

Microfabrication techniques are able to produce tiny mechanical elements to form microelectromechanical system (MEMS). Micromachined electric field mills (MEFM) have been investigated for use in place of larger traditional rotating field mills. In 2001, Horenstein et al. reported the first MEFM, which employed a comb drive to move a 10 μm × 10 μm aperture to cover and expose the underlying charge sense electrode [11]. Many types of MEFMs have been reported by other groups [12] - [20]. Most MEFM designs have the shutter moving laterally above the sensing electrodes and shielding the electrodes by its periodic movement [12] - [14]. Other designs have employed vertical movement shutters [15], [16]. However, these two vertical shutter systems only operate for sensing ac electric fields. In [17], a lateral moving shutter shields the sense electrodes which are on the same plane.

There are mainly three types of actuators applied in MEFMs to drive the shutter: thermal, piezoelectric and electrostatic. Thermal actuators can provide high driving force and large displacement [13] - [15]. In 2009, G. Wijeweera et al. built demonstrated the first MEFM to measure the electric field measurement below an HVDC transmission line. Thermal actuators were applied to provide sufficient displacement for the shutter to cover the 14 μm wide sensing electrodes. It had a resolution of 42 V/m [13]. PZT actuators can provide high force and high switching speed as well. In 2013, S. Ghionea et al. using PZT actuator implemented an ac electric field sensor which could detect 0.38 V/m/√Hz in vacuum [16]. Electrostatic actuators have fast switching speeds and low power consumption. In 2011, P.F Yang et al. presented an electrostatic comb driven MEFM and achieved a resolution of 40 V/m for dc electric field measurement [17].

In recent years, some other types of MEFMs have been reported. In 2008, T. Kobayashi et al. [18] created a micromachined vertical vibration induction probe. The probe is installed close to the electrified body, and the induced charge is generated with the vibration of the probe. In 2005, A. Roncin et al. [19] reported an electrostatic force deflected membrane supported by micro-springs. This type of sensor is immune to the shutter displacement issue of MEFM sensors when in the presence of large electric fields (> 100kV/m). The displacement of the membrane is interrogated by a laser motion monitoring system. It achieved electric field unmodulated measurement resolution of 5 kV/m for a dc electric field and 0.3 V/m for an ac electric field modulated measurement. In 2015, J. Huang et al. [21] presented a piezoelectric cantilever based ac electric field sensor. It used a charged electret material coating to provide a fixed dc bias to the cantilever, and achieved a sensitivity of 0.84 mV/ (kV/m).

3.3. Electric field sensors developed in this thesis

This thesis explored two types of MEMS electric field sensors. First, electrostatic force deflected micro-structures were used as sensor elements. In the presence of electric field, these structures would undergo mechanical deflection. Various sensing mechanisms and fabrication methods were explored. The second type of sensor explored was a new concept which is a vertically displaced MEMS field mill. Traditional lateral moving shutter MEMS field mills suffer lifting effect on the shutter when measuring high electric fields (this occurs in many designs for over 100 kV/m), impacting their sensitivity and signal. The developed vertical moving system provides a method for mitigating and compensating for this effect.

3.4. Thesis outline

The thesis is divided into 7 chapters. Topics covered in the various chapters are as described below.

- Chapter 2 gives background electric field sensor technologies, focusing primarily on dc electric field sensors.
- Chapter 3 presents the first contribution of this thesis, which was to optimize the membrane and micro-spring design of [19]. This was done by using an SOI wafer to make a device with superior mechanical performance. Fabrication results showed that the flatness of the membrane and shape of the micro-spring were greatly improved. Then, in order to have a compact circuit to measure the membrane displacement in the field, capacitance measurement techniques were explored. While successful in operation, results for this sensor effort showed the small signal electric field resolution limited to 16 kV/m.
- Chapter 4 presents an improved micro-structure employing more flexible micro-ribbon array. Results showed that this structure was softer and had more displacement in the electric field, but sensitivity was not improved. This is because the resolution was limited by noise due to mechanical vibration and electrical noise courses.
- Chapter 5 presents a compact laser position measurement system, which was built and integrated with an SOI membrane based sensor. When operated by using an ac signal to modulate (and amplify) the dc electric field, the highest resolution of 0.1 V/m was achieved.
- Chapter 6 presents a new type of MEMS electric field mill, which is the vertical moving shutter MEMS field mill. The design, fabrication and experimental testing of various versions are discussed.
- Chapter 7 gives a summary of the thesis and suggestion for future work.

Chapter 2 - Electric Field Sensors

This chapter introduces existing electric field sensors. It starts by introducing a traditional induction probe, followed by dc electric field mill, then introduces a MEMS field mill and the efforts of various groups to implement different types of MEMS field mills. After that is the review of the induction probe type sensor, then the force deflection type sensor, and finally, some other types of electric field sensors.

4.1. Induction Probe

4.1.1. Traditional induction probe

Figure 4.1 illustrates the basic working principle of an induction probe type electric field sensor. It consists of a sensing surface and a grounded guard ring. The surface is connected to a measurement circuit. When the sensing surface is exposed to an electric field, a charge will be induced on the surface. The charge held at the surface is matched by an equal charge from the measurement circuit.

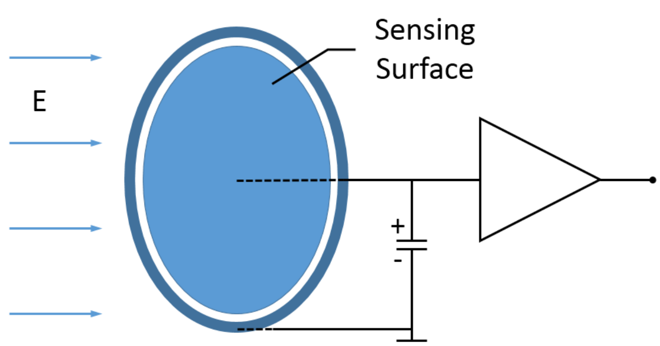

Figure 4.1 Induction probe type electric field sensor.

The main limitation of induction probe sensors is that they cannot be used for long term continuous monitoring of dc fields due to the zero level drift that is caused by the finite input impedance and input bias current requirements of the amplifier [7]. Another limitation is that they are not very sensitive when measuring a dc electric field. Figure 4.2 is an example of a commercialized handheld induction probe, and it is necessary to re-zero it every 20 minutes.

Figure 4.2 Surface dc Voltmeter Model SVM2, Manufactured by AlphaLab, Inc.

4.1.2. MEMS induction probe

In 2008, T. Kobayashi et al. [18] reported a zero drift free MEMS induction probe, which functioned by vertically vibrating the sense electrode's position. Figure 4.3 depicts the working principle of this probe. When the probe is vibrating at the amplitude of l by applying an ac voltage to the PZT actuator, the charges on the probe will fluctuate at the same frequency with the driving signal. The output of the measurement circuit is:

$$V_{meas,pp} = Ar\frac{C_s}{C_{meas}}V_s \qquad \text{4-1}$$

where A is the amplifier gain, C_{meas} is the total capacitance of the measurement system, and r is the charge modulation constant of the system. $V_{meas,pp}$ is the measurement of output peak-to-peak voltage. By measuring the capacitance change caused by charge variation, the sensor successfully solved the re-zeroing problem. Moreover, the fabricated sensors showed a good linear response to the voltage of an electrified body, which is comparable to that of commercially available electrostatic field sensors.

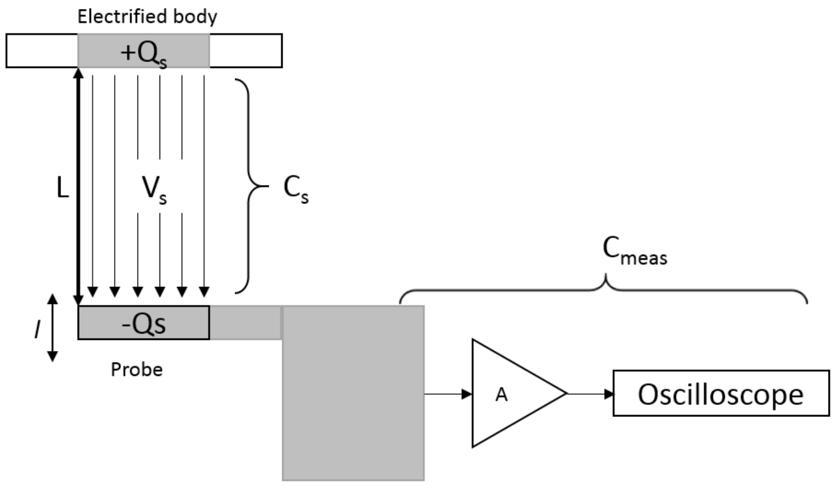

Figure 4.3 PZT thin film sensor and its measurement system.

There are two main problems with this device. First, the distance between probe and electrified body needs to be fixed; therefore it cannot be used in a handheld case. Second, its sensitivity is reduced with increasing distance between the sensor and the source of the electric field. This is because C_S decreases dramatically when L increases, which reduces $V_{meas,pp}$ according to equation (2-2). Therefore, it is only at its most sensitive when it is located very close to the voltage source.

4.2. Traditional dc electric field mill

Field mills are an improvement from the traditional induction probe, to overcome the frequent re-zero issue. Because they employ mechanical motion of a grounded shutter to "mill" an electric field. It is currently widely used in atmospheric and power transmission line field measurement.

The rotating shutter field mill shown in Figure 4.4 is a dc electric field measurement tool commonly used in industry. It uses the rotation of a grounded perforated shutter to "mill" the dc electric field into an ac field, then an underlying electrode can sense the induced ac charge. Companies which make dc electric field meters include Boltek, Mission Instruments, Vaisala Campbell Scientific and others.

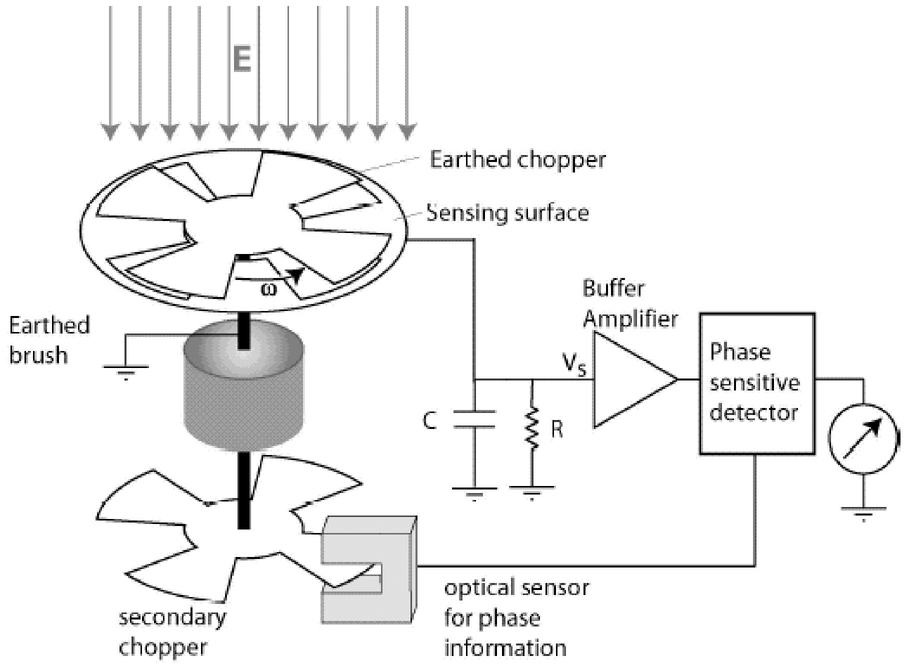

Figure 4.4 Field mill with its electronic circuit.

However, this field mill suffers from high power consumption (relative to battery lifetime) and frequent maintenance requirements. For example, the battery and some moving parts of the field mill wear out quickly and need to be replaced. The maintenance of these sensors is difficult and expensive for power utilities when monitoring HVDC installations and transmission lines due to the need for their placement in remote locations far from cities. Therefore, there is a necessity to develop a low power consumption and reliable sensor. Recent efforts use micromachined electric field mills (MEFM).

Figure 4.5 and Figure 4.6 show two examples of traditional field mills to measures the vertical component of the atmospheric electric field. With proper installation they can also be used to measure the electric field around HVDC power transmission line, as Figure 4.7 illustrates the typical electric field around power transmission lines. Figure 4.5 is the EFM-100 field sensor from Boltek [22]. It has a maximum measurement range of 20 kV/m, resolution of 0.01 kV/m, and weight of 1 kg. Figure 4.6 is the CS110 field mill from Campbell Scientific [23]. It has two measurement ranges, in (0 – 21 kV) the resolution is 3V/m, and in (21 – 212 kV), the resolution is 30 V/m. The weight of the CS110 field mill is 4 kg.

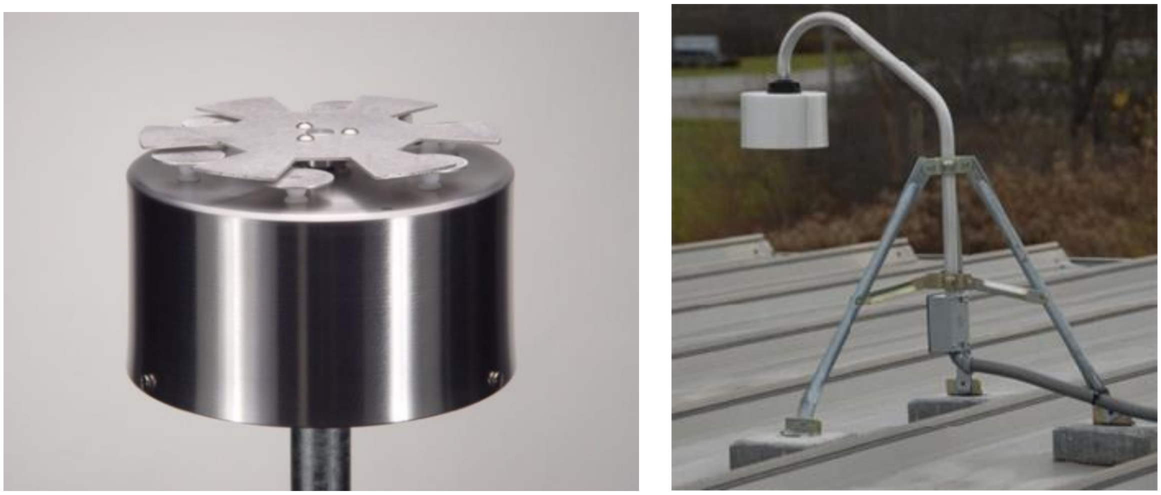

Figure 4.5 EFM-100 Electric Field Monitor and its installation, manufactured by Boltek.

Figure 4.6 CS110 electric field sensor and its installation, manufactured by Campbell Scientific.

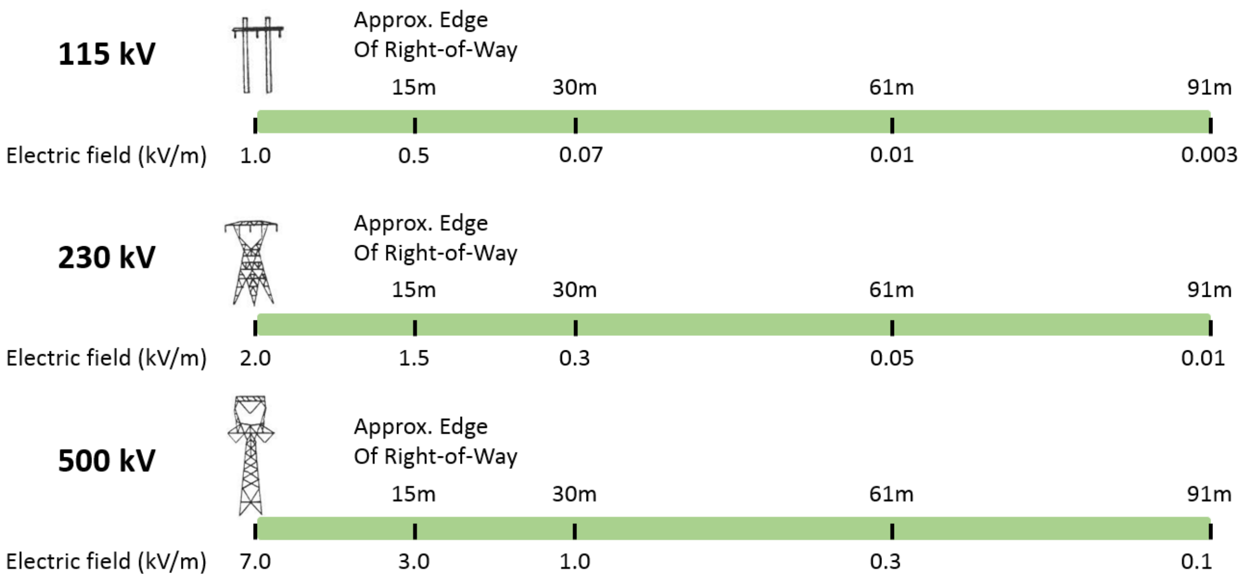

Figure 4.7 Typical electric field level for power transmission lines.

4.3. Micromachined field mills

4.3.1. Lateral vibration shutter field mills

The first MEMS based field mill was reported in 2001. M. N. Horenstein et al. developed a micro-aperture electrostatic field mill [11]. A comb drive moving shuttle with a viewing aperture of 10μm periodically exposed and covered a charge sensing electrode, generating an ac output signal. Using a 3.8 kHz sinusoidal drive voltage, a sensitivity of about 35 μV per kV/m was observed.

In 2006, X. Chen et al. reported a thermal driven field mill type sensor [14]. It consists of grounded shuttle electrodes, sense electrodes, and a bent beam thermal driver. The shutter is driven by the thermal driver and moved laterally, shielding the electrodes underneath periodically and generating an ac signal. When driving the thermal actuator by a square wave with an amplitude of ±2 V and frequency of 20 kHz, the sensitivity of the sensor was 240.8 V/m.

In 2009, Wijeweera et al. developed an MEFM using a thermally actuated resonant shutter to mill the dc field normal to the sensor, periodically shielding sense electrodes situated below the shutter [13]. The working principle is shown in Figure 4.8 and a picture of the sensor is shown in

Figure 4.9. This sensor was the first MEFM that demonstrated the measurement of an ac field under power lines. The shutter movement is driven by thermal actuators, thereby eliminating the wear and tear associated with rotating and moving elements of field mills. It also requires minimal operating voltage, with the shutter being driven by a 75 mV drive signal while consuming only 70 μW. Operating the chopper at its resonant frequency (4200 Hz) enables the measurement of both dc and ac fields (testing was done for 60 Hz ac fields). The sensor has a linear response to the electric-field amplitude and is capable of measuring a dc field as small as 42 V/m, due to the small interference of the lower thermal actuator voltage.

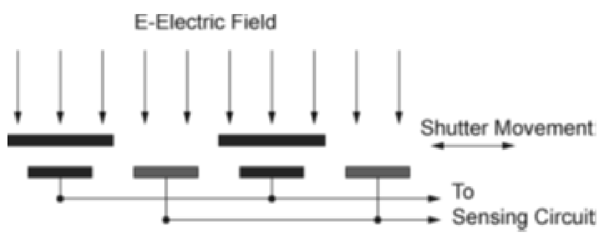

IEEE Trans. Power Delivery, vol. 24, pp. 988-995, July 2009.

Figure 4.8 Illustration of an electric field chopping by the shutter.

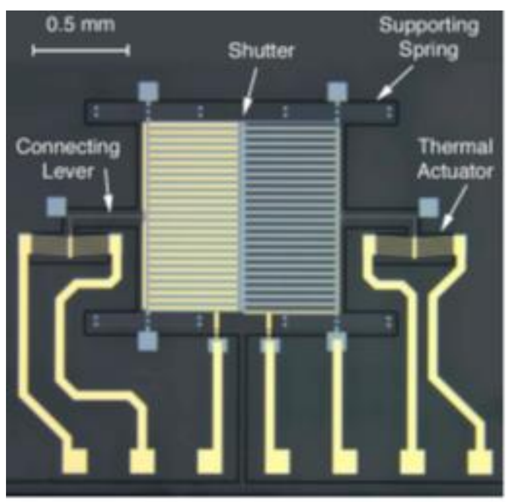

IEEE Trans. Power Delivery, vol. 24, pp. 988-995, July 2009.

Figure 4.9 Thermal actuator lateral movement shutter sensor.

The main issue of the lateral movement shutter sensor is loss of sensitivity when measuring large fields. This is because the force generated by a large field displaces the shutter vertically away from the sense electrodes. In addition, some of these sensors require operation in a vacuum for resonant movement, where resonance frequency is sensitive to the temperature and a vacuum package is easily electrically charged.

4.3.2. Shutter and sensing electrode in the same plane field mill

In 2011, P.F. Yang et al. [17] reported an SOI based resonant electric field sensor, wherein the grounded shutter and the sense electrodes are in the same plane, as shown in Figure 4.10. In the presence of an external electric field, the lateral vibrating grounded shutter covers and uncovers the sidewall of either positive or negative sensing electrodes, generating a differential current. The output current is given by:

$$I_{out} = \varepsilon E_n \frac{dA}{dt} \qquad (4\text{-}2)$$

where ε is the permittivity of free space, E_n is the component of the electric field normal to the sensing electrodes, A is the effective area of the sensing electrodes.

The minimum detectable electric field of this sensor is greater than 40 V/m. The main issue of this type of sensor is similar to other lateral movement shutter mills, in that the displacement of the shutter in a large field will affect the sensitivity.

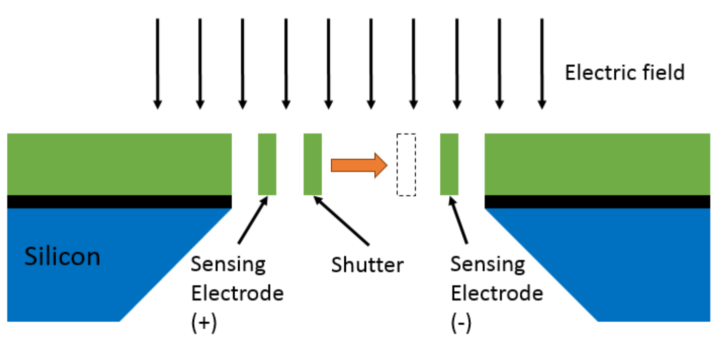

Figure 4.10 Electric field sensor with shutter and sensing electrode in the same plane.

4.3.3. Vertical vibration shutter field mill

In 2004, C. Gong et al. simulated miniature vibrating electric field sensors [24]. They demonstrated that the vertical movement shutter has the similar shielding effect. Even though, until now, no dc field detector has been reported using this concept, some groups have started to use it to detect ac fields. In 2013, Ghionea, S. et al. reported a vertical movement screen electrode field mill with lead-zirconate-titanate (PZT) piezoelectric actuators, as shown in Figure 4.11 [16].

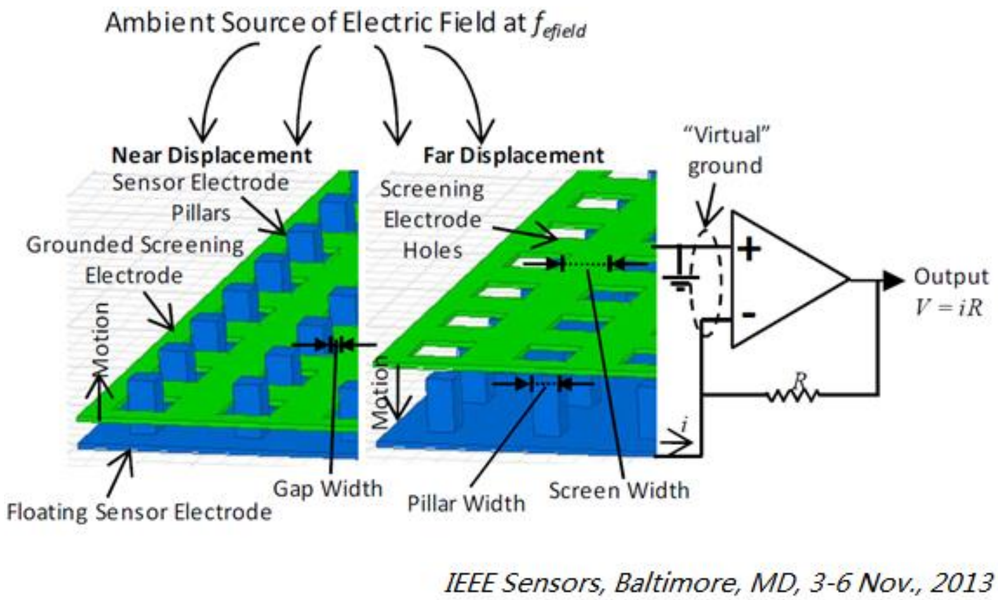

Figure 4.11 PZT actuated MEMS electric field sensor concept.

Operating the fabricated electric field sensor at its resonant frequency yielded a responsivity of 830 fA, and a limit of detection of 0.19 V/m/rtHz in a vacuum (0.30 V/m/rtHz in air), and 830 V/m (peak) when a 491 Hz E-field is applied.

The main issue of PZT actuator vertical shutter is that the drive PZT actuator requires relatively high voltage, and will interfere with the sensing signal. This makes it difficult to measure dc fields, and the work presented only showed measurement of ac electric fields.

4.4. Electrostatic force deflected membrane

In 2005, Roncin et al. developed an electrostatic force deflected sensor. The working principle is shown in Figure 4.12 [19]. A micro-spring supported membrane was displaced under application of an electric field. A laser deflection measurement system was used to monitor the membrane motion. This sensor has a measurement resolution of 5 kV/m for a dc field and 140 V/m for a 49 Hz ac field. When a 17 kV/m bias voltage was applied to the membrane, a 0.3 V/m ac field at 97 Hz was detectable. However, the laser system is power consuming and is not physically compact.

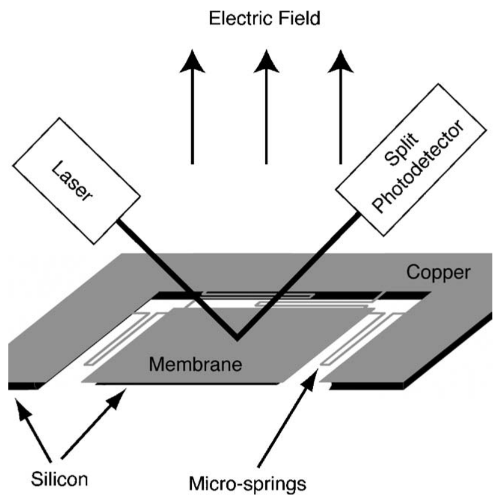

Figure 4.12 Schematic of electrostatic force deflected sensor.

4.5. Other micromachined electric field sensors

4.5.1. Electron deflection sensor

In 2014, Kirt R. Williams et al. reported another type of low-frequency, low-power electric-field sensor based on the deflection of an electron sheet, which is called a steered-electron electric-field (SEEF) sensor [25]. A heated cathode at the bottom emits electrons, and the steering electrodes forms them into a sheet. Without an external electric field, the currents collected at the two anodes are approximately the same. With an external electric field perpendicular to the sheet, pointing to the left, electrons are steered to the right; the current on anode 2 increases; and the current on anode 1 decreases by the same amount.

When operating the sensor in a vacuum at 1000 Hz, the measured sensitivity is 140 mV/m $Hz^{1/2}$. When operating the sensor in vacuum chamber at 1000 Hz, the measured sensitivity is 2.4 mV/m $Hz^{1/2}$.

The main problem of this type of sensor is that the sensor and components that are easily charged when exposed to an external electric field, such as a vacuum tube, anode chip, or spacer chip. This will deflect the ion beam and affect the field detection.

4.5.2. Electro-optic E-field sensor

According to the linear electro-optic (Pockels) effect, the magnitude of an externally applied electric field is proportional to the change in the index of refraction. Phase modulation and amplitude modulation can be applied to this type of sensor to detect the phase or amplitude variation within the external electric field. Discussion of the Electro-Optic technique is beyond this thesis, but it has been explored in [26], [27], and [28].

4.6. Comparison of different techniques

Table 2.1 compares the performance of MEMS electric field sensors in terms of measurement resolution/sensitivity and they are categorised by measurement techniques.

Table 4.1 Comparison of MEMS electric field sensors.

Category	Reference	Date	Sensing Mechanism	Resolution/Sensitivity
Lateral vibration shutter	M. N. Horenstein et al.	May 2001	Comb drive moving a shutter	35 μV per kV/m
	Chen et al. 2006	Nov. 2006	Thermal actuators drive a moving shutter	240.8 V/m
	Wijeweera et al.	July 2009	Thermal actuators drive a moving shutter	42 V/m
	P.F. Yang et al.	June 2011	Comb drive moving a shutter	40 V/m
Vertical vibration shutter	C. Gong et al.	Nov. 2013	PZT actuator moving a vertical shutter	0.19 V/m/rtHz in vacuum, 0.30 V/m/rtHz in air
Induction probe	T. Kobayashi et al.	2008	vibrating the sense electrode’s position	Linear response to -3 to 3kV
Electrostatic force deflected membrane	Roncin et al	2005	Electrostatic force deflected membrane	5 kV/m (without bias) 0.3 V/m (with bias)

Chapter 3 - Electrostatic Force Deflected SOI Membrane Sensor

In this thesis force deflection refers to the electrostatic force to deflect a micro-structure. As the deflection of the micro-structure is related to the strength of the electric field, the electric field can be sensed by measuring the micro-structure's deflection. In this chapter, section 3.1 covers force deflection theory. Section 3.2 shows simulations of the mechanical performance of the SOI membrane. Section 3.3 introduces the fabrication process. Section 3.4 discusses the capacitance method to test membrane displacement.

5.1. Force deflection theory introduction

5.1.1. Force deflection and ac modulation

Figure 5.1 illustrates the working principle of a force deflected membrane sensor. The mechanism consists of a membrane mirror suspended by a set of micro-springs, which are displaced vertically under the influence of the electric field from voltage source V_S. The voltage source V_S is located a distance of d from the membrane, and the membrane is electrically biased with the potential V_m. There is a relation between electric field strength and membrane displacement. Measuring the membrane deflection will be the way to sense the electric field, assuming the electric field generated between the source voltage and the membrane is uniform. Neglecting the fringing effect, the relationship between the electrostatic force on the membrane and the electric field is obtained by:

$$F = -\frac{1}{2}\varepsilon_0\varepsilon_r A\left(\frac{V_S - V_m}{d}\right)^2 = -\frac{1}{2}\varepsilon_0\varepsilon_r A E^2 \qquad (5\text{-}1)$$

where F is an attractive electrostatic force, A is the membrane area, E is the electric field between them, $\varepsilon_0 = 8.85\times10^{-12}\ F/m$ is vacuum permittivity, and ε_r is relative permittivity of air.

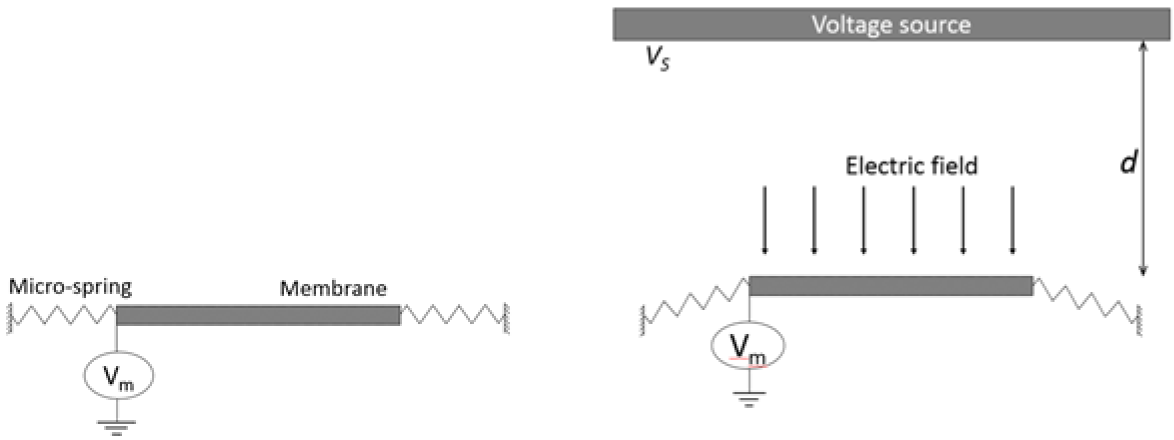

Figure 5.1 Force deflected membrane working principle.

For a dc voltage source $V_S = V_{dc}$ and the grounded membrane, equation (3-1) solves to equation (3-2), showing the relationship between the electric field and the electrostatic force on the membrane.

$$F = -\frac{1}{2}\varepsilon_0\varepsilon_r A\left(\frac{V_S}{d}\right)^2 \tag{5-2}$$

Assuming the micro-spring the membrane has spring constant of k, the force would cause a membrane displacement Δd_m of:

$$\Delta d_m = -\frac{1}{2k}\varepsilon_0\varepsilon_r AE^2 \tag{5-3}$$

For MEMS sensors, this displacement can be anywhere between a nm and a mm. The motion detector needs to be very sensitive to such tiny displacement and it is necessary to have a high signal to noise ratio. A variety of techniques can be used such as capacitance measurement, laser + photodetector, optical Grating, or MOSFET. Section 5.4 will explore these techniques.

Electrostatic force deflection based electric field sensors are non-linear, and so a movement of the membrane would be proportional to E^2. In other words, when electric field strength drops, the membrane movement would decrease is proportion to E^2. For small deflection, noise interferences can be an issue in the measuring of this movement. Modulation of the membrane motion would allow the use of bandpass filtering to assist in the reading of the sensor signal in exclusion of the noise. Modulation of the membrane motion can be achieved by applying an ac bias to the membrane such that $V_m = V_{ac}\sin(\omega t)$. In this case, equation (3-1) solves to:

$$F = -\frac{1}{2}\varepsilon_0\varepsilon_r A\left(\frac{V_{dc} - V_{ac}\sin(\omega t)}{d}\right)^2 \qquad (5\text{-}4)$$

Equation (3-4) can be expanded to equation (3-5).

$$F = -\frac{\varepsilon_0\varepsilon_r A}{2d^2}\left[V_{dc}^2 - 2V_{dc}V_{ac}\sin(\omega t) + V_{ac}^2\sin^2(\omega t)\right] \qquad (5\text{-}5)$$

There are three frequency components in equation (3-5): V_{dc}^2 is a dc component, $2V_{dc}V_{ac}\sin(\omega t)$ is an ac component with a frequency of ω, and $V_{ac}^2\sin^2(\omega t)$ has frequency of 2ω. Therefore, equation (3-5) indicates the force on the membrane would cause three different movements. First, a fixed movement of the membrane position proportional to V_{dc}^2 due to the dc electric field. This motion is given by equation (3-6). The second component of the movement of the membrane is proportional to $2V_{dc}V_{ac}\sin(\omega t)$, which is at the drive frequency of the membrane ac bias voltage V_m:

$$\Delta d = \frac{\varepsilon_0\varepsilon_r A}{kd^2}(V_{dc}V_{ac}\sin(\omega t)) \qquad (5\text{-}6)$$

This signal can be monitored using a filter tuned to the drive frequency. The noise outside the drive frequency can be minimized and removed giving higher measurement resolution. It should also be noted that the amplitude of the modulated signal is proportional to the product of V_{ac} and V_{dc}, and this allows the membrane bias voltage to act as a method to amplify the electric field being measured if desired. In essence, the modulation voltage allows the sensor sensitivity to be adjusted as desired.

The case where V_S is an ac voltage source also allows modulation of membrane motion. In this case, if V_S is an ac voltage source given by $V_S = V_{ac}\sin(\omega t)$, modulation of the membrane motion would be achieved by applying a dc bias voltage $V_m = V_{dc}$ to the membrane, and the resulting motion is again given by equation (3-6).

Figure 5.2 is a calculation of the force on the membrane, as given by equation (3-6), as a function of d and V_{ac} for the case where V_{dc} = 1 kV. The distance d ranges from 1 cm (which may correspond to the case of proximity voltage meter) to 1 m (which may correspond to the case of measuring a high voltage from a safe distance). We can see that the electrostatic force experienced by the membrane is in the range of a nN to a pN when V_{ac} = 100 V; it varies in the range of a pN to a fN when V_{ac} = 1 V. The spring constant of the micro-spring structure used in this calculation is 0.14 N/m, a value experimentally measured from a similar membrane to that of Figure 5.5 [20]. These electrostatic forces cause a membrane motion that is easily measured by the laser position sensor. It is important to note that the force on the membrane varies linearly with the ac bias voltage V_{ac}, showing that the sensitivity of the sensor can be adjusted by the amplitude of the membrane bias signal.

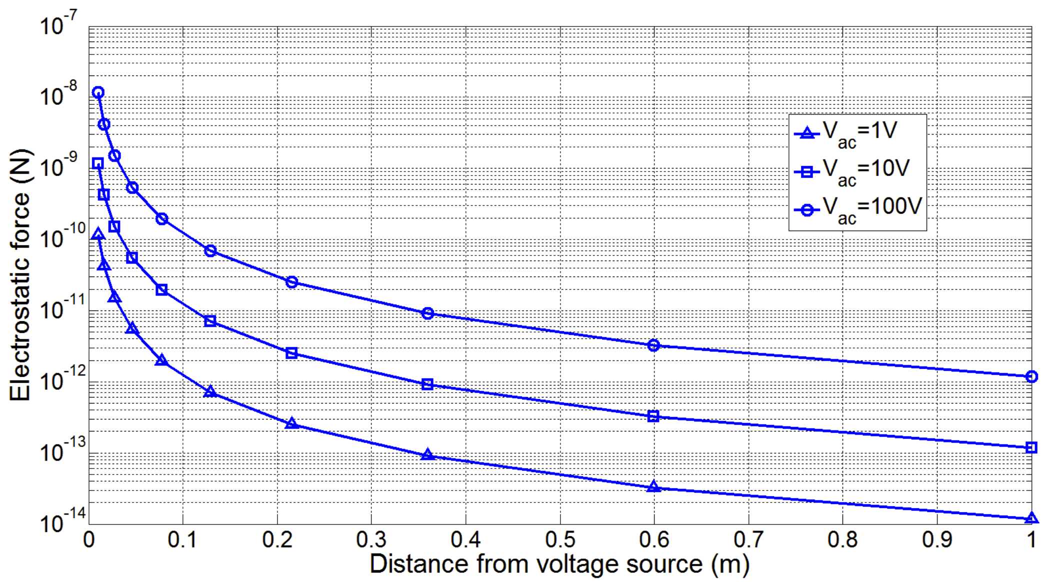

Figure 5.2 Electrostatic force vs. the distance to voltage source *d* and the membrane bias voltage V_{ac} under 1 kV dc source voltage.

5.2. SOI membrane electric field sensor design

Figure 3.3 shows a fabricated membrane sensor of Roncin et al. [19]. It is made of copper and supported by copper made micro-springs. This design has two main issues. First is the stress on the copper micro-spring which causes huge initial deformation. Figure 5.3 shows that all micro-springs curl down due to the copper thin film stress. Another issue is that the resonant frequency of this sensor is only 97 Hz. With this narrow working frequency range, it is easy to be interfered by multiple ambient noise sources, such as sound, air flow, and building vibration. This low working frequency limits the sensor to be applied to high frequency ac field detection.

To overcome the two issues in [19], micro-springs need to change to use a high Young's modulus material. Also, smaller size can help to increase the sensor resonant frequency. The SOI wafer is a good candidate for this purpose. A SOI (Silicon-on-Insulator) wafer is a sandwich structure including a device layer (active layer) on top, a buried oxide layer (insulating SiO_2 layer) in the middle, and a handle layer (bulk silicon) in the bottom. SOI wafers are produced by using SIMOX and wafer bonding technology to achieve a thinner and precise device layer and to ensure the requirement of thickness uniformity and low defect density. Figure 3.4 shows the structure of the SOI wafer being used in this work. It has a 5μm device layer, 0.2μm buried oxide layer, and 500 μm thick handle layer.

The SOI wafer fabrication process provides precise control of the thickness of the membrane and micro-springs and mitigates the stress issues which were a concern in [19]. Stress mitigation resulted in more predictable membrane mechanical characteristics. The SOI wafer process additionally allowed for smaller and thinner membranes (80% smaller surface area, and 6 times thinner) for lower mass and stiffer micro-springs, providing higher natural frequency. This enables the measurement of higher frequency ac electric fields, therefore, the new sensor would be more applicable for measuring an ac field with harmonics above 60 Hz.

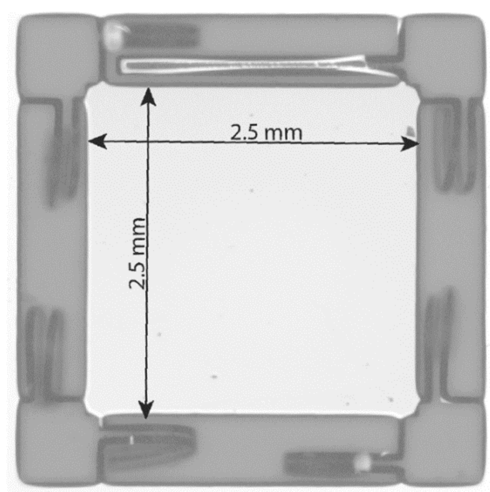

Figure 5.3 Copper spring supported membrane in [19].

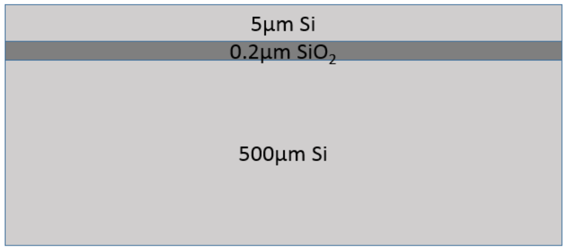

Figure 5.4 Structure of the SOI wafer been used in this project.

5.2.1. SOI membrane force deflection simulation

This section will discuss the simulation of SOI membrane mechanical performance, resonant frequency, and micro-spring linearity.

(1) Membrane displacement

A photograph of a fabricated SOI membrane is shown in Figure 3.5. The square membrane measures 1.15 mm × 1.15 mm, and each supporting micro-spring segment has a length of 1000 µm and width of 20 µm. The membrane and micro-springs are fabricated from single crystal silicon with a 5 µm thickness. The structure is coated with a 200 nm thick copper layer.

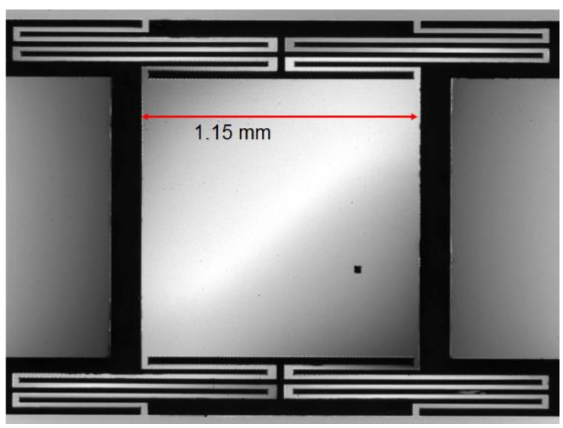

Figure 5.5 Copper coated silicon membrane supported by micro-springs.

The membrane was first designed and modeled in COMSOL software. The simulation ignored fringing effect as the membrane size is relatively large, and also ignored the electric field distortion as the membrane displacement is small compared to the distance to the voltage source. Therefore, the simulation was performed as an ideal case as to apply the calculated electrostatic force on the membrane shown in Figure 5.6. The structure design was optimized to achieve a membrane movement of approximately 0.1 nm to 10 μm, when exposed to dc electric fields ranging from 1 kV/m to 1000 kV/m respectively, as shown in Table 5.1. Figure 5.6 shows the simulation result of membrane deflection under a 1000 kV/m electric field, which is displaced 21.5 μm.

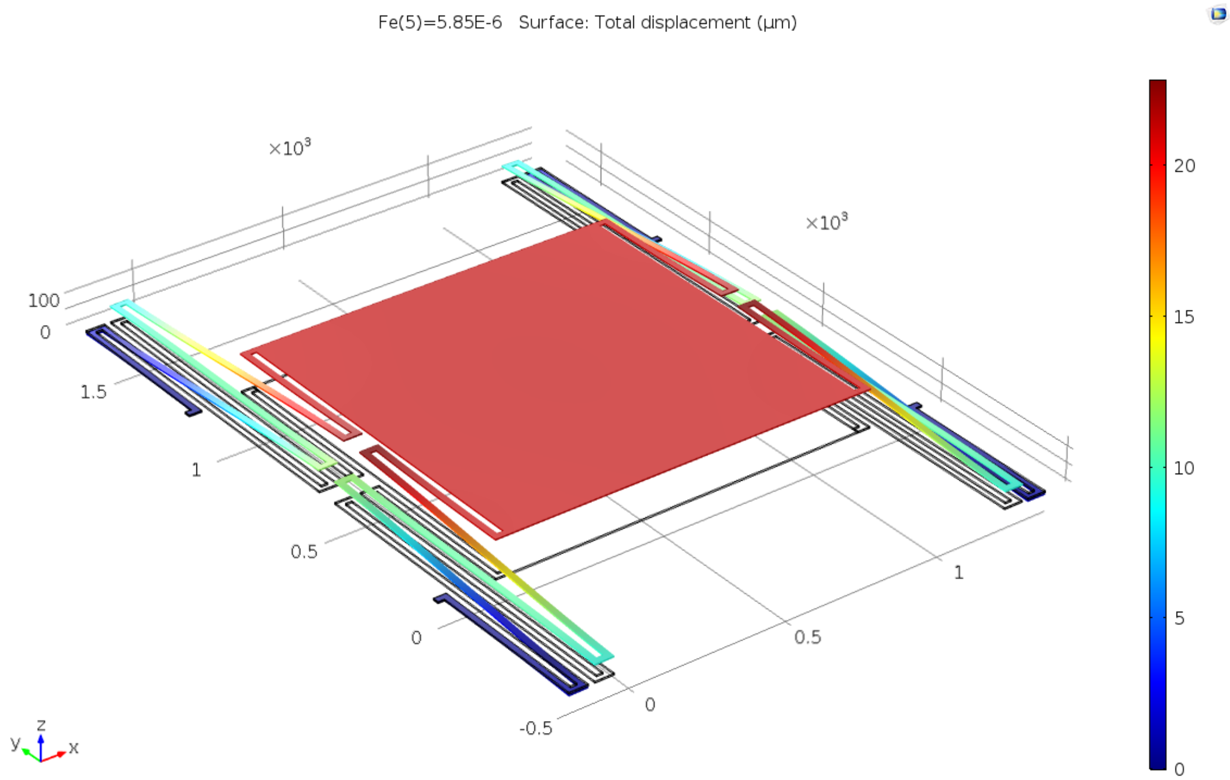

Figure 5.6 Membrane displacement simulation.

Table 5.1 Membrane displacement simulation results.

Electric field	Electrostatic force	Membrane Displacement
1 kV/m	5.85×10^{-12} N	2.15×10^{-5} μm
10 kV/m	5.85×10^{-10} N	2.15×10^{-3} μm
100 kV/m	5.85×10^{-8} N	0.215 μm
1000 kV/m	5.85×10^{-6} N	21.5 μm

(2) SOI membrane resonant frequency

It is important to note that the sensor, being a mechanical device, would have its maximum output when working at its mechanical resonant frequency. Therefore, a test was done to determine the mechanical resonant frequency of the spring-membrane system at room temperature. Figure

5.7 shows the sensor output. We can see that the sensor the sensor response is minimal for frequencies below 520 Hz, but for greater than 520 Hz, the output rapidly increases to a peak at its resonance of 610 Hz.

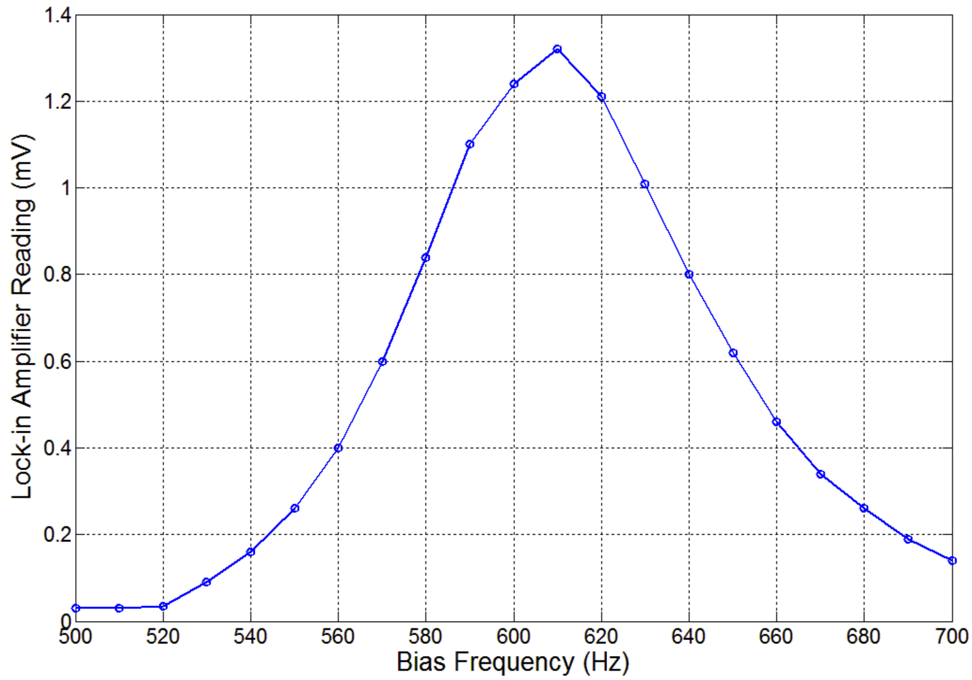

Figure 5.7 Sensor output variation with different modulation frequencies.

The operating frequency is an important factor that affects the sensor's response. While operating at resonant frequency will give maximum output, resonant frequency can shift when the ambient conditions change, causing a reduction in sensitivity. Figure 5.8 shows a simulation of the resonant frequency shift as a function of temperature for three different electric fields on the membrane. We can see that the resonant frequency shifts ~1.8 Hz for every 10 ºC. Relating this to the sensor's resonance of 610 Hz, a ± 10 Hz change from the 610 Hz resonance would require a ± 55 ºC temperature change. From Figure 3.7, we can see that the associated change in sensor sensitivity would be only 8%. Figure 3.8 also shows the change in sensor resonance due to the force from the external electric field. We can see that for electric fields larger than 100 kV/m, a small shift in resonance is seen, with a shift in frequency (approx. 1.8 Hz) from the 100 kV/m to the 1000 kV/m electric field.

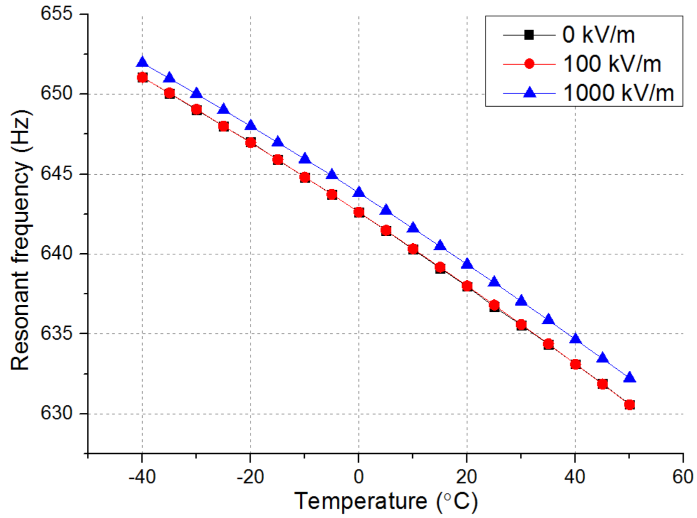

Figure 5.8 Simulation of sensor resonant frequency vs. temperature and external electric field.

(3) Micro-spring linearity

Another concern of the micro-spring supported structure is that the spring constant might be nonlinear, especially under a large deflection. Therefore, it is necessary to study the nonlinearity of the micro-spring. Figure 5.9 is the micro-spring model used for a nonlinear response study. Figure 3.10 is the COMSOL nonlinear simulation results. We can see that when the force is greater than 0.4×10^{-4} N, and the spring moving end displacement is over 215 μm, the spring response becomes nonlinear. This displacement is about 10% of the total S-shaped micro-spring length. Therefore, we can say that for this S-shape micro-spring, the linear deformation range is within 10% of the total length.

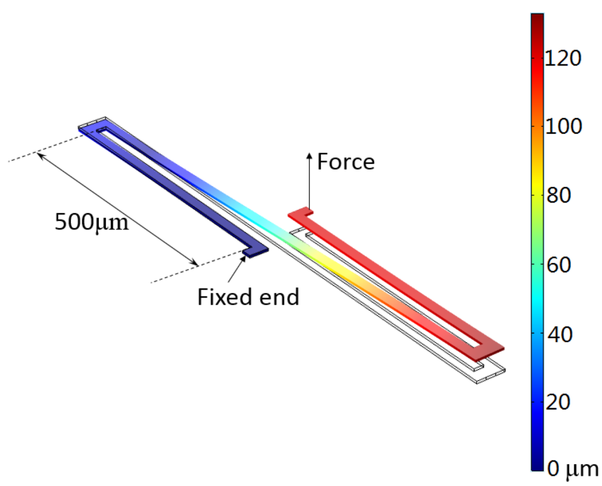

Figure 5.9 Micro-spring study model, spring width: 20 μm.

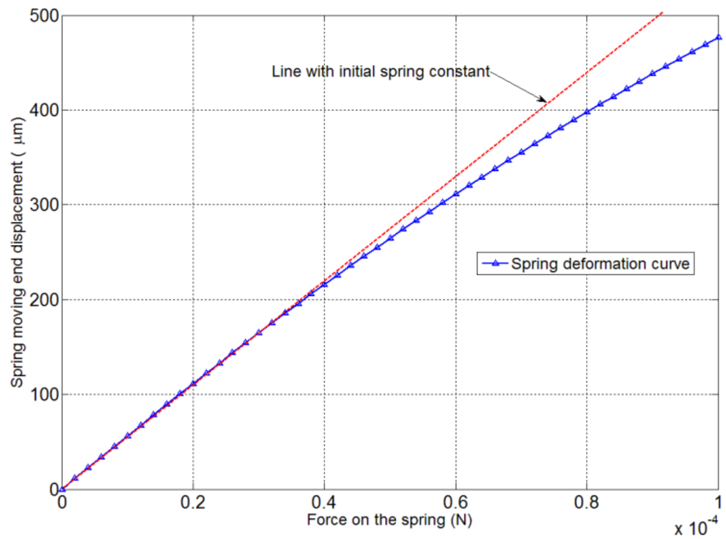

Figure 5.10 Micro-spring nonlinear response simulation.

5.3. SOI membrane fabrication

5.3.1. SOI membrane fabrication process

Figure 5.11 shows the main fabrication steps of the micromachined silicon membrane from the SOI wafer. A 500 µm thick silicon-on-insulator (SOI) was used as the membrane substrate with a device layer of 5 µm thick silicon (out of which is formed the membrane and micro-springs), and a 0.5 µm thick buried oxide (Figure 5.11 (a)). The first step (Figure 5.11 (b)) was to deposit a 200 nm protective silicon nitride layer on both sides of the wafer using a PECVD process. This was done by the SOI wafer supplier. Next, lithography is done to pattern the backside nitride. A plasma etch was then done to remove the backside nitride under the membrane location. This was done in our lab's Trion Phantom II ICP/RIE etch system. This was followed by a thinning of the wafer under the membrane location (Figure 5.11 (d)) using a KOH etch at 80 ºC for 416 minutes, until 35 µm of silicon remained. Subsequently, a sputtering process was used to deposit a 40 nm titanium adhesion film and 200 nm copper conductor on the front side of the wafer (Figure 5.11 (f)). This was done using the MRC 8667 sputter system. Then, the copper layer was lithographically patterned and chemically etched into the shape of the membrane and springs (Figure 5.11 (g)). A protective photoresist coating is deposited over the copper, followed by the etching of the remaining backside silicon using XeF_2 gas, and then the removal of the protective photoresist (Figure 5.11 (h)). This was followed by the removal of the exposed SiO_2 buried oxide using buffered HF etchant (Figure 5.11 (i)). The last step (Figure 5.11 (j)) was to release the structure by using a plasma etch to etch the silicon from the front side, using the patterned copper from step (g) as the etch stencil mask.

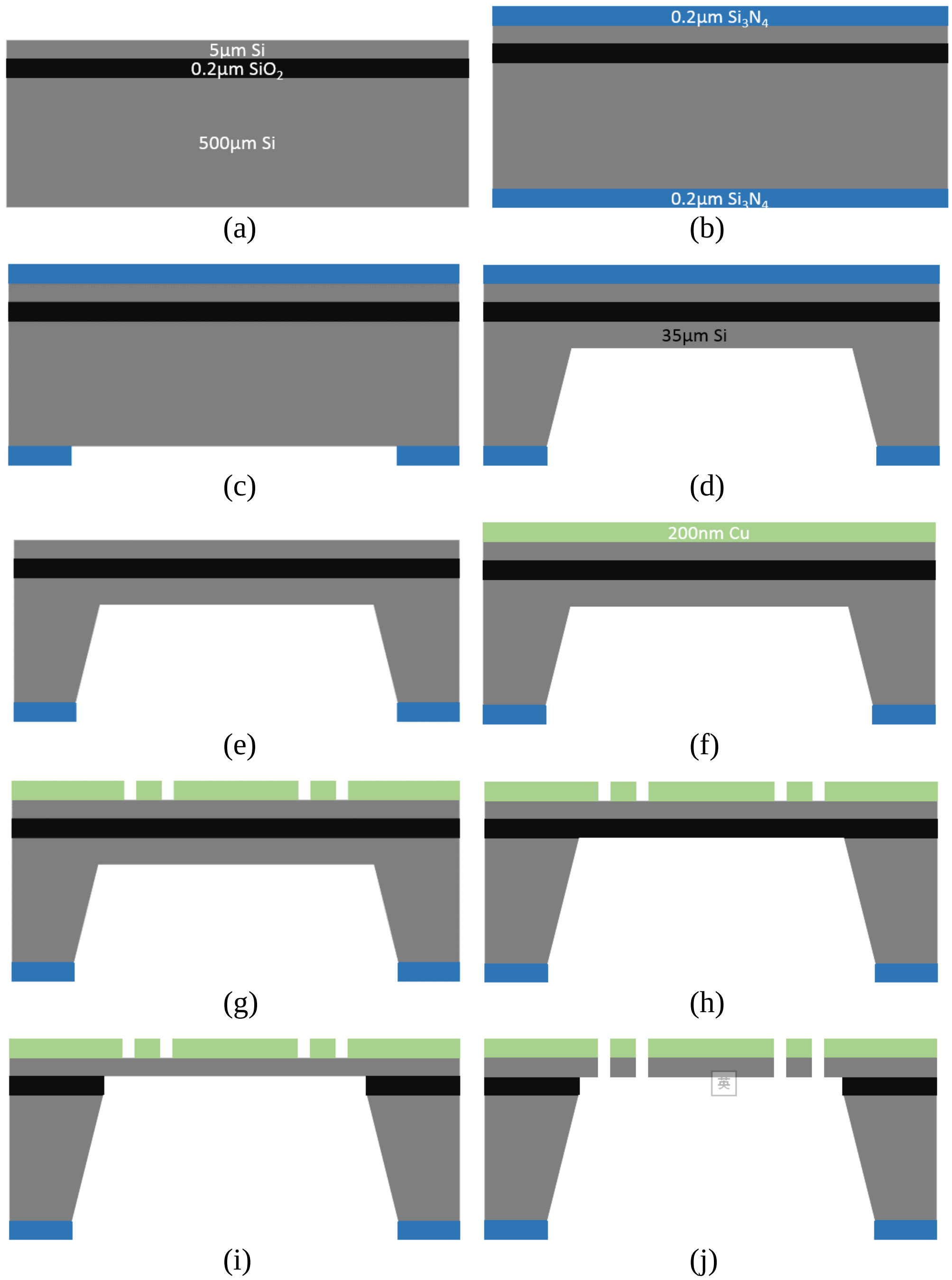

Figure 5.11 Illustration of main sensor fabrication steps.

5.3.2. SOI wafer fabrication experiences

The SOI membrane fabrication used multiple processes as shown in Figure 5.11, such as photo lithography, KOH etch, Si_4N_3 plasma etch, Al/Cu sputtering, XeF_2 silicon etch, silicon plasma etch, etc. In the fabrication process, many failures happened before the device was successfully fabricated. This section will discuss some of the lessons learned from these failures and the efforts to optimize the fabrication processes.

(1) Si_4N_3 plasma etch

Figure 5.11 step (c) shows the process to pattern the Si_4N_3 layer from the backside before step (d), the KOH etch of silicon. Patterning of Si_4N_3 has three steps: spin coating a layer of HPR 504 photoresist, the lithography processes, and then the plasma etch to remove the exposed Si_4N_3. In the beginning, the plasma etch of Si_4N_3 has some difficulties. The recipe of HPR504 photoresist spin coating used in the first attempt is shown in Table 5.2, and the plasma etch recipe is shown in

Table 5.3. After the plasma etch, the Si_4N_3 thin film was porous, meaning it was damaged during the plasma etch. In this situation, the Si_4N_3 layer was not able to protect the silicon under it during KOH etch process. There are two main factors which caused this issue. First, the photoresist layer was too thin. Second, the plasma etch RIE power was too high. These resulted in the plasma ions penetrating the photoresist layer and Si_4N_3 being etched. The improvements were made based on these two factors. To increase photoresist thickness, the spin speed needed to be reduced. In the second attempt, as shown in Table 5.4, the spin coating speed is reduced to 2000 rpm and the photoresist thickness increased to 1.8μm. Also, the plasma RIE power was reduced to 25 W as shown in Table 5.5. With this new recipe, the Si_4N_3 layer was successfully patterned with high quality, and the rest of the area was well preserved.

Table 5.2 Photoresist HPR 504 Lithograph process recipe 1.

	Step 1	Step 2	Step 3	Thickness
Spin time	5 s	10 s	30 s	1.4 μm
Spin speed	500 rpm	1000 rpm	3000 rpm	

Table 5.3 Si_4N_3 plasma etch recipe 1.

Chamber pressure	100 mTorr
CF_4	45 sccm
O_2	5 sccm
ICP Power	300 W
RIE power	100 W

Table 5.4 Photoresist HPR 504 Lithograph process recipe 2.

	Step 1	Step 2	Step 3	Thickness
Spin time	5 s	10 s	30 s	1.8 µm
Spin speed	500 rpm	1000 rpm	2000 rpm	

Table 5.5 Si_4N_3 plasma etch recipe 2.

Chamber pressure	100 mTorr
CF_4	45 sccm
O_2	5 sccm
ICP Power	300 W
RIE power	25 W

(2) Plasma etch to clean photoresist and copper damage

In Figure 5.11 step (g), after pattering the copper layer, a protection photoresist layer was spin coated on top of the copper layer to protect the front side silicon from the XeF_2 silicon etch (step (h)). After step (h) and (i), the membrane thickness was 5 µm, which made it fragile. In the first attempt the protection photoresist layer mentioned above was not removed before the structure release. In step (j), a plasma etch was used to remove the protection HPR504 photoresist above the copper, then, a silicon etch was used to release the structure. The photoresist needs to be removed first. The recipe which was used is shown in Table 3.6. The silicon was then etched by feeding different gases and adjusting the chamber pressure and RIE power, as shown in Table 5.7. When etch photoresist HPR504, the plasma RIE power was chosen to be 200 W. Under this high power, the etch speed of the photoresist was very high, and after it was completely etched, the copper started to be etched. After the HPR504 etch was run for 2 minutes and the silicon plasma etch for 10 minutes, the membrane surface became completely black. Figure 3.12 shows the results.

In the second attempt, after step (h), the photoresist was carefully removed by using the acetone to avoid a break. In the last step, silicon was etched by using the recipe shown in Table 5.7. The membrane was successfully released using this method.

Table 5.6 HPR504 plasma etch recipe.

Chamber pressure	100 mTorr
O_2	30 sccm
ICP Power	100 W
RIE power	200 W

Table 5.7 Silicon plasma etch recipe.

Chamber pressure	50 mTorr
SF_6	30 sccm
CHF_3	15 sccm
O_2	15 sccm
ICP Power	100 W
RIE power	50 W

Figure 5.12 Plasma photoresist clean use high RIE power.

(3) Sputtering vs thermal evaporation

In step (f), shown in Figure 5.11, a thin layer of Al/Cu is grown. Sputtering and thermal evaporation are common techniques to grow a thin film. Thermal Evaporation is one of the simplest of the physical vapor deposition (PVD) techniques. The material is heated in a vacuum chamber until its surface atoms have sufficient energy to leave the surface. At this point they will traverse the vacuum chamber (with thermal energies less than 1 eV) and coat a substrate positioned above the evaporating material (average working distances are 200 mm to 1 meter). Sputtering is a technique used to deposit thin films of a material onto a substrate surface. By first creating a gaseous plasma and then accelerating the ions from this plasma into target material, the target material is eroded by the arriving ions via energy transfer and is ejected in the form of neutral particles - either individual atoms, clusters of atoms, or molecules. As these neutral particles are ejected, they will travel in a straight line unless they come into contact with something, for example, other particles or a nearby surface. If a substrate such as a silicon wafer or glass is placed in the path of these ejected particles, it will be coated by a thin film of the source material.

In Figure 3.13 sample 1 and 2, the thermal evaporation process was used to deposit an aluminum film. They are very shiny and have good surface qualities. However, the SOI membranes suffer from stress. Bigger membranes, like 2 mm × 2 mm and 3 mm × 3 mm, were easily broken due to stress. In the smaller membranes that survived, we can still see that they are bowing. Then the sputtering process was used instead to develop a thin film. As the sputtered aluminum film's surface quality was sometimes not as shiny as the thermally evaporated counterparts, copper was chosen for the thin film material. Sample 3 was the result of the sputtering process. As we can see from the picture, five out of six devices survived, and there was less stress on these samples compared to those which come from thermal evaporation.

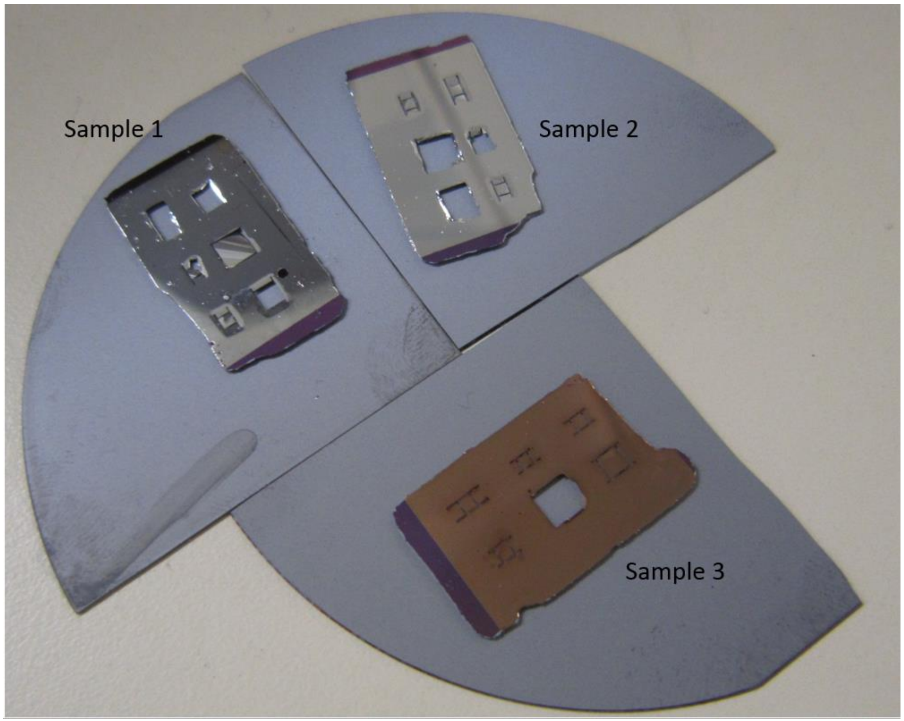

Figure 5.13 SOI membrane fabrication attempts.

(4) Sputtered thin film stress

In the beginning, the sputtered thin film suffered from stress. Table 5.8 is one of the example recipes used to sputter copper film. The stress on the resulting sample is so strong that the copper film was peeled off.

Table 5.8 High stress copper film sputter recipe.

Base pressure	5.8×10^{-3} mTorr
Sputter pressure	5.4 mTorr
Ar	41 sccm
Power	200 W
Time	2 minutes
Cu thickness	300 nm

After a literature review, it was found that sputtered thin film stress is determined by the film growth process, and the dependence of residual stress on process parameters and microstructure was systematically investigated by many research groups [36]-[37]. The most important factors in the process are Ar pressure, temperature, and sputtering power. A series of experiments were performed to explore how thin film stress is related to those parameters.

Table 5.9 and Table 5.10 show the sputtering process results for aluminum and copper thin films individually. For both materials, higher and lower power results in lower film stress. The recipe chosen for the copper film deposition for sample 3 is shown in Table 5.11. It used a high sputtering pressure of 20 mTorr.

Table 5.9 Sputtered aluminum thin film stress measurement.

Wafer #	Pressure (mTorr)	Power (W)	Film thickness (μm)	Radius (m)	Bow (μm)	Film stress (MPa)
1	10	200	0.5	46.3	12.46	26.3
2	10	300	0.82	55	10.22	57
3	20	200	0.03	204	2.56	9.9

Table 5.10 Sputtered copper thin film stress measurement.

Wafer #	Pressure (mTorr)	Power (W)	Film thickness (μm)	Radius (m)	Bow (μm)	Film stress (MPa)
1	10	200	0.85	15.1	29.4	272.6
2	10	300	1.33	18.9	23	268
3	20	200	0.79	85	5.6	36.5

Table 5.11 Low stress copper film sputter recipe.

Base pressure	9.4×10^{-3} mTorr
Sputter pressure	20 mTorr
Ar	141.1 sccm
Power	200 W
Time	2 minutes
Cu thickness	220 nm

(5) Silicon plasma anisotropic etch

The device release process (Figure 3.11 (j)) used plasma to etch the exposed silicon. The cross-section shape of the micro-spring is the main factor in determining the mechanical performance. To minimize the undercut caused by the plasma etch, it is important to obtain a better side wall quality. Therefore, it is necessary to study different plasma silicon etch recipes to achieve the best side wall quality and least undercut. Figure 3.14 shows a model of the silicon trench after the plasm etch, where V is the undercut and H the trench depth. If $V=H$, it becomes an isotropic etch, if $V<H$, the etch becomes anisotropic. The anisotropic rate (A) is calculated by:

$$A = 1 - \frac{V}{H} \tag{5-7}$$

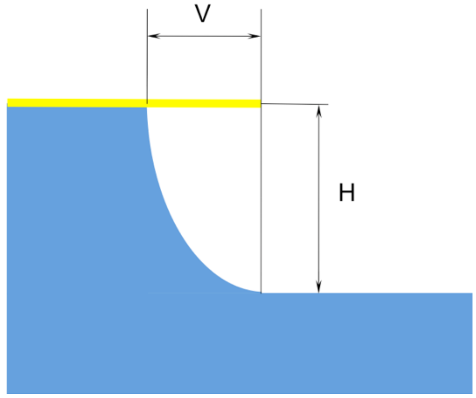

Figure 5.14   Silicon plasma etch undercut.

In [29] R. Legtenberg et al achieved anisotropic etching by employing a SiF_xO_y passivation layer during the etch process. This SiF_xO_y film works as the passivation layer that stops the fluorine atom from reaching the silicon beneath the layer on the sidewalls, while the passivation layer on the horizontal surface of the silicon is removed by the ion bombardment of the SF_x^+ ions accelerated by the electric field. When CHF_3 is added into the process, a similar reaction happens and both SiF_xO_y and CO_xF_y are generated [30]. Table 5.12 lists the experiment results, as we can see from the anisotropic ratio, recipe 3 has the highest anisotropic rate and therefore was used in the SOI membrane release process.

Table 5.12   Silicon anisotropic plasma etch experiment results.

	1	2	3	4
Pressure	100 sccm	100 sccm	50 sccm	50 sccm
RIE power	50 W	50 W	50 W	50 W
ICP power	100 W	100 W	100 W	100 W
SF_6	30 sccm	30 sccm	30 sccm	30 sccm
O_2	15 sccm	15 sccm	15sccm	15sccm
CHF_3	10 sccm	20 sccm	15 sccm	20 sccm
Depth	6.528 μm	20.64 μm	14.35 μm	15.45μm
undercut	2.5μm	4μm	3μm	3.25μm
Anisotropic	0.387	0.71	0.791	0.612

5.3.3. Spring constant measurement

The flexibility and spring constant of the membrane support micro-springs was measured after fabrication. This was done using an applied dc electric field to displace the membrane, and measuring motion using an optical microscope. Position accuracy was ±2 μm for this test. The membrane of Figure 3.5 was tested, with five measurements taken with an applied field ranging from 360 kV/m – 1090 kV/m. Results are shown in Table 5.13. The average spring constant of the supporting micro-springs was calculated to be 0.14 N/m.

Table 5.13 Measured membrane displacement vs. electric field.

Electric field (kV/m)	Displacement of the Membrane (μm)	Electrostatic Force (N)	Spring constant k (N/m)
360	7	7.7×10^{-7}	0.11
545	12	1.7×10^{-6}	0.15
727	22	3.1×10^{-6}	0.14
910	33	4.8×10^{-6}	0.15
1090	52	7.0×10^{-6}	0.13

5.4. Motion measurement techniques

When these fabricated membranes were used to detect an electric field, the membrane deflection was usually in the range of nm to μm. There are multiple ways to measure the membrane displacement. In this section, some of the methods will be discussed.

5.4.1. Grating electric field sensor

Grating can be applied for small displacement measurements. Figure 5.15 shows the concept designs of a membrane type force deflection electric field sensor motion measurement by employing grating. The substrate is made of a transparent material to allow optical transmission. The reflective membrane is supported by micro-springs. The membrane and the grated electrodes underneath form a phase sensitive diffraction grating. When the grating under the membrane is illuminated through the transparent substrate by a coherent light source, the reflected field will split into odd diffraction orders and specular reflection (or zeroth order). The output intensity i as a function of a small displacement of Δx is obtained by:

$$i = RI_{in}\frac{4\pi}{\lambda_0}\Delta x \qquad (5\text{-}8)$$

where R is the responsivity of the optical detector, and I_{in} is the intensity of the incoming light.

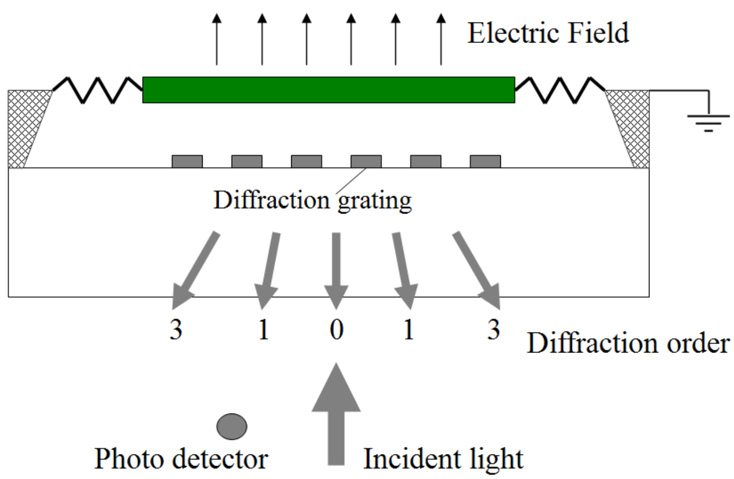

Figure 5.15 Schematic of grating sensors.

However, the fabrication and application of such sensor have two main potential difficulties:

(1) The membrane needs to be very flat and placed very close to the grated electrode; the fabrication process will be very challenging.

(2) A laser diode and a photodetector is used to produce and measure the intensity of diffracted light. Therefore, the measurement system is not very compact.

5.4.2. Field Effect transistor

Many integrated circuit components can be used for sensing applications. The characteristic of the field-effect transistor (FET) is influenced by the strength of the electric field. As such, the FET can be applied to multiple sensors [38][39][40]. It can also be used to detect small displacement. Figure 3.16 shows the working principle of a P channel MOSFET. When a small V_D is applied, the drain to source current, I_D, is:

$$I_D \approx \frac{\mu Z C_i}{L}(V_G - V_T)V_D, \quad For\ V_D << (V_G - V_T) \qquad (5\text{-}9)$$

where μ is the mobility of charge carriers, and Z and L are the width and length of the channel, respectively. C_i is the capacitance per unit area of the dielectrics between the channel and the gate,

V_G is the voltage difference between gate and source, V_D is the voltage difference between the gate and drain, and V_T is the threshold voltage of the FET.

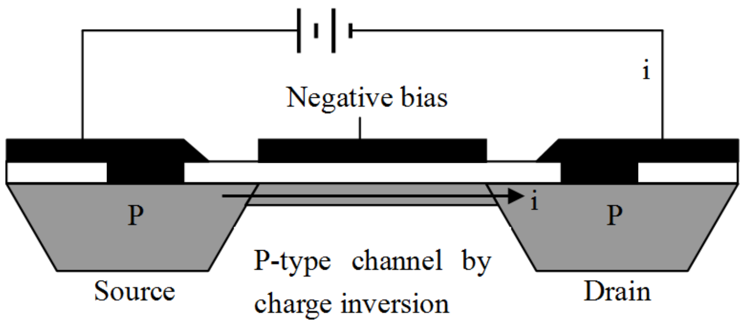

Figure 5.16 Schematic drawing of a P-channel MOSFET on state.

Equation (3-9) indicates that the MOSFET channel current allows mechanical sensing to be directly coupled to electronics signal processing and logic circuits, with minimal parasitic capacitance involved. Also, both the C_i and V_T terms are functions of the air gap between the gate and the channel as shown in equation (3-10) and (3-11).

$$\mathrm{C_i} = \frac{1}{\frac{1}{C_{dielect}} + \frac{1}{C_{media}}} = \frac{1}{\frac{t_{dielec}}{\varepsilon_{dielect}} + \frac{a}{\varepsilon_{media}}} \quad (5\text{-}10)$$

$$V_T = \Phi_{ms} + 2\Phi_F - \frac{Q_i}{C_i} - \frac{Q_d}{C_i} \quad (5\text{-}11)$$

where ε is the dielectric constant and t is the layers thickness, Φ_{ms} is the difference of the work function between the gate and the semiconductor, Φ_F is the flat-band voltage, Q_i is the trapped charge per unit area in the dielectric material, and Q_d is the accumulated charges in the channel.

Figure 3.17 demonstrates the schematic of the membrane displacement measurement using the MOSFET technique. The membrane serves as the gate. By adjusting the bias voltage on the membrane, the channel state can be controlled. When a fixed bias is applied to the membrane and the channel is turned on, if the device is exposed to an external electric field, the membrane will deflect. This lead to a capacitance change between gate and channel, and results in channel current fluctuations. Therefore, the strength of the electric field can be measured by measuring the channel current variation.

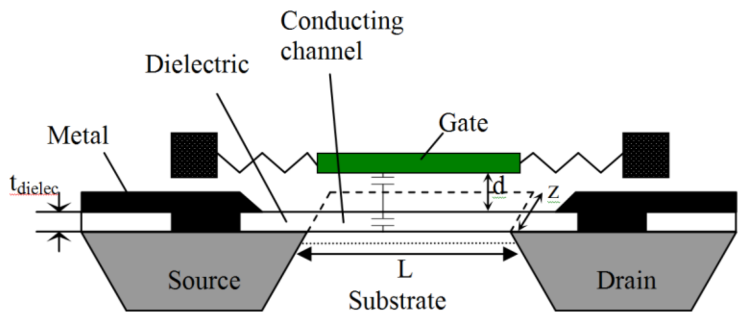

Figure 5.17 Schematic of membrane displacement measurement using MOSFET.

Overall, this is a way to measure membrane deflection using capacitance. It can provide enough sensitivity for small displacement detection and allows for compact measurement electronics. However, MOSFET capacitance structure also suffers from membrane stress, and it is hard to place the gauge close to the channel. A simpler capacitance measurement method is discussed in the next section.

5.4.3. Sensor motion capacitance measurement

As an improvement of the work in [19], the first consideration is to measure the membrane displacement by a capacitance measurement. In this way, it is possible to make a compact measurement system. Figure 3.18 shows the working principle of the capacitance measurement. A membrane fabricated from an SOI wafer is located over an electrode to form a capacitor. In the presence of an electric field, an attractive force will deflect the membrane towards the voltage source and change the capacitance.

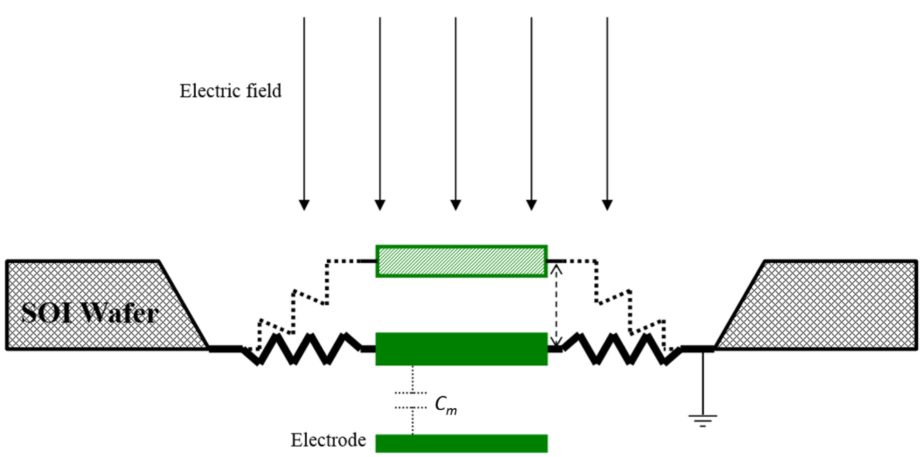

Figure 5.18 Schematic of SOI membrane capacitance measurement.

The electrostatic force pulling on the membrane due to the electric field normal to the senor is given by:

$$F_e = \frac{1}{2}\frac{\varepsilon A}{h^2}V_{DC}^2 = \frac{1}{2}\varepsilon A E^2 \tag{5-12}$$

where h is the distance separating the membrane and the voltage source, A is the surface area of the membrane, V is the voltage on the nearby voltage source, ε is the permittivity of air, and E is the strength of the electric field.

The restoring force on the springs, due to membrane motion, is given by:

$$F_s = k\Delta d \tag{5-13}$$

where k is the total spring constant of the four micro-springs supporting the membrane.

The relationship between the electric field normal to the membrane that causes membrane motion, and the variation of the capacitance measured by the position sensing electrode can be derived as follows. Equating $F_e = F_s$, we obtain:

$$k\Delta d = \frac{\varepsilon A E^2}{2} \tag{5-14}$$

Assuming a parallel plate capacitor model for the interrogating electrode adjacent to the membrane separated by distance d, and the displacement of the membrane being Δd, we have:

$$k\left(\frac{d + \Delta d}{\varepsilon A} - \frac{d}{\varepsilon A}\right) = \frac{E^2}{2} \tag{5-15}$$

Substituting the parallel plate capacitance model into equation (3-15), we obtain:

$$k\left(\frac{1}{C_{\text{m final}}} - \frac{1}{C_{\text{m initial}}}\right) = \frac{E^2}{2} \tag{5-16}$$

Finally, solving for the change in capacitance ΔC due to membrane motion (where $\Delta C = C_{m\ initial} - C_{m\ final}$), we obtain the relationship between measured ΔC and the electric field normal to the membrane.

$$\Delta C = \frac{C_{\text{m initial}}^2}{\frac{2k}{E^2} + C_{\text{m initial}}} \tag{5-17}$$

Equation (3-17) shows that ΔC is related to the initial capacitance of the membrane, and this initial capacitance depends on the initial gap between the membrane and sense electrode.

Figure 3.19 plots the calculated sensor response, $\Delta C/C_{m\ initial}$, for an initial air gap ranging from 5 μm to 20 μm. As we can see from the sensor response, at a lower electric field (< 300 kV/m), the capacitance variation is more sensitive to external fields. Over 300 kV/m, capacitance change reduces. We can also see from Figure 5.19 that the initial air gap determines the signal to noise ratio (SNR). A smaller air gap has a higher SNR. For example, the signal for d = 5 μm is about two times higher than the signal that is obtained for d =10 μm.

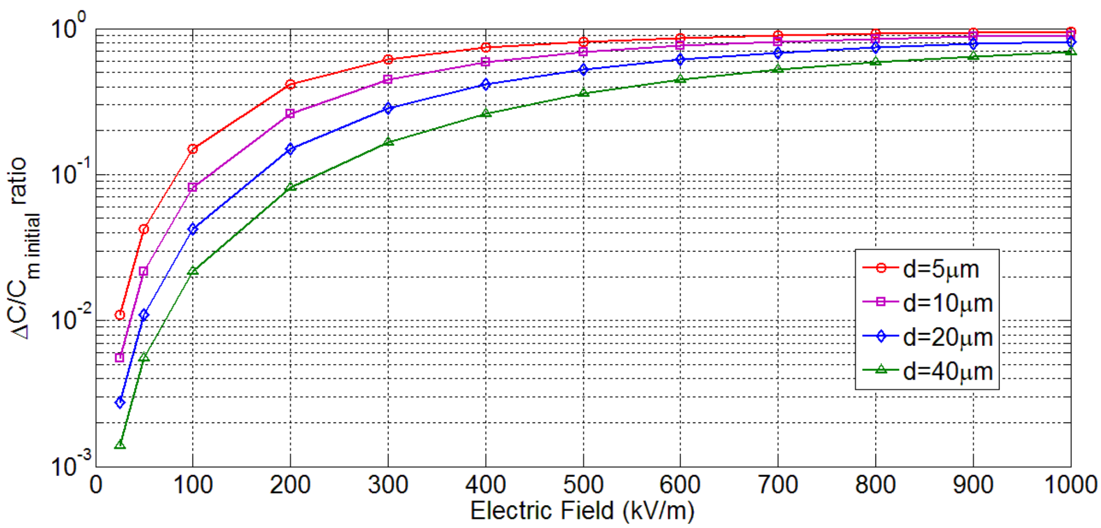

Figure 5.19 Sensor response for various initial d. Membrane size: 1 mm × 1 mm, spring constant k = 0.1 N/m.

Sensor response is also determined by the spring constant of the micro-spring. As we can see from Figure 5.20, with fixed initial air gap of 10 μm, $C_{m\ initial}$ is constant; when the spring becomes stiffer (spring constant shown changing from 0.1 N/m to 0.8 N/m) the capacitance variation ΔC becomes smaller, which results in a reduction in sensitivity.

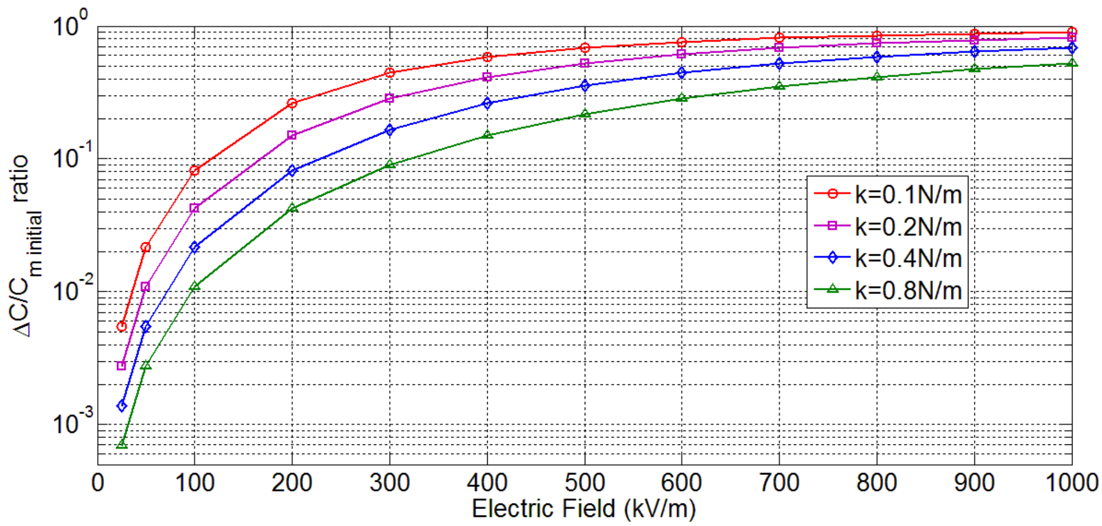

Figure 5.20 Sensor response for various spring constants. Membrane size: 1 mm × 1 mm, initial air gap 10 μm.

5.4.4. Capacitive sensor interface electronics

A signal processing circuit is needed for a capacitive sensor to convert capacitive change into voltage, current, frequency, pulse width, or digital output that can be read by an instrument. Challenges of capacitance measurement in MEMS sensors are:

(1) In most cases, the sensor capacitance value is very low, in the range of a few pF or less.

(2) Often it is necessary to measure a small sensor capacitor in the presence of much larger parasitic ones.

(3) Complete shielding of capacitive sensors is not possible; they can easily pick up interference from their environment, as a result, the amount of interference needs to be reduced with appropriate filtering techniques.

(4) In sensors with a large signal bandwidth, it is rather challenging to achieve the required resolution. In this section, different conversion techniques are explored to find out the most suitable method for a capacitive electric field sensor.

ac Bridge Circuit

The ac bridge is a classic method in capacitance to voltage conversion. It is similar to the resistive Wheatstone bridge where a balanced ratio of impedance results in a balanced condition as indicated by a voltage detector. Changes in one of the impedances cause an imbalance that is sensed. In an ac bridge, this detector can be an oscilloscope, voltage amplifier, or any device capable of registering small ac voltages. However, a major drawback of the ac bridge is its sensitivity to electrical interference between the bridge circuit and external bodies. Another potential problem is the stray capacitance between either end of the voltage detector and ground, resulting in current paths to ground, which can affect the bridge balance and cause nonlinearity in the sensor response.

Resonance shift circuit

Capacitance to frequency converters are simple and often consume less power compared to the capacitance to voltage circuits. The output of these circuits is a quasi-digital quantity (frequency), and there is no need for an analog to digital converter in the front-end. Figure 3.21 is one of the capacitance to frequency converter examples. It is a Colpitt oscillator, where the output frequency is proportional to the fixed inductance:

$$fosc \propto \frac{1}{\sqrt{\frac{C_1 C_2}{C_1 + C_2} L}} \tag{5-18}$$

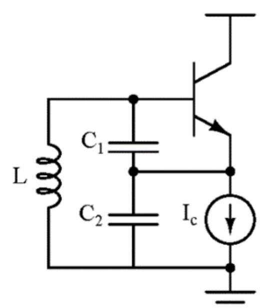

Figure 5.21 Basic Colpitt oscillator circuit.

The main drawback of oscillators is that its frequency measurement can be very sensitive to the parasitic capacitances involved in the measurement of a sensor and all external interferences.

RC circuit driven by high frequency square wave

Capacitance can also be measured by using an RC circuit. If it is driven at high frequencies (relative to its time constant), the current flow through the capacitor is given by:

$$i = C\frac{dV}{dt} \qquad (5\text{-}19)$$

where i is instantaneous current flow through the capacitor, C is capacitance in Farads, and dV/dt is the instantaneous rate of the voltage change.

Figure 3.22 shows the simulation of the RC circuit in Cadence PSPICE software. The resistor is 20 kΩ and the capacitor is 20 pF (similar in value to the MEMS device) which has a time constant of 0.4 ms. It is excited by a 0 V to 5 V square wave with the frequency of 50 MHz. At this frequency, the capacitor cannot fully charge and discharge. The voltage on the capacitor will fluctuate at a half the square wave voltage of 2.5 V, where charge time is equal to discharge time, as shown in Figure 3.23.

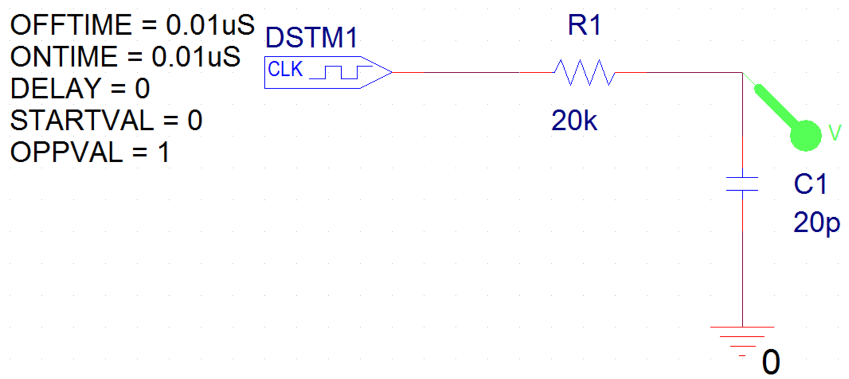

Figure 5.22 Capacitance square wave measurement simulation.

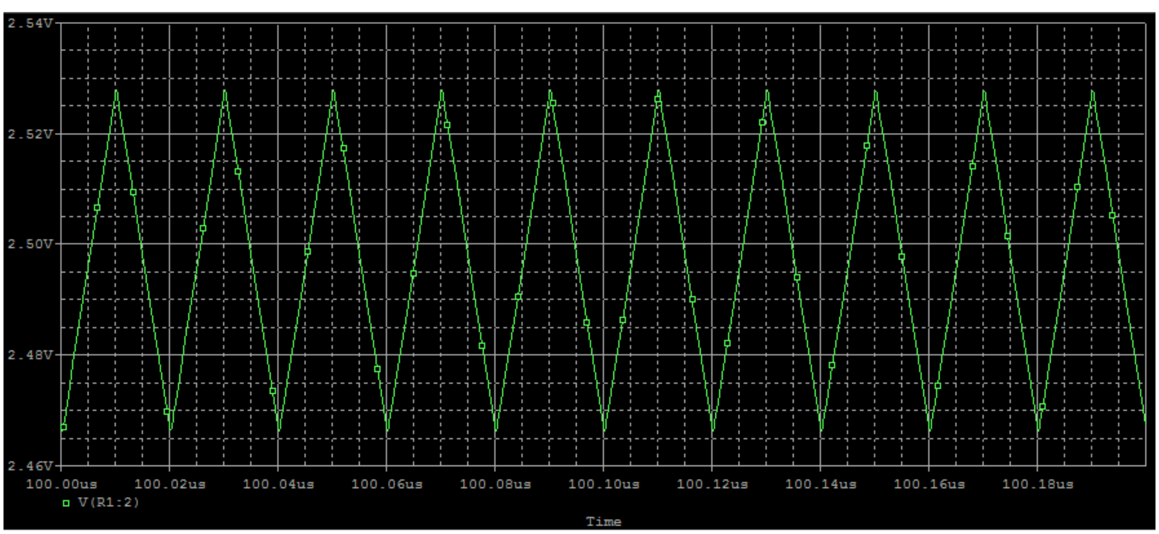

Figure 5.23 Capacitance square wave measurement simulation output.

As the voltage on the capacitor varies in a very small range, if the frequency is chosen to give the capacitor a small impedance compared to the resistor, the current in the circuit is close to a constant value of 2.5 V/20 kΩ=0.125 mA.

Figure 3.23 also shows the capacitor voltage variation is 0.062 V. From equation (3-19), we have

$$C = \frac{I \cdot t}{\Delta V} \tag{5-20}$$

where, I=0.125 mA, t=0.01μs and ΔV=0.06 V

Then the capacitance is calculated to be 20.16 pF, which is very close to the real value shown in Figure 5.22.

However, this method is not very sensitive when it comes to measuring capacitance in pF levels. In the above example, for 20 pF capacitance, the voltage variation is only 0.06 V; sensitivity is 3 mV/pF. If the noise level is higher than 3 mV, this method will fail to detect capacitance.

Phase shift circuit

As we know for a low pass filter, the output signal has a phase shift from the input signal:

$$\varphi = -arctan(2\pi fRC) \tag{5-21}$$

If the frequency of the input sine wave signal is at the cut-off frequency of the low pass filter, the input and output signal will have a 90 degree phase difference. The low pass filter cut-off frequency is

$$f_c = \frac{1}{2\pi RC} \tag{5-22}$$

To simulate phase shift due to a capacitance change, a circuit shown in figure 3.24 was built in Cadence PSPICE software. Initially the low pass filter capacitances, C_1 and C_2 are the same. The voltage across them goes to two op-amps to convert the sine wave to be a square wave. Another op-amp is used to subtract these two signals. C_2 is used to generate a reference signal, while C_1 is a virtual capacitance sensor. In the beginning, C_1= C_2=5 μF and V_{out} is 0, as shown in figure 3.25 (blue line). Figure 3.26 (blue line) shows that when C_1 changes to 10 µF, V_{out} becomes a pulse signal, which can be measured and used to determine the variation of the capacitance.

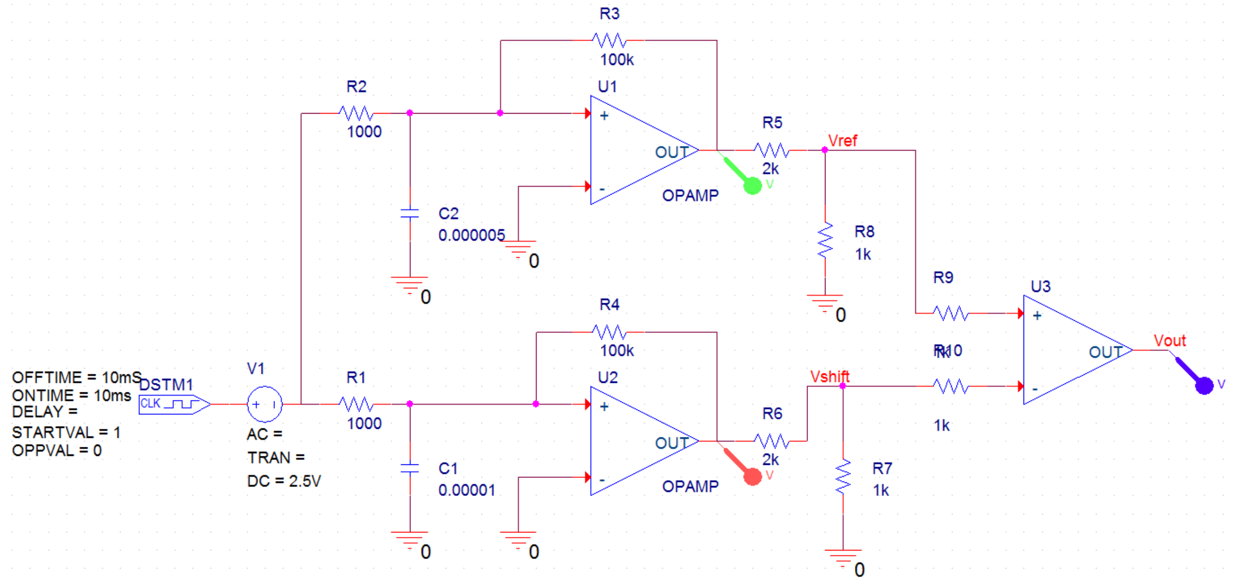

Figure 5.24 Phase shift capacitance measurement simulation.

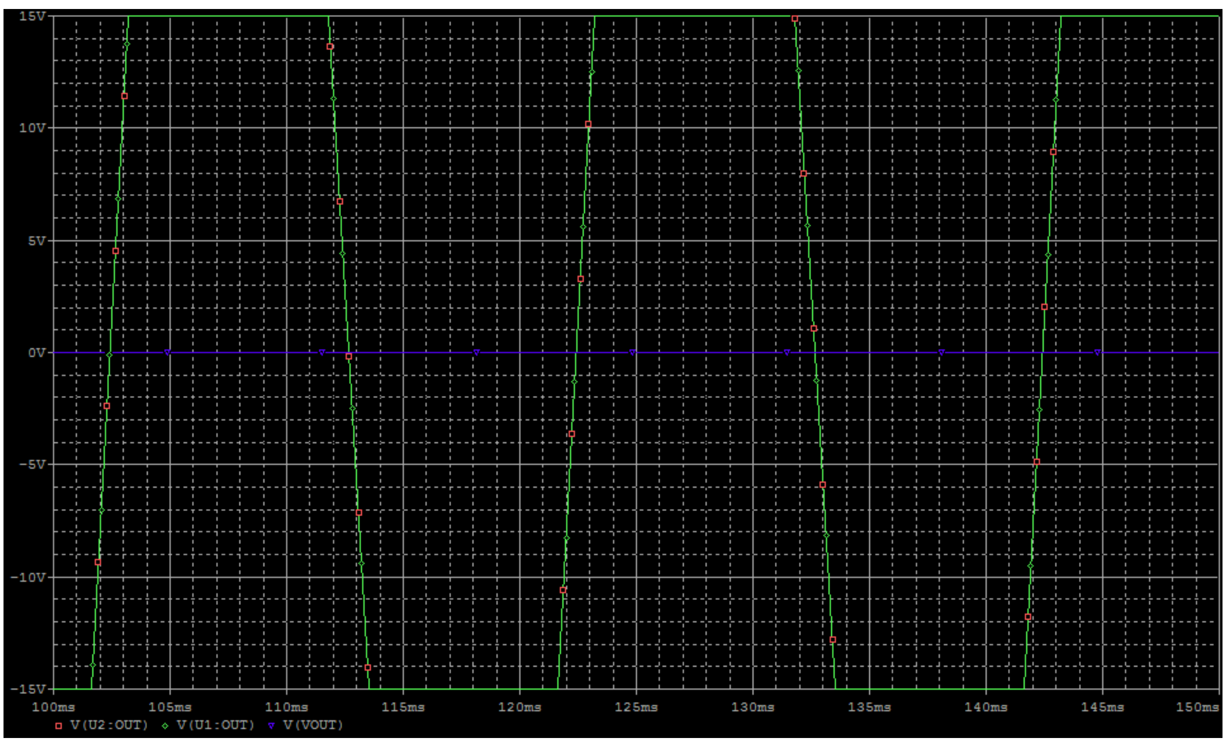

Figure 5.25 Phase shift capacitance measurement simulation result when $C_1=5\mu F$.

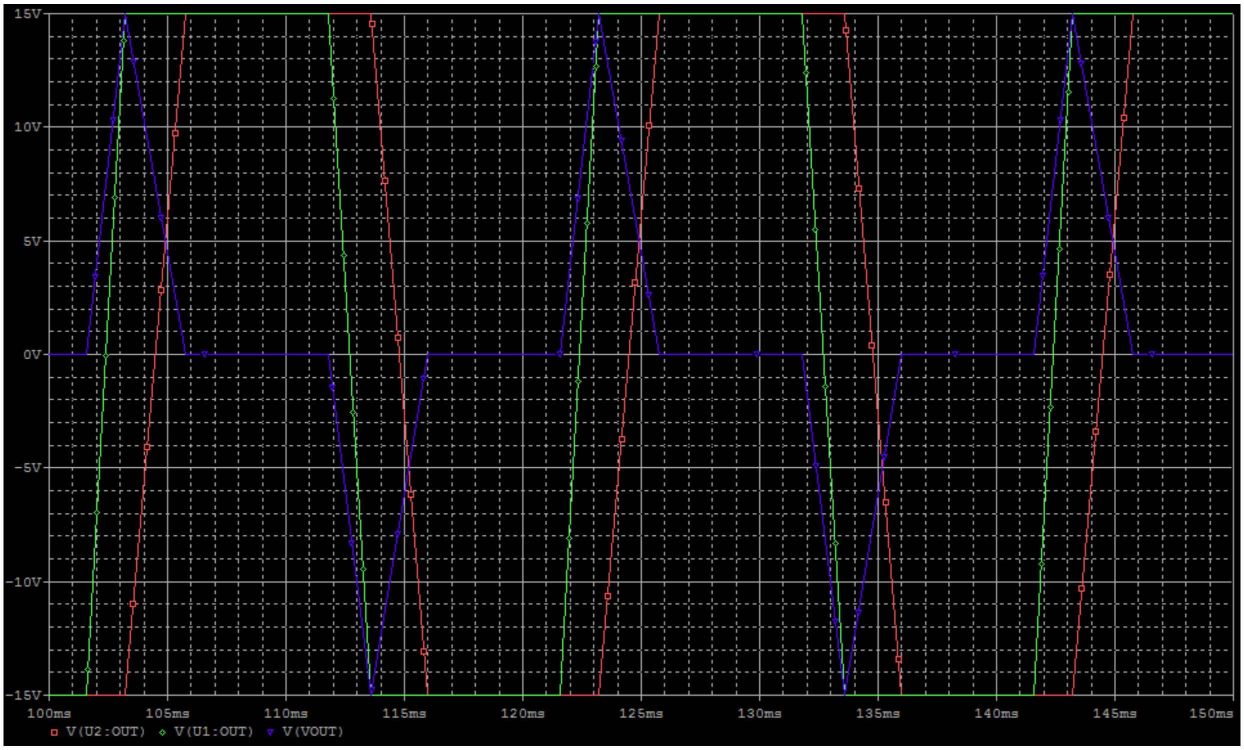

Figure 5.26 Phase shift capacitance measurement simulation result when $C_1=10\mu F$.

Capacitance to digital converter AD7747

The AD7747, which comes from Analog Devices, is a high-resolution capacitance to digital converter (CDC) based on the Σ-Δ technique. It accepts capacitance inputs up to 17 pF with 19.5-bit out of 24-bit effective resolution. Figure 3.27 shows the CDC simplified functional diagram. The measured capacitor, C_x, connects the Σ-Δ modulator input and ground. A square-wave excitation signal is applied on the C_x during the conversion and the modulator continuously samples the charge going through the C_x. The digital filter processes the modulator output, which is a stream of 0 s and 1 s containing the information in 0 and 1 density. The data from the digital filter is scaled, applying the calibration coefficients, and the final result can be read through the serial interface.

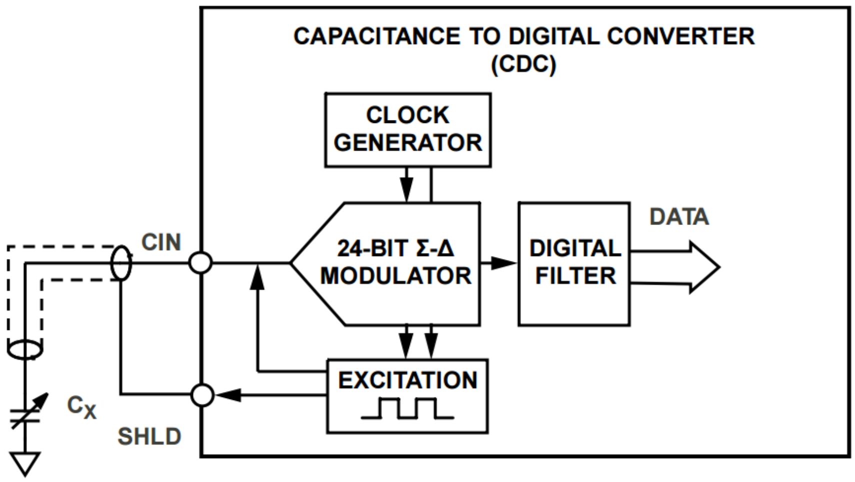

Figure 5.27 CDC simplified block diagram.

The AD7747 measures capacitance between CIN and ground. Any capacitance to ground on the signal path between CIN and a sensor is included in the conversion result. This parasitic capacitance can easily be in the same order as the capacitance of the sensor itself. If that parasitic capacitance is stable, it can be treated as an unchanging capacitive offset. However, the parasitic capacitance often changes as a result of the mechanical movement, changing ambient temperature, ambient humidity, etc. These changes are seen as drift in the conversion result and may significantly compromise the system accuracy.

To eliminate the CIN parasitic capacitance to ground, the A7747 SHLD signal can be used for shielding the connection between the sensor and CIN, as shown in figure 3.27. The SHLD output is basically the same signal waveform as the excitation of the CIN pin; the SHLD is driven to the same voltage potential as the CIN pin. Therefore, there is no ac current between CIN and SHLD pins, and any capacitance between these pins does not affect the CIN charge transfer. Ideally, the CIN to SHLD capacitance does not provide any contribution to the AD7747 result.

The main drawback of CDC is its long measurement time due to the oversampling technique. AD7747 output data rate ranges from 4.6 Hz to 45 Hz. The lower rate means more conversion time and less noise level. In the experiments discussed in section 0, an 8.1 Hz data rate is applied showing that it is able to provide l nF noise level. The slow measurement speed limit AD7747 applies in an ac electric field measurement, but with the measurement range, accuracy, and technique of eliminating parasitic capacitance, it becomes the best candidate for our capacitance dc electric field sensor.

5.5. SOI membrane capacitance testing

5.5.1. SOI membrane capacitance test setup

Figure 3.28 depicts the sensor structure and its measurement system. Below the membrane is the capacitance measuring electrode, used to measure the position movement of the membrane. The SOI membrane is fabricated using the process shown in figure 3.11 and the capacitance measuring electrode used to measure the membrane movement is fabricated on a Pyrex glass substrate. First, the electrode (aluminum metal) is deposited on the Pyrex using a sputtering process. The Pyrex is placed in close proximity to the membrane sensor, separated by a thin spacer material. The spacer initially chooses a 150 µm tape; this gives the capacitance a large initial *d*. As shown in figure 3.31, a smaller initial *d* provides higher sensitivity. Then SPR 220 photoresist was used to form a 5 µm thick spacer. However, no bonding process was used to fix the SOI membrane on the spacer; the actual *d* is bigger than 5 µm.

The variation of the capacitance due to membrane motion is measured by the AD7747 and is converted to a digital signal. A microcontroller reads the signal by I^2C bus, then the digital data is sent to MATLAB for further processing. The first version of the AD7747 capacitance interagation system is shown in Figure 5.29. The microcontroller is the PIC32 32-bit on the development board of the Digilent Cerebot MX7 from Digilent.

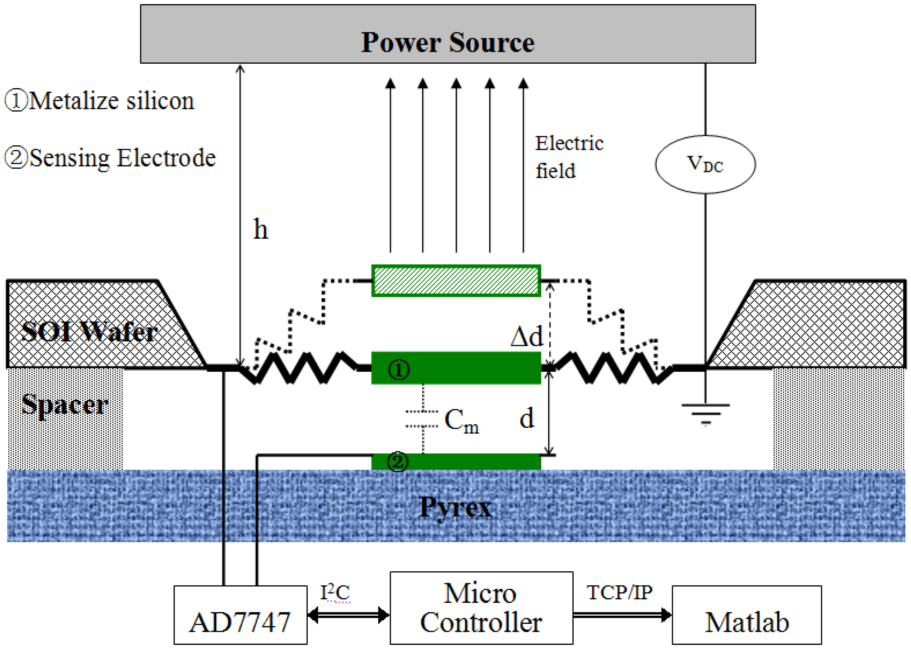

Figure 5.28 dc capacitance measurement schematic.

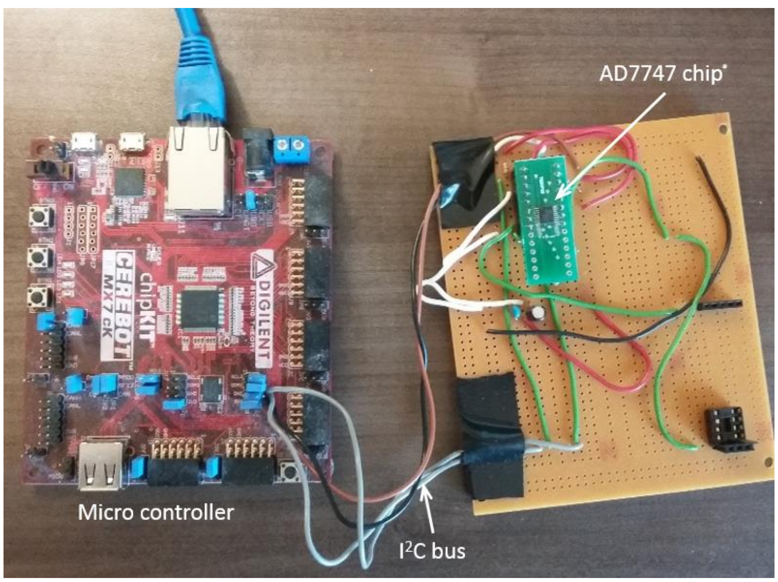

Figure 5.29 First version of AD7747 capacitance interagation system.

5.5.2. SOI membrane capacitance test results

The capacitance interrogation system of the membrane motion was then implemented and tested. The Pyrex glass containing the interrogating electrode was placed adjacent to the membrane sensor, spaced a short distance (10's of micrometers) from the sensor using a thin polymer spacer.

The sensor membrane was electrically grounded, and a biased metal plate was placed parallel to it, approximately 650 µm from the membrane, in order to generate an electric field normal to the membrane. The measurement electronics shows a little drifting for long periods of testing, which will be improved by using a grounded enclosure and replacing the cables with shielded cables (will be introduced in section 6.4). Figure 5.30 shows the output of the AD7747 chip for two applied dc electric field levels: 94 kV/m and 55 kV/m. The application of the dc field can clearly be seen, with a ΔC_m variation of 5.8 fF under application of the 94 kV/m field.

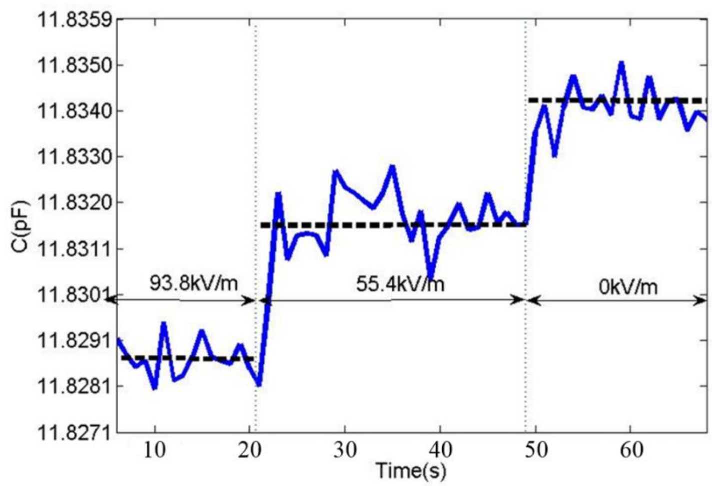

Figure 5.30 SOI membrane sensor dc field test result.

From the data shown in Figure 5.30, the measured spring constant shown in Table 5.13, and equation 3-16, the initial $C_{m\ initial}$ was found to be 0.4 pF. From this value, we find the thickness of the polymer spacer separating the sensor from the interrogating capacitive electrode to be 27 µm.

Based on the time averaged noise level in the measurement of Figure 5.30 (1.2 seconds), the resolution of this prototype sensor is about 16 kV/m.

Compared to the work in [19], 16 kV/m is close to the results without using a lock-in amplifier. To further improve the sensitivity, a smaller gap between membrane and measurement electrode is needed. But this is limited by the membrane curvature and the out of plane deformation of the micro-springs. Figure 5.31 shows an image of the membrane and micro-spring from a Fogale optical 3D surface topography system. The curvature of the membrane is measured in the range of 10-30 µm and the micro-spring out of plane deformation is about 20 µm. From Figure 5.32, the relationship between $d_{initial}$ and sensitivity, we see that the membrane curvature prohibits the improvement of sensitivity.

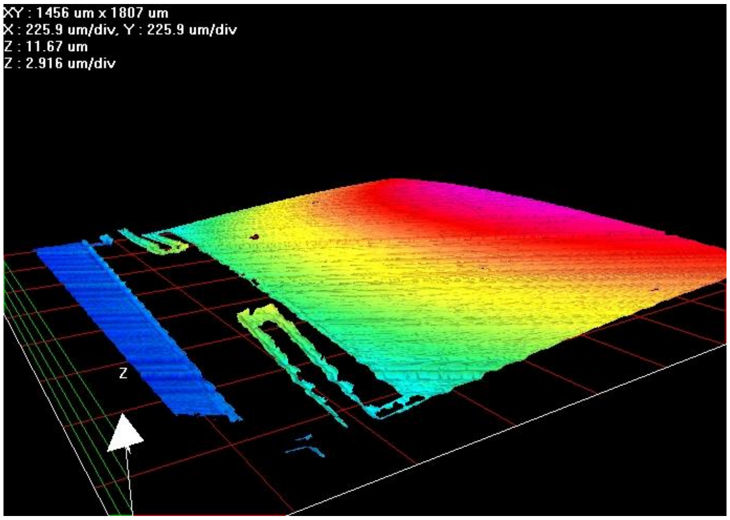

Figure 5.31 Membrane curvature and spring deformation observed by a Fogale system.

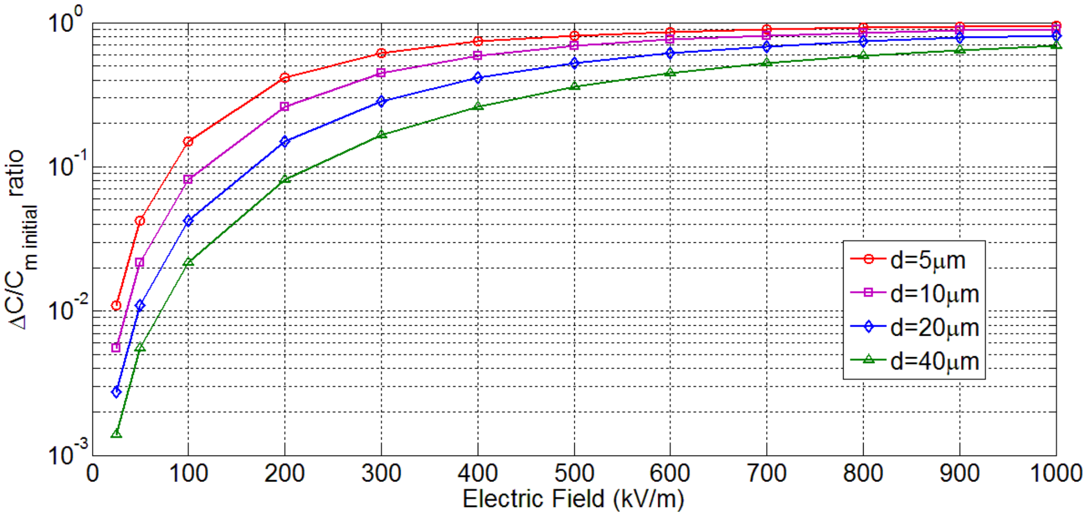

Figure 5.32 Capacitance sensor sensitivity vs. initial distance.

5.6. ac Modulation on Capacitance Measurement

In order to improve the capacitance measurement sensitivity, a circuit was designed to couple the external electric field with an ac signal. The output signal of this circuit includes the information of an electric field and an ac signal with a specific frequency. A lock-in amplifier was then used to filter out noise signals at all other frequencies and get a very clean response. The circuit schematic is shown in Figure 5.33.

For an input signal V_1 and V_3, op-amp U_1 serves as a non-inverting amplifier, while for input V_2, op-amp U_1 is an inverting amplifier. Thus:

$$V_{out1} = V_1(1 + j\omega_1 R_1 C_1) + V_2 j\omega_2 R_1 C_1 + V_3(1 + j\omega_2 R_1 C_1) \qquad (5\text{-}23)$$

Since ω_2 is 100 times less than ω_1, the related items can be ignored. Then (3-23) becomes

$$V_{out_1} = V_1(1 + j\omega_1 R_1 C_1)$$

Op-amp U_2 is used to subtract the non-amplified item V_1, then

$$V_{out_2} = jV_1\omega_1 R_1 C_1$$

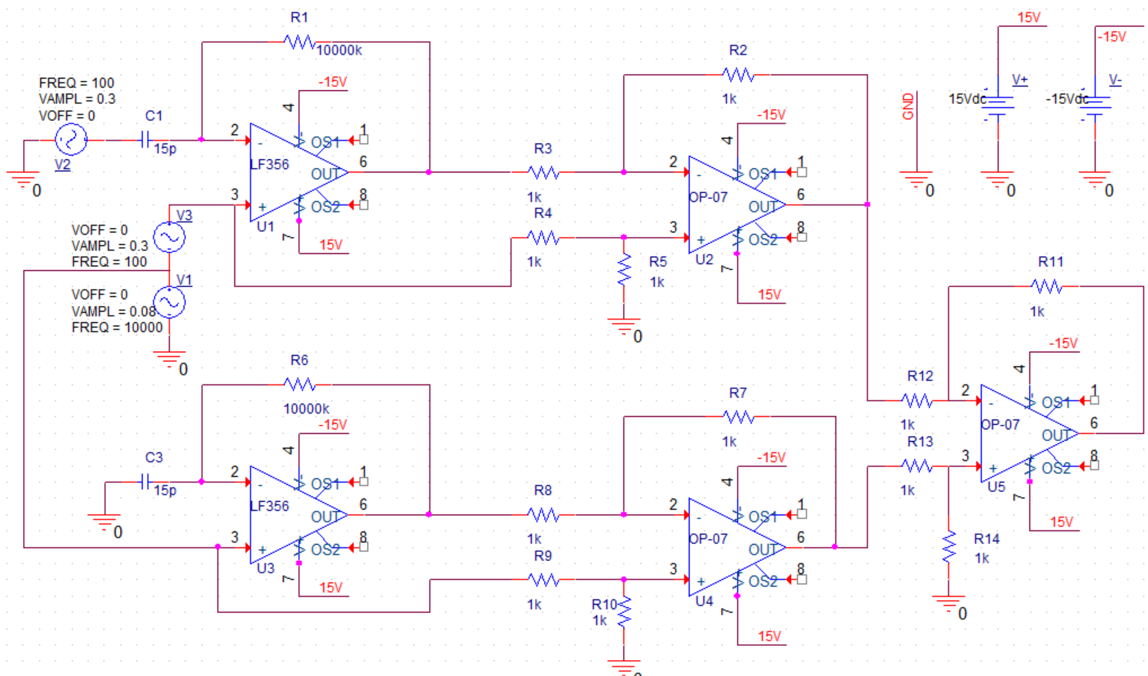

Figure 5.33 Lock-in capacitance measurement schematic.

U_3 and U_4 are identical amplifiers to U_1 and U_2, to provide the same signal for the next differential amplifier U_5. Therefore, V_{out3} is:

$$V_{out_3} = jV_1\omega_1 R_1 \Delta C \qquad (5\text{-}24)$$

As the capacitance change ΔC is caused by the coupling of V_2 and the external electric field:

$$\Delta C = \frac{\varepsilon A}{d_0} - \frac{\varepsilon A}{d_0 + \Delta d}$$

$$\Delta C = \varepsilon A \frac{\Delta d}{d_0\left(d_0 + \Delta d\right)}$$

Assuming $\Delta d << d_0$, then

$$\Delta C = \varepsilon A \frac{\Delta d}{d_0^2} \tag{5-25}$$

And so we have

$$\Delta \mathrm{d} = \frac{F}{k}$$

where k is the spring constant of the actuator, then

$$\Delta \mathrm{d} = \frac{-\frac{1}{2}\varepsilon A E^2}{k}$$

$$\Delta \mathrm{d} = -\frac{\varepsilon A}{2kL}\left(V_s - V_2\right)^2$$

$$\Delta \mathrm{d} = -\frac{\varepsilon A}{2kL}\left(V_s^2 - 2V_s V_2 + V_2^2\right) \tag{5-26}$$

Substituting (3-26) into (3-25) we get:

$$\Delta C = -\frac{\left(\varepsilon A\right)^2}{2kL^2 d_0^2}\left(V_s^2 - 2V_s V_2 + V_2^2\right) \tag{5-27}$$

Substituting (3-27) into (3-24) we get:

$$V_{out_3} = -\frac{\left(\varepsilon A\right)^2 jV_1 \omega_1 R_1}{2kL^2 d_0^2}\left(V_s^2 - 2V_s V_2 + V_2^2\right) \tag{5-28}$$

The term $2V_SV_1V_2$ in the equation (3-28) shows that the bias ac signal V_2 and measurement signal V_1 introduced an oscillation to the ribbons or membrane. Assuming

$$V_1 = Asin\left(\omega_1 t + \varphi_1\right) \tag{5-29}$$

$$V_2 = Bsin\left(\omega_2 t + \varphi_2\right) \tag{5-30}$$

where A and B are the magnitude of each signal, ω_1, ω_2 are their angle frequency, φ_1, φ_2 are their initial offsets. Then

$$2V_sV_1V_2 = 2V_sAsin\left(\omega_1\mathrm{t} + \varphi_1\right)Bsin\left(\omega_2\mathrm{t} + \varphi_2\right)$$

$$\Rightarrow 2V_sV_1V_2 = 2V_sABsin\left(\omega_1\mathrm{t} + \varphi_1\right)sin\left(\omega_2\mathrm{t} + \varphi_2\right)$$

$$\Rightarrow 2V_sV_1V_2 = 2V_sAB(-\frac{1}{2}\left(\cos\left(\omega_1\mathrm{t} + \varphi_1 + \omega_2\mathrm{t} + \varphi_2\right) - \cos\left(\omega_1\mathrm{t} + \varphi_1 - \omega_2\mathrm{t} + \varphi_2\right)\right)$$

$$\Rightarrow 2V_sV_1V_2 = -V_sAB\left(\cos\left((\omega_1 + \omega_2)\mathrm{t} + \varphi_1 + \varphi_2\right) - \cos\left((\omega_1 - \omega_2)\mathrm{t} + \varphi_1 - \varphi_2\right)\right)$$

$$\Rightarrow 2V_sV_1V_2 = V_s\mathrm{AB}\cos\left((\omega_1 - \omega_2)\mathrm{t} + \varphi_1 - \varphi_2\right) - V_sAB\cos\left((\omega_1 + \omega_2)\mathrm{t} + \varphi_1 + \varphi_2\right) \tag{5-31}$$

From equation (3-31), we can see that $2V_SV_1V_2$ has two frequencies of $\omega_1 + \omega_2$ and $\omega_1 - \omega_2$, and is proportional to the dc power source V_s. Thus, the signal can be detected by using a lock-in amplifier, which can assist in reducing the effect of environmental noise. The challenges in applying this circuit to measure capacitance are the following:

(1) Need to have high quality reference signal at the frequency of $\omega_1 + \omega_2$ or $\omega_1 - \omega_2$, which is not applicable in our lab.

(2) $\omega_1 + \omega_2$ and $\omega_1 - \omega_2$ need to be different enough to be distinguished from noise which has a frequency of ω_1. While in this circuit ω_2 is 100 times less than ω_1, $\omega_1 + \omega_2$, and $\omega_1 - \omega_2$ are almost the same.

Both challenges are not easy to overcome; therefore, the circuit was not tested in this work.

5.7. Summary

This chapter discussed the first SOI wafer based MEMS sensor that has been fabricated in our lab. The membrane with micro-spring structure was designed to achieve a membrane movement of approximately 0.1 nm to 10 µm, when exposed to dc electric fields ranging from 1 kV/m to 1000 kV/m respectively. Multiple motion techniques were studied including grating, field effect transistor and capacitance motion measurement methods. Finally the AD7747 capacitance to digital convertor chip was selected to measure the membrane motion. A capacitance interrogation system was built to interrogate the membrane motion. It successfully detected a dc electric field with a noise averaged resolution of 16 kV/m. The curvature of the SOI membrane prevented resolution improvement.

Due to the intrinsic stress of the silicon layer, the curvature of the SOI membrane is measured in the range of 10-30 µm. This prevent locating the membrane closer to the sensing electrode, and therefore, affect further improve the sensor sensitivity.

Chapter 4 - Ribbon Array Capacitance Sensor

Chapter 3 showed that the sensitivity of an SOI membrane capacitance interrogation sensor is hard to improve. This is due to the membrane curvature which gives extra distance between the membrane and the sensing electrode. Also, as the micro-spring is made of single crystal silicon which has a high Young's modulus of 130-180 GPa, the stiffness of the micro-springs is high, which results in less deformation under a weak electric field. In this new design, a metal based ribbon array was considered to improve the sensor performance. It is designed to have more flexibility, and the same electric field can introduce more displacement (as ribbons are working independently, in this chapter, the displacement refers to the overall effective displacement of the ribbon structure). There are three main factors for this. First, the metal material usually has a smaller Young's modulus (aluminum is 64 GPa, copper is 117 GPa). Second, the ribbon array is designed to have a smaller thickness (only 200 – 500 nm). Third, the whole structure of the ribbon array is a micro-spring. The ribbon array also may have better surface flatness if it controls the stress well, which allows a closer distance between the ribbon array and the electrode underneath.

The working principle of a ribbon array capacitance sensor is shown in Figure 6.1. A micromachined ribbon array is placed over the electrode, and they form a capacitor *C*. A spacer between them gives the initial distance *d*. When the sensor is exposed to an electric field, the ribbon array is deflected by electrostatic force. The changed distance from the ribbon array to the electrode causes the capacitance to change. Measuring the variation of capacitance can get the strength of the corresponding electric field.

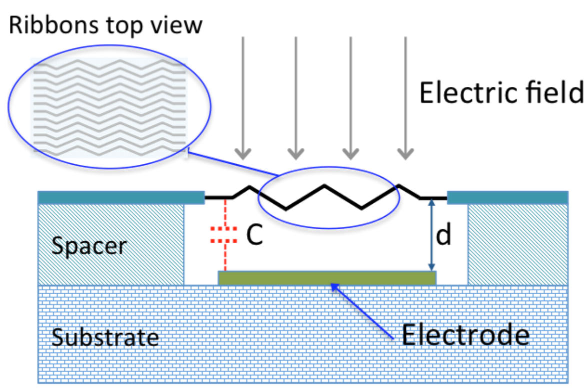

Figure 6.1 Ribbon array capacitance measurement schematic.

6.1. Ribbon design

Ribbon arrays of various length, jog angle, width, and other dimensions were first designed and modeled in COMSOL software. Optimization of the structural design was done to achieve a maximum ribbon deformation of approximately 10 nm to few μm, when exposed to electric fields from 10 kV/m to 200 kV/m. The simulation performed in section 6.1.1 to 6.1.3 ignored the fringing effect and the distortion of the electric field when ribbon moves. The calculated electrostatic forces were applied to the normal to the ribbon. In reality, fringing effect may lead to greater ribbon displacement as it will create a stronger electric field, while the distortion of the electric field is very small compared to the distance to voltage source and can be ignored.

6.1.1. Ribbon connection simulation

The first scenario considered is if the ribbons are too flexible and have random movement, they might easily stick to each other. Adding connections in between helps separate them. The first simulation is to simulate how connections impact the spring constant. Figure 4.2 shows the simulation results. Simulation parameters and spring constant calculation are summarized in Table 6.1. The spring constant is calculated by using electrostatic force divided by the maximum displacement of the ribbon. As shown in Table 6.1, the single ribbon spring constant is 9.1×10^{-4} N/m and requires a force of 1×10^{-10} N to deflect 0.11μm, while the whole ribbon array with 20 ribbons needs 20 times the force, 2×10^{-9} N, to have the same displacement. This indicates that the connection will not affect the ribbon mechanical performance.

However, the fabrication result of the ribbon array with connections shows that the connections introduce lateral stress, which causes the ribbon array to curl up laterally by about 300 – 500 μm. Therefore, the connection between ribbons was not helpful to the design.

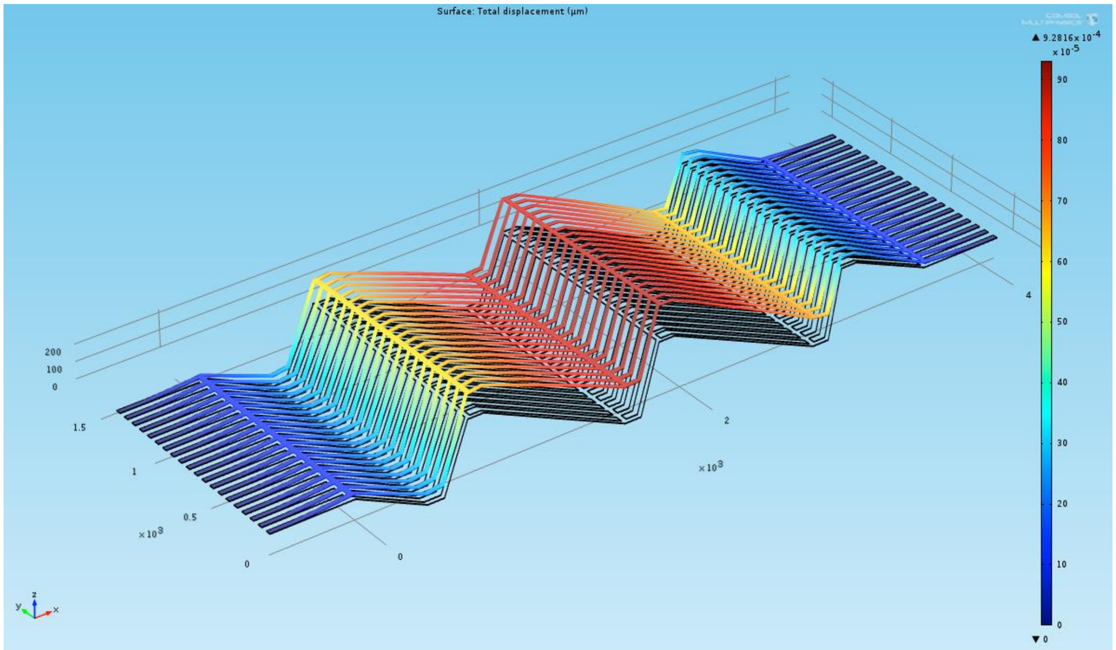

Figure 6.2 Ribbon array with connections simulation.

Table 6.1 Ribbon array with connections simulation results.

Ribbon material	Al
Width	21.2 μm
Wiggle angle	45º
Wiggle length	353 μm
Ribbon number	20
Thickness	1 μm
Maximum displacement	0.11 μm
Total force	2×10^{-9} N
Total Spring constant	1.8×10^{-2} N/m
Single ribbon force	1×10^{-10} N
Single ribbon spring constant	9.1×10^{-4} N/m

6.1.2. Effect of width

The ribbon width is another important factor that determines ribbon mechanical behaviors. A simulation was performed to compare two ribbons with a width of 21.2 μm and 42.4 μm. Table 4.2 lists the simulation parameters and results. Under the same force, the displacement of 42.4 μm width ribbon is 0.055 μm, while the 21.2 μm ribbon has a displacement of 0.11 μm. This indicates that the spring constant is linearly proportional to the ribbon width.

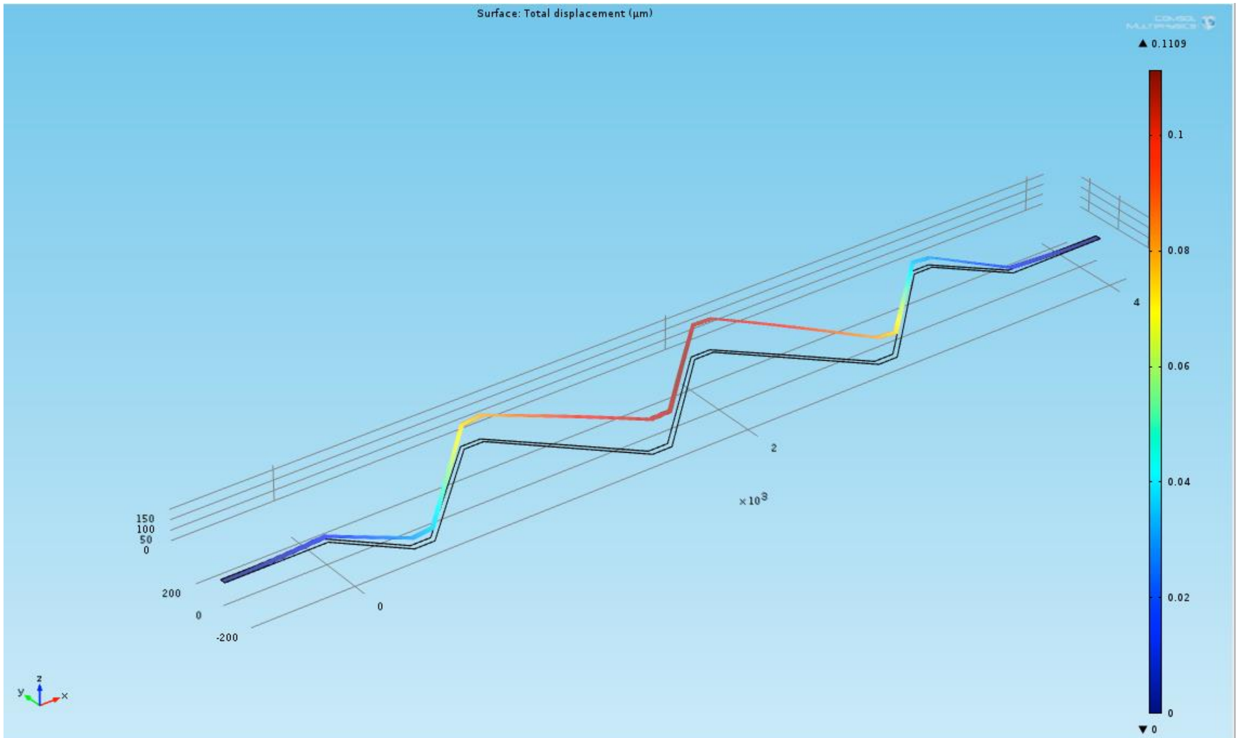

(a) Ribbon width 21.2 µm;

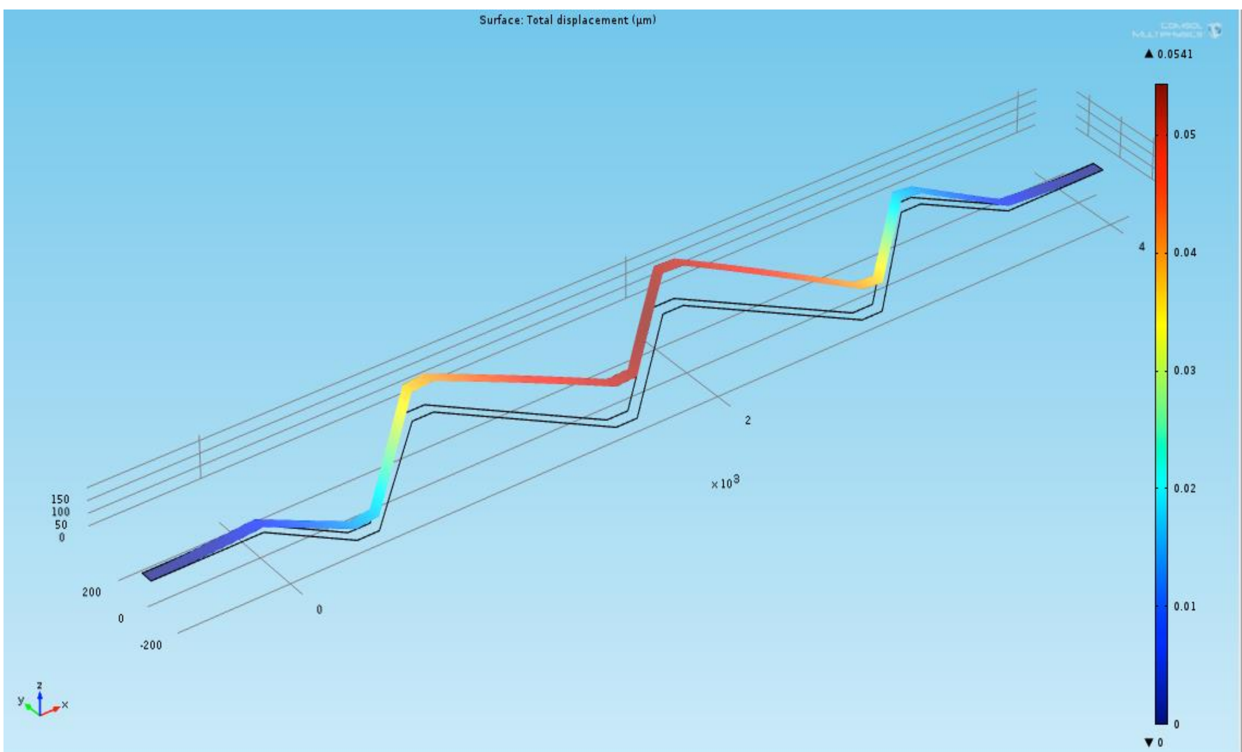

(b) Ribbon width 42.4 µm;

Figure 6.3 Ribbon array with different ribbon width simulation.

Table 6.2 Ribbon with different width simulation.

	Ribbon 1	Ribbon 2
Ribbon material	Al	Al
Width	21.2 μm	42.4 μm
Wiggle angle	45°	45°
Wiggle length	353 μm	353 μm
Thickness	1 μm	1 μm
Maximum displacement	0.11 μm	0.055 μm
Single ribbon force	1×10^{-10} N	1×10^{-10} N
Single ribbon spring constant	9.1×10^{-4} N/m	1.82×10^{-3} N/m

6.1.3. Varying Jog Angles

Jog Angles is the angle between the ribbon beam and the base line as shown in Figure 6.4. If the distance between the two ends of the ribbon is fixed, and the number of spring wiggles is also fixed, a greater jog angle makes the total ribbon length longer, and it will have more ribbon area. The longer ribbon has more flexibility, and the more area allows the ribbon to get more electrostatic force when exposed to the same electric field. However, it will increase the micro-spring width, which increases the ribbon deformation caused by intrinsic stress. It is worth studying the relation of the ribbon jog angle to find a balance between the flexibility and stress.

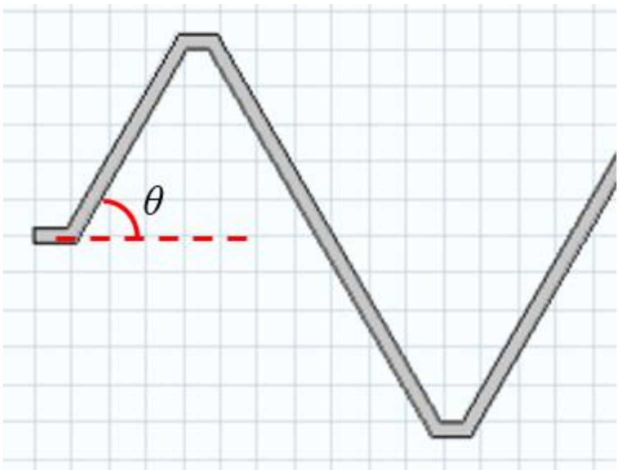

Figure 6.4 Jog angle defination.

In the simulation, a ribbon with 3500 μm end-to-end distance was chosen, with width of 20 μm and thickness of 1.5 μm. Ribbons with three different angles were simulated. Their sizes are shown in Figure 6.5, and Table 6.3 lists the results.

As shown in Table 6.3, when the jog angle varied from 30º to 60º, the spring constant changes from 3.33×10^{-3} N/m to 2.28×10^{-3} N/m, which is about 1.46 times softer. Under the same electric field, the displacement of 60º ribbon was about 2.4 times longer than the 30º ribbon.

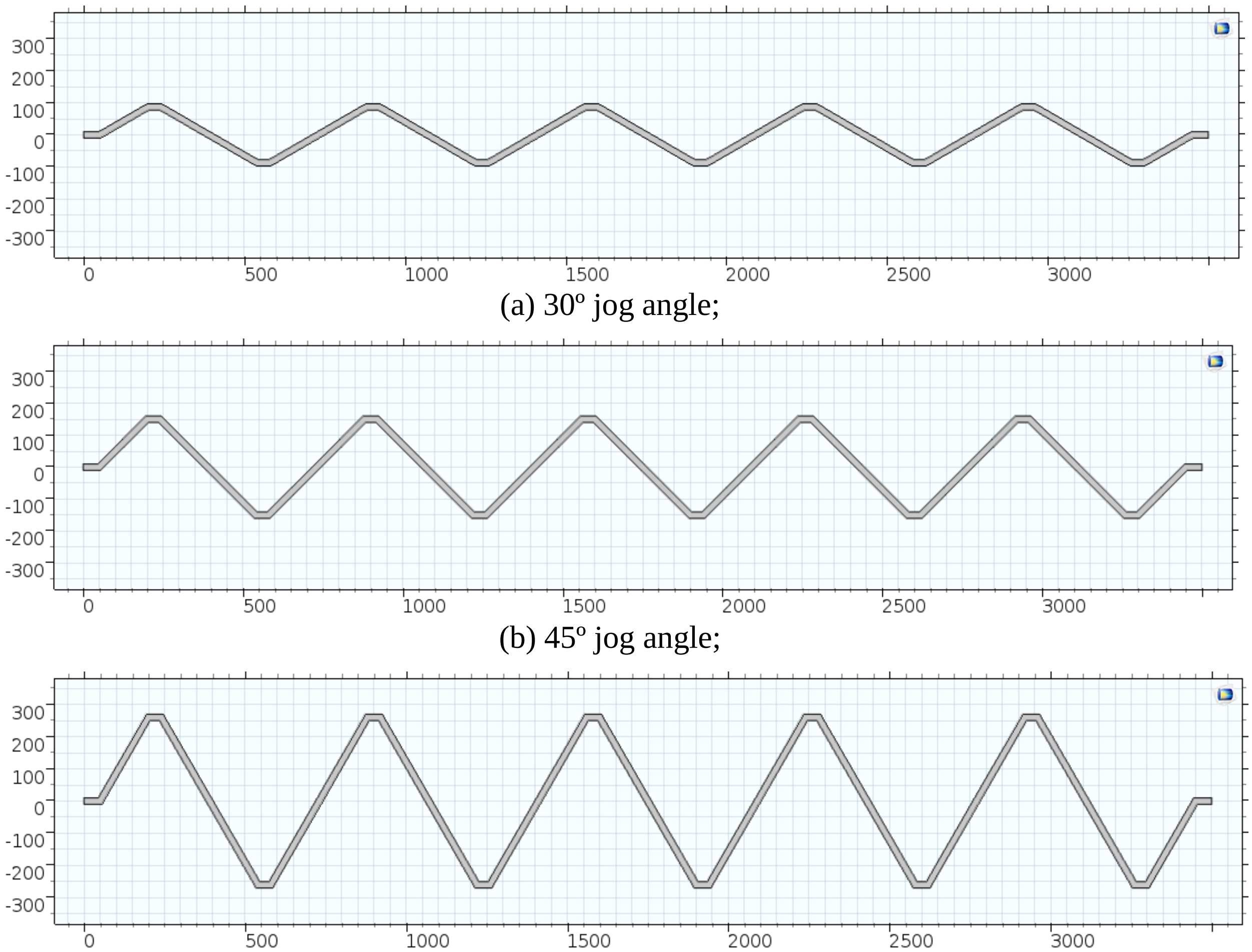

(a) 30º jog angle;

(b) 45º jog angle;

(c) 60º jog angle;

Figure 6.5 Ribbon with different jog angles.

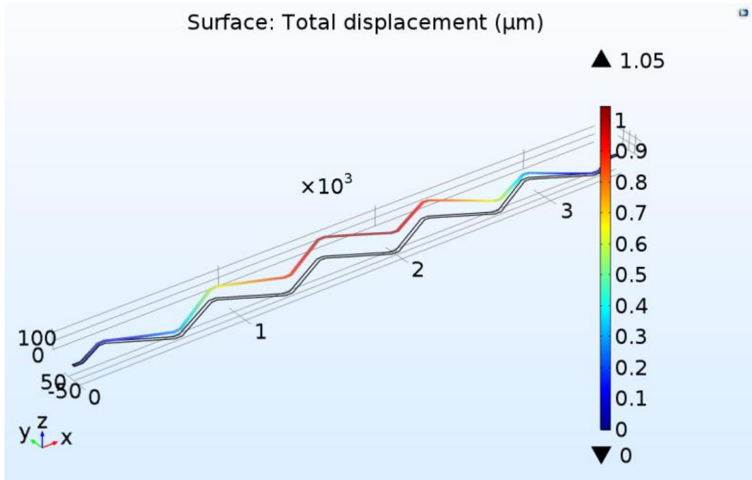

(a) 30º ribbon displacement;

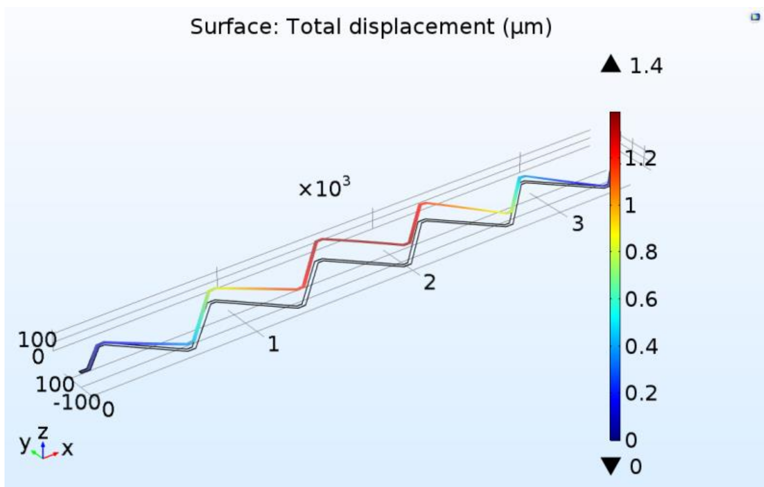

(b) 45º ribbon displacement;

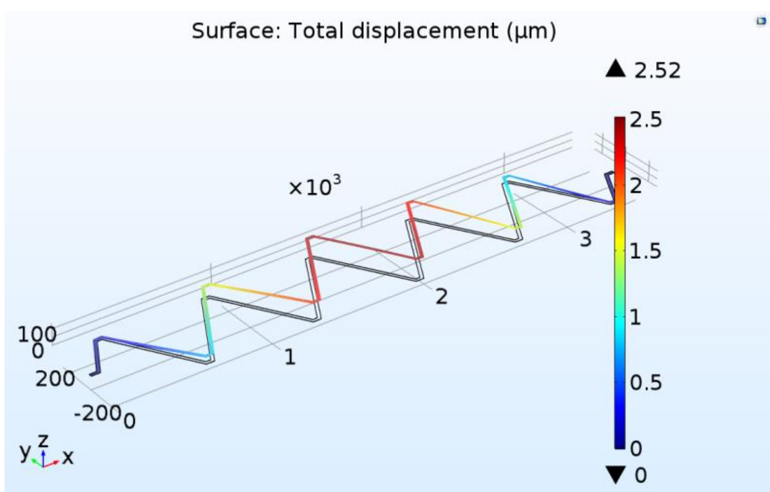

(c) 45º ribbon displacement;

Figure 6.6 Ribbon with different jog angles simulation.

Table 6.3 Ribbon with different jog angle simulation results.

θ	Electric field	d_{max}	ES force	Spring Constant
30º	100 kV/m	1.05 μm	3.5×10^{-9} N	3.33×10^{-3} N/m
45º	100 kV/m	1.4 μm	4.2×10^{-9} N	3×10^{-3} N/m
60º	100 kV/m	2.52 μm	5.75×10^{-9} N	2.28×10^{-3} N/m

6.1.4. Effect of gravity

As discussed in the previous sections, the aluminum ribbon is designed to be so flexible that even gravity will introduce a small deformation to the structure. A deformation even less than μm will result in an initial capacitance difference. This section will study how gravity affects the initial ribbon deformation, and then the results to optimize the design will be used.

The gravity force on the ribbon can be described by equation (4-1).

$$F_{gravity} = \rho_{Al} g V \tag{6-1}$$

where ρ_{Al}=2.7×10^3 kg/m^3, g=9.8 m/s^2.

Assume the thickness of the ribbon is 1.5 μm, and the width is 20 μm. The gravity load as force per unit area is:

$$\frac{F_{gravity}}{A} = \rho_{Al} g h \tag{6-2}$$

where A is the total ribbon area and h is the ribbon thickness. Then (4-2) can be solved as:

$$\frac{F_{gravity}}{A} = 3.97\times10^{-2}\, N/m^2 \tag{6-3}$$

Ribbons with a jog angle 30º were used in the simulation. The force per area from equation (4-3) was applied on ribbons with different lengths. The displacements caused by gravity are shown in Figure 6.7. As shown in Table 6.4, the longer ribbon is heavier, softer, and has a larger deformation caused by the gravity. When the ribbon end-to-end distance was 3500 μm, the gravity caused ribbon deformation was 1 μm. This introduces significant initial capacitance variation when a sensor is placed with a different angle.

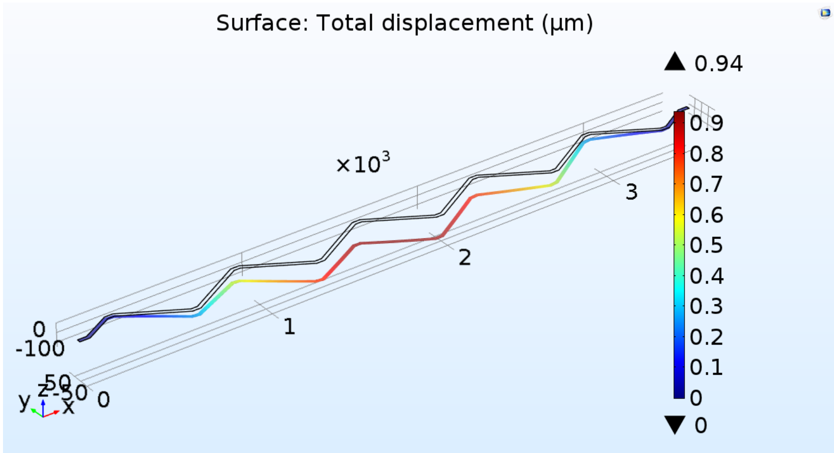

(a) 3500µm length;

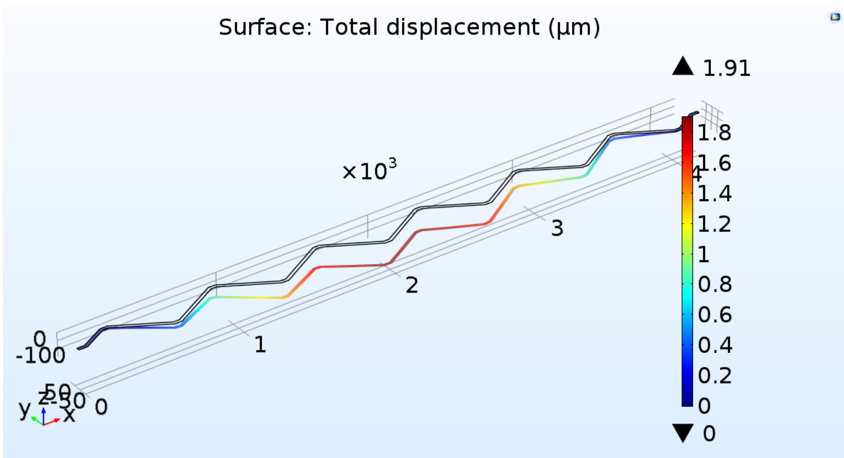

(b) 4175µm length;

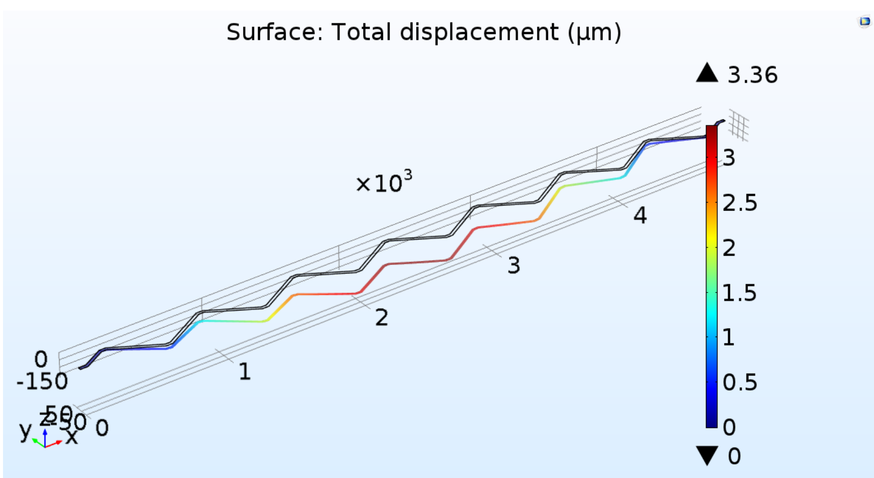

(c) 5000µm length;

Figure 6.7 Gravity effect on ribbons.

Table 6.4 Gravity effect on ribbons simulation results.

θ	Total length	Gravity	d_{max}
30º	3500 μm	3.15×10^{-9} N	0.94 μm
30º	4175 μm	3.76×10^{-9} N	1.91 μm
30º	5000 μm	4.37×10^{-9} N	3.36 μm

6.2. Ribbon array fabrication process

A fabricated ribbon array sensor is shown in Figure 6.8. The dimension is described in figure 4.8. The total length of each ribbon is 3.6 mm with a jog angle of 30º. The total number of ribbons in the array is 58, and the gaps between the two adjacent ribbons are 10 μm. The ribbon array was fabricated from a single crystal silicon, measuring 380 μm in thickness. The structure was coated with 0.5 μm of aluminum metal using a sputtering process.

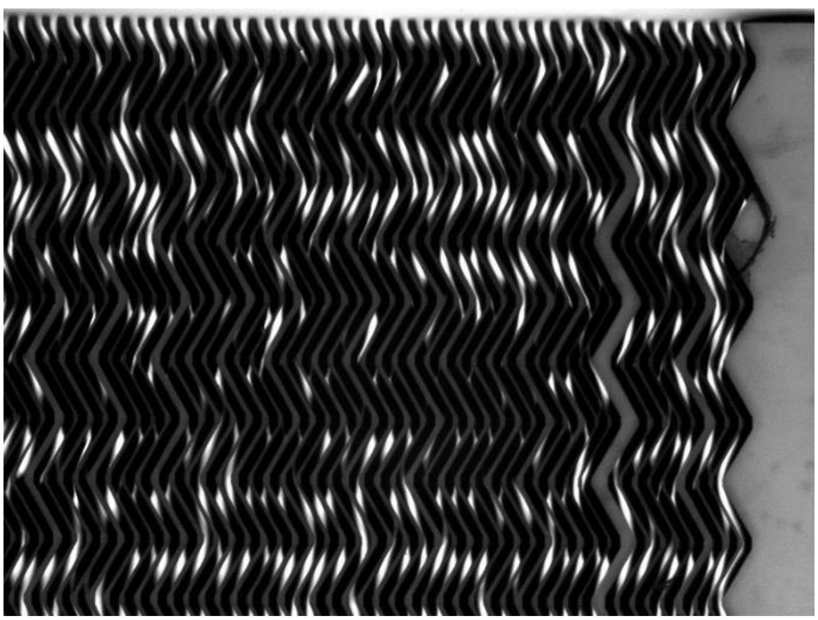

Figure 6.8 fabricated aluminum ribbon array.

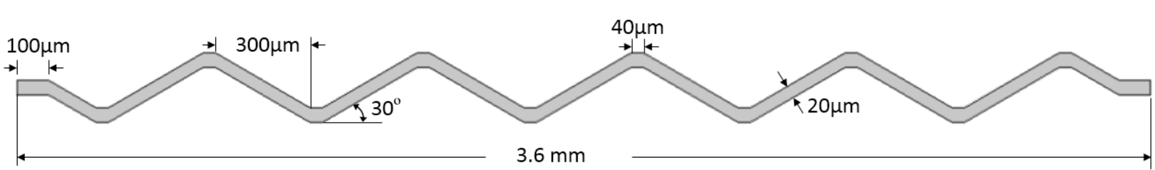

Figure 6.9 Ribbon dimension.

The fabrication process starts from a nitride silicon wafer with a 200 nm nitride layer on both sides of the wafer. The first step was to plasma etch using CF_4 and O_2 gases to open the backside of the wafer where the back etch was needed (Trion Phantom II Plasma etcher). Then the wafer was immersed in a KOH solution at 80 ºC for 330 minutes, which left an approximately 40 µm thin layer of silicon, as shown in figure 4.9 (c). The silicon etch rate is measured as 1.03 µm/min. After, the nitride layer at the front side was removed by a plasma etch using CF_4 and O_2 gases, followed by a sputtering process to deposit about a 30 nm titanium adhesion layer and a 1 µm aluminum film (MRC 8667 sputter system). After patterning the aluminum thin film to be ribbon arrays (step (e, f)), the 40 µm silicon layer left in step (c) was removed by using an XeF_2 etch and the ribbon arrays were released (step (g)).

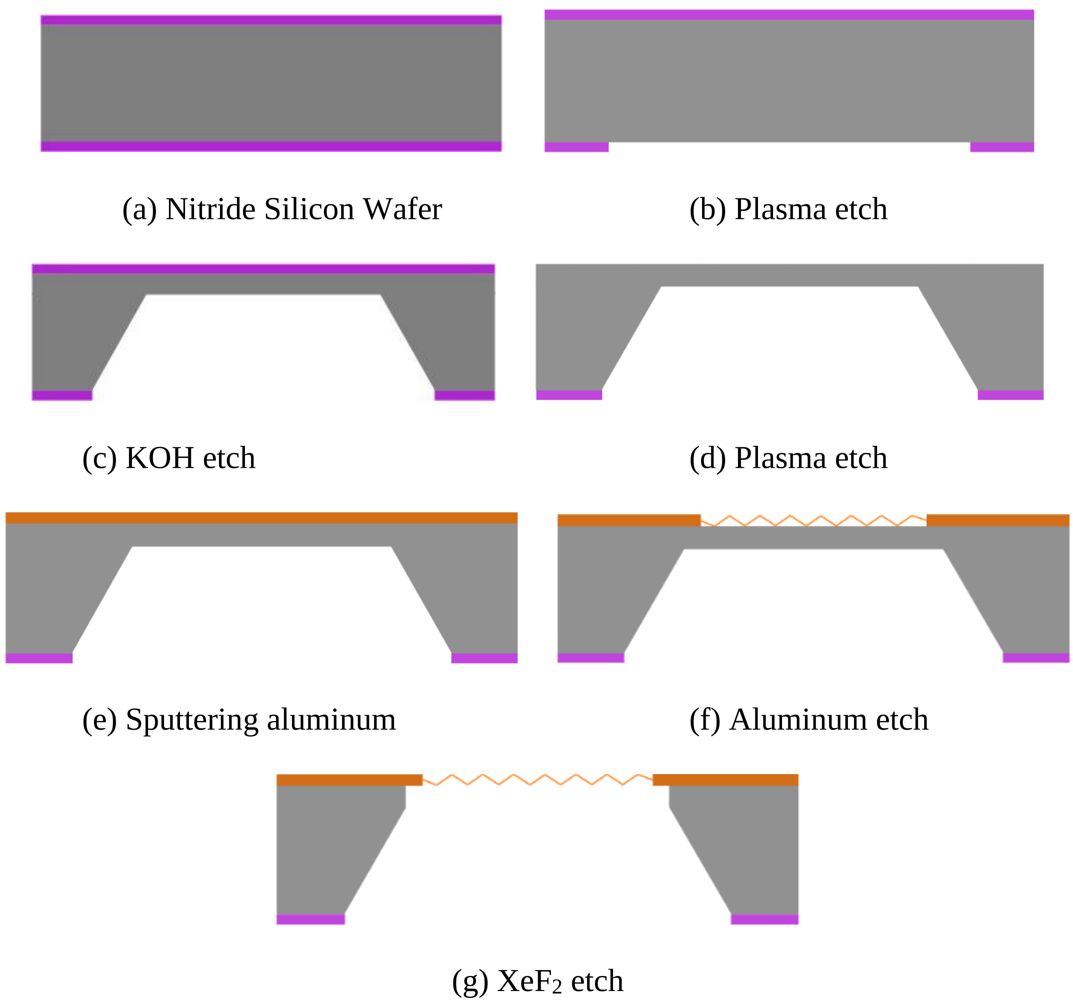

Figure 6.10 Ribbon array fabrication process.

The electrodes used to form the capacitor with the ribbon array were fabricated on a Pyrex glass substrate. First the electrode (aluminum metal) was deposited on the Pyrex using the sputtering process, followed by the aluminum etch patterning process. The Pyrex was then placed in close proximity to the ribbon array sensor, separated by a thin spacer material.

6.3. Ribbon array capacitance test results

The capacitive interrogation system of the ribbon array motion was then implemented and tested. The Pyrex glass containing the interrogating electrode was placed adjacent to the ribbon array sensor, which was spaced a short distance (average 34.2 μm) from the sensor. The sensor membrane was electrically grounded and a biased metal plate was placed approximately 5 mm above and parallel to the sensor in order to generate a normal electric field. Figure 6.11 show the measurement results of the distance between the ribbons and electrode underneath. Figure 6.12 shows the output of the AD7747 chip for six applied dc electric fields from 0 kV/m to 200 kV/m. Application of the 200 kV/m dc field result in a ΔC_m variation of 0.165 pF with a noise level of 8fF(±1 fF). The minimum electric field that can be sensed is:

$$E_n = \sqrt{\frac{8\,fF}{165\,fF}} \times 200kV/m = 44kV/m \quad (\pm 3kV/m) \tag{6-4}$$

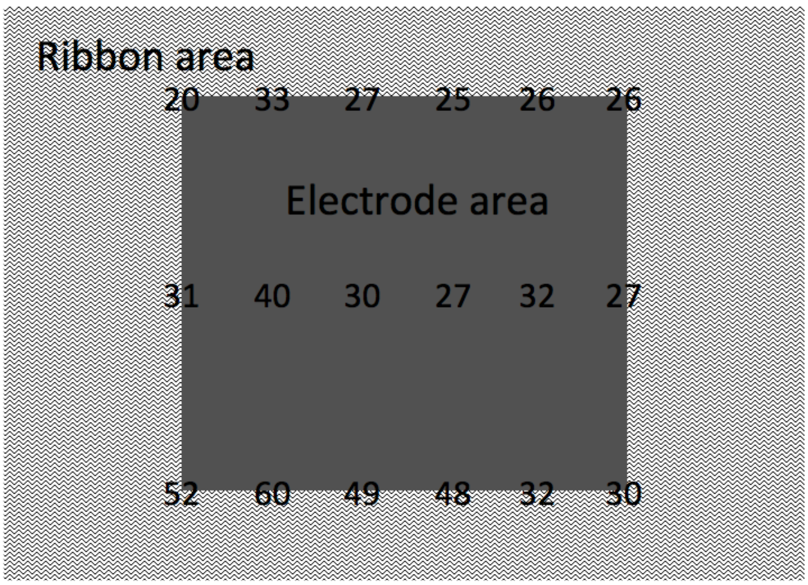

Figure 6.11 Ribbon heights (μm, ±2 μm) over electrode 3 mm×3 mm.

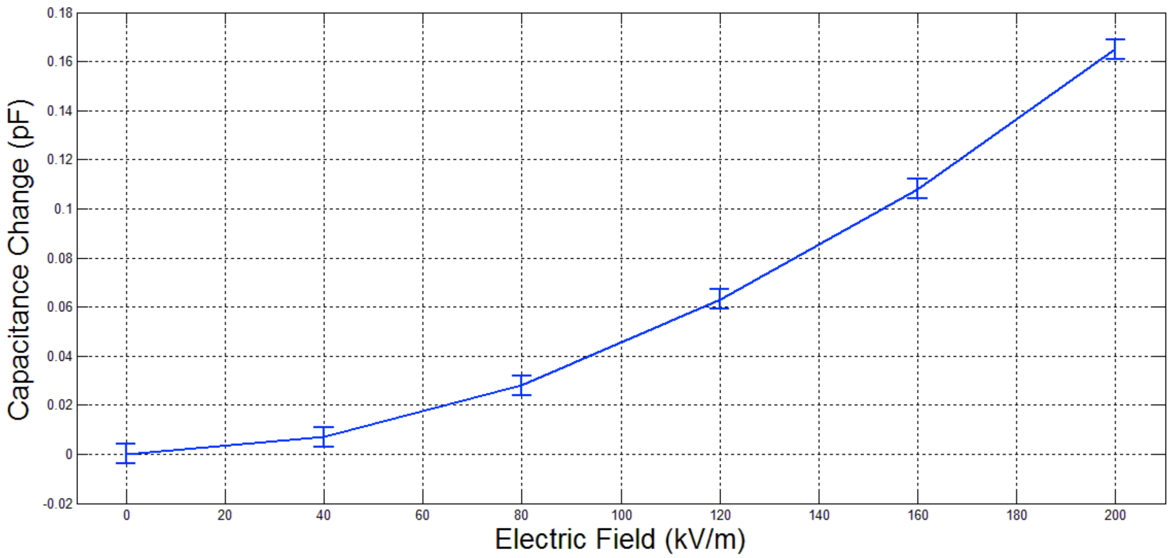

Figure 6.12 Ribbon array sensor measurement result (±4 fF).

6.4. Capacitance measurement sensor enclosure

An improved measurement setup was developed, in order to improve the drifting issue of the measurement electronics introduced in section 5.5. Figure 6.13 shows a simple package schematic, and Figure 6.14 shows the enclosure assembly.

Compared to the setup in section 5.5.1, the sensor and circuit are now packaged in a grounded aluminum box and separated by a grounded metal, which helps minimize the interference from external electric fields. The sensor is fixed on the top of a foam to help reduce environment mechanical vibration. A 3 cm × 3 cm window is opened on the top of the box to expose the sensor to an electric field. The sensor is wired to the AD7747 capacitance to digit convertor through hole in the separator board.

The measurement circuit is also improved. Compared to the first version (Figure 5.29), all the components are properly soldered and the sensor and measurement circuits are connected by SMB coax cables. This type of cable is shielded and helps prevent noise interfered sensor signal on the transmission path.

Using this assembled sensor enclosure to measure the electric field, the test results are very similar to the results shown in Figure 6.12.

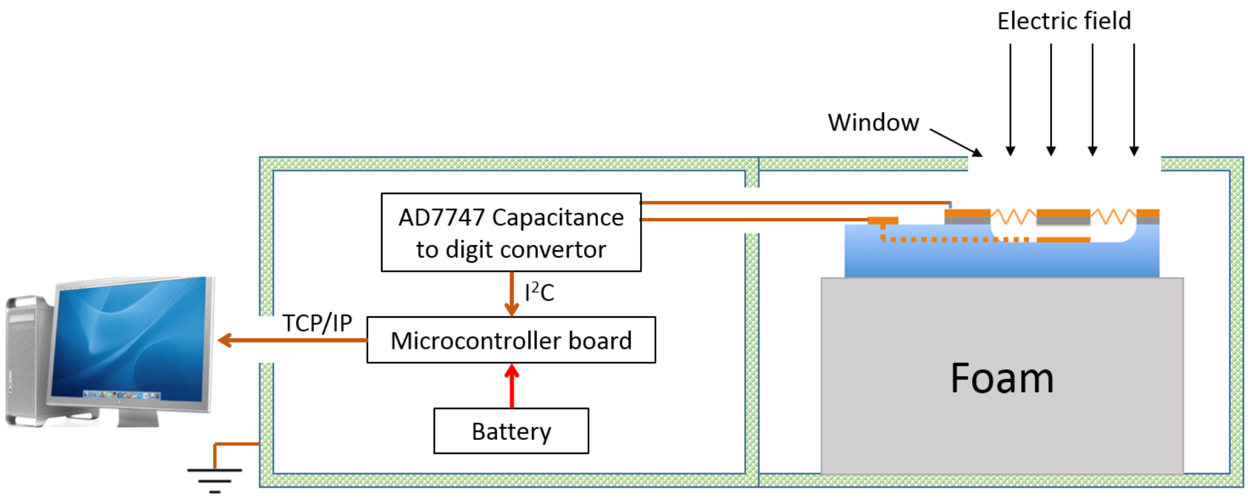

Figure 6.13 Sensor package schematic diagram.

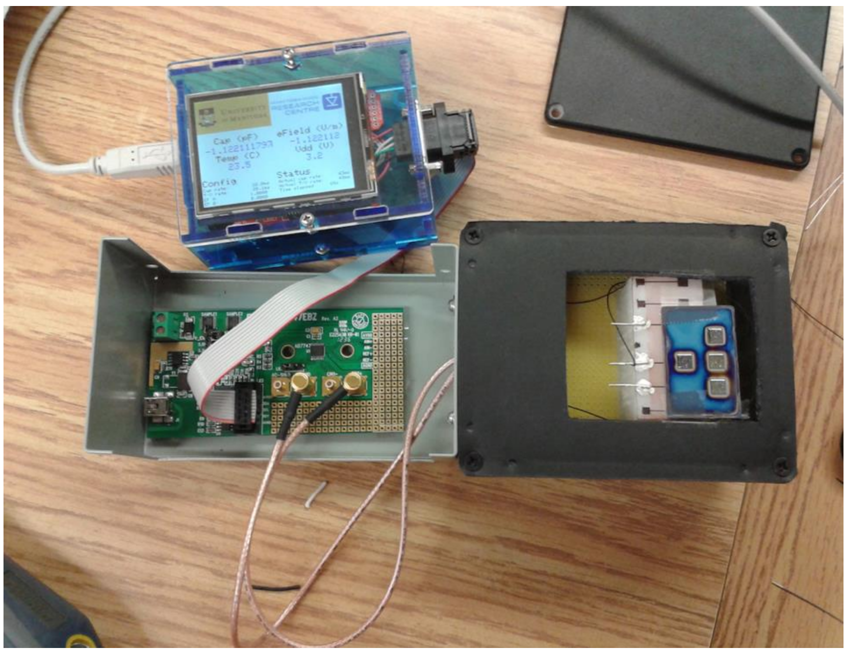

Figure 6.14 Sensor enclosure assembly.

6.5. Summary

Chapter 3 and 4 discussed the SOI membrane and ribbon array sensor using the capacitance interrogation system. When applying them to test an electric field, both sensors achieved similar sensitivity. The ribbon array was designed to have more flexibility and was thought to have more deformation under an electric field and give more capacitance variation. However, it turned out that sensitivity was not improved. Table 6.5 compares the main characteristics of these two sensors. The ribbon array is about 160 times softer and 70 times lighter than the SOI membrane, but their resolution is very close: the SOI membrane is 39 kV/m and ribbon array is 44 kV/m. There are two main reasons for this:

(1) Both membrane and ribbon array are not flat; both of them suffer from intrinsic stress. The SOI membrane surface has 10-30 µm curvature and the ribbon array has 20-50 µm initial deformation. This initial unflattening of the structure prevents the electrodes from being placed close to the actuator. This significantly reduces the performance of the sensors.

(2) Both sensors have a similar noise level. The softer micro-spring provides more flexibility, but the noise level will linearly increase according to the spring constant. This leads to a similar signal noise ratio.

Table 6.5 Comparison of SOI membrane and Ribbon array sensor.

	SOI membrane	Ribbon array
Spring constant	0.14 N/m	8.6×10^{-4} N/m
Mass	1.9×10^{-8} kg	2.75×10^{-10} kg
Resonant frequency	734 Hz	336 Hz
Capacitance measurement resolution	39 kV/m	44 kV/m

The main noise source for the capacitance measurement SOI membrane or ribbon array sensor is mechanical noise. External mechanical vibrations would transfer to the SOI membrane or ribbon array structures. These are caused mainly by ambient factors such as air flow, acoustic (room noise and microphonics), and building vibrations. Intrinsic mechanical noise has Brownian motion. It is due to the dynamic unbalanced forces caused by the random impacts of molecules on a small particle or structure (for example, bacteria and dust motes), it can be a large force on a tiny MEMS component [46].

Electronic noise, for example thermal (Johnson or Nyquist) noise [41] is also a concern of MEMS sensors. The thermal noise represents random noise derived from the thermal properties of a resistor. However, since sensors discussed in this thesis are large in size and have good conductivity, the thermal noise can be ignored.

In order to improve the sensitivity, the optical measurement method was considered again. In chapter 7, the SOI membrane sensor with improved measurement electronics and a reduced size the laser interrogation setup will be introduced.

Chapter 5 - SOI Membrane Sensor Optical Measurement

As discussed in chapter 3 and 4, the purpose of capacitance measurement is to have a compact size for the measurement electronics. However, due to intrinsic stress and similar signal to noise ratio, the efforts to improve the performance of both the SOI membrane and the ribbon were limited. In this section, the optical measurement method will be explored to find out whether it can further improve the sensitivity and resolution. First, measurement principle and setup will be introduced, then the ac modulation technique will be discussed, after that, the SOI membrane ac modulation measurement tests are discussed. This includes initial testing, a bias voltage study, the modulation frequency effect, sensor testing at resonant frequency, and testing under a power line.

7.1. Optical measurement introduction

Figure 5.1 illustrates the working principle of this sensor. The mechanism consists of a membrane mirror suspended by a set of micro-springs, which will be displaced vertically under the influence of the electric field being measured (from source V_S). The vertical displacement of the membrane is indicative of the electric field strength and is measured using a laser position sensor. With no external electric field, the laser beam reflected by membrane falls on the center of the split photodetector as indicated on Figure 5.1a. When the membrane is displaced into an electric field (Figure 5.1b) normal to it, the laser spot moves on the photodetector surface, giving an indication of the strength of the electric field. The difference between the output currents of the photodetectors A and B is used as the sensing signal.

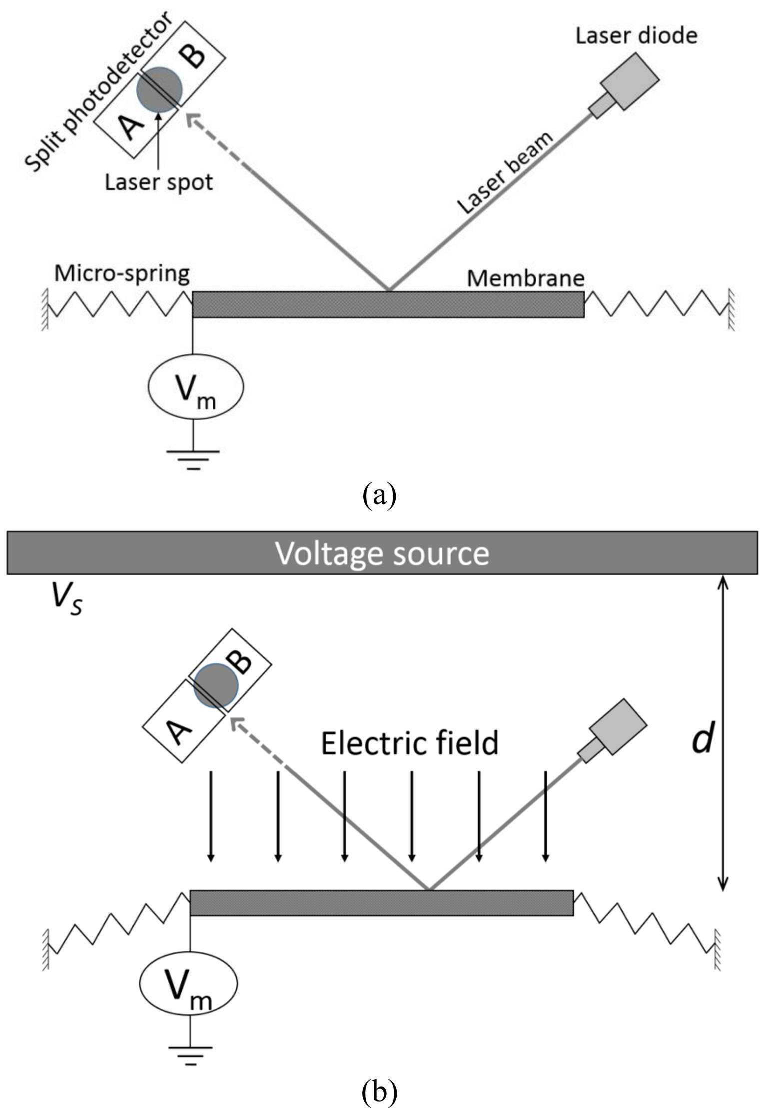

Figure 7.1 Optical sensor working principle. (a) Shows the case when no external electric field is present. (b) Shows the case with an external electric field caused by voltage V_S.

7.2. SOI membrane optical interrogation

Using the membrane fabricated earlier (Figure 3.5) for the test, step voltages of 120 V, 97 V, 72 V, and 0 V were applied to the conductor below the membrane (Figure 5.2). During dc testing, this conductor was located 0.65 ± 0.01 mm under the membrane. When the conductor was supplied 120 V, 97 V and 72 V, it produced an electric field of 185 kV/m, 149 kV/m, 110 kV/m and 0 kV/m (±5%). During the test, output responses were recorded using an 8-bit digital oscilloscope, and shown in Figure 7.3. In both pulse and step response, the consistent working performance is demonstrated.

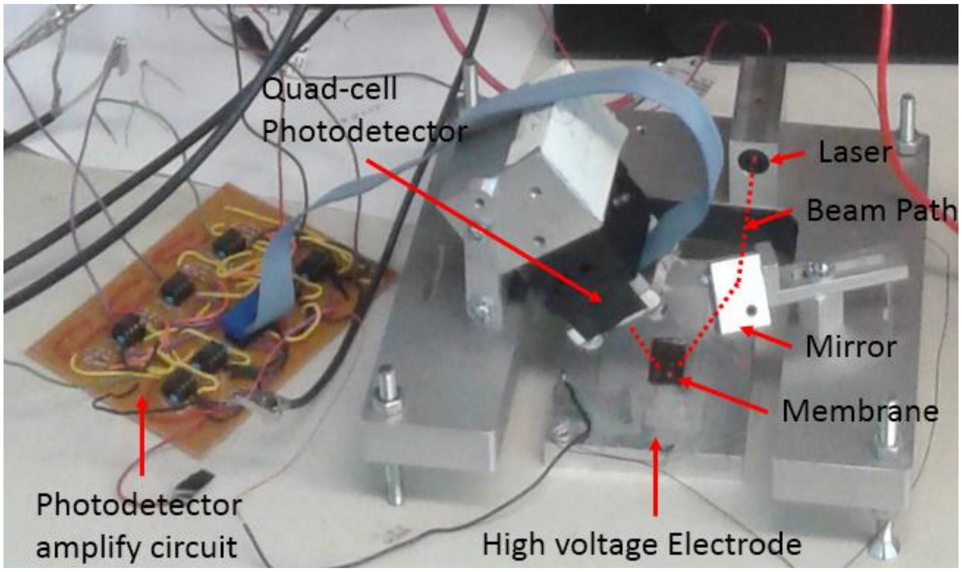

Figure 7.2 SOI membrane optical measurement test assembly.

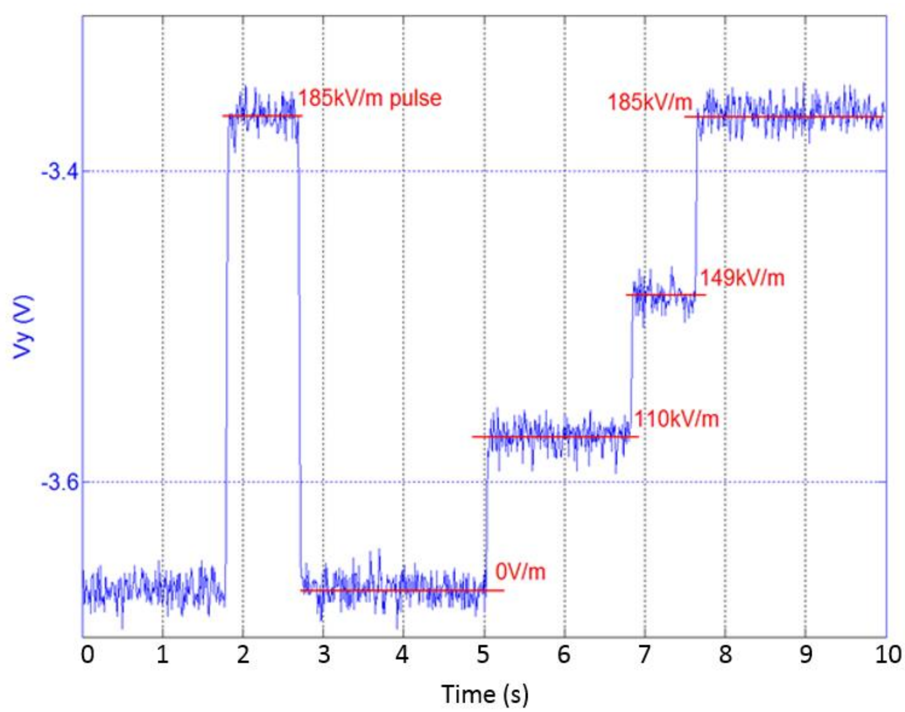

Figure 7.3 dc optical measurement.

In Figure 7.3, the signal moves 320 mV (±5 mV) in response to the 185 kV/m (±5%) dc electric field. The noise envelope is taken as 20 mV (±5 mV), as it includes the full deviation of on-off state during the test. Sensor resolution can be calculated as:

$$E_n = \sqrt{\frac{20mV}{320mV}} \times 185kV/m = 46\,kV/m \;\; (\pm 6\,kV/m) \tag{7-1}$$

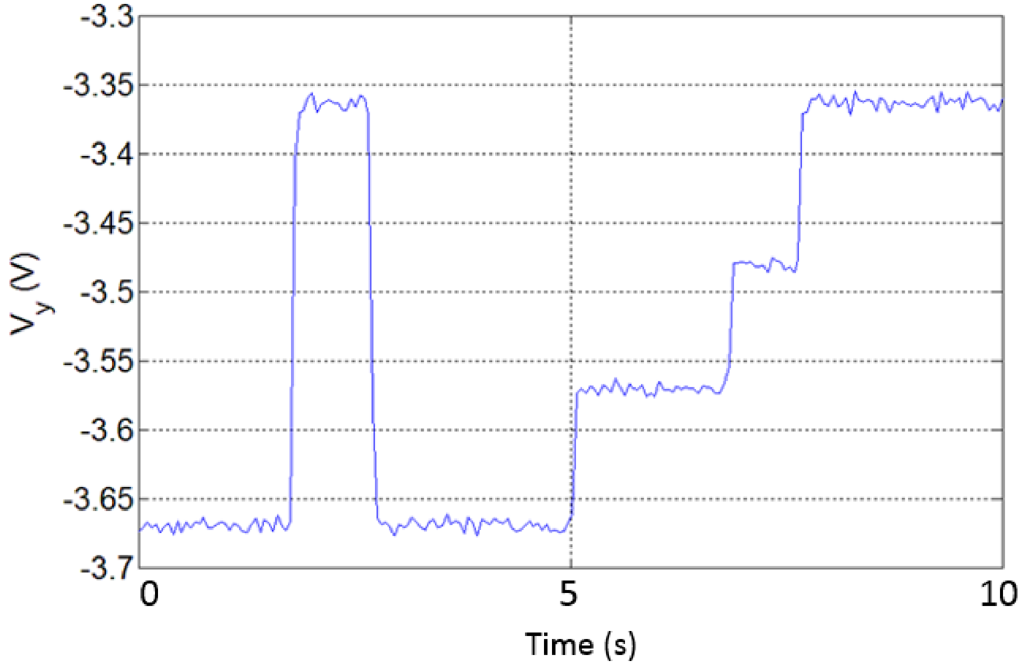

Figure 7.4 dc optical measurement, membrane 2, with 500 ms average.

To increase the SNR, the signal shown in Figure 7.3 can be smoothed by averaging samples. This is done by inputting the data of Figure 7.3 into to Matlab software, and averaging samples every 500ms. As shown in Figure 7.4, after average the noise envelope drops to about 10 mV (±3 mV), then the sensitivity slightly improves to 33 kV/m (±5 kV/m).

$$E_n = \sqrt{\frac{10mV}{320mV}} \times 185kV/m = 33\,kV/m \;\;\; (\pm 5\,kV/m) \tag{7-2}$$

7.3. Compact laser position monitoring system

The membrane sensor and laser position monitoring system have been integrated together in a compact acrylic frame for portability, as shown in Figure 7.5. This acrylic frame has shown to be robust, with testing showing the laser position sensor remaining in alignment for a testing period of over a year, during which the sensor was transported between laboratory and outdoor test sites, sometimes in luggage on an aircraft. The acrylic frame was used to hold the sensor for the high voltage measurements of section 4. For the measurements of section 3, due to the required close proximity of the field source, it was not used.

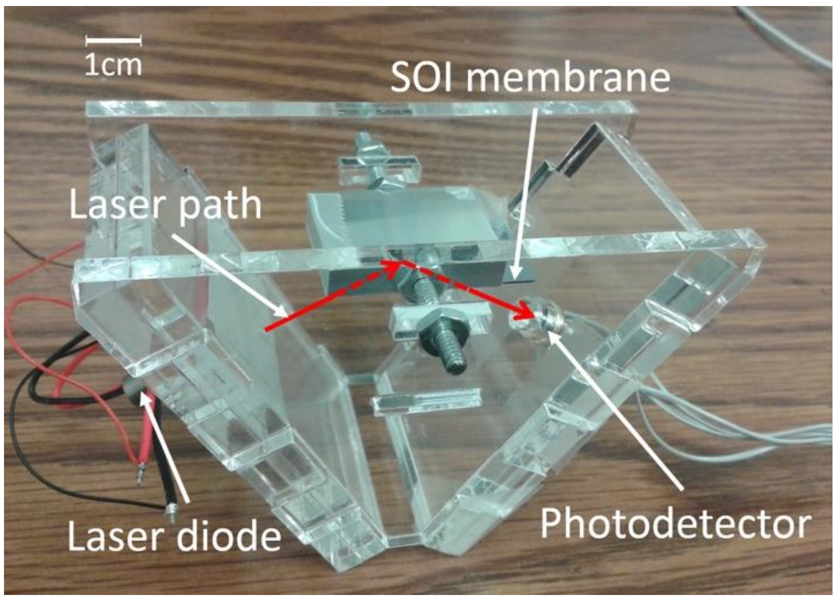

Figure 7.5 Sensor and laser position system integrated in the acrylic frame.

7.4. SOI membrane ac modulation measurement

7.4.1. SOI membrane initial testing

Initial testing was done using a metal plate placed a distance $d = 0.65$ mm away from the sensor and biased to a voltage V_S, as shown in Figure 5.6. The sensor membrane was biased to a voltage V_m , and is used to modulate the motion of the membrane, as discussed in section 5.1. Two operation modes were used. If V_S is a dc voltage, then V_m should be an ac voltage to modulate membrane motion. Whereas, if V_S is an ac voltage, then V_m should be a dc voltage to modulate membrane motion. The modulated motion of the membrane was monitored by the laser position measurement system, and the output of the split photodetector was input to current to voltage converters and a subsequent differential amplifier. This circuit had a gain of 10^5. A lock-in amplifier was then used to provide additional signal gain with bandpass filtering centered at the modulation frequency, thereby reducing noise from other frequencies to enhance resolution. The lock-in amplifier output was also integrated over time, to further reduce noise. The equipment used in this section include: E3632A Agilent dc Power Supply, 33120A Agilent Function Generator, SR510 Lock-in amplifier from Stanford Research System, 34461A Agilent Digital Multimeter.

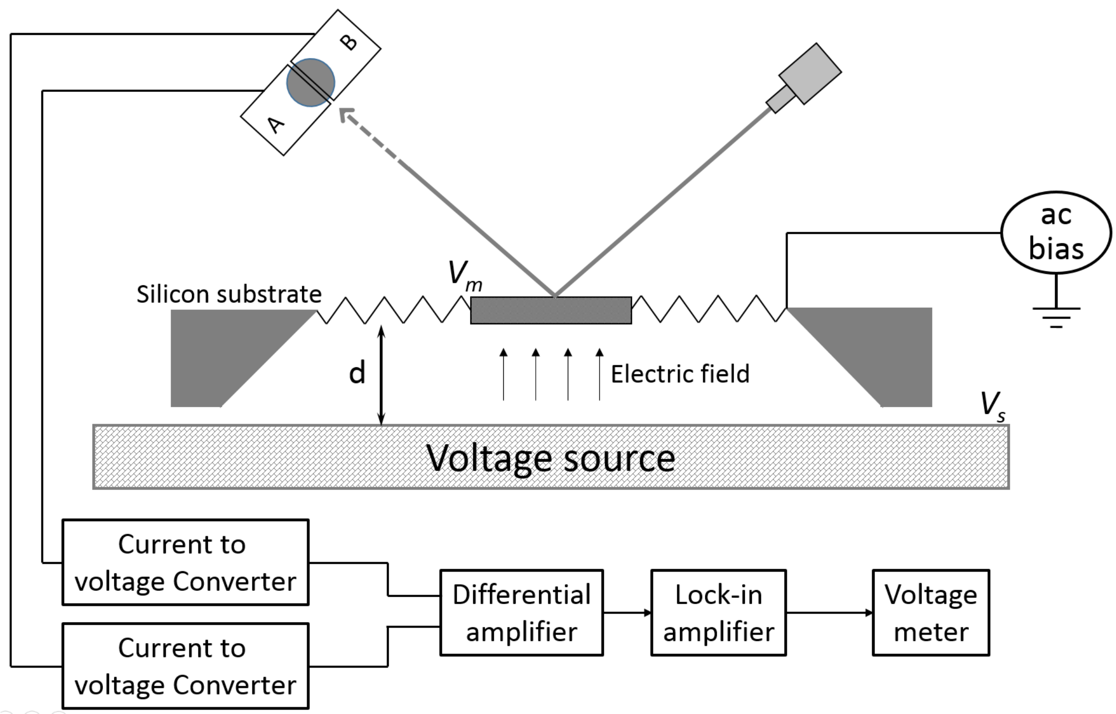

Figure 7.6 SOI membrane ac modulation initial sensor testing schematic diagram.

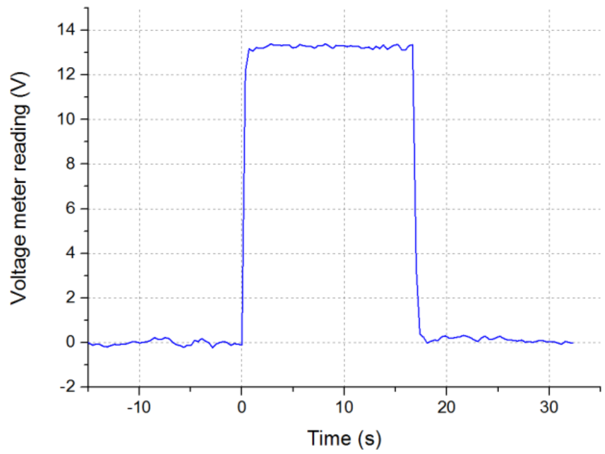

(a) Integration time 300 ms;

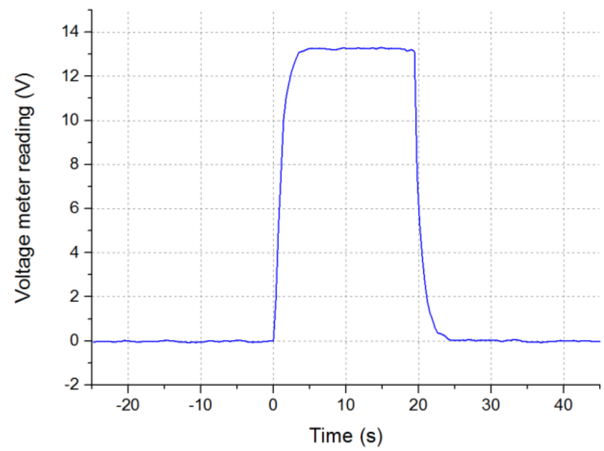

(b) Integration time 1 s;

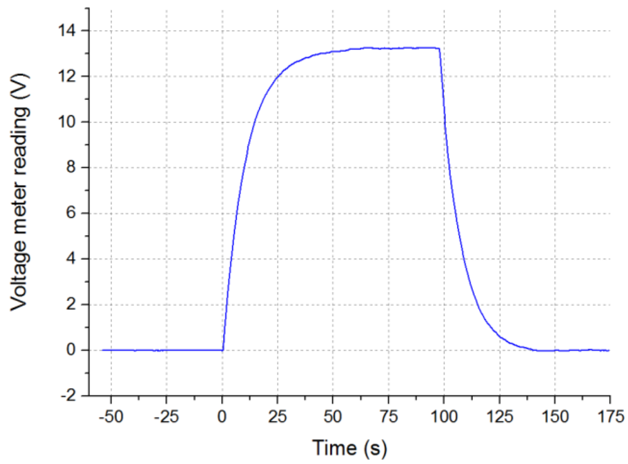

(c) Integration time 10 s;

Figure 7.7 Sensor response with varied Lock in amplifier integration time for a 100 kV/m electric field, and a membrane bias voltage of *10sin(ωt)* V at 500 Hz.

Using the configuration of Figure 5.6, a pulsed dc voltage with V_S = 65 V was used to create a pulsed 100 kV/m electric field at the sensor surface. The membrane was biased with a voltage V_m = 10sin(ωt) V at 500 Hz to modulate its motion. It should be noted that this is below the sensor membrane's resonant frequency. The measurement result is shown in Figure 5.7a with the lock-in amplifier gain set to 2×10^4 and integration time set to 300 ms. The signal to noise ratio for this measurement is 31:1. Figures 5.7b and 5.7c show the result for longer integration times, which results in reduced noise. In Figure 5.7b with 1s integration time, the signal to noise ratio is 120:1, and in Figure 5.7c, with 10s integration time, the signal to noise ratio is 440:1. However, longer integration times result in the lock-in amplifier output taking more time to reach steady state. We can see that for 300 ms, the integration time steady state is reached at approximately 1s, and this required time increases for the longer integration periods.

7.4.2. Effect of membrane bias voltage amplitude:

As mentioned in section 2.1, the application of the ac/dc bias signal to the sensor membrane enables modulation of the amplitude of the sensor membrane motion. Therefore, the sensor's measurement sensitivity can be controlled (enhanced or reduced) by applying an appropriate membrane bias voltage. This adjustable gain ability is a valuable capability of this electric field sensor, as it allows the sensor to measure a wide range of electric field strengths. For example, electric fields in households may range from 3-70 V/m at a distance of 30 cm, while the electric fields found under HVDC transmission lines can be tens of kV/m [31]. The dc electric field under a thundercloud can be over 100 kV/m [32]. Therefore, the ability to adjust the sensor gain allows the same sensor to cover all the above mentioned situations.

Experimental demonstration of the ability to adjust the sensor sensitivity was performed. An normal dc electric field was applied to the membrane using a voltage source V_S = 30 V located at a distance d = 0.65 mm from the membrane, resulting in a 46 kV/m dc field. The membrane was biased with a 500 Hz sinusoidal signal with varying amplitudes (1 V, 2 V, 4 V, 8 V, and 10 V). The measurement result is shown in Figure 5.8, where we can see that the sensor sensitivity varies from 0.74 mV/(kV/m) to 7.4 mV/(kV/m), for ac bias amplitudes of 1 V to 10 V. A summary of the results is shown in Table 7.1. We see that the sensitivity improves linearly with the amplitude of the bias voltage V_m, as expected. In a practical sensor implementation, the bias voltage V_m can be adjusted as needed by a microprocessor controlled amplifier biased on a desired sensitivity, only need to avoid sensor electronics saturate when using a bias voltage that is too high.

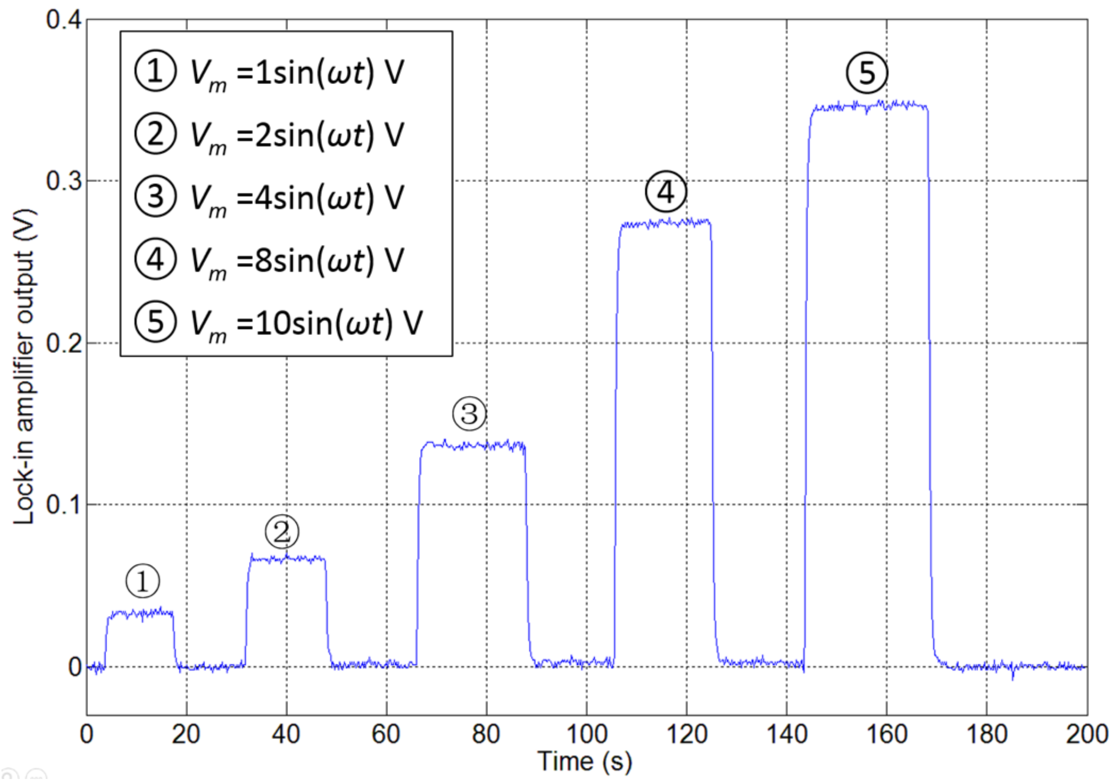

Figure 7.8 Sensor test with a 46 kV/m dc field, for various ac bias voltages at 500 Hz. The lock-in amplifier was set to a gain of 5,000x and an integration time of 300 ms.

Table 7.1 Summaries results of Figure 7.8.

ac bias amplitude (V)	Output (mV)	Sensitivity mV/(kV/m)
10.0	340	7.4
8.0	270	5.9
4.0	140	3.0
2.0	67	1.5
1.0	34	0.74

7.4.3. Sensor response vs. modulation frequency

It is important to note that the sensor, being a mechanical device, would have its maximum output when working at its mechanical resonant frequency. Therefore, a test was done to determine the mechanical resonant frequency of the spring-membrane system at room temperature. Using the setup of Figure 5.6, a dc voltage of V_S = 1 V was used to generate a 1.54 kV/m dc field. Then the membrane was biased with an ac voltage of V_m = 8sin(ωt) V, who's frequency was swept from

500 - 700 Hz. Figure 5.9 shows the sensor output. We can see that the sensor's output is minimally a function of frequency below 520 Hz, but for greater than 520 Hz the output rapidly increases to a peak at its resonance of 610 Hz.

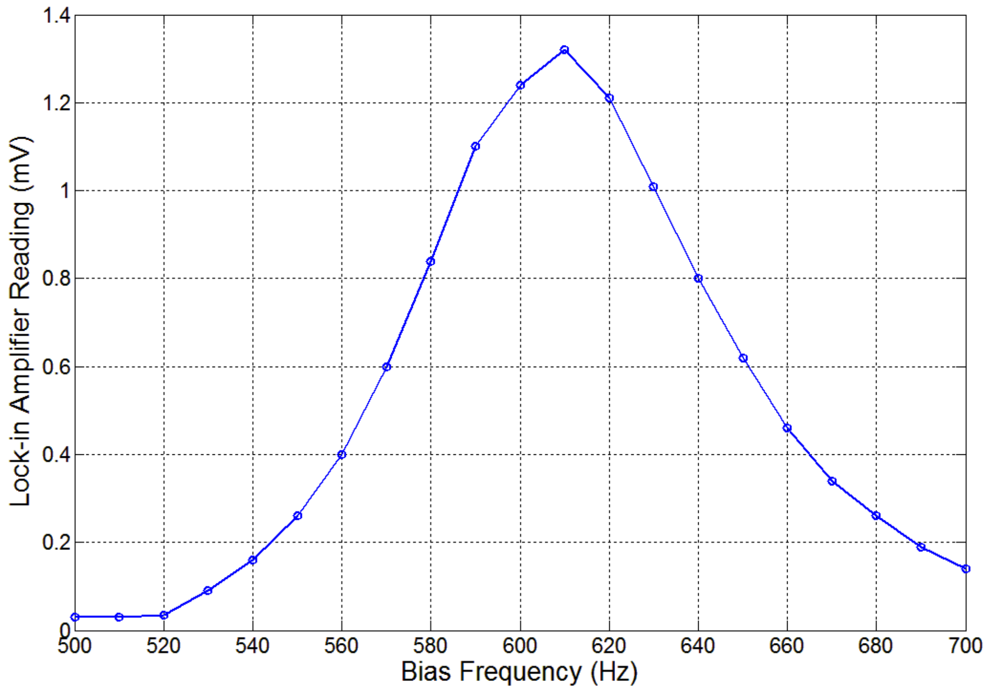

Figure 7.9 Sensor output variation with different modulation frequencies.

In the case of the earlier measurements in Figures 5.8 and 5.9, a 500 Hz modulation voltage was used. Using 500 kHz is to give a small period before there is rapid change in resonance. Relating this with the results in Figure 7.10, which shows a ~1.8 Hz reduction to resonance frequency for every 10 ºC, a drop of 20 Hz in resonance frequency (from 520 Hz to 500 Hz) would take a ~100 ºC temperature increase on the sensor. Therefore, the 500 Hz operation point of Figure 7.8 and Figure 7.9 can be considered a stable operating point, when considering the effects of large temperature changes or high electric fields.

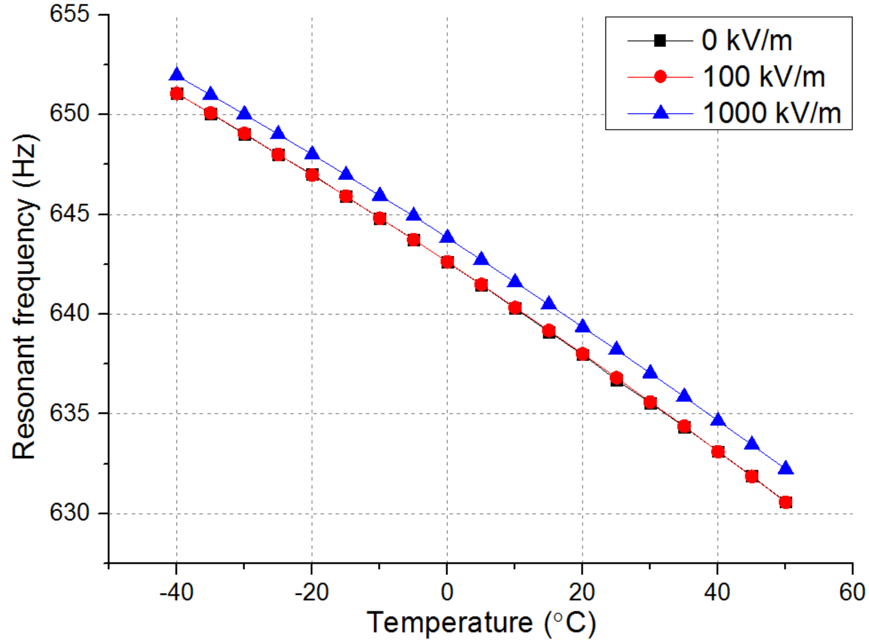

Figure 7.10 Simulation of sensor resonant frequency vs. temperature and external electric field.

7.4.4. Sensor tests at resonance and using high bias voltage:

Figure 7.11 shows an exploration of sensor sensitivity and resolution was undertaken. Sensor output was increased by operating at resonance (610 Hz) and with V_m >100 V applied to the membrane. A transformer with a 1:11.8 turns ratio was used to increase the amplitude of the modulating ac bias voltage V_m from 10 V to 118 V. Figure 5.10 shows the measurement result for a pulsed dc voltage V_S = 50 mV to create a normal electric field of 77 V/m. The lock-in amplifier gain was set to 2×10^5 with an integration time of 10 s. The sensor output was 13.5 V, with the sensitivity being 180 mV/(V/m). The noise envelope was about 20 mV, which giving a noise limited resolution (E_{min}) of:

$$E_{\min} = \frac{20mV}{13.5V} \times 77\frac{V}{m} = 0.1\frac{V}{m} \qquad (7\text{-}3)$$

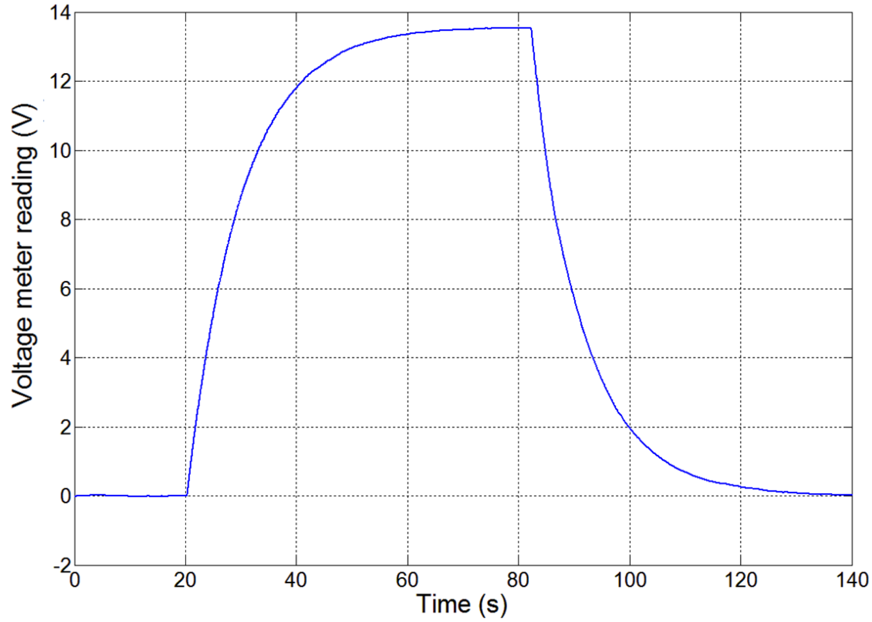

Figure 7.11 Sensor tested with a normal dc electric field of 77 V/m, and membrane biased with V_m = 118sin(ωt) V at resonance of 610 Hz.

Figure 7.12 shows a sensor measurement of a normal ac electric field. To provide a comparison with the data of Figure 5.10, similar conditions were created. An normal 77 V/m ac electric field at membrane resonance was applied by setting $V_S = 50\sin(\omega t)\ mV$ at a frequency of 610 Hz. The sensor membrane was biased with a voltage of 120 V dc. For the ac field measurement of Figure 7.12, the sensitivity was calculated to be 180 mV/(V/m), and the noise limited resolution was E_{min} = 0.1 V/m. We can see that the measured results of Figure 7.11 and Figure 7.12 are very similar, showing that the sensor's measurement of either ac or dc fields provides similar sensitivity and resolution.

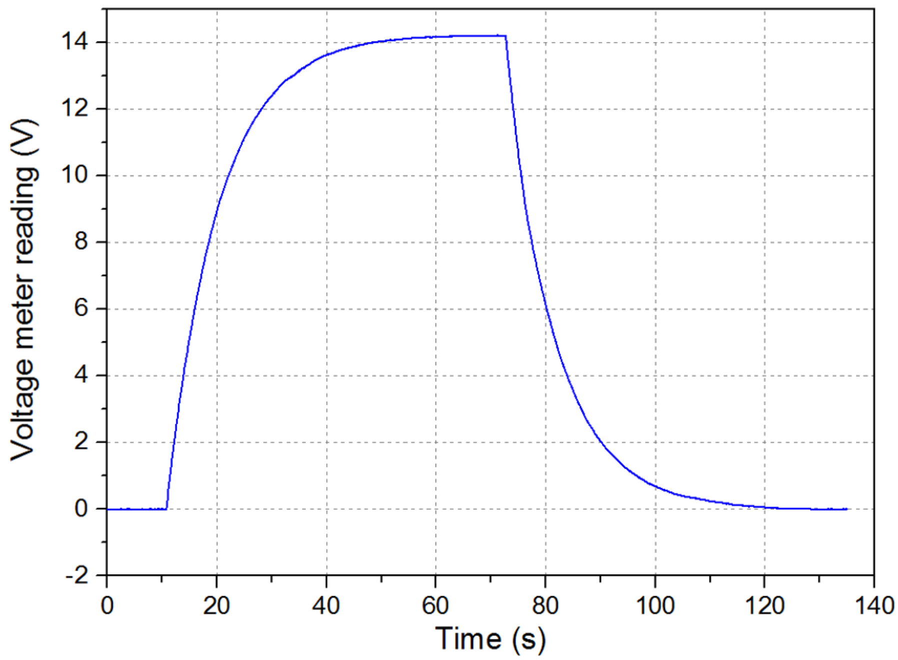

Figure 7.12 Sensor tested with a normal ac electric field of 77 V/m at 610 Hz, and a membrane biased with V_m = 120 V.

7.4.5. Electric field under a power line

It is known that the electric field distribution under power lines is non-uniform, therefore, in this section we calculate the field distribution in this situation. Figure 7.13 shows the model used to calculate the electric field under a power line. Considering a transmission line conductor with radius *r* located a distance of *d* above the ground and operating at voltage V_S, the electric field distribution at a given point can be expressed as:

$$|E_A| = \sqrt{|E_1|^2 + |E_2|^2 - 2|E_1||E_2|\cos\theta} \tag{7-4}$$

where

$$|E_1| = \frac{\lambda}{2\pi\varepsilon_0} \cdot \frac{1}{\sqrt{x_P^2 + (d - y_P)^2}}$$

$$|E_2| = \frac{\lambda}{2\pi\varepsilon_0} \cdot \frac{1}{\sqrt{x_P^2 + (d + y_P)^2}}$$

$$\theta = \arctan\frac{d - y_P}{x_P} + \arctan\frac{d + y_P}{x_P}$$

When the sensor is located on the ground directly below the transmission line ($x_P = 0$, $y_P = 0$), the strength of the electric field is:

$$|E_O| = \frac{2V_S}{d \cdot \ln\frac{2d - r}{r}} \tag{7-5}$$

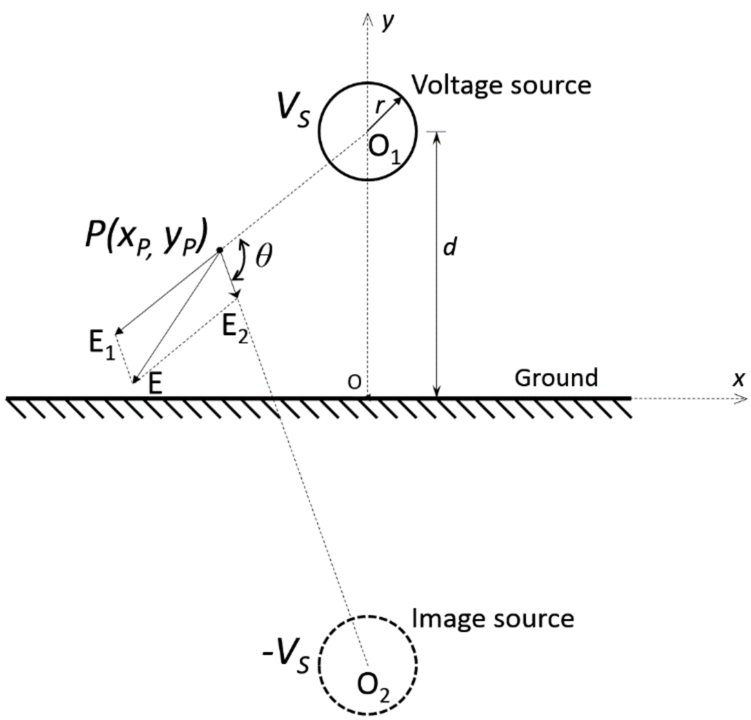

Figure 7.13 Electric field distribution along a line calculation model.

7.4.6. Sensor Testing Under Mock Transmission Line

In an HVDC power transmission line scenario, the voltage is typically 100s of kV and the height of these lines are approximately 10s m above the ground. In our high voltage laboratory, a setup was constructed to simulate this situation, as shown in Figure 7.14. A 2 m long copper pipe (diameter 0.0381 m) was placed 0.75 m above a grounded metal sheet. The sensor system was located directly under the copper pipe in a small hole on the ground sheet so that the sensing membrane was in the same plane of the ground sheet. For these measurements, the sensor was integrated in the acrylic frame (Figure 7.5) with the laser position monitoring system. Re-alignment of the laser position detector was done at this time.

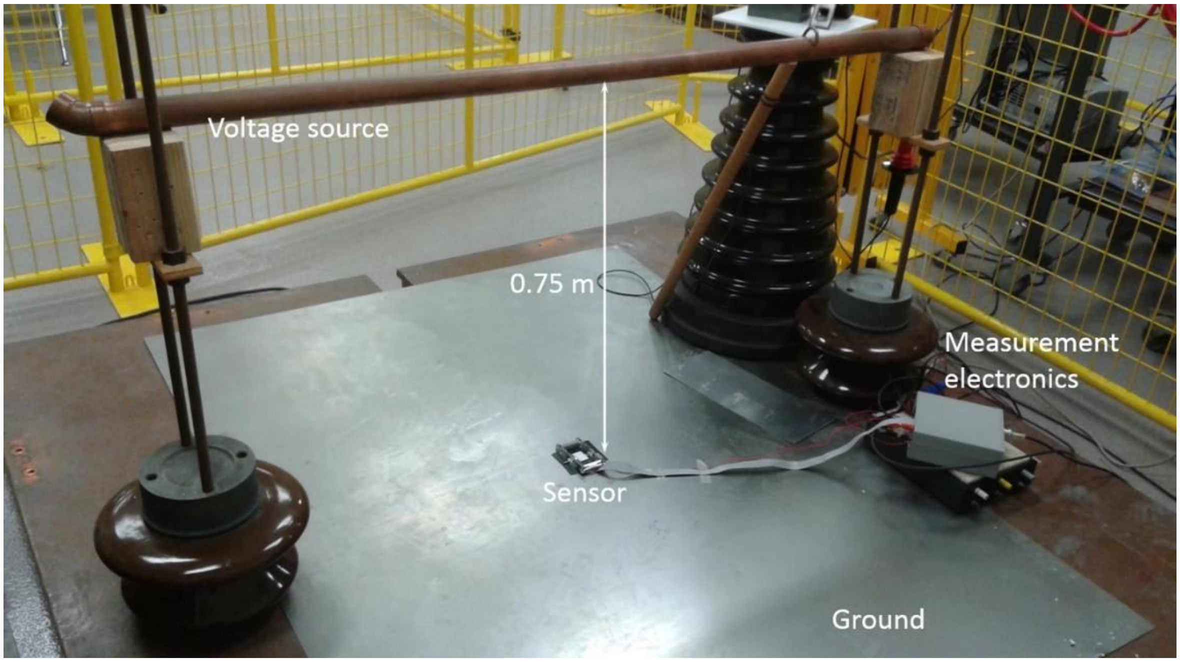

Figure 7.14 Compact laser monitor system, measuring the electric field from a biased copper pipe 0.75 m above the sensor.

This test has two main differences from the earlier tests base on the schematic diagram of Figure 7.6. First, the distance from the voltage source to the sensor is longer. Second, the electric field distribution generates from the copper pipe is non-uniform, therefore the field distribution needs to be calculated. Electric field distribution on the ground level as a function of the distance from the position directly below the transmission line was simulated using COMSOL software. Figure 7.15 shows this result. We can see that the electric field drops in amplitude rapidly, from the center point directly below the transmission line. Therefore, the sensor was placed directly below the transmission line in experiments. At the center point (directly below the transmission line), the electric field for 20 kV and 10 kV line voltages was calculated to be 12.2 kV/m and 6.1 kV/m respectively.

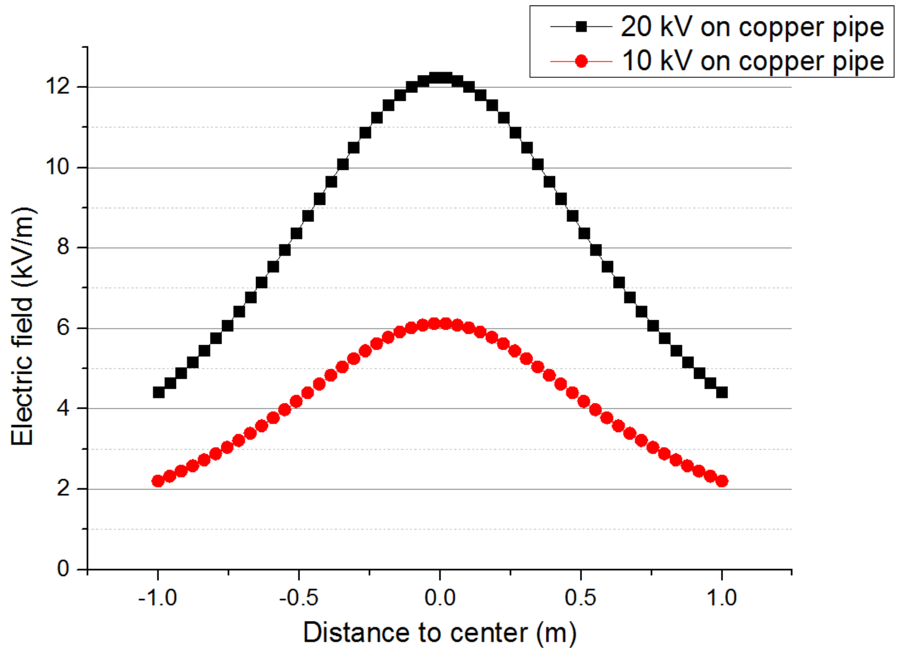

Figure 7.15 Electric field distribution along a line simulation.

Measurements in the high voltage laboratory were done with 10 kV_{dc} and 20 kV_{dc} voltages applied to the copper pipe. The high voltage is adjusted manually, with each adjustment taking 5-10 seconds. The sensor was tested at both non-resonant frequency and resonant frequency. First, a measurement was done with sensor operating at resonance for highest sensitivity, with V_m = 118sin(ωt) V at 610 Hz. The output is shown in Figure 7.16. For 20 kV_{dc} applied to the copper pipe, the noise level was measured to be about 6 mV (lock-in amplifier integration time 1s, gain was 2000) and the sensor response was 4.4 V. The sensor sensitivity was calculated to be 360 mV/(kV/m), and the resolution 17 V/m.

Second, a measurement was done with the sensor not at resonance, with the sensor membrane biased to V_m = 118sin(ωt) V at 500 Hz. Figure 7.17 shows the sensor response for 20 kV_{dc} applied to the copper pipe. The noise level was measured to be about 6 mV (lock-in amplifier integration time 1s) and the sensor response was 0.11V. The sensor sensitivity as calculated to be 9 mV/(kV/m), and the resolution 670 V/m.

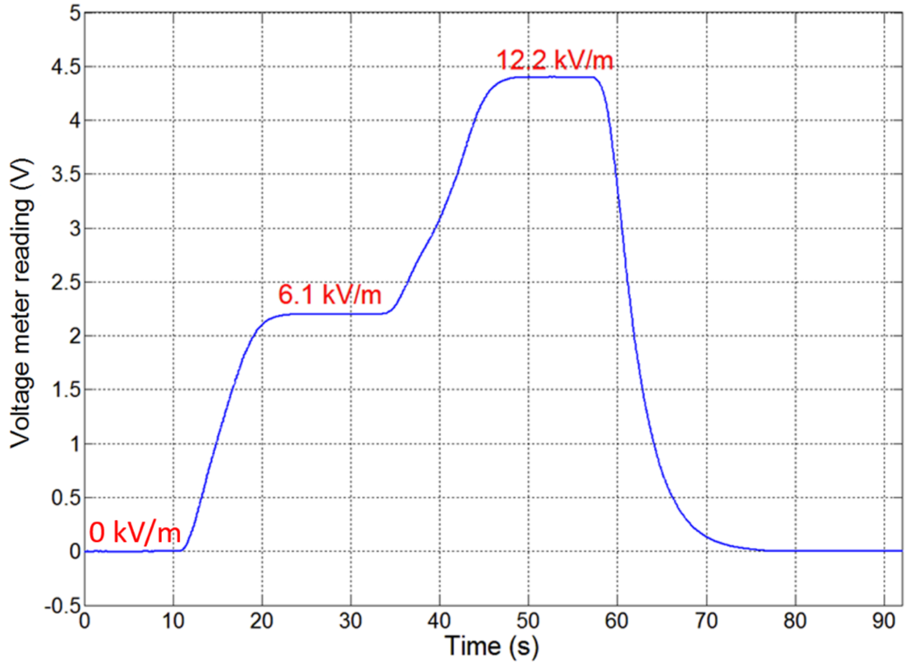

Figure 7.16 Sensor measurement of mock dc transmission line, with $V_m = 118\sin(\omega t)$ V at 610 Hz (resonant sensor operation), using 1s lock-in amplifier integration time.

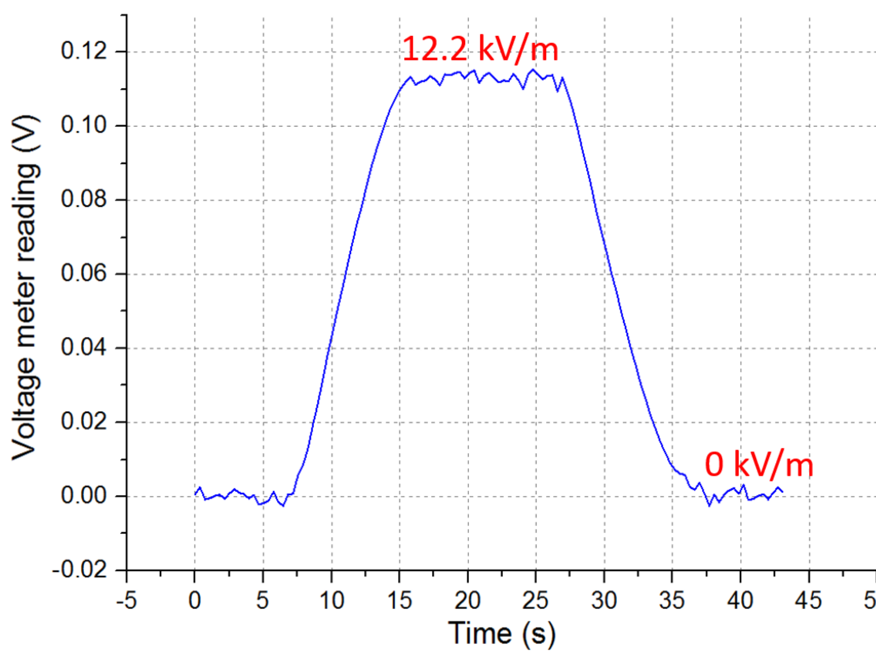

Figure 7.17 Sensor measurement of mock dc transmission line, with $V_m = 118 sin(\omega t)$ V at 500 Hz (non-resonant sensor operation), using 1s lock-in amplifier integration time.

7.5. Summary

This chapter discussed a fabricated SOI membrane integrated with a compact laser monitoring system. The sensor was demonstrated to measure both ac and dc electric fields, and operates by using modulation of the normal electric field. In the case of an dc electric field, an ac bias voltage on the membrane was used to modulate the sensor signal. The reverse was done for an ac electric field measurement, with a dc bias on the membrane used to modulate the ac electric field. The sensor demonstrated variable sensitivity by controlling the membrane bias voltage to modulate the field, with the sensor output linearly scaled by the modulated bias voltage. This enables the sensor to measure a wide range of electric fields. Sensor sensitivity and resolution limitation were explored using weak dc and ac electric fields. In these experiments, the sensor demonstrated a peak sensitivity of 180 mV/(V/m), and noise limited resolution of 0.1 V/m. The sensor was also applied to measure an electric field under a mock transmission line located 0.75 m over the sensor. With the sensor operating at resonant frequency, the sensor sensitivity was 360 mV/(kV/m), and resolution was 17 V/m.

Chapter 6 - Vertical Moving Shutter Field Mill

Chapter 4 discussed various traditional electric field sensors. A significant issue with existing MEFM designs is that the shielding shutter (which is driven with lateral movement) can be pulled (upwards) towards the electric field source when in the presence of large fields. This affects the sensitivity of the MEFM, leading to inaccurate measurements, since the induced charge on MEFM electrodes is very sensitive to the gap between the shielding shutter and the underlying sense electrodes.

A new design has been developed in this thesis that employs a vertical moving shutter to provide the shielding effect from the electric field normal to the sensor. The shutter is moved by thermal actuators. In this chapter, the working principle of a vertical movement shutter will be introduced in section 6.1. Simulation are shown, and experimentally verified using a scale model in a bench top measurement. Section 6.2 presents simulations of the performance of various designs and their thermal actuators. Two designs were selected for fabrication. These are discussed sections 6.3 and 6.4. Finally, section 6.5 presents the summary of this chapter.

8.1. Vertical moving shutter field mill concept

Figure 6.1 shows a schematic of the vertical moving shutter field mill. The shutter is centrally located with interdigitated electrodes on the sides. Figure 6.2 shows the field mill in operation, with the electrically grounded shutter raised vertically. We can see that when the shutter is raised above the sense electrodes, the electric field on the electrodes is reduced, and so the induced charge on the electrodes reduced. As a result, a higher shutter position has a better shielding effect.

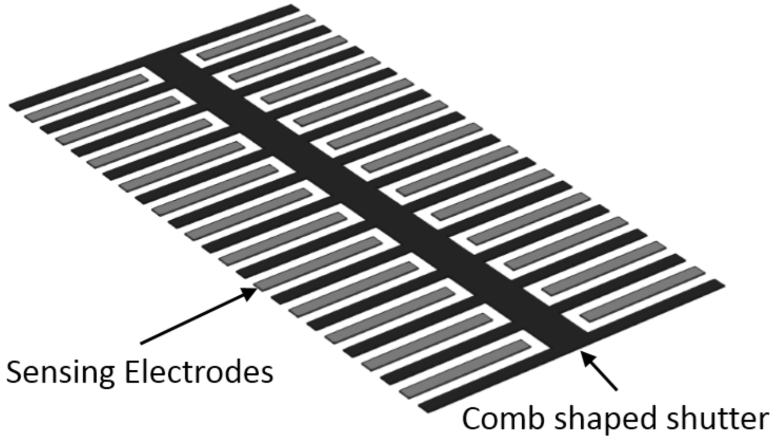

Figure 8.1 Visualization of comb shaped shutter and sensing electrodes.

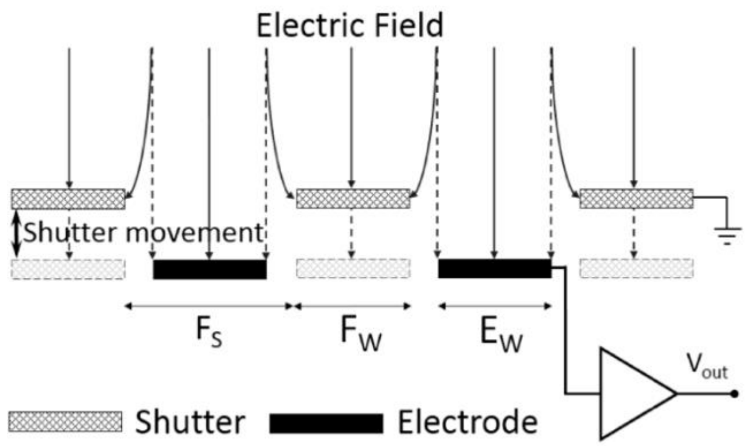

Figure 8.2 Schematic of a vertically moving shutter resulting in variable electric field shielding on underlying sense electrodes.

By implementing a periodic movement of the shutter, the sense electrodes will see an alternating electric field normal to the sensor, and so an alternating charge. Initially, when the shutter is lowered to the electrode height, the amount of charge induced on the electrodes is maximum, and can be calculated using Gauss's Law. Ignoring fringing effects, for an electrode area of A the magnitude of charge Q induced by an electric field E is given by:

$$Q = e_0 AE \tag{8-1}$$

If each vertical movement of the shutter results in a charge change of ΔQ, and the vibration frequency is f, then the induced ac current can be written as:

$$i = f\Delta Q \tag{8-2}$$

Equations (6-1) and (6-2) show that the electric field E can be measured by monitoring the current i induced on the sense electrodes. We can also see that the sensitivity of the sensor can be increased by increasing the sensing area and/or increasing the speed of shutter movement over the electrodes.

8.1.1. Double side comb shutter design simulation

Of importance is the dimensions of the comb fingers in comparison to the underlying sense electrodes. The performance of this design was investigated using COMSOL Multiphysics 4.4 software. The model built in COMSOL is shown in figure 6.3. It consists of an air box, an electrically grounded shutter, sense electrodes, and an electrically grounded guard strip to minimize fringing. In the case of practical design, the grounded guard strip would minimize induced charge on the device substrate. The electric field is defined in the simulation by a location on top of the air box, which is 200 µm away from the device, and is biased to a potential of 0.2 V. This results in a 1 kV/m dc electric field on the sensor.

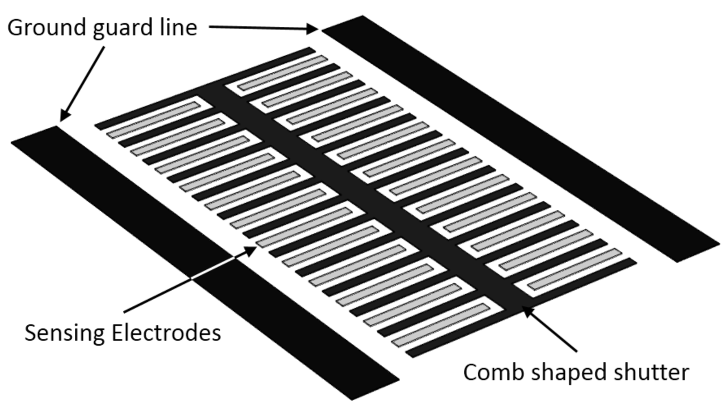

Figure 8.3 Model built in COMSOL to explore shutter dimensions.

Figure 8.4 plots the inducted charge variation (ΔQ%) on the sense electrodes as a function of shutter height for: electrode width E_W=10 µm, electrode length E_L=100 µm, comb finger width F_W=10 µm, comb finger length F_L=100 µm, finger spacing F_S=16-30 µm, and for a sensor having 24 electrodes/shutter fingers (12 per side). We can see that narrower finger spacing results in superior electrode shielding, due to reduced fringing. Figure 8.5 explores induced charge ΔQ on the sense electrodes as a function of shutter finger lengths F_L ranging from 60 μm to 120 μm. It shows that for finger lengths beyond 100 μm minimal improvement occurs. The simulation model is demonstrated in Appendix A.

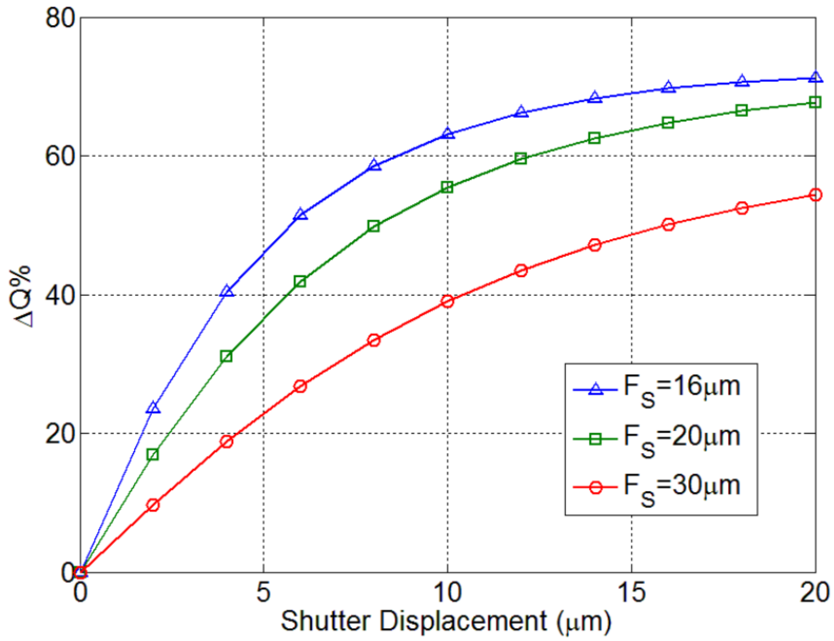

Figure 8.4 Percent shielding of underlying electrodes as a function of shutter height.

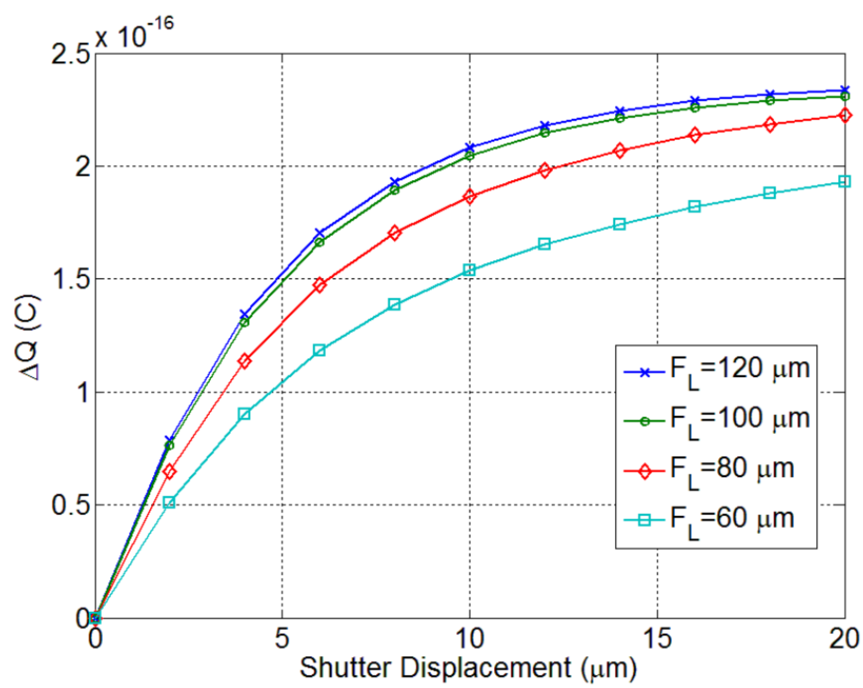

Figure 8.5 Differential charge on sense electrodes as a function of shutter height.

8.1.2. Large scale model study

The simulation results of the previous section were explored experimentally, in order to verify the above COMSOL models. A large-scale model was fabricated to verify the shielding effect of the vertically moving shutter. The shutter and electrodes were fabricated from a 1 mm thick aluminum metal as shown in Figure 8.6. The dimension of the shutter and electrodes are also described in Figure 8.6. The gap between the shutter fingers is 1.6 cm, and the sensing electrodes finger width is 1 cm and the length is 10 cm. This is in proportion to the size of the device shown in Figure 8.8.

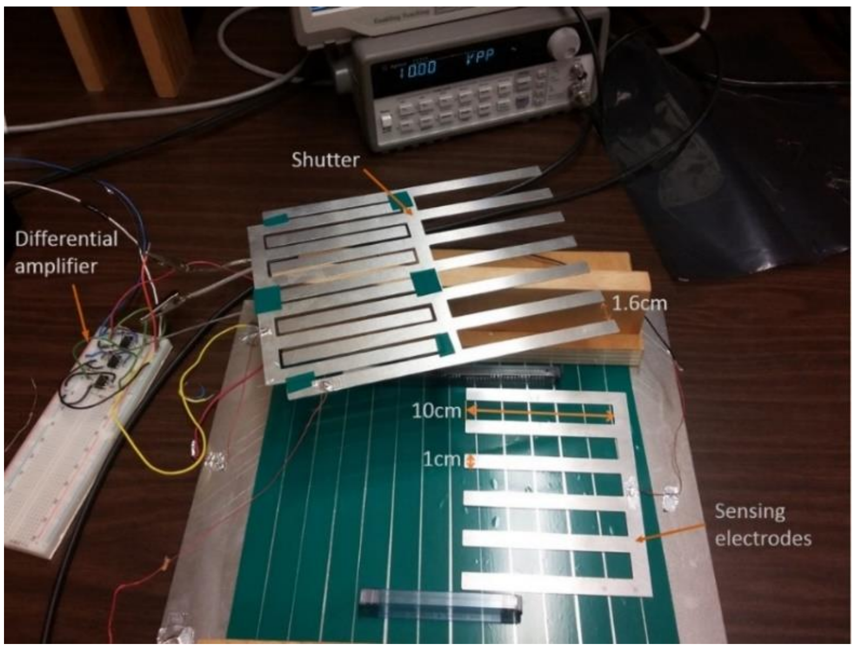

Figure 8.6 Shutter, sensing electrodes and amplifier.

Figure 8.7 demonstrates the experiment's working principle. There are two sensing electrodes; one is placed at the same height as the shutter, and the other electrode is height adjustable. In the test a 1:11.8 transformer is used to amplify a 10 V and 1 kHz sine wave (from a signal generator). This 118V 1 kHz signal is provided to a metal plate 3 cm above the shutter. The electric field generated is calculated to be 3.9 kV/m. The circuit in Figure 8.7 measures the induced charge on each electrode. Initially, with both the electrodes are at the same height, the induced charge on each electrode is the same, and so the V_{out} should be zero (neglecting any circuit offset voltage). As the moveable electrode is changed in height, V_{out} becomes non-zero. Figure 8.8 shows the test setup, and we can see from the figure that when the signal is provided to the metal plates, the sensed output signal is displayed on the oscilloscope. The equipment used in this test include: E3632A Agilent dc Power Supply, 33120A Agilent Function Generator, Tektronix TBS 1052B-EDU Digital Oscilloscope.

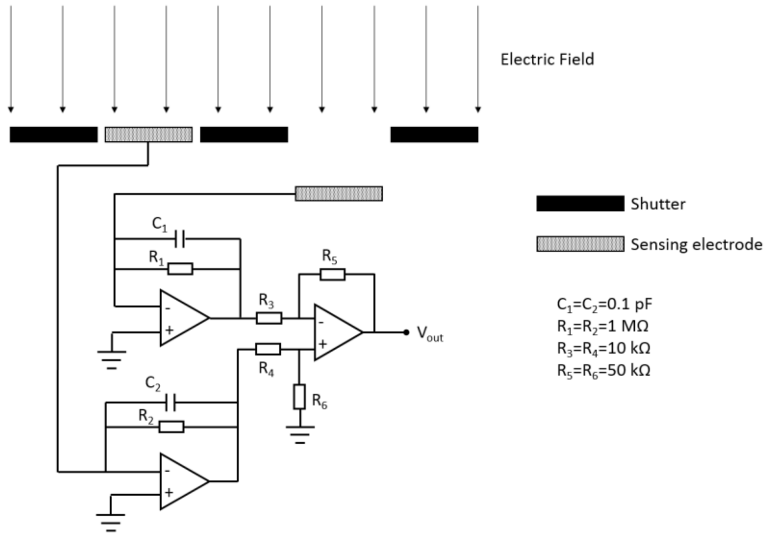

Figure 8.7 Schematic of the experimental setup and electronics.

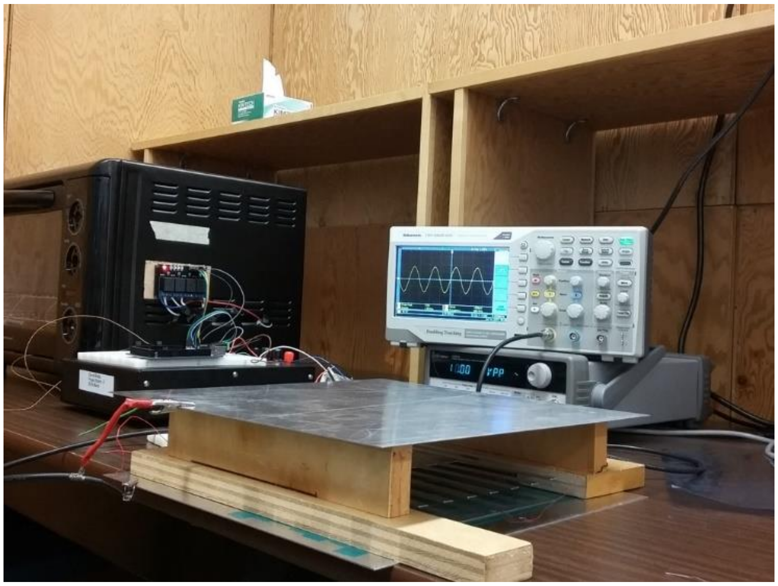

Figure 8.8 Large scale model shutter shielding effect test setup.

The first measurement taken was for the case with both electrodes at the same height (zero state) as the shutter. V_{out} was measured to be 1.1 V, as expected due to the voltage divider of resistors R_4 and R_6. This zero state voltage is then to be subtracted from the experimental data.

The second measurement taken was done with the height adjustable electrode disconnected from the amplifier, so as to provide no signal to the circuit. This condition simulates the output if the movable electrode was 100% shielded. The measured response signal peak-to-peak voltage was 4.1 V, or 3.1 V after the zero state condition is subtracted. Table 8.1 shows the test results for the moveable electrode at different positions (and connected to the circuit). In Table 8.1, the Output Variation column is the case with the 1.1 V zero state voltage subtracted from the data. Figure 8.9 plots the normalized output variation data together with the scaled data from Figure 8.4 where F_s is 16 μm. We can see from Figure 8.9, these two lines are very close, which proves the functionality of the shielding effect and of the COMSOL simulation and model.

Table 8.1 Large scale model shutter shielding effect test results.

Electrode Movement (mm)	V_{out} (±0.1 V)	Output variation (V)	Normalized signal variation
0	1.1	0	0%
3	1.9	0.8	28%
7	2.7	1.6	55%
10	2.9	1.8	62%
13	3.1	2	69%
16	3.2	2.1	72%

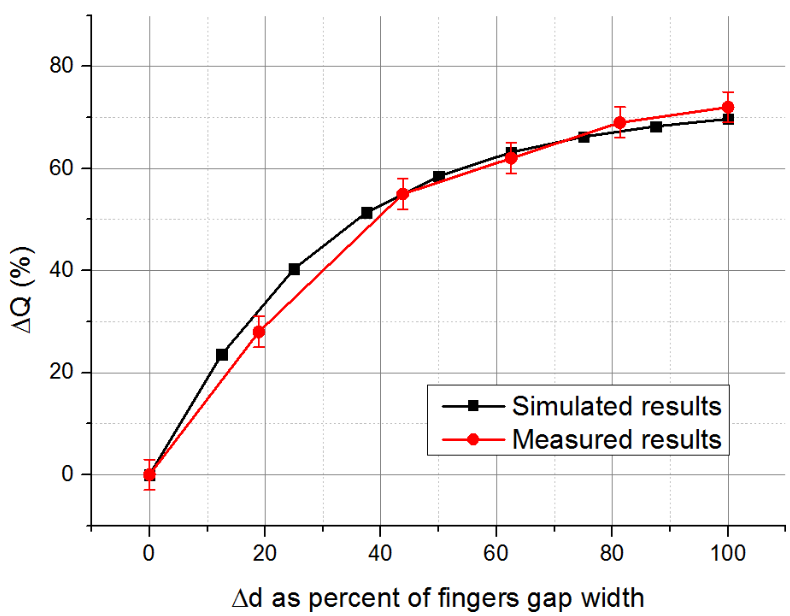

Figure 8.9 Normalized measurement response vs. simulation.

8.2. Thermal actuation of the shutter

The vertical movement of the shutter was designed to be driven by a thermal actuator. This method was selected due to the low required voltage, with gives low electrical interference compared to electrostatic actuation. Various thermal actuator designs were considered and are discussed below.

8.2.1. Design 1: SiO_2-Al thermal actuator

(1) Vertical displacement simulation

A vertical field mill employing an SiO_2–Al bi-material thermal actuators is shown in Figure 8.10. It possesses a metalized double-sided comb shape shutter supported on both sides by U-shaped thermal actuators for vertical shutter motion. The actuators are formed from aluminum coated with SiO_2, and have a titanium thin film heater at the tip of the U. Electric current flow heats the structure, which results in bending of the U-shaped actuator and lifting of the structure, as shown in Figure 8.11. Also, seen in Figure 8.10 are four flexible aluminum ground lines on either side of the actuators. They connect the shutter to the substrate electrically and also provide heat dissipation. As listed in Table 8.2, SiO_2 has a low thermal expansion coefficient (only 0.5×10^{-6} K^{-1}) and a high melting point (1710 ºC). Therefore, it allows the actuator to work at a relatively high temperature compared to polymer materials. This can minimize the effect of ambient temperature fluctuation on the sensor performance.

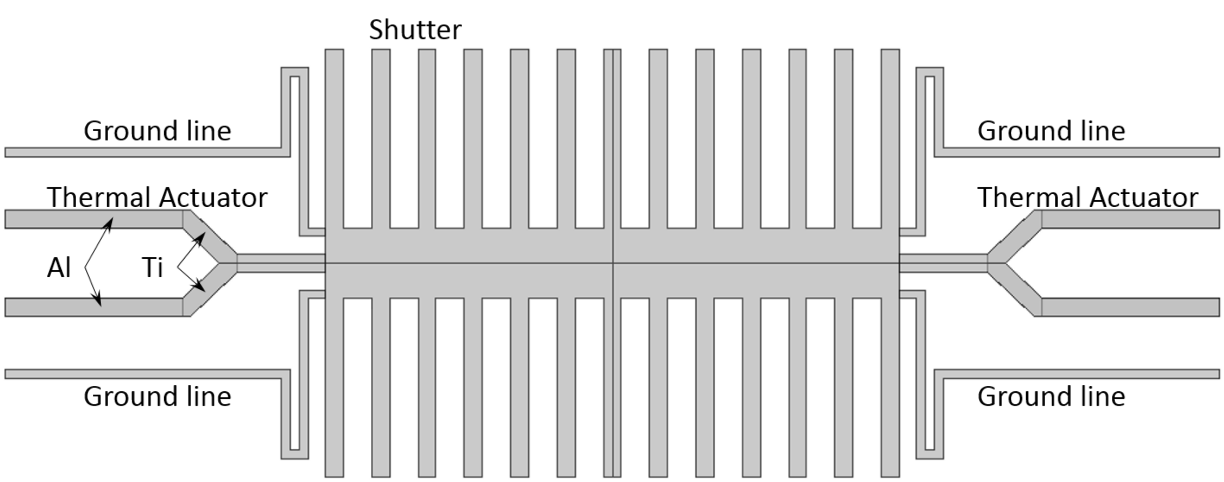

Figure 8.10 Schematic of the sensor design with thermal actuator.

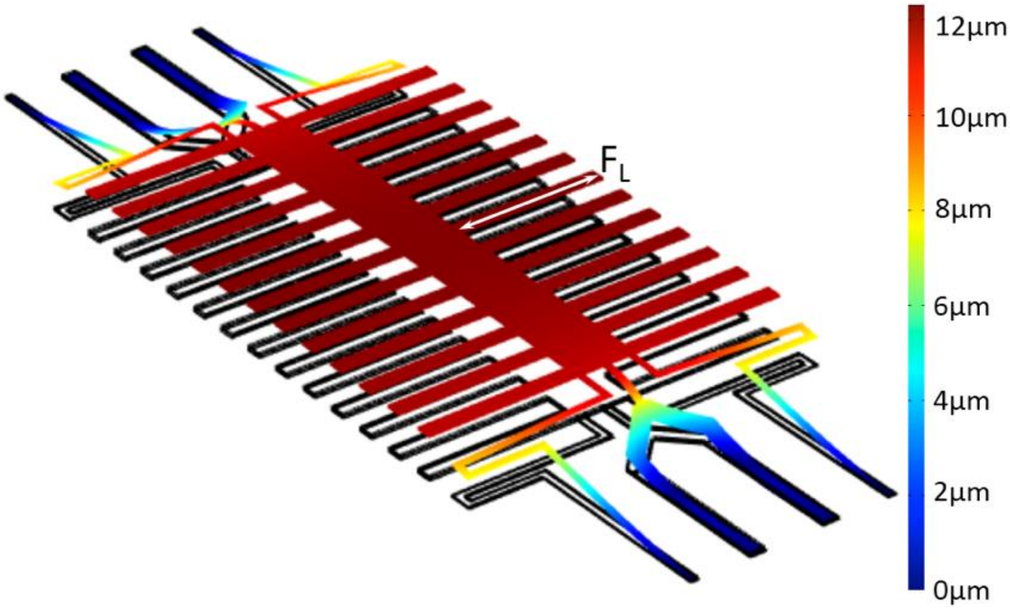

Figure 8.11 Simulation of shutter displacement during actuation.

Table 8.2 SiO_2 mechanical properties.

Melting point	1710 ºC
Young's Modulus	70 GPa (wet growth)
Coeff. of Thermal Expansion	0.5×10^{-6} K^{-1}
Tensile Strength	225-275 MPa
Thermal conductivity	1.4 Wm^{-1} K^{-1}

(2) Thermal dynamic simulation

Dynamic performance is another indicator of performance of the shutter and thermal actuator. According to equation (6-2), higher vibration frequencies provides greater output current, and so sensor signal. Vibration frequency is limited by the thermal time constant and resonant frequency. For the thermal actuator, there are three modes of heat transfer: conduction, convection, and radiation. However, previous studies indicated that for an operation temperatures below few 100s ºC and for the close spacing between the heater and substrate, convection and radiation can be neglected [44], [45].

The actuation performance of this structure was simulated in COMSOL Multiphysics. A 12 finger per side comb-shutter was simulated, with electrode width E_W=10 μm, electrode length

E_L=100 μm, comb finger width F_W=10 μm, comb finger length F_L=100 μm, finger spacing F_S=16 μm, and for a sensor having 24 electrodes/shutter fingers (12 per side).

Figure 8.12 shows the actuation performance of the device. The thermal cool down time of the actuator was calculated to be ~130 μs (7 kHz). For a peak shutter, vertical operation height of 12 μm, we see that this would require heating the thermal actuator by ~350 ºC.

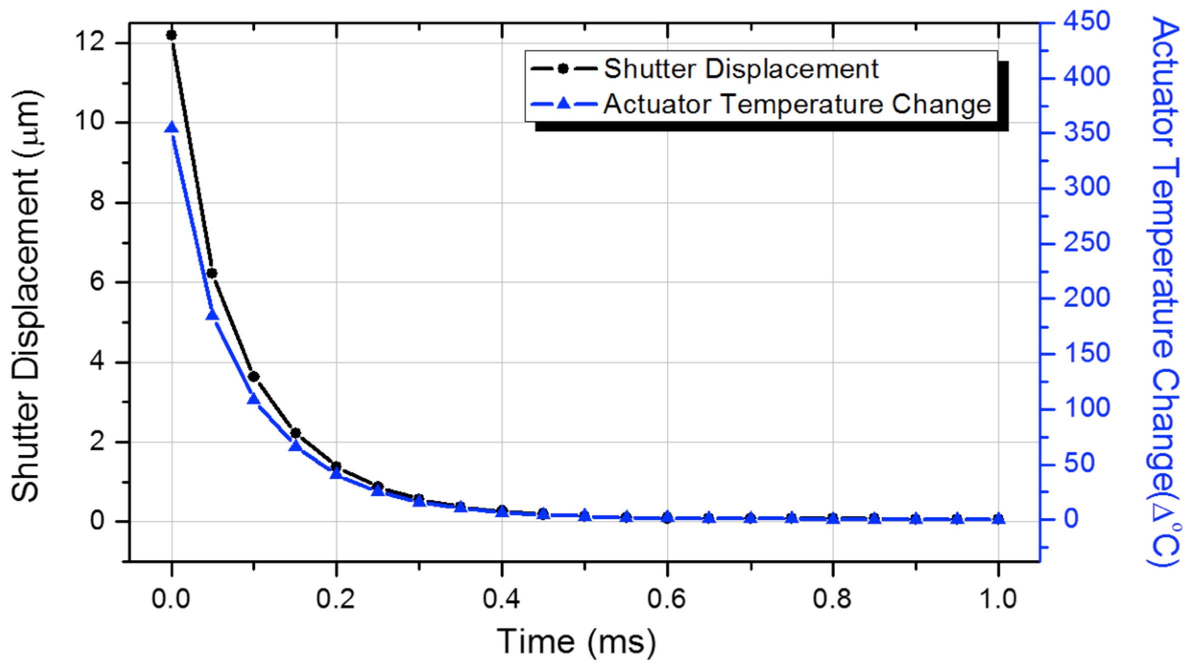

Figure 8.12 SiO_2-Al thermal actuator cooling transient simulation.

Table 8.3 compares the sensor output at different operation frequencies. At 7 kHz, which is the device's cooldown thermal time constant, the shutter would fall from 12 μm to 2.5 μm, a 9.5 μm movement. At other drive frequencies, more or less time would be available for the thermal actuator to cool down. This would give different movement distances, but the faster or slower shutter movement speed would also affect the measured signal. The table shows that for 7 kHz movement we obtain the highest output current 0.98 pA. This is similar in performance to the lateral moving MEFM device in [13], when scaled with the electrode area. It should be mentioned that higher output current can be easily obtained by connecting multiple actuators in parallel, thus effectively increasing the collection area for the entire sensor array.

Table 8.3 Sensor output current as a function of shutter height and frequency for 1 kV/m dc electric field.

Shutter height range (μm)	ΔQ (C)	Cooldown Time (ms)	Frequency (Hz)	Output current (pA)
0.6 - 12	1.9×10^{-16}	0.3	3 333	0.63
1 - 12	1.8×10^{-16}	0.25	4 000	0.72
1.38 -12	1.7×10^{-16}	0.2	5 000	0.85
1.9 - 12	1.5×10^{-16}	0.166	6 000	0.9
2.2 - 12	1.4×10^{-16}	0.13	7 000	0.98
2.8 - 12	1.2×10^{-16}	0.125	8 000	0.96
3.8 - 12	0.9×10^{-16}	0.1	10 000	0.9
6.2 – 12	0.45×10^{-16}	0.05	20 000	0.9

(3) Thermal actuator interference simulation

Interference by the actuator drive signal on the sensing signal can be an issue in MEMS sensors. For example, the device introduced in [16] was a vertical moving shutter field mill that used PZT material to drive the shutter. However, the interference by the 4 V 13 kHz peak-to-peak voltage PZT ac drive signal significantly affected the ability to detect dc fields. By contrast, the thermal actuators of this work operate at low voltages and so reduce potential interference. The simulated structure shown in Figure 8.13 was used to determine the potential interference by the thermal actuators. The design used 350 ºC heating on the actuator, requiring 4 mW and a ± 2 V driving voltage. The simulation shows that only 1.8×10^{-18} C of charge is induced on the sensor electrodes from this drive voltage. Compared to the results in Figure 8.5, this is approximately 1% of the induced charge caused by an external 1 kV/m dc electric field. Thus, the resolution limit of the sensor itself would be 10 V/m, neglecting noise in other electronics.

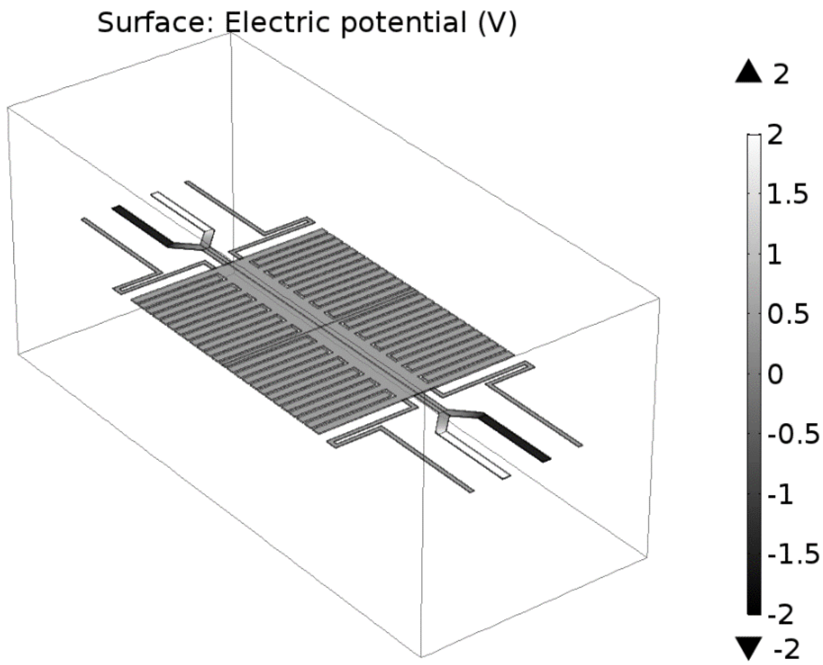

Figure 8.13 Thermal actuator interference simulation.

8.2.2. Design 2: SU-8 –aluminum thermal actuator

The second design considered was an SU-8 based actuator. The use of the epoxy-based negative photoresist SU-8 2000 as a MEMS structural material has drawn a great deal of attention recently. SU-8 features a high glass temperature of up to 240 ºC, a large thermal expansion coefficient of 5.2×10^{-16} K^{-1}, and low intrinsic stress[42][43]. It also has a low Young's modulus of 2×10^{9} Pa. Table 8.4 lists SU-8's mechanical properties. Compared to SiO_2, it is able to provide more deformation under low temperature. Two shapes for the actuator were considered, fork shaped and bridge shaped. The Fork shaped sensor has a free moving end, but it might suffer the intrinsic stress of aluminum. The Bridge shaped sensor is fixed both ends, which helps keep the actuator shape, but it might lose some of the flexibility. Therefore, both shapes were designed at the same time to compare their performance. In this section, two SU-8 –aluminum thermal actuator designs, fork-shaped and bridge-shaped, will be discussed.

Table 8.4 SU-8 mechanical properties.

Softening point	210 ºC
Thermal Stability in Air	279 ºC
Young's Modulus	2.0 GPa
Coeff. of Thermal Expansion	52×10^{-6} K^{-1}
Tensile Strength	60 MPa
Thermal conductivity	0.2 $Wm^{-1}K^{-1}$

(1) Bridge-shaped thermal actuator

The first design is a bridge-shaped shutter, as shown in Figure 8.14. Thermal actuators of this design are located on both ends of the shutter. As we can see from the simulation results, with a heat source of 0.5 mW on each titanium heater and 0.4 mW on the aluminum cantilever, the shutter is able to move up 16 µm with a temperature increase to 410 K (210 ºC) Figure 8.15. COMSOL simulation model is demonstrated in Appendix B.

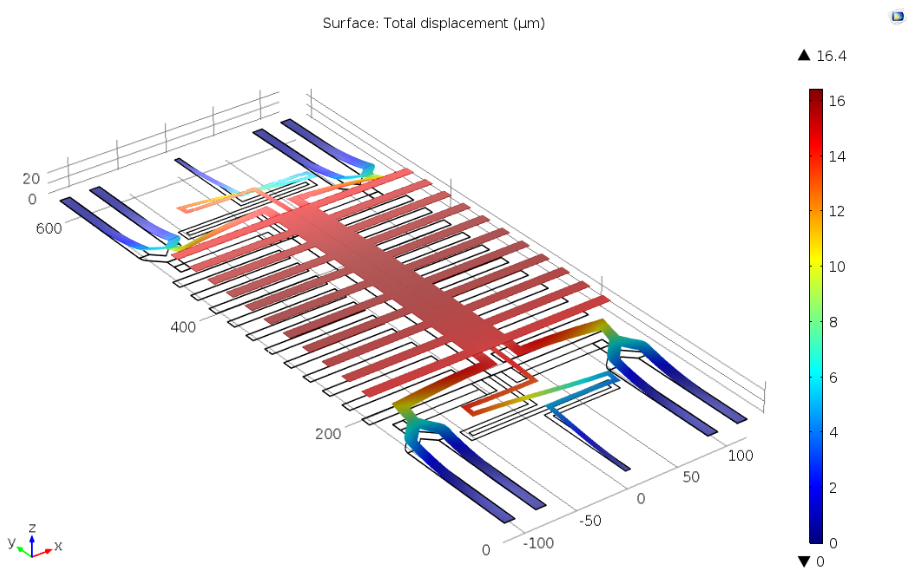

Figure 8.14 Bridge-shaped thermal actuator simulation.

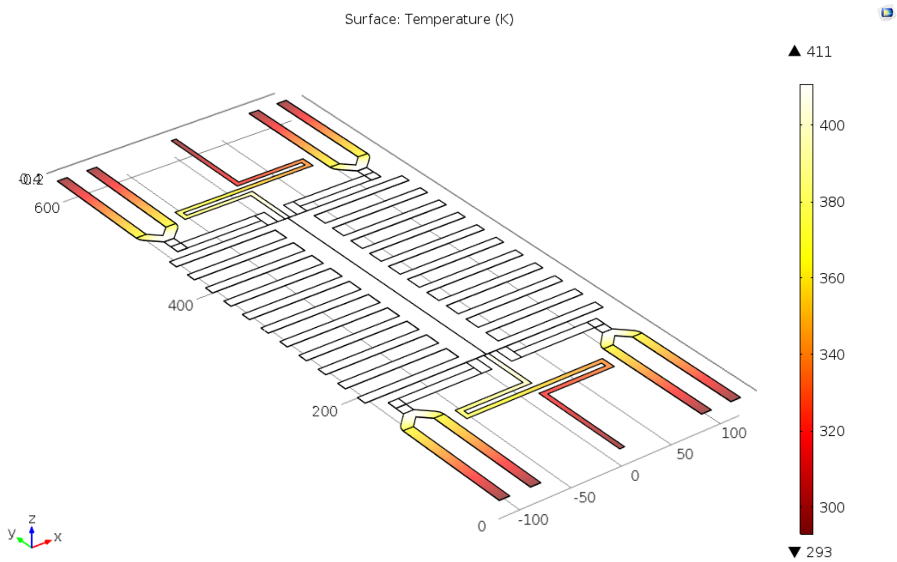

Figure 8.15 Bridge-shaped thermal actuator temperature distribution.

(2) Fork-shaped thermal actuator

The fork-shaped actuator with shutter is shown in Figure 8.16. It has two thermal actuators to provide vertical displacement. For each of the thermal actuators, the total length of the titanium heater is 75 µm and aluminum is 570 µm, and both are 0.5 µm thick. Since the conductivity of aluminum is 50 times higher than titanium, when the titanium heater generates 1 mW heat, aluminum area will produce 0.76 mW of heat. With this heat load, the tip of the shutter fingers are displaced 29 µm, as shown in Figure 8.16. The temperature distribution is shown in Figure 8.17; the highest temperature on the actuator is 372 K (189 ºC). The COMSOL simulation model is demonstrated in Appendix C.

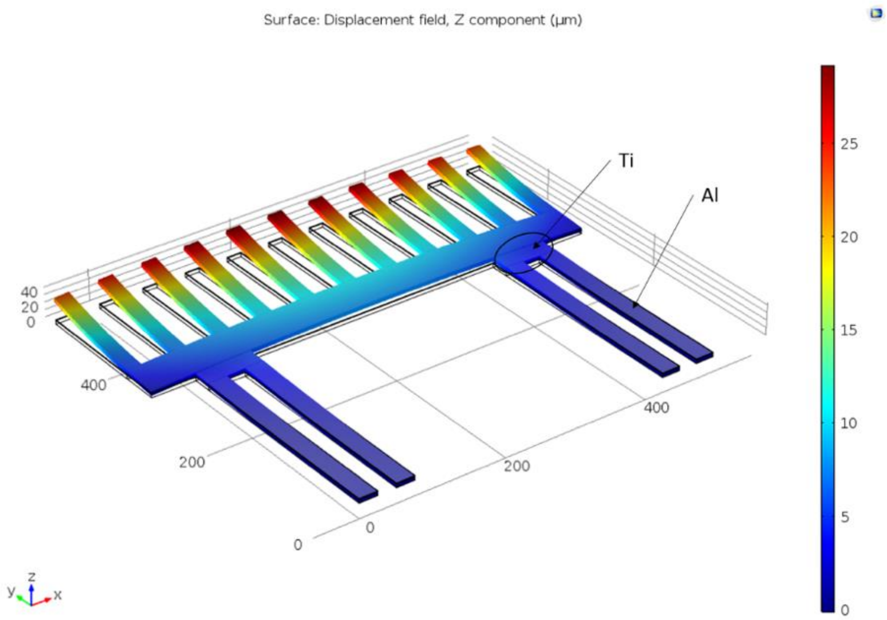

Figure 8.16 SU-8-Al fork-shaped thermal actuator displacement simulation.

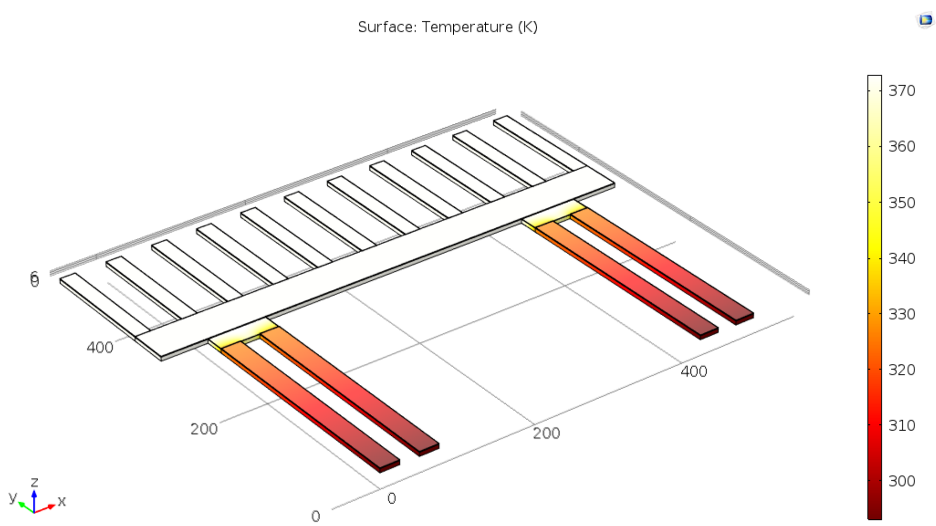

Figure 8.17 SU-8-Al fork-shaped thermal actuator temperature simulation.

8.2.3. Design 3: Si-Al thermal actuator

In order to solve the SU-8 thermal instability issue in the second design, silicon and aluminum are chosen to act as the thermal actuator. Silicon's chemical and physical properties are thermally stable even when the temperature rises to as high as 1414 ºC. Silicon has a much higher Young's modulus which reduces the actuator stress. Table 8.5 lists the main mechanical properties of the silicon.

Table 8.5 Silicon mechanical properties.

Melting point	1414 ºC
Young's Modulus	130-180 GPa
Coeff. of Thermal Expansion	2.6×10^{-6} K^{-1}
Thermal conductivity	130 $Wm^{-1}K^{-1}$

(1) Bridge-shaped thermal actuator

In the first design, a titanium heater is applied to provide an additional displacement. Figure 8.18 shows the simulation model. The actuator width is 40 µm, the finger spacing is 80µm, the aluminum part length is 1500 µm, the titanium heater length is 140 µm, the thickness of titanium and aluminum is 1 µm, and the silicon thickness is 10 µm. As the electrical conductivities of aluminum and titanium are 3.77×10^{7} S/m and 2.6×10^{6} S/m respectively, providing a 100 mA current, each titanium heater has a power of 13.5 mW, and each aluminum beam has a power of 10 mW. The COMSOL simulation shows that the shutter displacement is 44 µm, as shown in Figure 8.19, and the highest temperature is 583 K (320 ºC) (see Figure 8.20 for the temperature distribution).

This simulation assumes there is no electromigration. However, as the cross-section of aluminum is 10 µm×1 µm, the current density of 11 mA is 1×10^{6} A/cm^{2}. This is over the maximum current density of 1×10^{5} A/cm^{2} that aluminum support to avoid electromigration.. Therefore, in reality, the fabricated sensor based on this simulation needs to run with lower power or larger cross-section aluminum conductors. Alternatively, the aluminum can be replaced by another material that has higher electromigration resistance, such as copper.

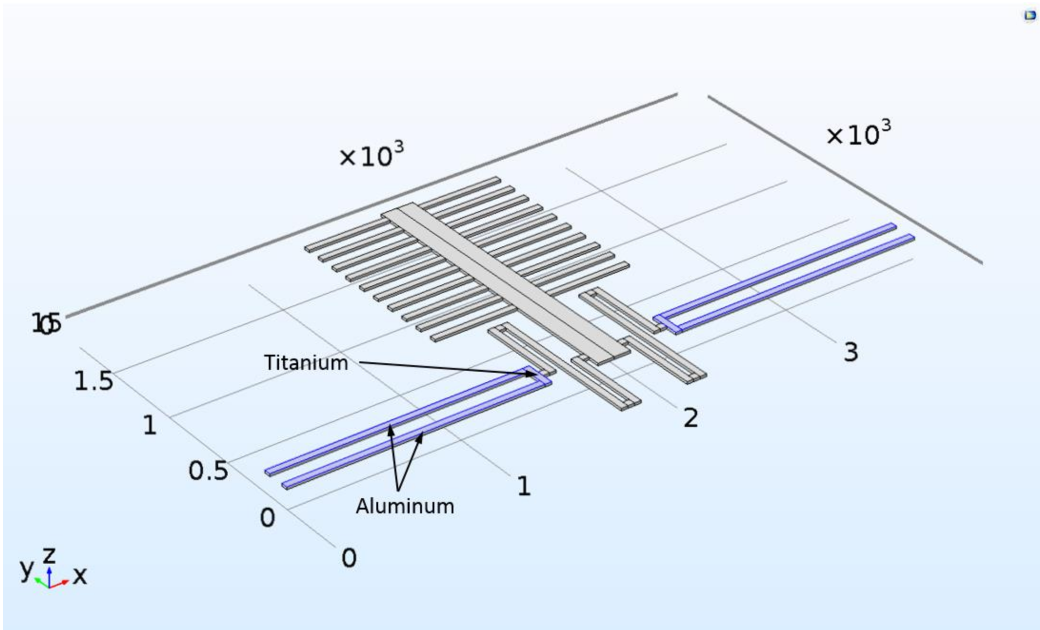

Figure 8.18 Titanium heater silicon based vertical shutter model.

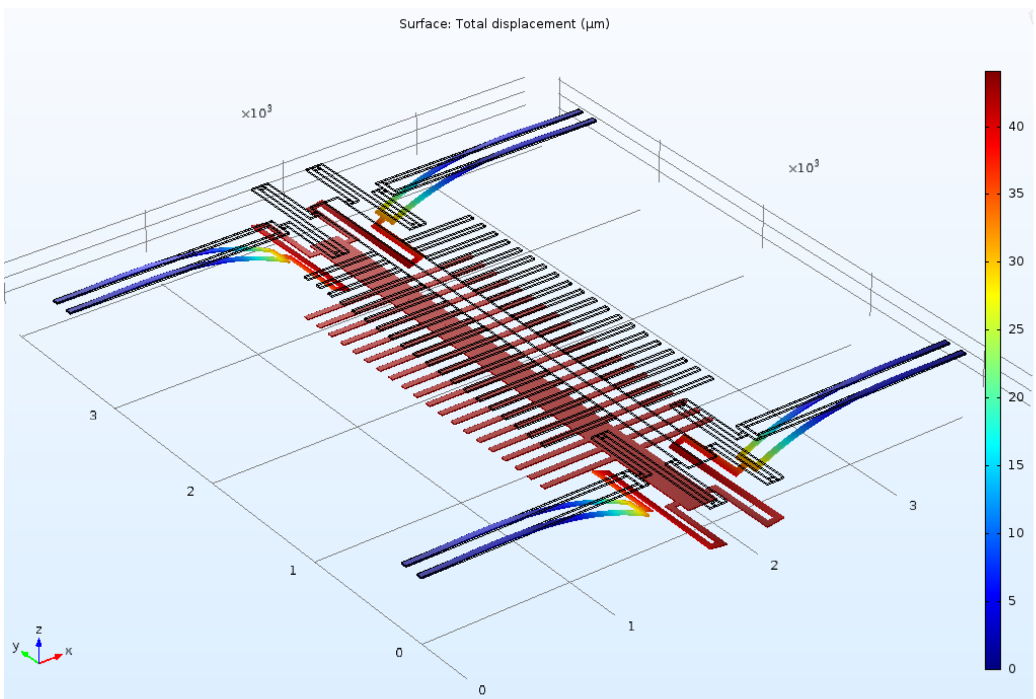

Figure 8.19 Si-Al thermal actuator with titanium heater shutter movement simulation.

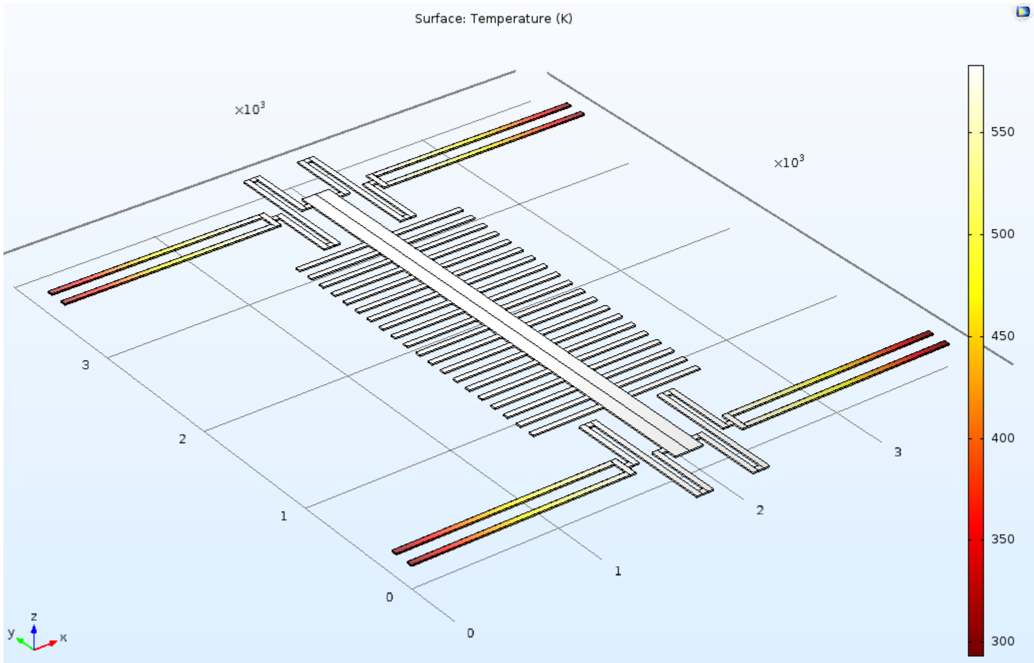

Figure 8.20 Si-Al thermal actuator with titanium heater temperature distribution.

If a titanium heater is not used, the shutter is still expected to have significant movement. To compare the performance with and without the titanium heater, a simulation is performed using aluminum and silicon as a thermal actuator. Providing the same current, 100 mA, the generated power on each thermal actuator is 21 mW. The COMSOL simulation results are shown in Figure 8.21 and Figure 8.22. The shutter can move to 21.1 μm and the temperature can increase to 427 K (154 ºC). The shutter movement is about 58% of the movement of the actuator with the titanium shutter.

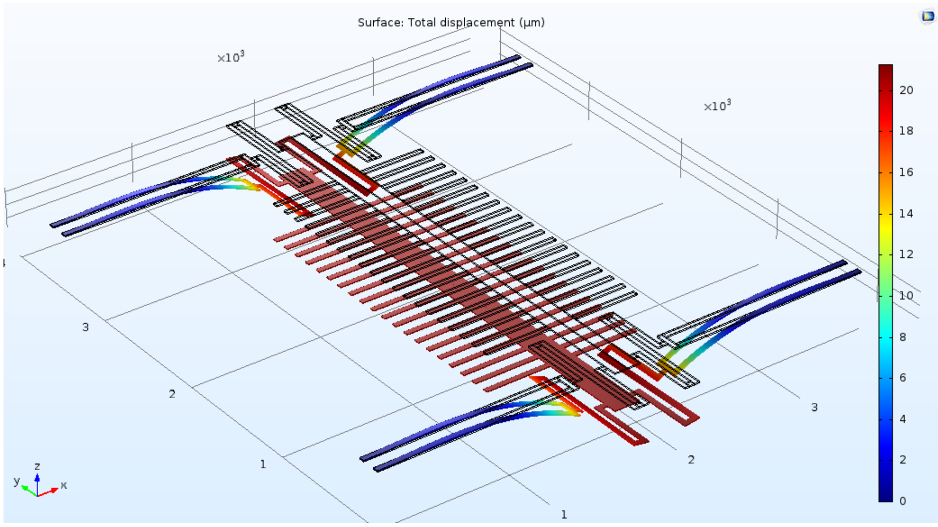

Figure 8.21 Bridge shaped Si-Al thermal actuator without the titanium heater shutter movement simulation.

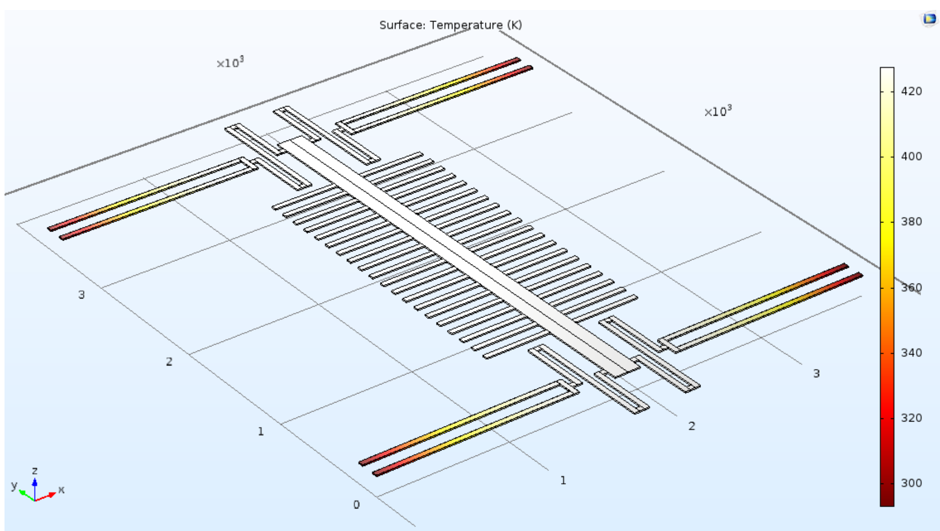

Figure 8.22 Bridge shaped Si-Al thermal actuator temperature simulation.

(2) Fork-shaped thermal actuator

A fork shaped actuator was also designed. The actuator width was 40 μm, the aluminum part length was 1500 μm, the titanium heater length was 140 μm, and the silicon thickness was 10 μm. Providing a 100 mA current, each titanium heater has a power of 13.5 mW, and each aluminum beam has a power of 10 mW. The COMSOL simulation shows that the average shutter displacement is 130 μm, as shown in Figure 8.23, with the temperature increasing to 582 K (309 ºC) (see Figure 8.24).

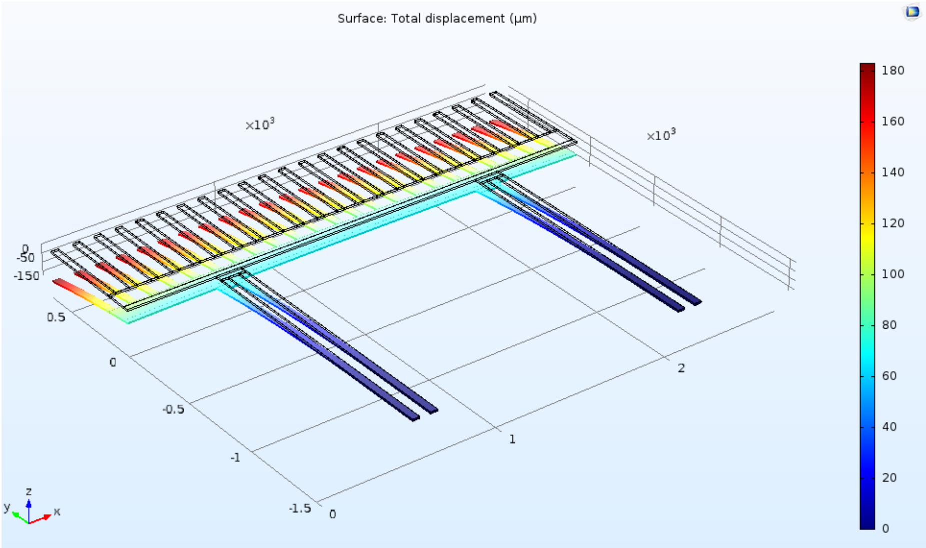

Figure 8.23 Fork shaped Si-Al thermal actuator shutter movement simulation.

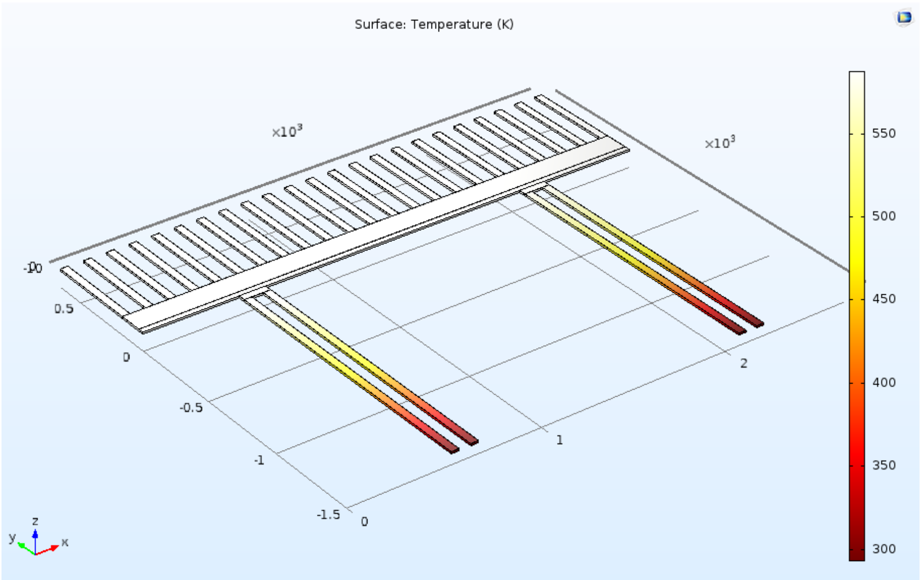

Figure 8.24 Fork shaped Si-Al thermal actuator temperature simulation.

Similarly, the actuator without the titanium heater was also simulated. Providing 21 mW to each of the actuator, the average displacement of shutter is 68 μm, as shown in Figure 8.25, with the temperature increasing to 426 K (153 ºC) (see Figure 8.26).

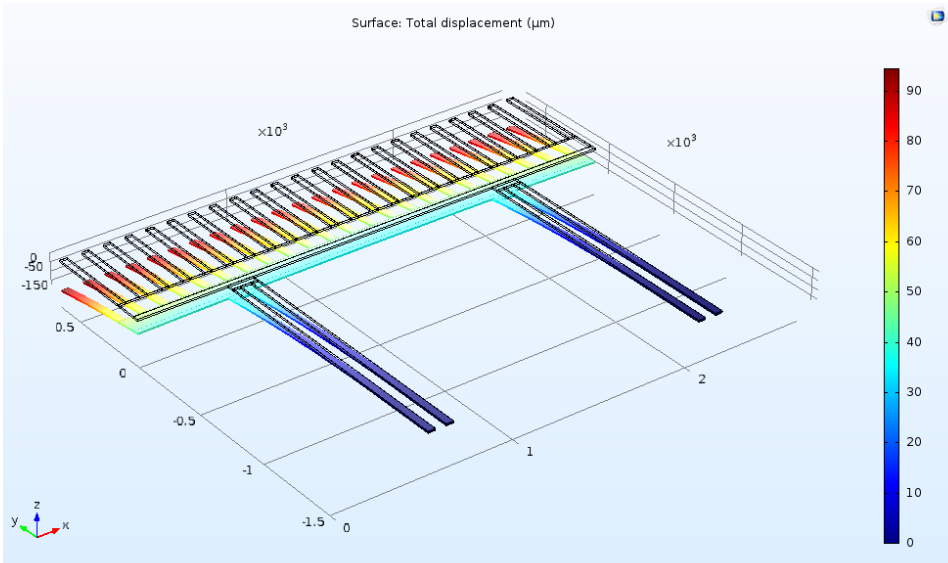

Figure 8.25 Fork shaped Si-Al thermal actuator shutter movement simulation without heater.

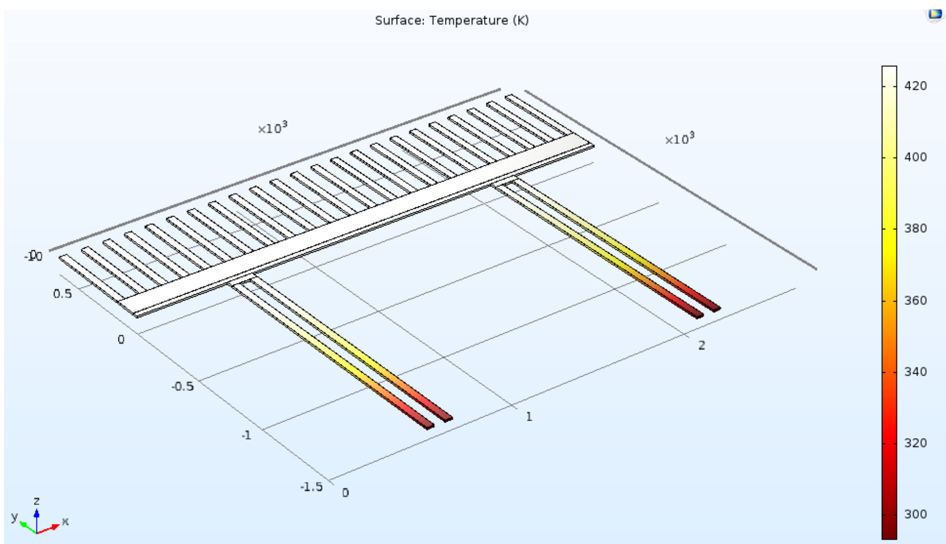

Figure 8.26 Fork shaped Si-Al thermal actuator temperature simulation without heater.

(3) Si-Al thermal actuator shutter movement vs. charge variation

As we can see from the above Si-Al thermal actuator shutter movement simulations, the shutter is moving downward during operation. In this case, the sensing electrodes will see more of the electric field resulting in an increase in induced charge on the electrodes. Figure 8.27 plots the inducted charge variation (ΔQ%) on the sensing electrodes as a function of shutter height for both bridge shaped and fork shaped shutters. The dimension of the shutter and sensing electrodes is exactly the same as the fabricated devices of section 8.3.2. For the fabricated device, the bridge shaped device has 32 sensing electrodes while the fork shaped one has 22 sensing electrodes. Both devices have the same size of electrode 40 μm × 500 μm, finger size 40 μm × 500 μm, and finger spacing 80 μm. In the simulation, the dc field is 1 kV/m. The COMSOL simulation model is shown in appendix A.

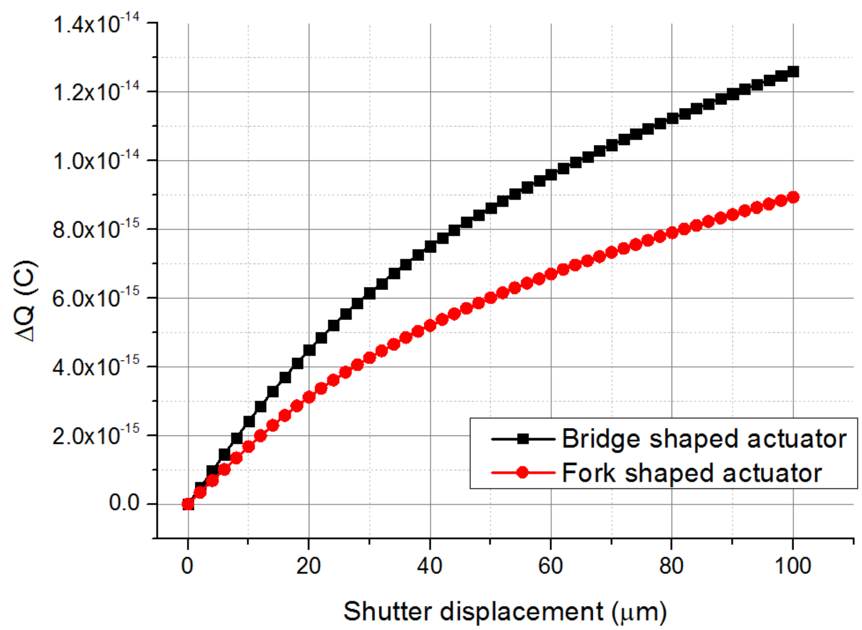

Figure 8.27 Si-Al thermal actuator shutter movement vs. charge variation simulation.

8.2.4. Si-Al actuator resonant frequency

Si-Al sensor resonant frequency was also simulated with a silicon thickness of 5 μm, 10 μm, and 15 μm, and the aluminum thickness was 1 μm. Table 8.6 lists the simulation results for both the bridge shaped actuator and fork shaped actuator.

Table 8.6 Si-Al sensor resonant frequency simulation results.

Si thickness	Bridge shaped Resonant frequency	Fork shaped Resonant frequency
5 μm	644 Hz	699 Hz
10 μm	1236 Hz	1281 Hz
15 μm	2398 Hz	1863 Hz

8.2.5. Si-Al sensor spring constant

Si-Al sensor spring constant simulation was also performed using silicon thickness of 5 µm, 10 µm, and 15 µm, and aluminum thickness is 1 µm, when applying 20 µN force on the actuator, the displacement is 58.8 µm, 8.3 µm, and 2.6 µm. The calculated spring constants for both birdge shaped actuator and fork shaped actuator are listed in Table 8.7.

Table 8.7 Si-Al sensor spring constant simulation results.

Si thickness	Bridge-shaped spring constant	Fork-shaped spring constant
5 µm	0.34 N/m	0.12 N/m
10 µm	2.4 N/m	0.95 N/m
15 µm	7.7 N/m	3.2 N/m

8.2.6. Si-Al thermal actuator thermal dynamic simulation

As discussed in section 8.2.1, thermal actuation speed also determines the output signal strength. Given an aluminum thickness of 1 µm and silicon thickness of 10 µm, with a 0.1 A current going through the actuator, each actuator has a power of 21 mW. Figure 8.28 illustrates the simulated cooling transient performance for both types of actuators. Initially, with the given power, the bridge shaped shutter lowered 21 µm and fork shaped shutter lowered 68 µm. 10 ms after power is off, which is 100 Hz, bridge shaped shutter raised to about 7 µm, while the fork shaped shutter raised to 47 µm. Within this 10 ms, the bridge shaped shutter moves 14 µm and the fork shaped shutter moves 21 µm. The faster operation speed can be achieved by reducing the shutter moving distance. Table 8.8 lists the operating shutter frequencies, its corresponding moving distances, and expecting output current.

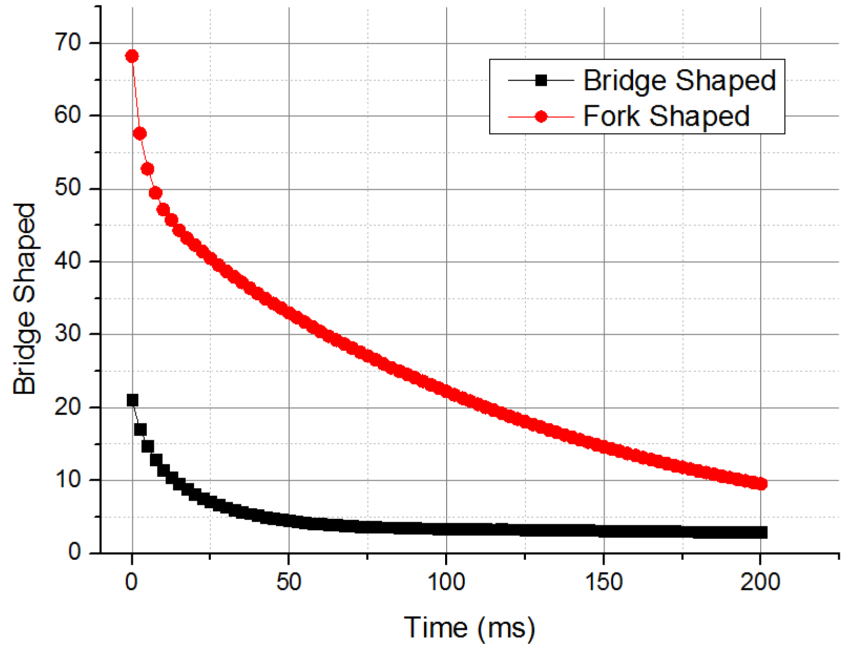

Figure 8.28 Si-Al actuator cooling transient simulation.

Table 8.8 The simulated Sensor output current as a function of shutter height and frequency for 1 kV/m dc electric field.

Bridge-shaped shutter (32 sensing electrodes)			
Operation frequency	Shutter movement distance	Charge variation	Output Current
1000 Hz	2.3 μm	5.6×10^{-16} C	0.6 pA
500 Hz	4.2 μm	1×10^{-15} C	0.5 pA
250 Hz	5.1μm	1.2×10^{-15} C	0.31 pA
100 Hz	9.7 μm	2.3×10^{-15} C	0.23 pA
50 Hz	12.9 μm	3.1×10^{-15} C	0.15 pA
Fork-shaped shutter (22 sensing electrodes)			
Operation frequency	Shutter movement distance	Charge variation	Output Current
1000 Hz	4.8 μm	8.2×10^{-16} C	0.82 pA
500 Hz	9.2 μm	1.6×10^{-15} C	0.77 pA
250 Hz	13.4 μm	2.2×10^{-15} C	0.55 pA
100 Hz	22.5 μm	3.4×10^{-15} C	0.34 pA
50 Hz	27.9 μm	4.1×10^{-15} C	0.2 pA

8.3. The fabrication of designs 2 and 3

In this section, the fabrication processes and results of design 2 and 3 will be discussed. The fabrication of the SU-8-Al thermal actuator design will be discussed in section 8.3.1, and the fabrication of the Si-Al thermal actuator design will be discussed in section 8.3.2.

8.3.1. SU-8-Al thermal actuator fabrication

8.3.1.1. Fabrication process

The SU-8-Al thermal actuator fabrication process is illustrated in Figure 8.29. The process starts from a 250 μm silicon wafer. The first step is to grow a 1.2 μm thick SiO_2 layer on both sides of the wafer using the wet thermal oxidization process. Then the back side SiO_2 layer is patterned to expose the silicon. Followed by a KOH back etch process for 210 minutes to etch 215 μm silicon and leave 35 μm, as shown in Figure 8.29 (d). After the KOH etch, the SiO_2 layer on the front side has about 800 nm left. A 5 μm thick SU-8 layer is then spin coated on top of the front side, patterned by a lithography process, and a 0.5 μm thick Titanium layer is sputtered on the top of the sample(Figure 8.29 (h)). After patterning the titanium heater, a 1 μm thick aluminum layer is sputtered on the front side. Then, the aluminum is patterned to form a thermal actuator and shutter (Figure 8.29 (k)). The last step is to release the structure by using an XeF_2 etch to remove the 35μm silicon on the back.

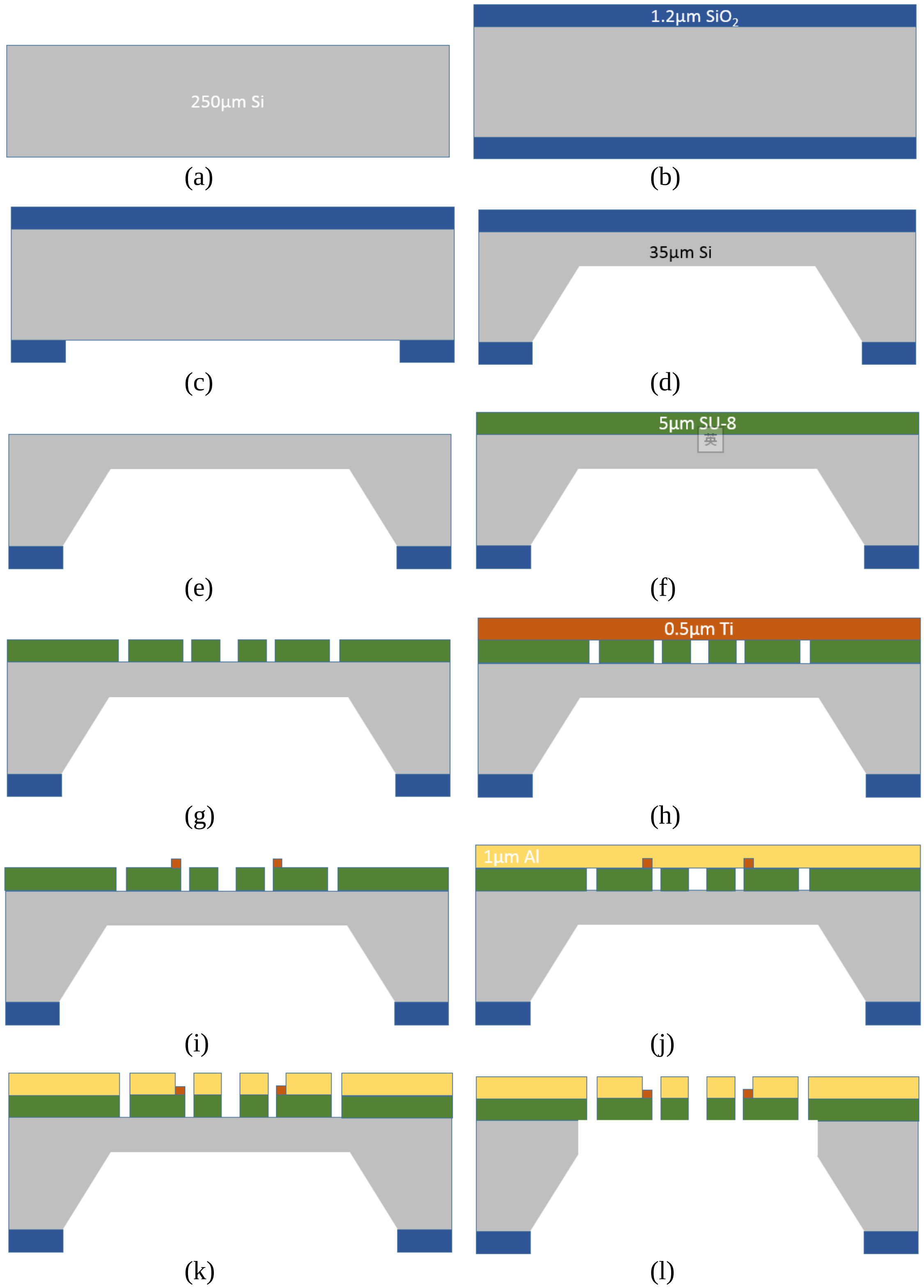

Figure 8.29 SU-8-Al thermal actuator fabrication process.

8.3.1.2. Fabrication attempt 1

The first batch of fabricated samples is shown in Figure 8.30 (a) and (b). As we can see from the samples, the titanium heater exists in the middle of the U shape thermal actuator, and the sensor structure is well-shaped. However, the aluminum on the ground line is broken; this is due to the over etch in the aluminum etch process. Another issue is that the finger and shutter are still connected, so, the device is not successfully released. Figure 8.31 demonstrates how the connection is formed and the process to remove the connection. In the SU-8 lithography pattern process, the SU-8 between fingers and shutters was not completely separated. There is a small amount of SU-8 left on the substrate. To fix this, an O_2 plasma etch process was used to complete the SU-8 patterning. The overall SU-8 thickness is reduced to 3 μm because of the plasma etch.

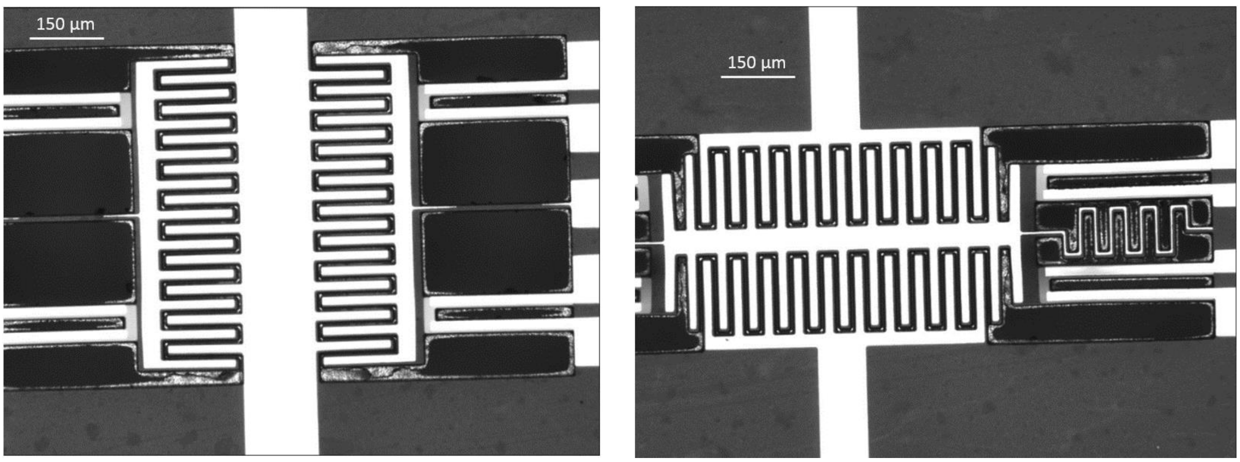

(a)Fork-shaped thermal actuator; (b)Bridge-shaped thermal actuator;

Figure 8.30 SU-8-Al thermal acturators release unsuccessfully.

Figure 8.31 SU-8 finger and shutter release.

8.3.1.3. Fabrication attempt 2

After solving the SU-8 patterning issue, the samples were released successfully. Figure 8.32 and Figure 8.33 shows the fabricated samples of the fork-shaped shutter and bridge-shaped shutter, respectively.

A low-stress recipe was used in the aluminum sputtering process, as shown in Table 5.9; the sputtering pressure is 20 mTorr and sputtering power is 200 W. From Figure 8.32, the SU-8-Al bilayer fork-shaped thermal actuator is completely curled down. There are two main factors for this: first, the actuator is still suffering from stress from the metal thin film. As we know SU-8 has very low stress, and aluminum stress is already minimized in the sputter process, the stress of aluminum film is still much higher than SU-8 (Figure 8.34); this results in structure deformation. Second, during the XeF_2 etch process, the heat generated in the fork area causes permanent deformation. The heat generated has a long dissipation path through the ground line which has a small cross-section area. The heat accumulated in the fork area raises the temperature which makes the SU-8 softer. Both reasons cause the fork to curl heavily, as shown in Figure 8.32, while the bridge design, which has both ends fixed, maintains a flat shape (Figure 8.33).

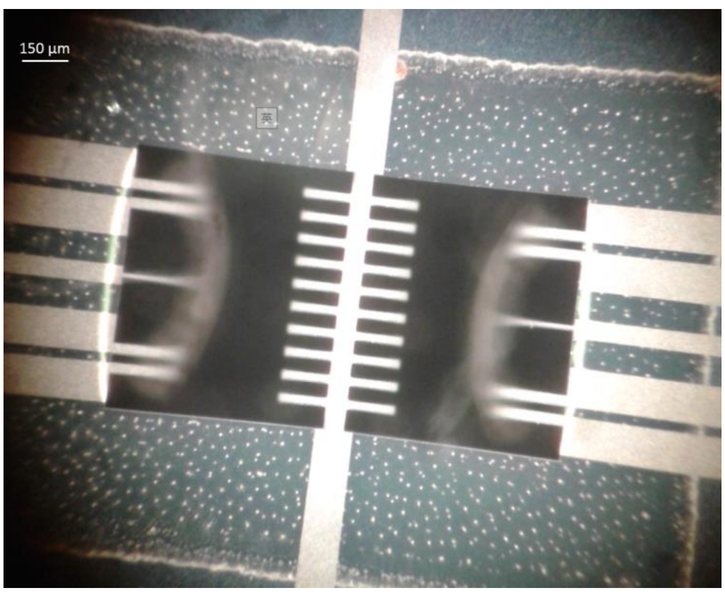

Figure 8.32 Fork thermal actuator fabrication result.

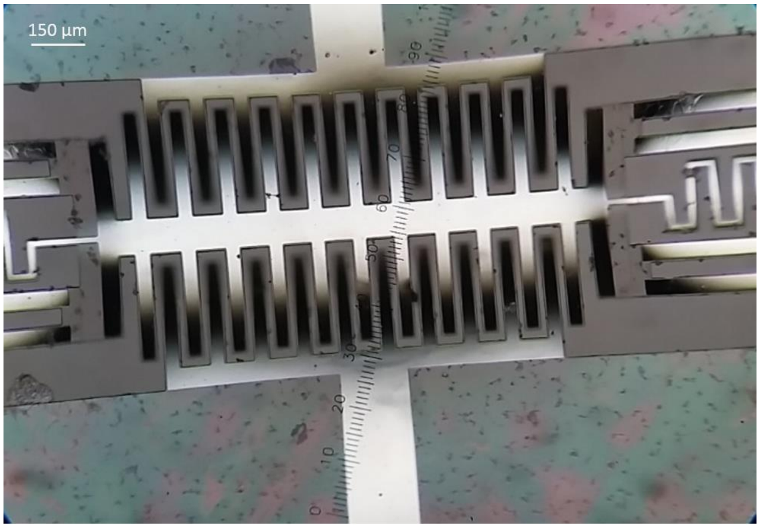

Figure 8.33 Before wire bonding bake at 100 ºC.

8.3.1.4. The relief of the aluminum tensile stress

The tensile stress of aluminum leads to the structure being bent down. To balance this stress, a solution is to use a compressive stress thin film, such as copper. The idea is to first measure the stress of the fresh spin coated SU-8 layer. Then hard bake samples for 20 minutes, and measure the stress after the bake. Then sputter a 150 nm aluminum layer using 18 mT pressure and 200 W dc power, and measure the stress. Last, sputter a layer of the different thickness copper layer (70 nm, 150 nm, and 220 nm), and measure the stress of each sample. Stresses were measured by the Toho FLX-2320 thin film stress measurement system. As we can see from the test results shown in Figure 8.34, the thicker layer of copper tends to balance tensile stress more. With a proper thickness of copper, most of the aluminum tensile stress can be balanced.

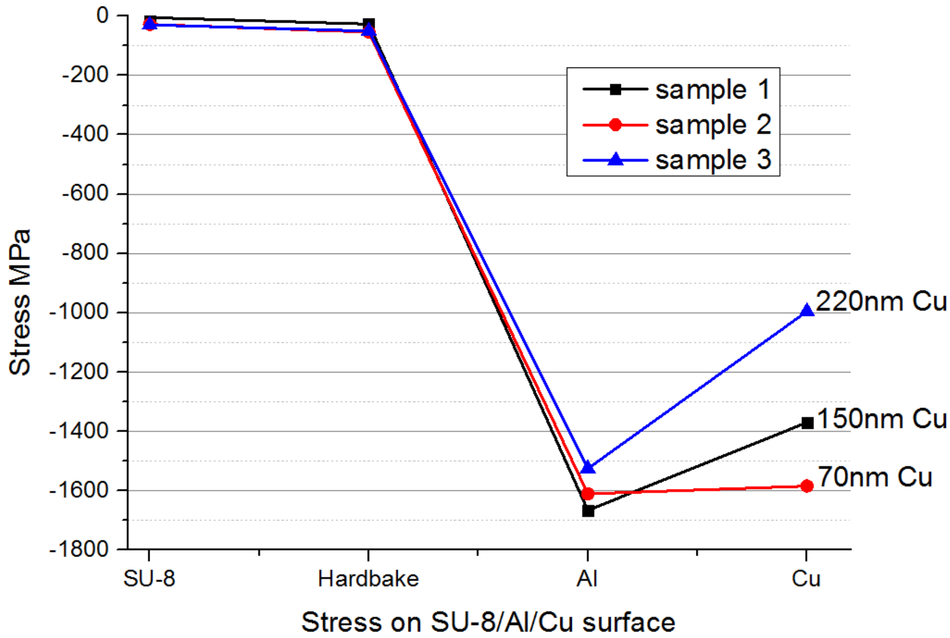

Figure 8.34 SU-8, aluminum, and copper stress study.

8.3.1.5. The wire bonding result for the sensor:

After fabricating the device, wires were bonded to the contact pads of the bridge-shaped actuator. After the sensor was baked at 100 ºC for one hour, the structure became permanently deformed, as shown in Figure 8.35. The reason for this is that at 100 ºC, the SU-8 becomes softer. Then, due to the aluminum film intrinsic stress, it bends down, but after the temperature comes back up to room temperature, SU-8 cannot overcome the aluminum stress to restore its original shape. This indicates that SU-8 is not a good material for a thermal actuator.

Also, in the last step of the fabrication process, the sensor needs to use XeF_2 to etch Si. When the silicon becomes thinner, due to the aluminum stress, the actuator will curl up and expose the titanium to XeF_2 gas, and result in the etch of titanium.

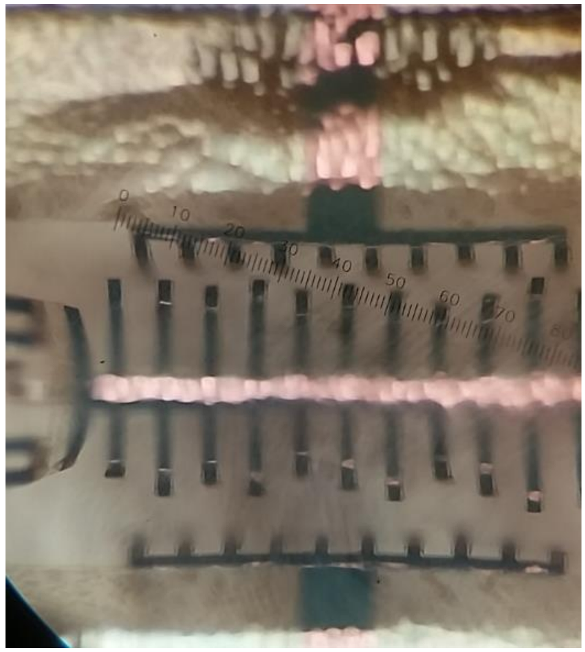

Figure 8.35 After wire bonding bake at 100 ºC for 1 hour.

8.3.2. Si-Al thermal actuator fabrication

8.3.2.1.Fabrication process

Si-Al thermal actuator fabrication process is illustrated in Figure 8.36. The process starts from a 250 µm silicon wafer. The first step is to grow a 1.2 µm thick SiO_2 layer on both sides of the wafer using wet thermal oxidizing process. Then use 10:1 HF solution to pattern the SiO_2 layer on the back side to expose silicon followed by a KOH back etch process for 210 minutes to etch 215 µm silicon and left 35 µm as shown in Figure 8.36 (d). After KOH etch, the SiO_2 layer left about 800 nm. Then a 1 µm thick aluminum thin layer is sputtered on the front side then pattern the aluminum and SiO_2. Using patterned aluminum as a mask silicon etch to etch 5-10 µm front side silicon. After this, another aluminum etch will be used to pattern the aluminum to separate the actuator and shutter. The last step is to release the structure by a plasma etch to remove the 25 - 30 µm silicon on the back.

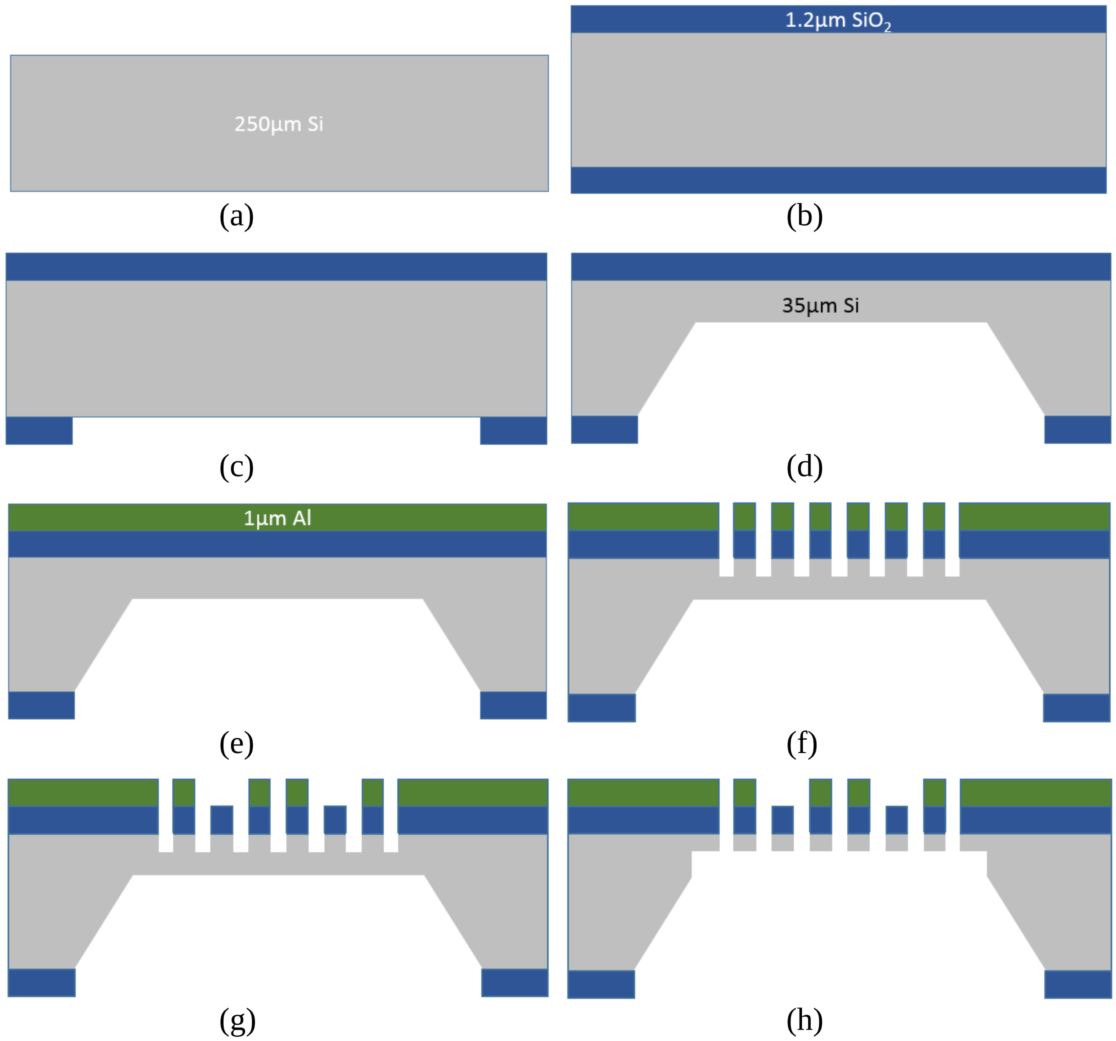

Figure 8.36 Si-Al thermal actuator fabrication process.

8.3.2.2. Fabrication attempt 1:

The first fabrication attempt has a titanium heater; it is sputtered and patterned between step (d) and (e). However, multiple fabrication results show that titanium was very easy to be etched in step (h) when CHF_3, SF_6 and O_2 gas were used to plasma etch silicon. The fluorine irons in these gases can etch titanium. Therefore, these released sample actuators usually have resistances of over 1 MΩ. This indicates that the titanium heater did not survive this process.

8.3.2.3. Fabrication attempt 2:

The above simulation of the actuator without a titanium heater shows that if only use aluminum as the heater, the shutter is still able to work. In the second attempt, thermal actuator only used aluminum as the top layer. Fabrication results show that both fork-shaped and bridge-shaped actuators fabricated successfully, as shown from Figure 8.37 and Figure 8.38. Figure 8.37 is the fabricated fork-shaped actuator, and Figure 8.38 is the bridge-shaped actuator. As we can see from these figures, in both samples shutter and fingers are aligned well; their height difference is measured about 5 µm. The shutter and actuator are also successfully separated. Shutter and finger thickness is estimated to be about 10 µm. The resistance of actuator plus wirings to the electrical pad on the sample is measured to be 10-16 Ω. The measurment results agree to calculated resistance of 9-12 Ω. The difference may come from the fabricated device cross section size is smaller than design.

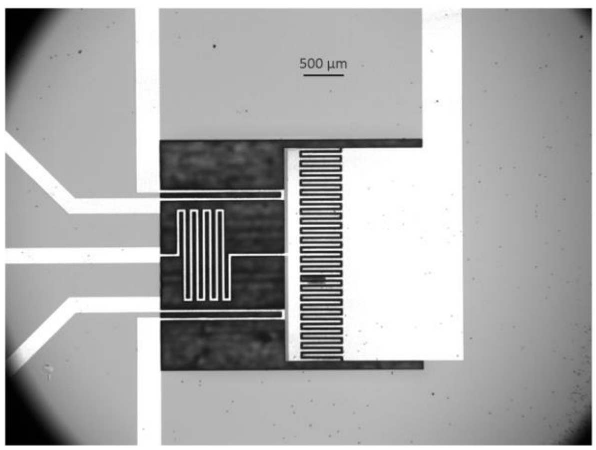

Figure 8.37 Si-Al fabricated fork-shaped actuator.

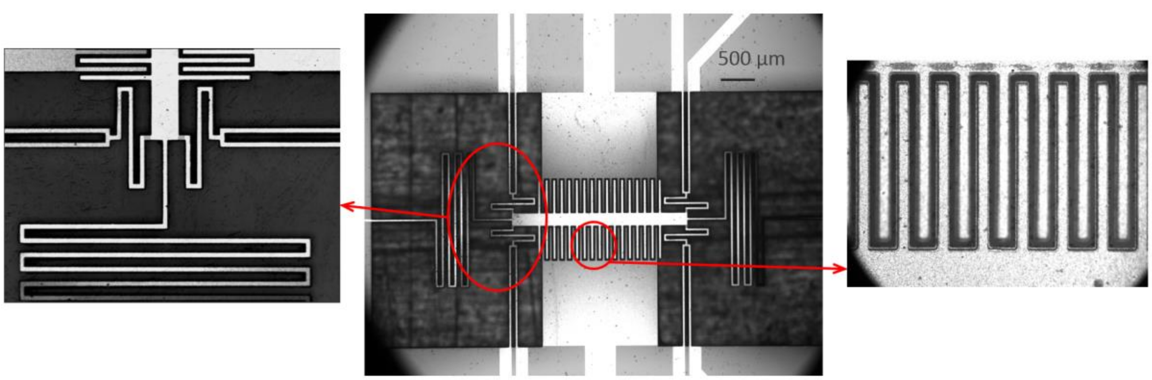

Figure 8.38 Si-Al fabricated bridge-shaped actuator.

8.4. The test of Si-Al thermal actuator

The testing of the sensor was done in two steps. The first step is to verify the actuator thermal dynamic performance by heating up the whole sensor and moving the sensor by a sine wave source. The second step is to verify the grounded shutter's shielding effect and the sensor response.

8.4.1. Heating up the sensor in an oven

The fork shaped sensor shown in Figure 8.37 and bridge shaped sensor shown in Figure 8.38 were used for this test. The sensor was fixed on a metal plate, then put into an oven at a temperature of 110 ºC. A thermocouple was connected to the metal plate to measure the metal plate temperature. It was assumed that the sensor attained the same temperature as the plate. The sensor and the plate were placed in the oven for 10 minutes for the temperature to reach equilibrium. The apparatus was then taken out and placed under a microscope. Twenty times magnification was used to focus on the shutter. After about 2 minutes, the thermocouple reading is 100 ºC. The temperature reading of the thermocouple and the knob position were recorded. The apparatus was then left to cool for thirty minutes until the thermocouple reading was at room temperature of 25 ºC. Then the microscope was refocused on the shutter, and the new knob position was recorded. The difference between the two knob measurements is the distance the shutter moved between the temperature readings. The shutter's movement was measured to be 25 µm for bridge shaped shutter and 47 µm for fork shaped shutter.

It should be mentioned that the thermal condition of this test is different from the simulation discussed in section 8.4.2 and 8.4.3, which have the highest temperature in the middle of the U-shape actuator. While in this test, the whole body of the shutter, including fingers, has the same temperature. Therefore, under the same temperature in this experiment, the test shutter will have more displacement.

The shutter movement distance at a given temperature is determined by the silicon thickness of the actuator. Figure 8.39 plots the simulated results for the shutter movement at 100 ºC for both fork shaped and bridge shaped shutter with silicon thickness vary from 6 µm to 16 µm. As we can see from the simulated results, the shutters displacement is very similar to a shutter with 12.5 µm thick silicon. Figure 8.40 plots the movement of a shutter with silicon thickness of 12.5 µm at various temperature from 25 to 100 ºC.

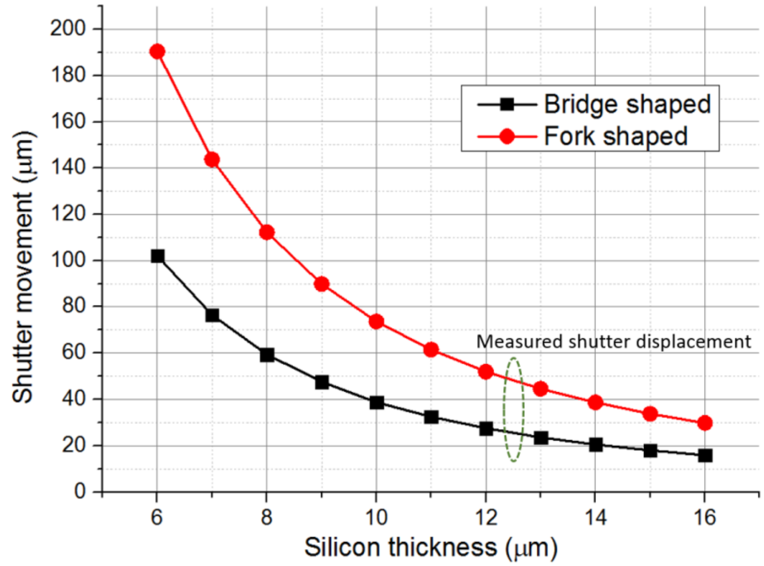

Figure 8.39 Shutter movement simulation for sensor heat up with various silicon thickness at 100 ºC.

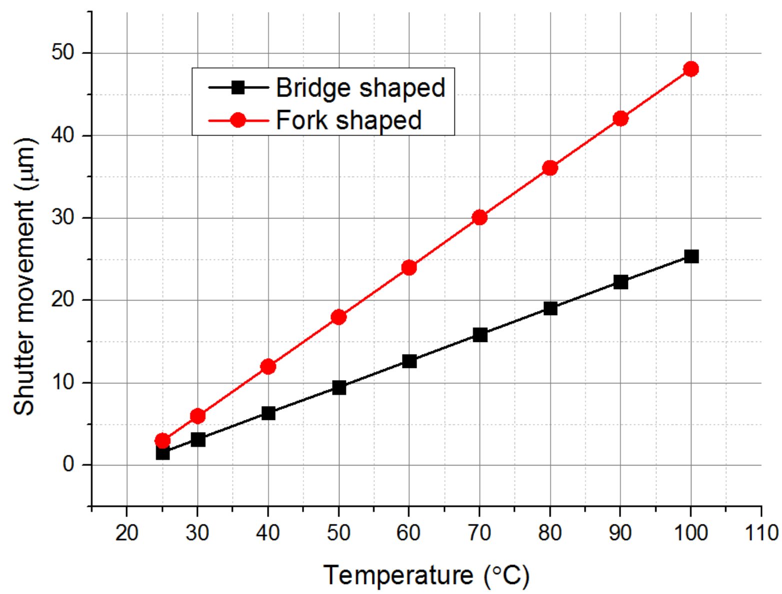

Figure 8.40 A Shutter with 12.5 μm thick silicon movement at temperature 25 – 100 ºC.

8.4.2. Driving shutter with thermal actuator

In this test, fork shaped shutter shown in Figure 8.37 and bridge shaped shutter shown in Figure 8.38 were driven into vertical motion with its thermal actuator. Before providing the voltage on the actuators, each actuator was connected to a 200 Ω resistor in series to limit the current flow. Then a sine wave at the frequency of 1 Hz (actuator vibration frequency is 2 Hz) was applied. The peak-to-peak current on the thermal actuator and measured displacement under the microscope are listed in Table 8.9 for the fork-shaped actuator, and Table 8.10 for the bridge-shaped actuator.

Table 8.9 Fork-shaped thermal actuator test.

Sine wave amplitude	Peak-to-Peak current	Actuator displacement
15 V	70 mA	11 μm
17.5 V	81 mA	18 μm
20 V	93 mA	24 μm

Table 8.10 Bridge-shaped thermal actuator test.

Sine wave amplitude	Peak-to-Peak current	Actuator displacement
15 V	70 mA	6 μm
17.5 V	81 mA	9 μm
20 V	93 mA	12 μm

8.4.3. Sensor experimental testing

8.4.3.1.dc electric field measurement:

In this test, the sensors shown in Figure 8.37 and Figure 8.38 were used to test their ability to measure a dc electric field. The test setup schematic is shown in Figure 8.41. The sensor is placed on an electrically grounded metal plate, which has a 0.5 mm thick masking tape on its surface so as to act as an electrical insulator. Another metal plate is placed 3 cm above the bottom metal plate, and a dc voltage can be applied to this top plate to generate the electric field. The thermal actuators of the sensor are driven by a sine wave from a function generator with the frequency of f. The shutter movement frequency will be $2f$, and this will be the same as the frequency of the induced current on the sensor electrodes from the dc electric field. The sensor response signal (ac current) is fed to a pre-amplifier. The schematic diagram for the pre-amplifier is illustrated in Figure 8.42. It consists of a current-to-voltage converter and a proportional amplifier. The gain of the current-to-voltage converter is 10×10^7 V/A for a signal less than 1 kHz. The gain of the proportional amplifier is $R_3/R_2 = 10$. Figure 8.43 shows the frequency response of the pre-amplifier. The output of the pre-amplifier is then feed to a lock-in amplifier. The output signal of the lock-in amplifier can be observed by an oscilloscope.

The thermal actuators were driven with a 20 V sine wave at 500 Hz. The voltage on the top metal plate is 30 V, which will result in a 1 kV/m electric field. According to Table 8.8, the output current of the bridge-shape and fork-shape shutter sensors should be 5.8 pA and 3.8 pA respectively. However, no signal was detected from the sensor in this experiment. Further investigation found that a measureable conductivity exists between the sensing electrodes, thermal actuators and the ground line (Figure 8.44). These unexpected conductivities introduce a leakage path to ground for the induced charge on the sensor electrodes. Additionally, leakage from the drive signal to the thermal actuators was found to saturate the lock-in amplifier. The fix of this isolation issue will be discussed in section 8.5.

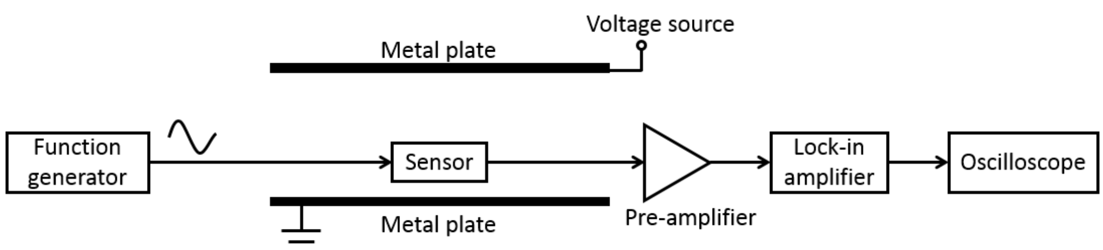

Figure 8.41 dc electric field test setup schematic diagram.

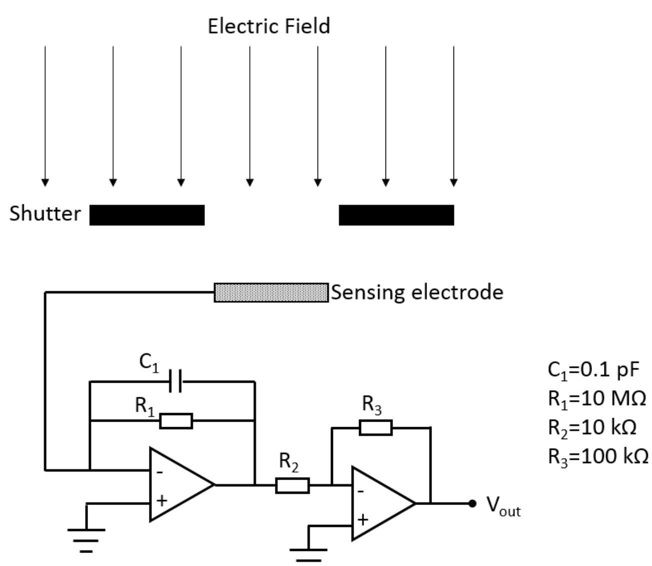

Figure 8.42 Sensor test pre-amplifier schematic diagram.

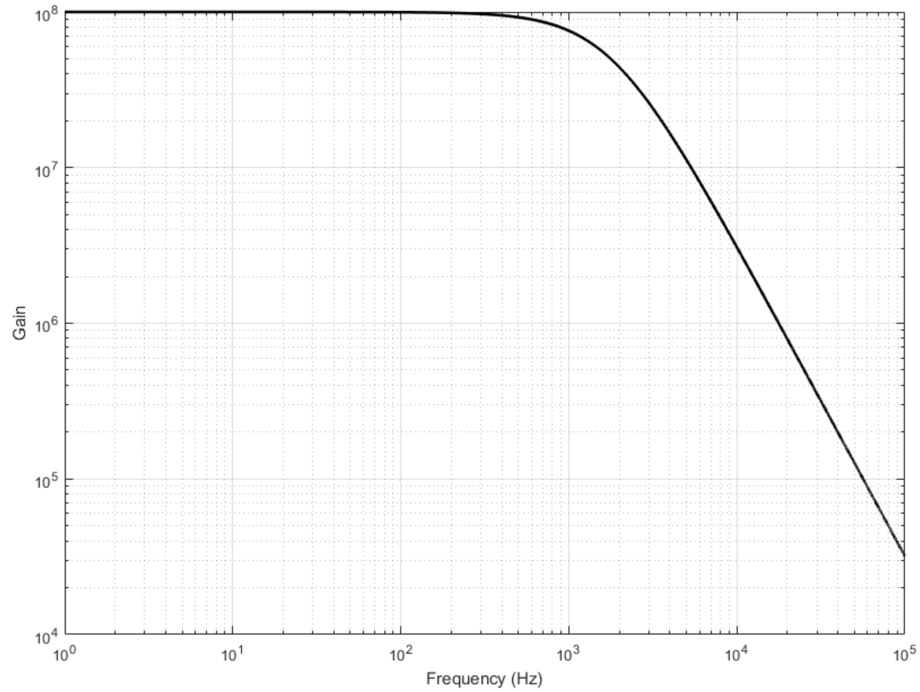

Figure 8.43 Pre-amplifier frequency response.

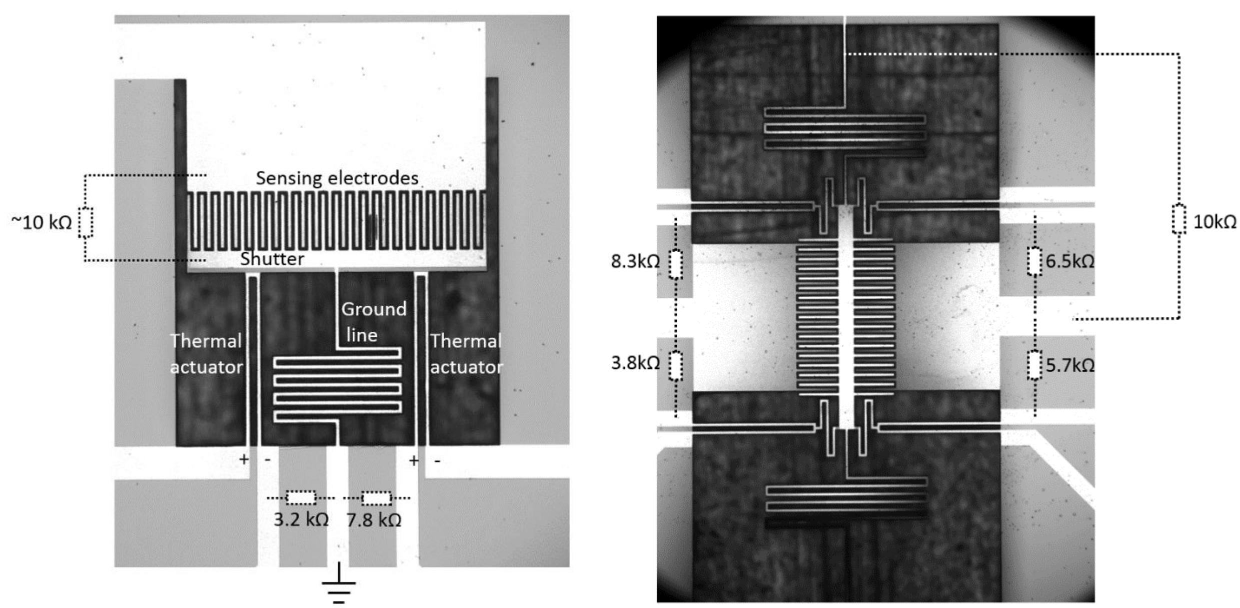

Figure 8.44 Conductivity between the sensing electrodes, thermal actuators and the ground line.

8.4.3.2. Shielding effect test:

As the device fabricated from section 8.3.2.3 has electrical isolation issue, how to test the sample to verify it is working? The solution is to drive the thermal actuators movement by external heating. When the sensor presents in an electric field, the induced charge still tend to flow to the virtual ground end of the current to voltage amplifier as shown in Figure 8.45. The shutter height can be adjusted by controlling the external heater temperature, which results in different induced current. The shutter's periodic movement can be simulated by replacing the external dc electric field with an ac electric field.

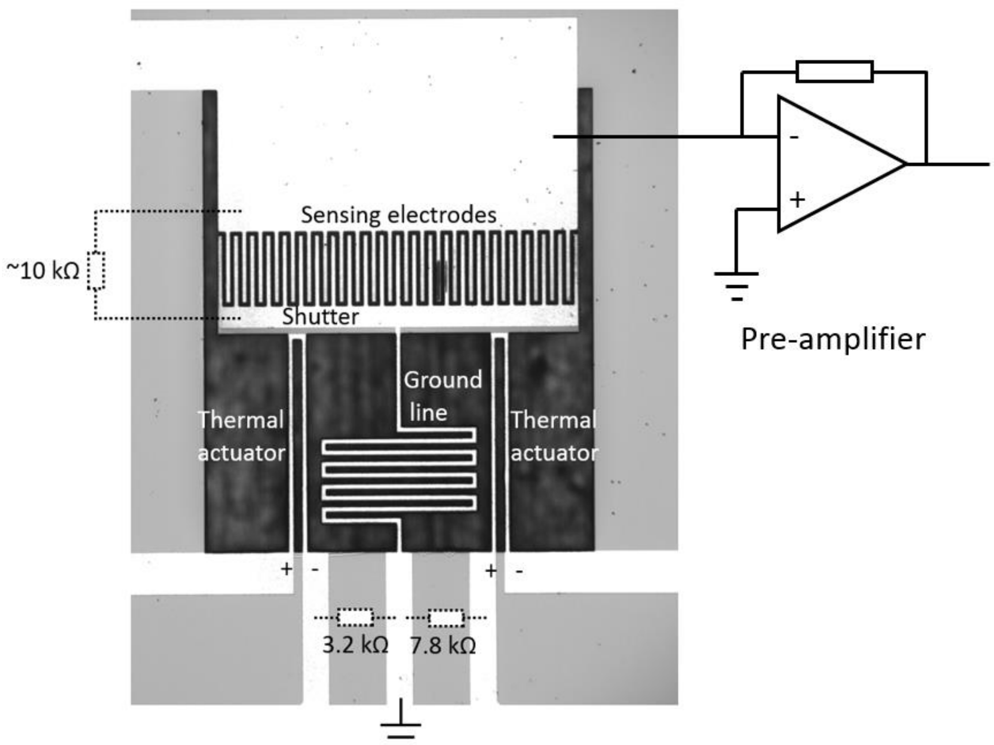

Figure 8.45 Testing for the sensor with sensing electrodes electrically connects to ground.

In the test, the sensor was placed in an ac electric field, and the induced charge on the electrodes was measured at different heights of the sensor's shielding shutter. Shutter height was changed by placing the sensor on an aluminum plate, which was on a digital hot plate. By heating the thermal actuators using the hot plate, the shutter can be lowered without any interfering signal from thermal actuator drive voltage. A thermocouple was connected to the aluminum plate, to directly measure the temperature of the plate. Since the sensor is fabricated from silicon and ~5 mm from the thermocouple, which is a good thermal conductor, it is assumed it is as the same temperature as the aluminum plate.

The fork shaped sensor shown in Figure 8.37 was tested first. Figure 8.46 shows the shielding effect test setup schematic. And Figure 8.47 shows the schematic of preamplifier. A coaxial cable was used to provide the ac electric field. The distance from the tip of coaxial cable to the sensor was closely spaced at 3 mm. so as to minimize charging other parts of the sample substrate. A function generator provided 10 V sine wave ac voltage at 1 kHz. It was connected to a transformer with a 1:11.8 turns ratio to increase the ac voltage amplitude to 118 V. The average amplitude of the generated ac electric field at the sensor surface was determined by COMSOL simulation, and found to be 9.4 kV/m. The simulation model is shown in Figure 8.48.

The sensor response to the ac electric field is shown in Figure 8.49. The test was done first heating the sensor to 100 ºC, then turning off the digital hotplate. While the sensor slowly cooled over an ~ 1 hour period, readings were taken at 100 ºC, 90 ºC, 80 ºC, 70 ºC, 60 ºC, 50 ºC, 40 ºC, 30 ºC, and 25 ºC. Figure 8.50 plots the measured sensor responses. As we can see, when temperature is higher, the sensor signal is higher. This is expected as thermal actuator has aluminum on the top of silicon, and the shutter's height is lower than sensing electrode when it is heated. The bridge shaped actuator was also tested and the result is also plotted in Figure 8.51. The equipment used in this test are: E3632A Agilent dc Power Supply, 33120A Agilent Function Generator,Tektronix TBS 1052B-EDU Digital Oscilloscope and Thermolyne Mirak hotplate.

The measured shutter displacement at 100 ºC from section 6.4.1 was 25 μm for bridge shaped shutter and 47 μm for fork shaped shutter. Referring to the simulated shielding effect of the shutter for these shutter displacements which was calculated in Figure 6.27, it would be expected that at a 9.4 kV/m electric field at 1 kHz, the signal on the oscilloscope (with the 10^8 A/V gain of the pre-amplifier) would be 5.6×10^{-3} V for the fork shaped shutter and 5.1×10^{-3} V for the bridge shaped shutter. The simulated and measurement value is indicated in Figure 6.51 (fork-shaped) and in Figure 6.51 (bridge-shaped) for comparison. As we can see that simulation results are in close agreement with the measured results.

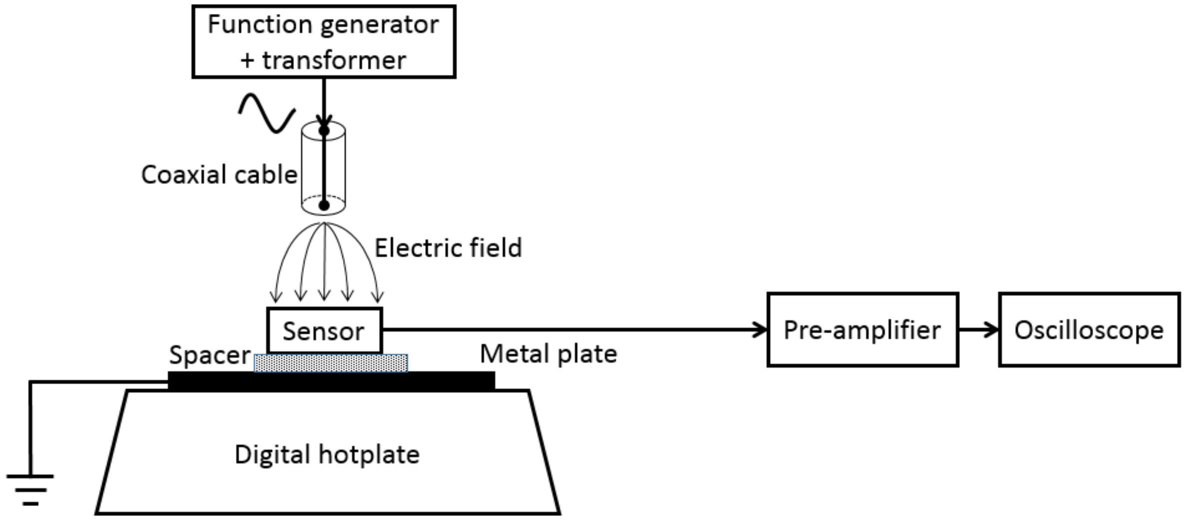

Figure 8.46 Shielding effect test schematic diagram.

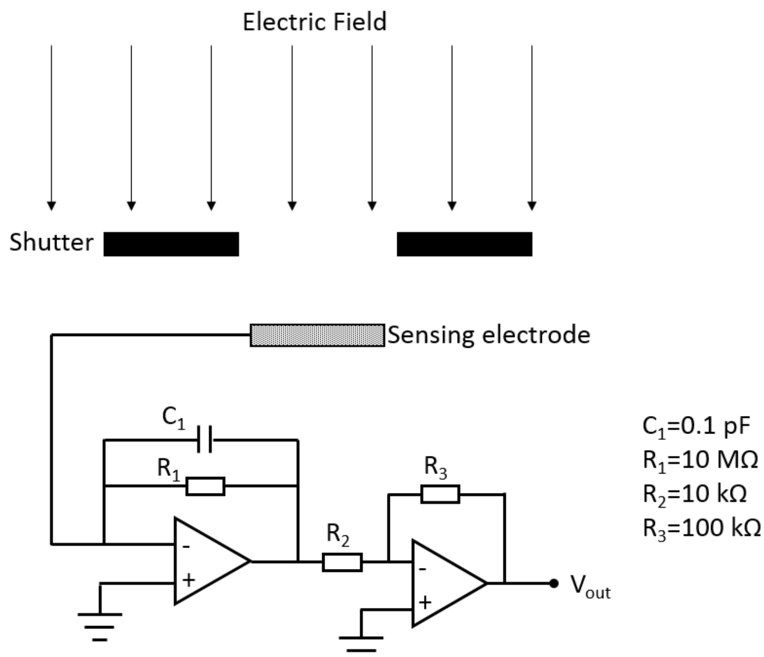

Figure 8.47 Sensor test pre-amplifier schematic diagram.

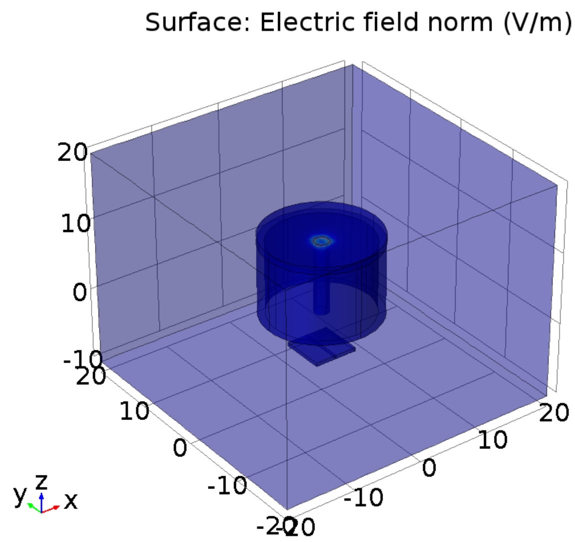

Figure 8.48 Coaxial cable generated electric field simulation model.

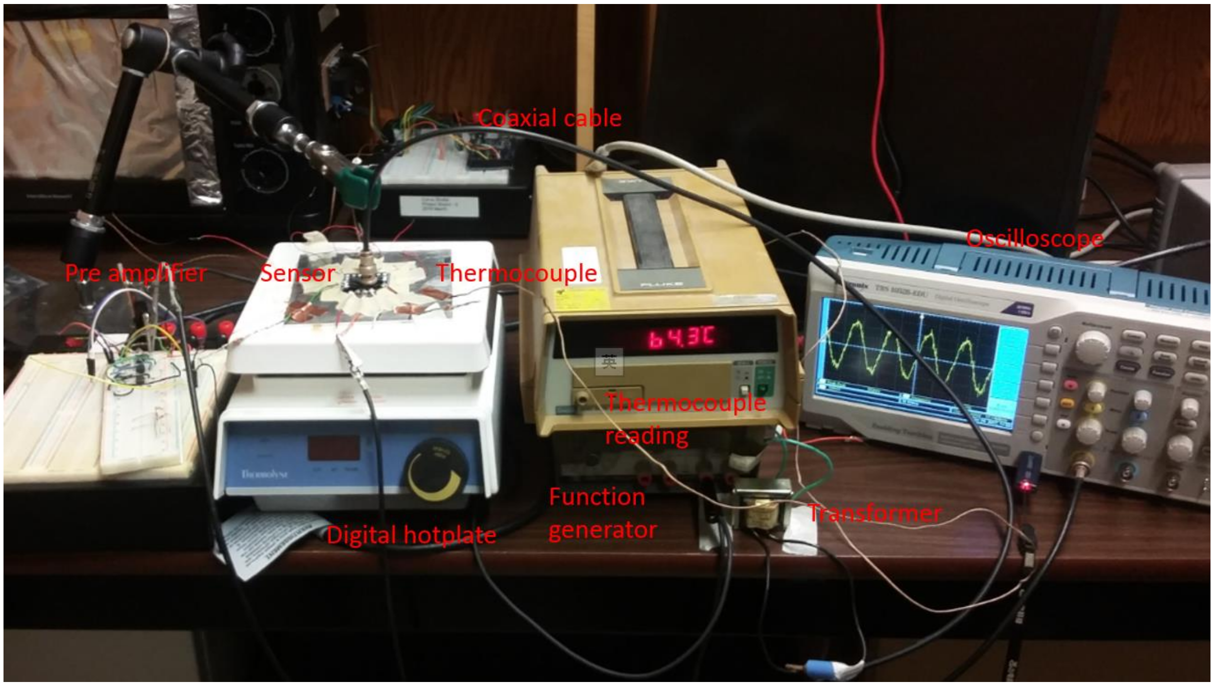

Figure 8.49 Shielding effect test setup.

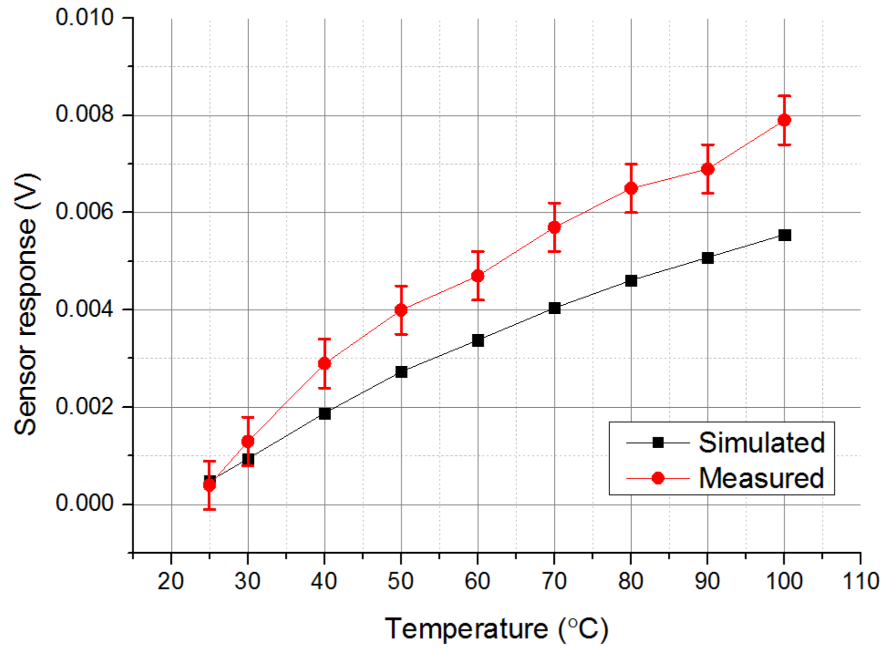

Figure 8.50 Fork shaped shutter response simulation vs. measurement.

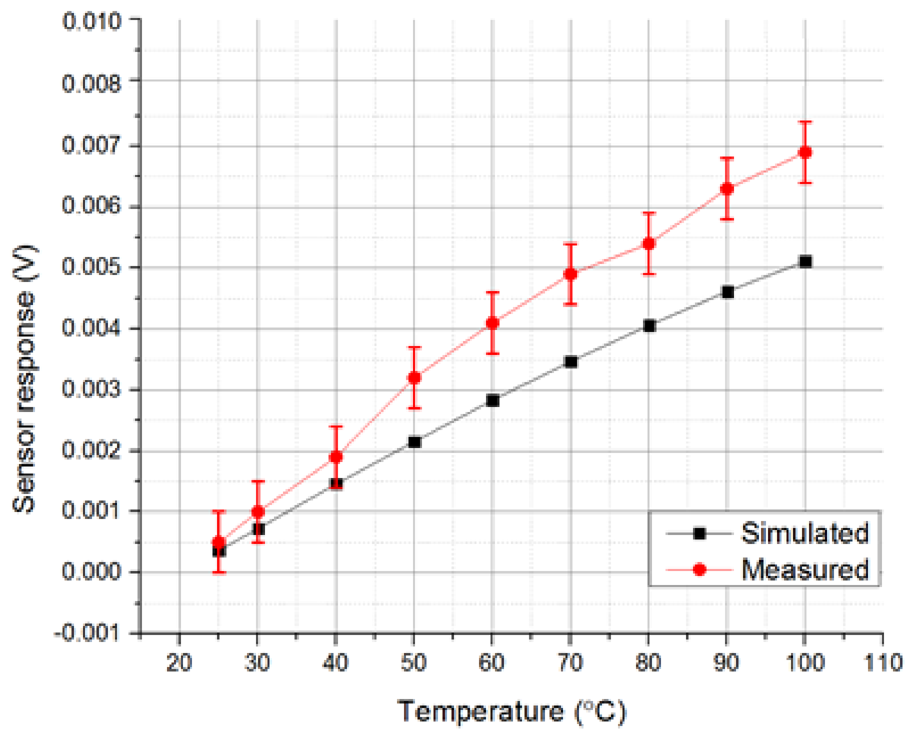

Figure 8.51 Bridge shaped shutter response simulation vs. measurement.

8.5. The fix of isolation issue

The sensors tested in section 8.4 had electrical isolation issue between the sensing electrodes, grounded shutter and thermal actuators. In the device fabrication, the silicon is coated with SiO_2 as an electrical insulator, and then coated with aluminum. There are two possibilities for this unexpected conductivity:

- Aluminum residue residing on the sidewall (section 8.5.1.1).
- Bad quality of the SiO_2 isolation layer (section 8.5.1.2).

Efforts to address both possible issues were undertaken, and the results are discussed below. After these efforts, it was found that the root cause of this issue was bad quality of the SiO_2 layer, which becomes porous after KOH etching. The solution was to remove the SiO_2 layer and grow a new SiO_2 layer by a thermal oxidation process.

8.5.1.1. Aluminum residue on sidewall

The fabrication process that was developed required the coating of aluminum twice, either by sputtering or thermal evaporation. The second aluminum coating was deemed necessary because it was found that the initial aluminum layer became damaged after patterning the underlying SiO_2 layer. And so, it was decided to remove this aluminum and deposit a second aluminum layer, which is to be patterned to be the device, wiring, and electrical pads. After fabrication, it was discovered that there was electrical leakage between normally separate aluminum wiring elements.

It was assumed that the leakage issue was due to aluminum residue on the sidewall. This could be caused by incomplete photoresist removal on the feature sidewalls during lithography, since the photoresist is thicker in those locations. And incomplete photoresist removal would result in aluminum residue remaining on the sidewalls.

Attempts to resolve this issue:

The first attempt was to remove the first aluminum layer and reform the second aluminum layer, with an improved lithography process to help remove the photoresist (HPR504 photoresist) hiding on the sidewall. The height of the sidewall is ~1 µm (0.5 µm SiO_2 + 0.5 µm Al). In the spin coating process, a higher spin speed was used to get thinner photoresist. Previously, the spin speed was 3000 rpm and the photoresist thickness was 1.5 µm thick. The spin speed was increased to

5000 rpm, and the photoresist thickness was reduced to 1.2 µm. Additionally, the UV exposure time and photoresist development time were increased. UV exposure time was increased from 5 seconds to 10 seconds and developing time was increased from 45 seconds to 90 seconds. The second aluminum layer was again etched. However, similar leakage resistances were still found to exist between sensing electrodes, grounded shutter, and thermal actuators. The possible reasons could be:

(1) That we were unsuccessful in removing the sidewall residue.

(2) That the sidewall residue was not a problem.

A second attempt was done to gather more information. One possibility is to avoid using a two aluminum process. This would prevent a sidewall residue problem, but would require the aluminum to not be damaged during the SiO_2 etch. There are two ways to etch SiO_2: BOE etch (buffered HF acid) or plasma etch. In experimenting with both ways, the lithography using the protective photoresist layer (1.5 µm thick) was modified to add a 20 minute hard bake at 120 °C.

Plasma etching of SiO_2 was explored first, and the SiO_2 was etched successfully without damage to the aluminum layer. After that, the aluminum layer was patterned. However, conductivity was still found to exist between the sensing electrodes, grounded shutter, and thermal actuators. This experiment showed that aluminum residue on the sidewall is not the main cause of unexpected conductivity.

The second attempt was to use BOE to etch SiO_2. However, it was discovered that due to porous SiO_2 (because SiO_2 becomes slightly damaged after KOH etch) the photoresist failed to protect the aluminum, since the aluminum can be attacked from below during the SiO_2 etch (see Figure 8.52). Given that the SiO_2 itself is porous, it was decided that like that was the reason for the electrical leakage. Essentially, it is failing to electrically isolate the aluminum from the underlying silicon. The consequence is the aluminum layer contact to the p-type doped silicon substrate, providing an extra conductivity path.

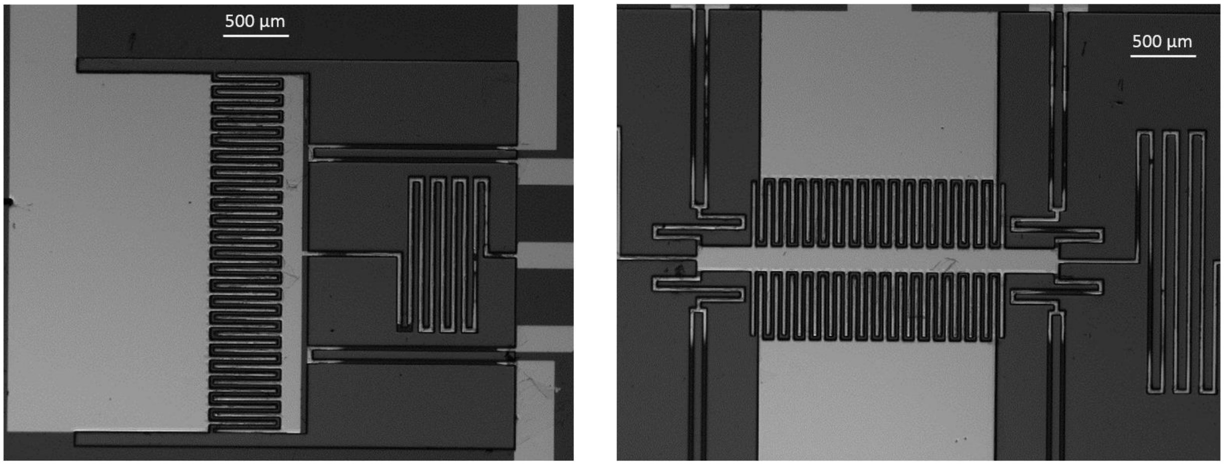

Figure 8.52 Aluminum damaged after using BOE to etch SiO_2.

8.5.1.2. Preventing bad quality of the SiO_2 isolation layer

Based on what learnt from attempt 3 above, the SiO_2 layer used as the mask from the KOH etch was removed and then a new SiO_2 layer was grown using thermal oxidation process. The original SiO_2 was etched in a BOE solution for 20 minutes. Then the sample was put into a piranha solution to clean the surface for 10 minutes. Next thermal oxidation in the furnace at 1100 ºC for 2 hours was done, and the thickness of the grown SiO_2 layer was measured to be about 500 nm. Then aluminum thermal evaporated and patterned for the SiO_2 etch, front side silicon etch for about 20 µm deep. Then, lithography was again done for the aluminum conductor patterning. Then the sensors were successfully released by a silicon etch from the backside of the wafer.

The resistance between electrical pads was measured. The sensing electrode, grounded shutter, and thermal actuators were found to be isolated completely. The resistances of thermal actuators plus the wiring on the sample are measured in the range of 10-15 Ω (the calculation is 9-12 Ω). This resistance includes the thermal actuator and wiring. The only exception is on the fork-shaped sensor, were the thermal actuators and grounded shutter are still electrically connected. However, it was discovered by microscope inspection that a little aluminum still exists between them, as can be seen from Figure 8.53. Overall, this fabrication result proved that the SiO_2 layer quality was the key problem that caused the electrical isolation issue.

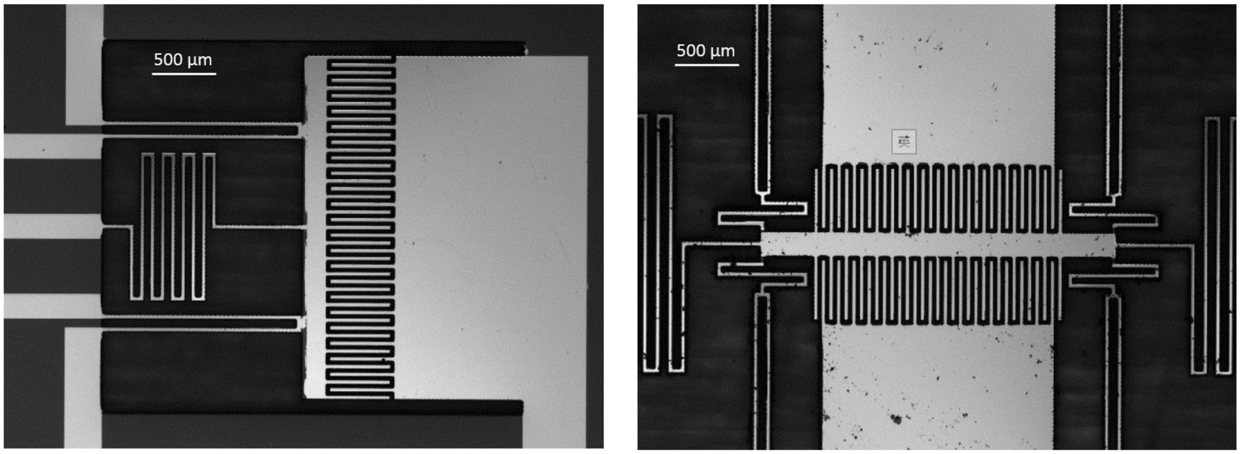

Figure 8.53 Released sensors based on re-grow SiO_2 isolation layer.

8.5.1.3. Sensor testing

In this test, bridge shaped shutter from fabrication attempt 4 was tested (Figure 8.53). It had a silicon thickness of 20 µm (± 2 µm), and width 25 µm (± 3 µm, less than the designed size of 40 µm due to SF_6 plasma etch undercut and also the overetch from the release process). Before the test, wires were bonded to electrical pads, and a 100 Ω series resistor (as a current limiter) was attached to each thermal actuator. The actuators were verified to be working first, by putting the sample into an oven and heated up to 100 ºC. They were removed and the shutter movement was measured under a microscope. The fork shaped shutter movement was measured to be 40 µm and bridge shaped shutter movement was measured to be 18 µm. The thermal actuators were then tested by directly driving them. The voltage was gradually increased from 1 V to 9 V, and the shutter movement was measured by using a microscope. The bridge-shaped shutter movement was measured to be about 11 µm (± 2 µm) at 9 V (82 mA). Unfortunately, when the voltage increased to 10 V, three actuators were burned as shown in Figure 8.54. The current to burn the actuator occurred at about 10 V / 110 Ω = 91 mA. Under this current, the highest temperature on the actuator is simulated to be 300 ºC (cross section 40 µm × 0.5µm) to 530 ºC (cross section 30 µm × 0.4 µm. Also, the current density is calculated to be in the range of 4.5×10^5 - 7.5×10^5 A/cm^2, which is higher than the electromigration limit for aluminum wiring in IC circuits (1×10^5 A/cm^2).

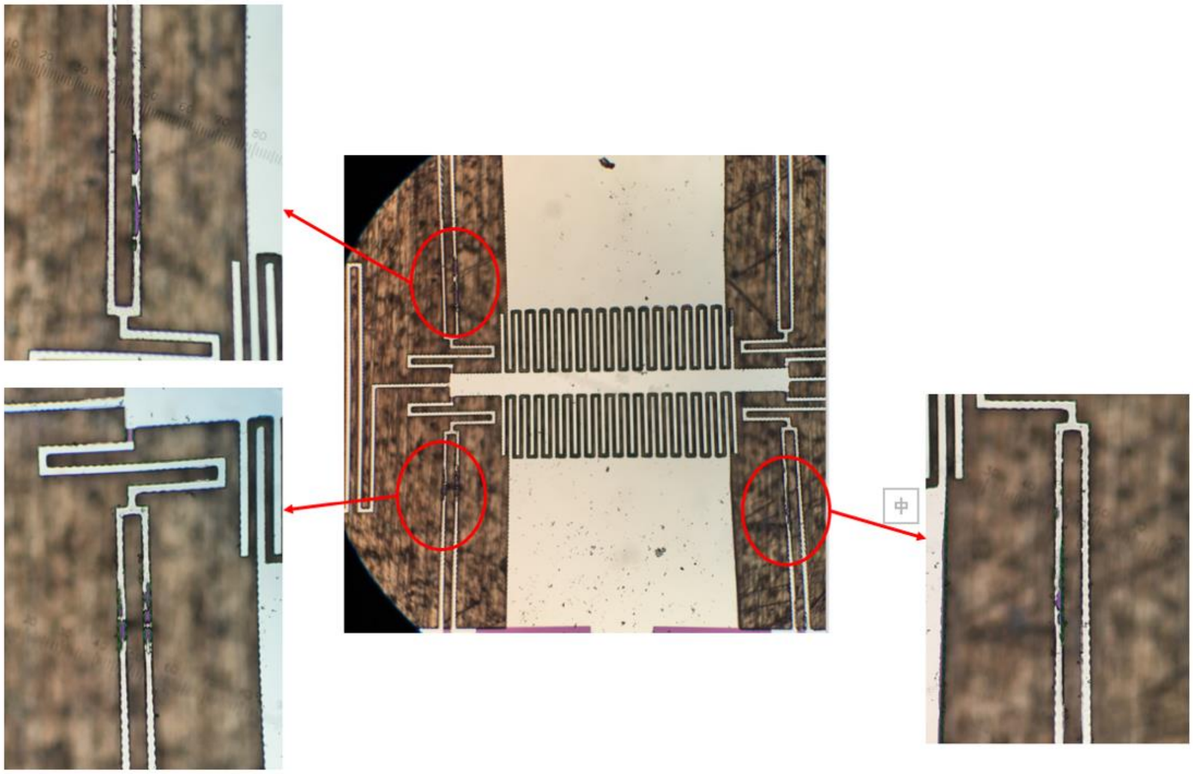

Figure 8.54 The burned actuators.

8.6. Summary

This chapter presented a vertical movement shutter type electric field mill. Several types of actuators were designed, fabricated and tested. To improve the actuator thermal dynamic performance, the effect of a titanium heater was also simulated. Devices fabricated from SU-8-Al were found to suffer from the intrinsic stress of aluminum thin film. It was also discovered that SU-8 suffers permanent deformation when heated up. Si-Al based devices were then designed and fabricated. The first sample had a titanium heater, however, the titanium failed to survive the plasma silicon etch process. The fabrication process was changed to avoid using a titanium heater. The sample was successfully fabricated with measured actuator resistance in the range of 10-16 Ω (plus wiring). When testing it by applying a current, the measured shutter movement agrees with the simulation results. However, an electrical isolation issue between the sensing electrodes and ground was present. The root cause of the isolation issue was poor quality of the SiO_2 insulation layer, which was caused by the KOH etching. The solution was to remove the SiO_2 layer and grow a new SiO_2 layer after the KOH etch.

8.6.1. Minimize thermal actuator size

Some consideration can be given to a different thermal actuator size. Consider the sensor fabricated in section 8.3.2.3 as an example. It has thermal actuator length of 1500 μm and silicon thickness of ~12.5 μm. If the length was reduced to half (750 μm) and the silicon thickness reduced to 4 μm, according to equation (7-1), the cantilever flexibility will increase about 4 times,

$$\mathrm{k} = \frac{Ewt^3}{4l^3} \qquad (8\text{-}3)$$

where E is the Young's modulus, t is thickness, w is width, and l is length. The increase in flexibility would then require less heat and so less power to move the actuator. Heat reduction also would result in a lower drive current. This would help increase sensor lifetime, as the electromigration effect would be reduced. Other materials with lower electromigration tendency than aluminum could be considered to increase lifetime. An example could be to replace the aluminum metal with copper.

Consideration should, however, be given to thermal dissipation. The thinner silicon would reduce it, but the shorter length similarly shortens the heat dissipation path. Considered together, a slight increase in the thermal time constant would result. However, according to the discussion in section 8.1.1, a smaller sized shutter would require less movement to achieve relatively higher response. Therefore, requiring less thermal actuator driving power, and so a further reduction in drive current. Overall then, the dynamic thermal response can be potentially improved.

8.6.2. Narrower finger space

In section 8.1.1 discussed the shielding effect on various finger spacing, where narrower finger spacing shows better shielding effect. Again consider the sensor fabricated in section 8.3.2.3 as an example. It has finger spacing of 80 μm, while the sensing electrodes width is 40 μm. If we were to reduce the finger spacing to 60 μm, the shielding effect would increase ~5%, giving a larger charge variation ($\Delta Q\%$). Moreover, if we were to reduce the sensing electrode width to 20 μm, and reduce finger spacing to be 40 μm, the shielding effect will increase about 14%. The simulation results are shown in Figure 8.55.

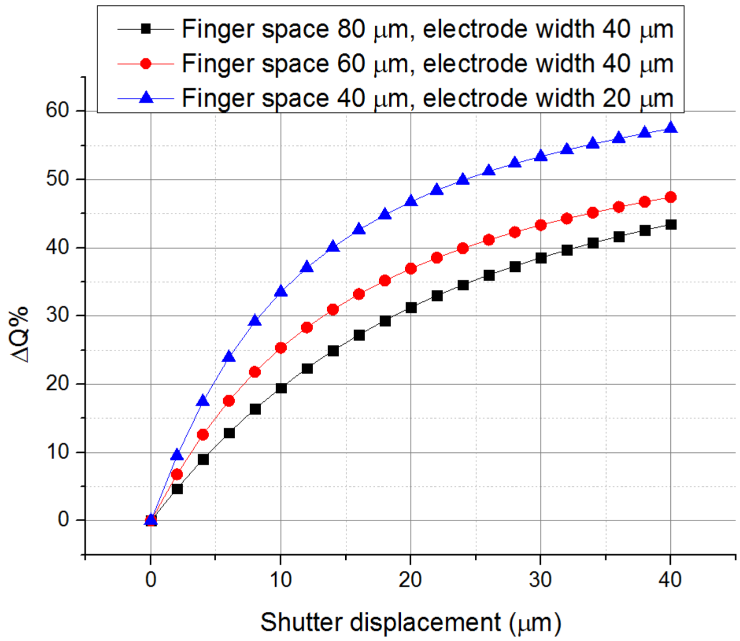

Figure 8.55 Narrower finger spacing shielding effect simulation.

Chapter 7 – Summary, conclusions and future Work

9.1. Summary

The focus of this work is on the dc electric field sensor design, fabrication and testing. The main contributions are:

(1) Designed the first SOI membrane based electric field sensor. I also developed the SOI wafer fabrication process for the Nano Systems Fabrication Laboratory (NSFL) at University of Manitoba.

(2) Developed a capacitive interrogation system to measure the displacement of the SOI membrane and the ribbon array sensors.

(3) Designed the first ribbon array based electric field sensor.

(4) Designed a new type of electric field mill that employs a vertically moving shutter. This included the concept design, scaled model testing, design of three types of thermal actuators (SiO_2/Al, polymer SU-8/Al, and Si/Al), fabrication of SU-8/Al and Si/Al actuator based sensor, and testing of Si/Al actuator based sensor.

9.2. Conclusions and future work

In this thesis, several types of micromachined electric field sensors have been studied. They can be classified into two categories: electrostatic force deflection sensors and vertical movement shutter field mills. Compared to other micromachined electric field mill (MEFM) sensors, both types of sensors overcome the issue of grounded shutter displacement under a large electric field and provide comparable or even higher performance.

9.2.1. Electrostatic force deflected SOI membrane sensor

This is the first SOI wafer based MEMS sensor that has been fabricated in our lab. The membrane with micro-spring structure was designed to achieve a membrane movement of approximately 0.1 nm to 10 μm, when exposed to dc electric fields ranging from 1 kV/m to 1000 kV/m respectively. Multiple motion techniques were studied including grating, field effect transistor and capacitance motion measurement methods. Finally the AD7747 capacitance to digital convertor chip was selected to measure the membrane motion. A capacitance interrogation system was built to interrogate the membrane motion. It successfully detected a dc electric field with a noise averaged resolution of 16 kV/m. The curvature of the SOI membrane prevented resolution improvement.

As a future work, if we were to fabricate the membrane from a bulk silicon wafer, it will improve the membrane flatness. In section 8.3, a process to fabricate a silicon based thin film structure was successfully applied and achieved ~5 μm deformation for a structure of over 1500 μm long and 10 μm thick.

9.2.2. Ribbon array capacitance sensor

The ribbon array sensor was designed to improve the sensor flexibility and therefore improve the sensor sensitivity. The effect of various parameters were investigated, including the connection between ribbons, ribbon width, jog angles, and gravity. It was fabricated from an aluminum thin film. A grounded sensor enclosure box was built and SMB coax cables were applied to solve the signal drifting issue in SOI capacitance measurement. The fabricated ribbon array achieved a resolution of 44 kV/m for dc electric field. However, the stress in the aluminum metal limited resolution, as close spacing to the electrode was not possible.

9.2.3. SOI membrane sensor optical measurement

A compact laser position monitoring system was built for the SOI membrane. The sensor was demonstrated to measure both ac and dc electric fields, and operates by using modulation of the electric field normal to the sensor. When implemented, the sensor resolution was 33 kV/m for a simply grounded sensing membrane. Subsequently, the force on the sensor was modulated by applying an ac bias to the membrane. It enables the sensor to have variable sensitivity by controlling the membrane bias voltage to modulate the electric field normal to the sensor, with the sensor output linearly scaled by the modulated bias voltage. Sensor sensitivity and resolution limitation were explored by using weak dc and ac electric fields. In these experiments, with 118.8 V (peak to peak) ac bias signal, the sensor demonstrated a peak sensitivity of 180 mV/(V/m), and noise limited resolution of 0.1 V/m. The sensor was also applied to measure an electric field under a mock transmission line located 0.75 m over the sensor. With the sensor operating at resonant frequency, the sensor sensitivity was 360 mV/(kV/m), and resolution was 17 V/m.

9.2.4. Vertical moving shutter field mill

This is a new type of MEFM concept that employed a vertical moving shutter. One or two pairs of bi-material thermal actuators were used to provide vertical movement for the grounded shutter. Two shapes of actuator were considered – fork and bridge. Three groups of thermal actuator materials were modeled: SiO_2-Al, SU-8-Al, and Si-Al. Due to the high stress of SiO_2, the first attempt was to fabricate an SU-8-Al actuator. In testing the fabricated samples, it was found that SU-8 has a permanent deformation issue at high temperature. Later efforts were focused on the Si-Al actuator. The sensor mechanical performance test shows that when heated to 100 °C, the fork shaped shutter is able to move 47 μm and bridge shaped shutter is able to move 25 μm. A scale model experiment demonstrates that the shielding effect is almost the same as the simulation. The sensing principle was also verified by using an ac electric field as the field source, with the thermal actuators driven to movement with heating from a digital hot plate. These test results also agreed with the theoretical calculated results.

As discussed in section 8.6, the future optimization for the vertical field mill design could include miniaturization of the sensor. A smaller sized actuator would have less overall stress, which would make possible the use of a thinner silicon layer. This would then result in a more flexible thermal actuator. Finger spacing is another factor that affects sensor performance. Employing a narrower finger spacing would result in better shielding effect.

A future optimization for the vertical field mill design could include miniaturization of the sensor. A smaller sized actuator would have less overall stress, which would make possible the use of a thinner silicon layer. This would then result in a more flexible thermal actuator. Finger spacing is another factor that affects sensor performance. Employing a narrower finger spacing would result in better shielding effect.

Appendix A Charge simulation model

This COMSOL model is built to simulate the shielding effect of vertical movement shutter in section 8.1.1 and 8.2.3. The differences of the model used in these two section are the number and size of the fingers and sensing electrodes as states in each of the section. In the model, the grounded shutter and sensing electrodes are surrounded by four grounded plate to minimize the electric field to affect the simulation results from side, as shown in Figure A.1. Figure A.2 shows the sensing electrodes. The model is placed in an air box, where the bottom is grounded and the top (Figure A.3) has a voltage to generate the electric field.

In this model, the electric field is limited in a small air box and the sensor is surrounded by wide grounded plates. These conditions provide an ideal shielding effect environment. In reality, there is a big space and may not have grounded plates around, the sensor performance may slightly different than simulation, as the electric field can reach the sensing electrodes from the bottom.

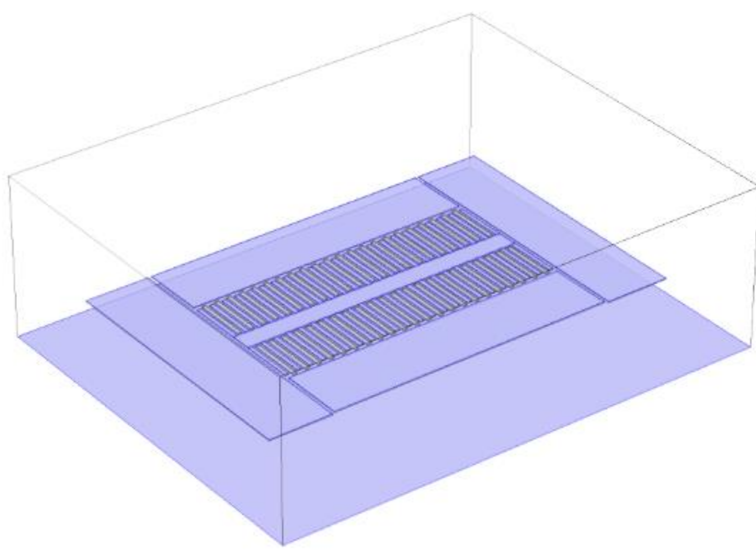

Figure A.1 The grounded parts in charge simulation model.

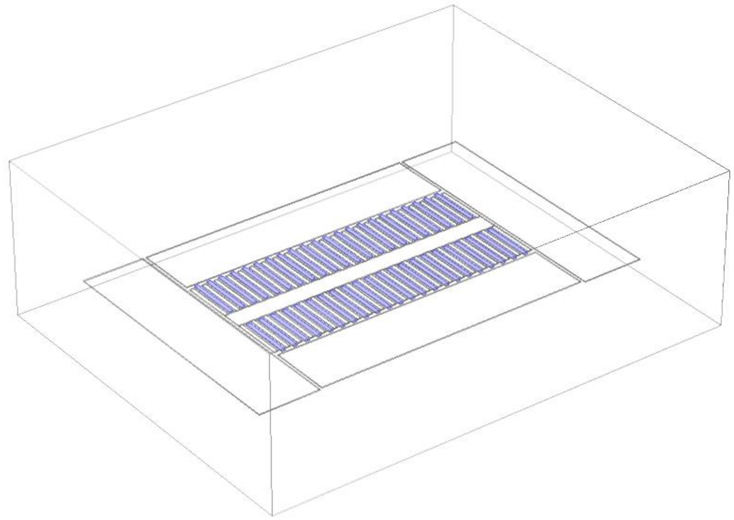

Figure A.2 The sensing electrodes in charge simulation model

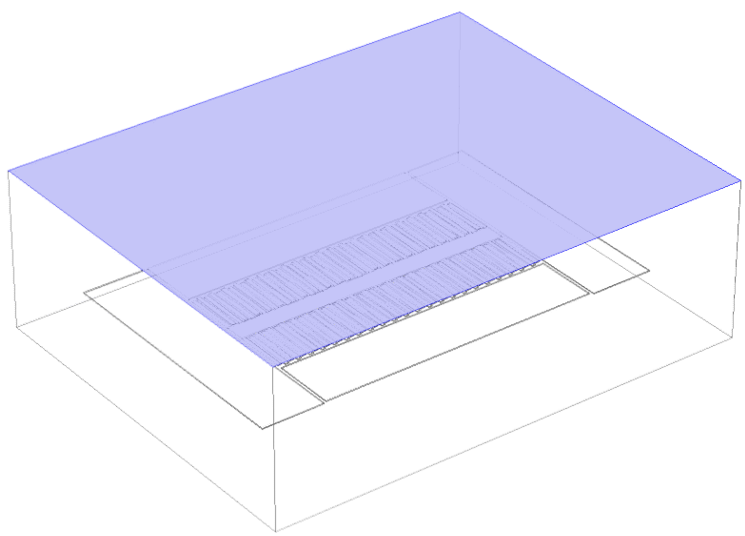

Figure A.3 Voltage on the top of the air box.

Appendix B SU-8 –Aluminum Bridge shaped thermal actuator simulation model

To make the simulation runs faster, the model build only quarter of the bridge shaped actuator as shown in Figure B.1. The location of the titanium heater is shown in Figure B.2, and Figure B.3 shows the location of the Aluminum on the thermal actuator. The calculated resistance of aluminum and titanium are 1.6 Ω and 2 Ω respectively. As stated in section 8.2.2, in the simulation a heat source of 0.5 mW is applied on the titanium heater and a 0.4 mW heat source is appled on on the aluminum cantilever. In this model, it contains half of the thermal actuator, therefore, 0.25 mW is applied on the titanium and 0.2 mW is applied on the aluminum. This power need 11 mA current. The simulation assumes there is no electromigration. However, as the cross-section of aluminum is 10 μm×0.2 μm, the current density of 11 mA is 5.5×10^5 A/cm^2. This is over the maximum current density of 1×10^5 A/cm^2 that aluminum can support to avoid electromigration. Therefore, in reality, the fabricated sensor based on this simulation need to run with larger cross-section aluminum conductors. Alternatively, the aluminum can be replaced by another material that has higher electromigration resistance, such as copper.

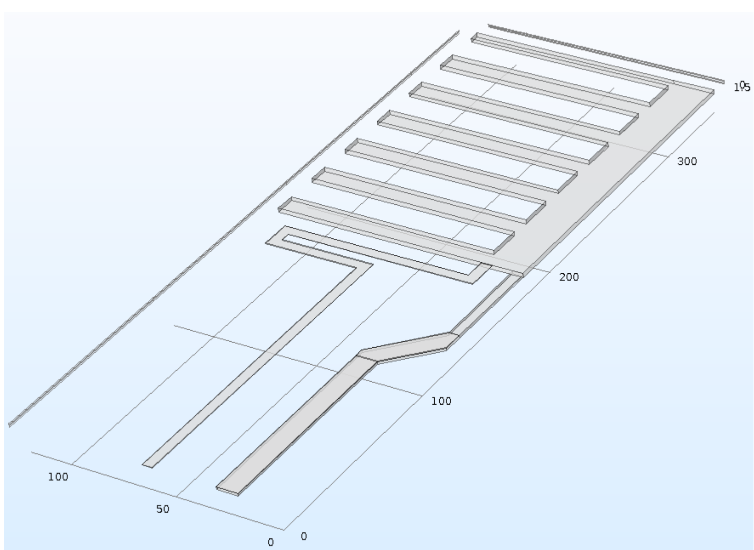

Figure B.1 COMSOL model of the SU-8 –Aluminum bride-shaped actuator.

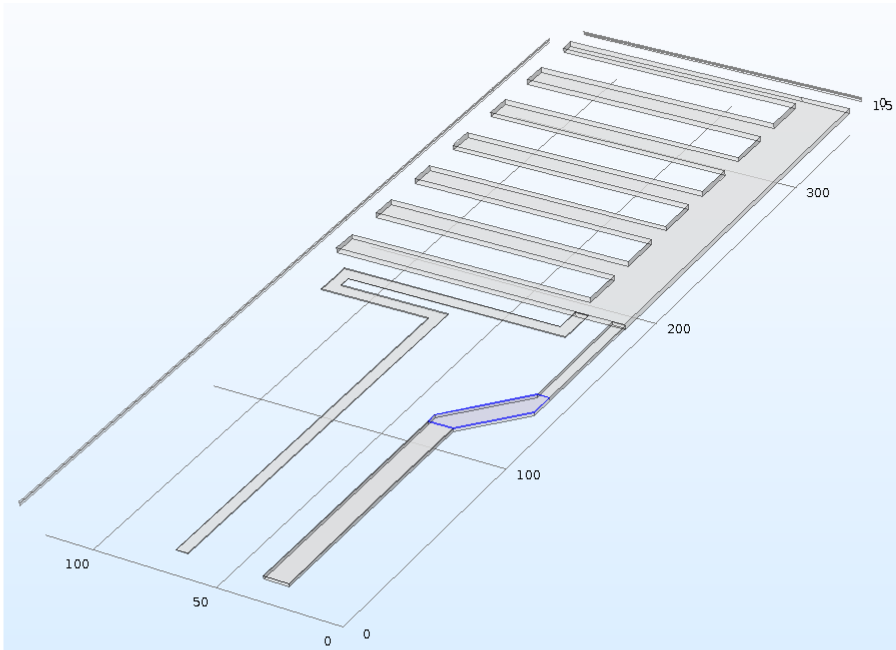

Figure B.2 Titanium heater on the SU-8 –Aluminum bride-shaped actuator.

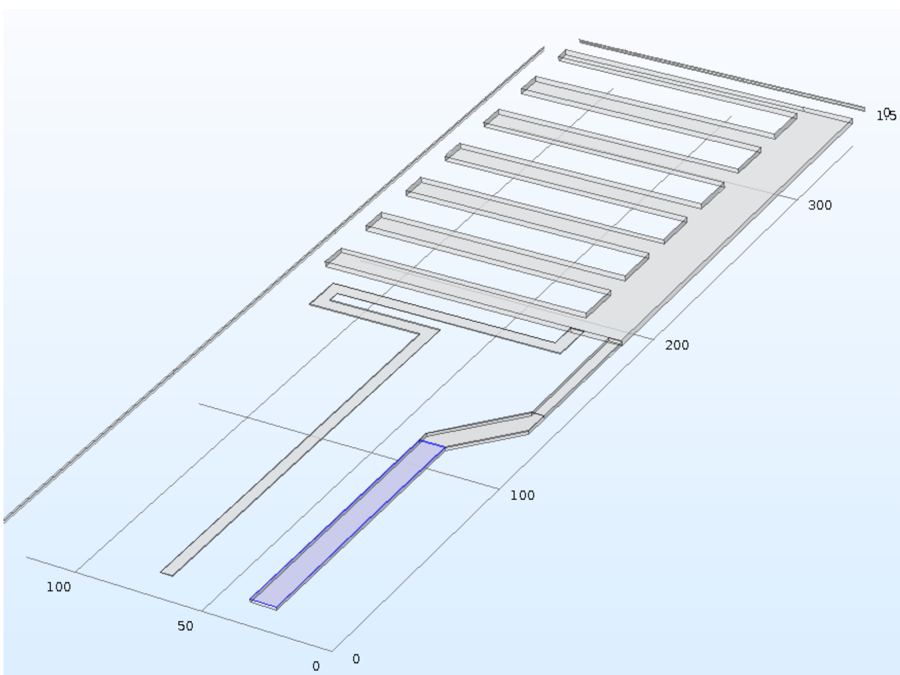

Figure B.3 Aluminum heater on the SU-8 –Aluminum bride-shaped actuator.

Appendix C SU-8 –Aluminum fork-shaped thermal actuator simulation model

The bridge shaped actuator simulation model built in COMSOL is shown in Figure C.1. The location of the titanium heater is shown in Figure C.2, and Figure C.3 shows the location of the aluminum on the thermal actuator. The calculated resistance of aluminum and titanium are 1.5 Ω and 2 Ω respectively. As stated in section 8.2.2, in the simulation a heat source of 1 mW is applied on the titanium heater and a 0.76 mW heat source is appled on on the aluminum cantilever. This power needs 7 mA current. The simulation assumes there is no electromigration.

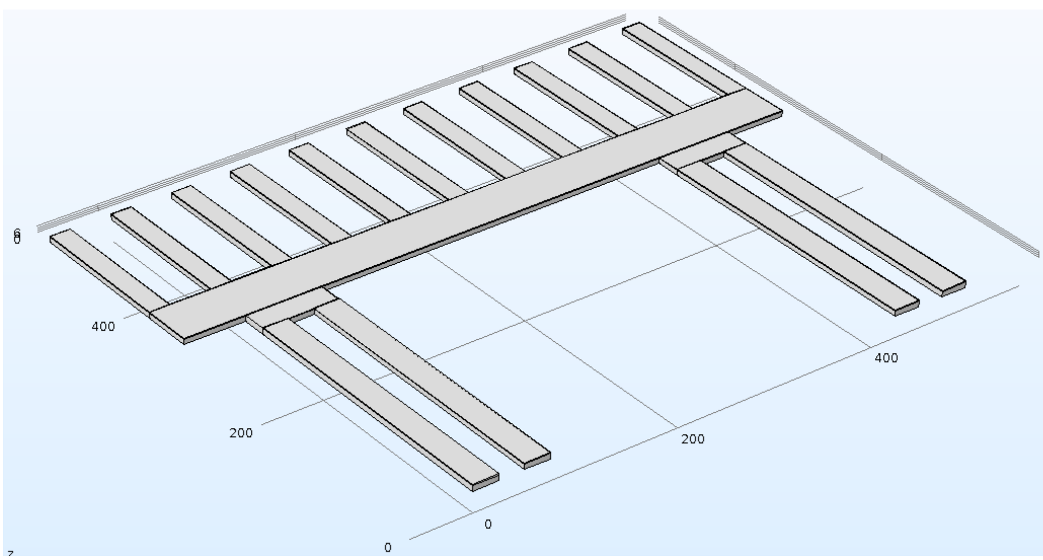

Figure C.1 COMSOL model of the SU-8 –Aluminum fork-shaped actuator.

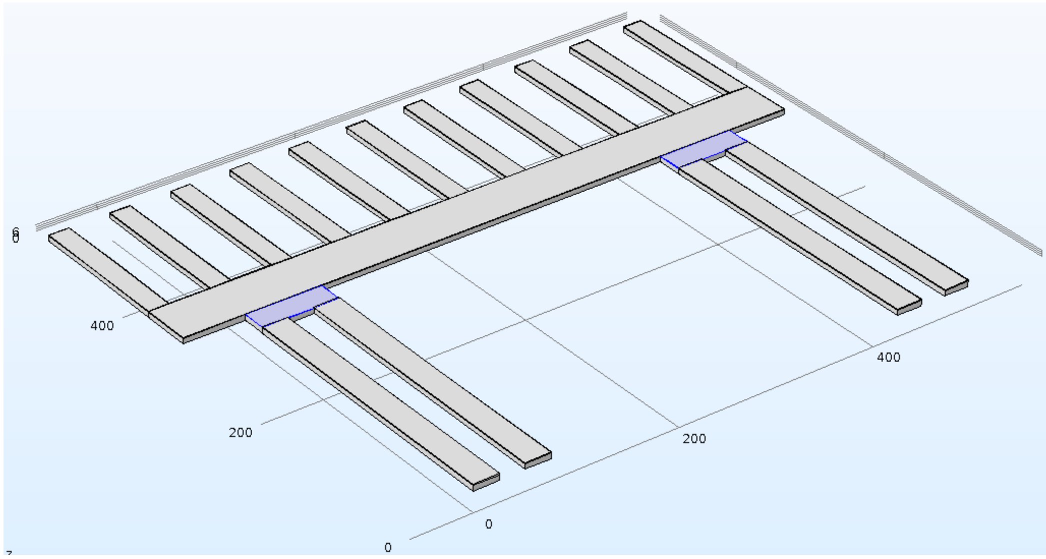

Figure C.2 Titanium heater on the SU-8 –Aluminum fork-shaped actuator.

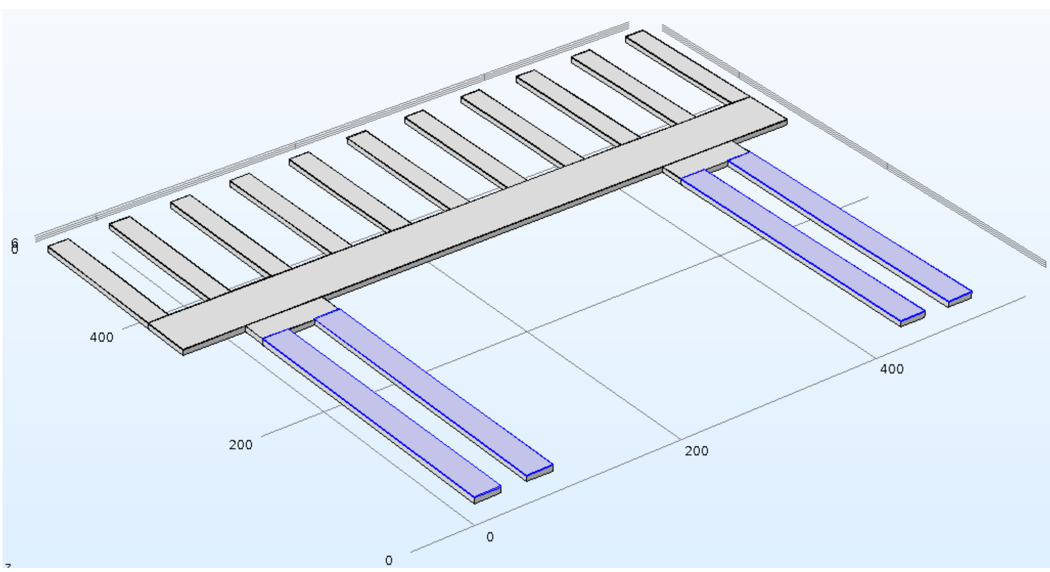

Figure C.3 Aluminum heater on the SU-8 –Aluminum fork-shaped actuator.

Appendix D Sensor angle in the field

The sensors described in this thesis need to be placed in the same plane with ground to achieve the highest sensitivity. Because if the sensor angle in the field, the sensor response will decrease with increase of the angle. A model (Figure D.1) was built to investigate the relationship between the angle and the electric field normal to the sensor. Figure D.2 and Figure D.3 shows the potential and ground applied to this model. Simulation was performed with angle from 0^o to 90^o. The electric field normal to sensor is affected by sensor angle, fringing effect, and ground plane hole shielding effect etc. Overall, the sensor response will decrease with increase of the angle. Figure D.4 shows the simulation results.

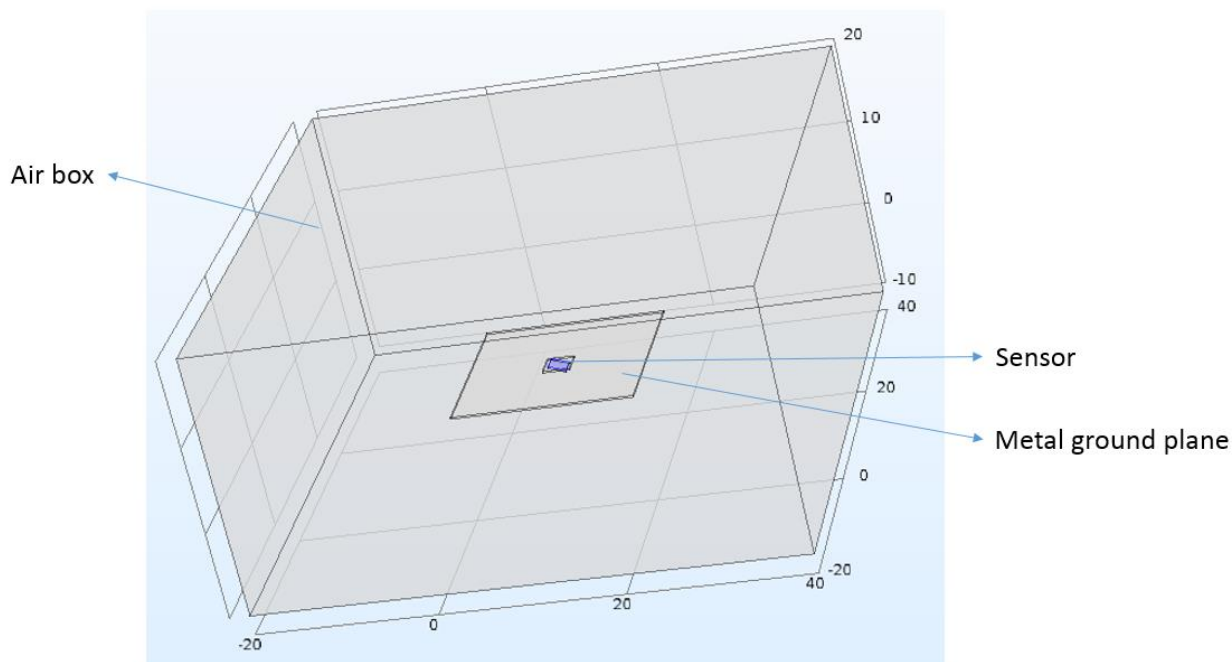

Figure D.1 Model for sensor angle in the field.

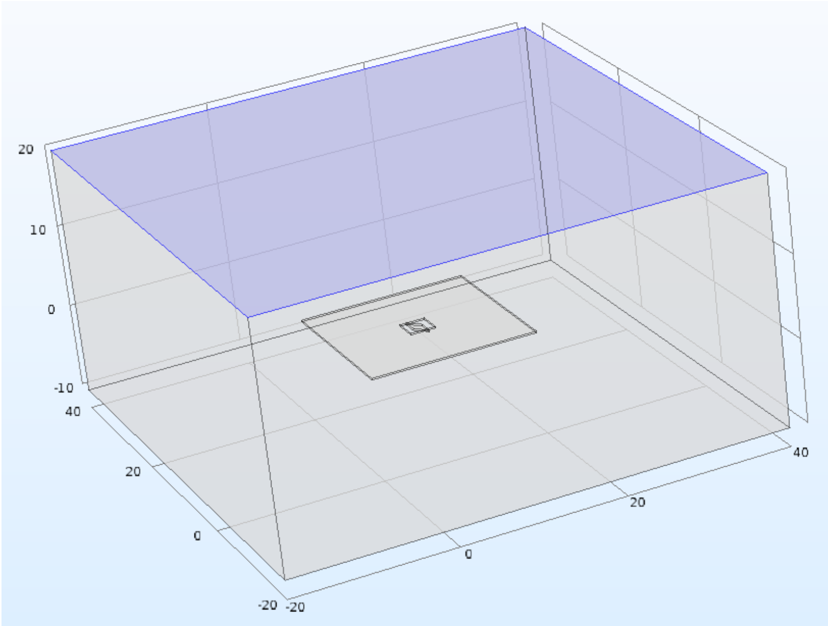

Figure D.2 Model top apply a positive potential.

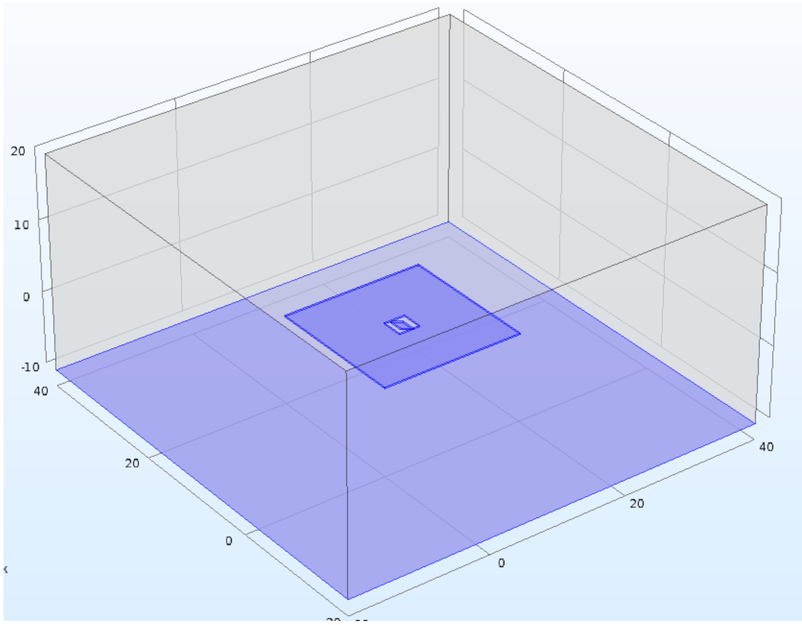

Figure D.3 Model grounded parts.

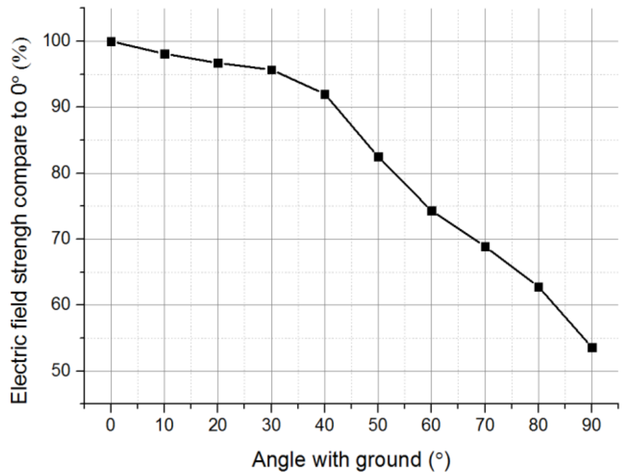

Figure D.4 Simulation results of sensor angle vs. electric field normal to sensor.

References

[1] M.Z. Jacobson, M.A. Delucchi, "Providing all global energy with wind, water, and solar power, Part I: Technologies, energy resources, quantities and areas of infrastructure, and materials", Energy Policy, Vol.39 (3), pp.1154 – 1169, 2011.

[2] R.W.D. Doncker, C. Meyer, R.U. Lenke, F. Mura, "Power electronics for future utility applications", Power electronics and drive systems, PEDS '07. 7th International conference, Bangkok, pp. K-1 - K-8, 27-30 Nov. 2007.

[3] P.S. Maruvada, R.D. Dallaire, R. Pedneault, "Development of field-mill instruments for ground-level and above-ground electric field measurement under HVDC transmission lines", IEEE Transactions on Power Apparatus and Systems, Vol. PAS-102, No. 3, pp. 738-744, March 1983.

[4] C.J. Miller, "The measurement of electric fields in live line working", vol. PAS-86. IEEE Transactions, pp. 493-498, 1967.

[5] D.M. Taylor and P.E. Secker, "Industrial electrostatics: fundamentals and measurements", New York: John Willey & Sons Inc, pp. 1-20, 1994.

[6] J. Montanya and J. Bergas, "Electric field measurements at ground level as a basis for lightning hazard warning", Elsevier. Journal of Electrostatics, vol. 60, pp. 241-246. 2004.

[7] AlphaLab, Inc, "Surface DC Voltmeter SVM2", AlphaLab, Inc company website,Web. 17 April 2018. https://www.alphalabinc.com/product/svm2/

[8] C. Li, X. Shen, and R. Zeng, "Optical electric-field sensor based on angular optical bias using single β-BaB_2O_4 crystal", Applied Optics, vol. 52, Issue 31, pp. 7580-7585, 2013.

[9] A.R. Johnston and H. Kirkham, "A Miniaturized space-potential DC electric field meter " *IEEE Trans. Power Delivery*, vol. 4, pp. 1253-1261, April 1989.

[10] H. Kirkham, "On the measurement of stationary electric fields in air", Conference on Precision Electromagnetic Measurements, pp. 524-525, June 2002.

[11] Mark N. Horenstein and Patrick R. Stone, "A micro-aperture electrostatic field mill based on MEMS technology", Elsevier. Journal of Electrostatics, vol. 51-52, pp. 515–521, May 2001.

[12] P.S. Riehl, K.L. Scott, R.S. Muller, R.T. Howe, and J.A. Yasaitis “Electrostatic charge and field sensors based on micromechanical resonators”, IEEE Journal of Microelectromechanical Systems, vol. 12, pp. 577–589, October 2003.

[13] G. Wijeweera, B. Bahreyni, C. Shafai, A. Rajapakse, and D.R. Swatek, “Micromachined Electric Field Sensor to Measure ac and dc Fields in Power Systems”, IEEE Trans. Power Delivery, vol. 24, pp. 988-995, July 2009.

[14] X.X Chen, C.R Peng, H. Tao, C. Ye, Q. Bai, S.F. Chen, and S.H. Xia, “Thermally driven micro-electrostatic field meter”, Sensors and Actuators A, vol. 132, pp. 677–682, 2006.

[15] T. Chen, C. Shafai, A. Rajapakse, B.Y. Park, “Micromachined Electric Field Mill Employing A Vertical Moving Shutter”, Eurosensors 2014, the 28th European Conference on Solid-State Transducers, vol. 87, Brescia, Italy, pp. 452-455, 7-10 September, 2014.

[16] S. Ghionea, G. Smith, J. Pulskamp, S. Bedair, C. Meyer, and D. Hull, “MEMS Electric-Field Sensor With Lead Zirconate Titanate (PZT)-Actuated Electrodes”, IEEE Sensors, Baltimore, MD, 3-6 Nov., 2013.

[17] P.F. Yang, C. Peng, H.Y. Zhang, S.G Liu, D.M. Fang, and S.H. Xia, “A high sensitivity SOI electric-field sensor with novel comb-shaped microelectrodes”, 16th International Transducers Conference, pp. 1034-1037, 5-9 June, 2011.

[18] T. Kobayashi, S. Oyama, M. Takahashi, R. Maeda, and T. Itoh, “Microelectromechanical systems-based electrostatic field sensor using Pb (Zr, Ti) O3 thin films”, Japanese Journal of Applied Physics, vol. 47, pp. 7533-7536, 2008.

[19] A. Roncin, C. Shafai, and D.R. Swatek, “Electric field sensor using electrostatic force deflection of a micro-spring supported membrane”, Sensors and Actuators A, vol. 123-124, pp. 179-184, September 2005.

[20] T. Chen, C. Shafai, “MEM Electric Field Sensor using Force Deflection with Capacitance Interrogation,” 2013 IEEE Power & Energy Society General Meeting, Vancouver, Canada, 21-25 July, 2013.

[21] J. Huang, X. Wu, X. Wang, X. Yan, L. Lin, "A novel high-sensitivity electrostatic biased electric field sensor." Journal of Micromechanics and Microengineering, vol. 25, 095008(9pp), 2015.

[22] Boltek Corporation, "EFM-100C RS485 Electric Field Monitor", Boltek Corporation company website,Web. 17 April 2018, http://www.boltek.com/product/efm-100c-electric-field-monitor

[23] CS110 Electric Field Meter Sensor, Campbell Scientific, [Online]. Available: “https://www.campbellsci.ca/cs110-sensor”

[24] Chao Gong, Shanhong Xia, Kai Deng, Qing Bai and Shaofeng Chen, “Design and simulation of miniature vibrating electric field sensors”, Sensors, 2004. Proceedings of IEEE, vol. 3, pp. 1589-1592, Oct. 2004

[25] Kirt R.Willianms, Dirk P. H.De Bruyker, Scott J.Limb, Eric M. Amendt, Vacuum Steered-Electron Electric field Sensor. Journal of Microelectromechanical System, Vol.23(1), pp.157-167, Feb. 2014

[26] Hong-Sik Jung, Electro-optic Electric field Sensor Utilizing Ti:LiNbO3 Symmetric Mach-Zehnder Interferometers, Journal of the Optical Society of Korea, Vol. 16, No. 1, March 2012, pp. 47-52, 2012

[27] C. H. Bulmer and W. K. Burns, “Linear interferometric modulators in Ti:LiNbO3,” J. Lightwave Technol. LT-2, 512-521 (1984).

[28] D. H. Naghski, J. T. Boyd, H. E. Jackson, S. Sriram, S. A. Kingsley, and J. Latess, “An integrated photonic Mach-Zehnder interferometer with no electrodes for sensing electric fields,” J. Lightwave Technol. 12, 1092-1098 (1994).

[29] Rob Legtenberg, Henri Jansen, Meint de Boer, and Miko Elwenspoe, “Anisotrapic Reactive Ion Etching of Silicon Using SF6/O2/CHF3 Gas Mixtures”, J. Electrochem. Soc., Vol. 142, No. 6, June 1995.

[30] Gottlieb S. Oehrlein, Steve W. Robey, and J. Lennart Lindström, ‘Surface processes in CF4/O2 reactive etching of silicon’, Appl. Phys. Lett. 52, 1170 (1988).

[31] L.Z. Ya, Ultra-high Voltage AC/DC Grids, Elsevier. Academic Press, pp. 313-315, 2015.

[32] M.A. Abdu, and D. Pancheva, “Aeronomy of the Earth's Atmosphere and Ionosphere”, Springer Dordrecht Heidelberg London New York, pp. 445-450, 2011.

[33] R. Miles, T. Bond, G. Meyer, “Report on Non-contact DC electric field sensors”, Lawrence Livermore National Laboratory, miles7@lllnl.gov, June 23, 2009.

[34] K.H.Müller, “Stress and microstructure of sputter-deposited thin films: Molecular dynamics investigations”, Journal of Applied Physics, 62, 1796 (1987); doi: 10.1063/1.339559

[35] Tansel Karabacak,a Jay. J. Senkevich, Gwo-Ching Wang, and Toh-Ming Lu, “Stress reduction in sputter deposited films using nanostructured compliant layers by high working-gas pressures”, American Vacuum Society, DOI: 10.1116/1.1861940, 2005

[36] R. Koch, “Stress in Evaporated and Sputtered Thin Films – A Comparison”, Surface and coating technology, Vol. 204, Issues 12-13, pp. 1973-1982, March 15, 2010

[37] G.C.A.M. Janssen, “Stress and strain in polycrystalline thin films”, Thin solid films, Vol. 515, Issue 17, pp. 6654-6664, 13 June 2007

[38] Plaza, J.A., M.A. Benitez, J. Esteve, and E.Lora-Tamayo, “New FET accelerometer based on surface micromachining”, Sensors and Acruators A: physical, Vol. 61, pp. 342-345, 1997

[39] Svensson, L., J.A. Plaza, M.A. Benitez, J.Esteve, and E. Lora-Tamayo, Surface micromachining technology applied on the fabrication of a FET pressure sensor. Journal of Micromechanics and Microengineering, Vol. 6, pp. 80-83, 1996

[40] Kuhnel, W. Silicon condenser microphone with integrated field-effect transistor. Sensors and Actuators A: Physical, Vol. 26, pp. 521-525, 1991

[41] F Mohd-Yasin1, D J Nagel and C E Korman, “Noise in Mems”, Measurement science and technology, Vol.21(1), p.012001 (22pp) ,2010

[42] Thomas Winterstein 1, Matthias Staab, Christian Nakic, Hans-Jürgen Feige, Jürgen Vogel and Helmut F. Schlaak, “SU-8 Electrothermal Actuators: Optimization of Fabrication and Excitation for Long-Term Use”, Micromachines, Vol 5, pp.1310-1322, doi:10.3390/mi5041310, 2014

[43] Winterstein, T.; Schlaak, H.F. “Electrothermal pseudo bimorph actuators made of SU-8 with improved mechanical performance” In Proceedings of ACTUATOR14, 14th International Conference on New Actuators and 8th International Exhibition on Smart Actuators and Drive Systems, Bremen, Germany, pp. 609–612. June 2014;

[44] R. Hickey, D. Sameoto, T. Hubbard, M. Kujath, “Time and Frequency response of two arm micromachined thermal actuators”, J. Micromech. Microeng., vol. 13 pp. 40-46, 2003.

[45] Q. A. Huang, N. K. S. Lee, “Analysis and design of polysilicon thermal flexure actuator”, J. Micromech. Microeng, vol. 9, pp. 64–70, 1999.

[46] T.B. Gabrielson. "Mechanical-thermal noise in micromachined acoustic and vibration sensors," IEEE Trans, Electron. Devices, Vol. 40, pp. 903-909, May 1993.